Radiative transfer modeling of Sagittarius B2

INAUGURAL – DISSERTATION

zur

Erlangung des Doktorgrades
der Mathematisch – Naturwissenschaftlichen Fakultät
der Universität zu Köln

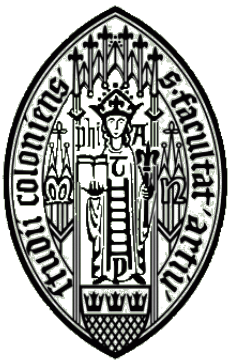

vorgelegt von

Anika Schmiedeke
aus Königs Wusterhausen

Köln 2017

Berichterstatter: Prof. Dr. Peter Schilke
Prof. Dr. Stefanie Walch-Gassner

Tag der mündlichen Prüfung: 04. Juli 2016

Für meine Familie

"The universe is full of magical things
patiently waiting for our wits to grow sharper."

Eden Phillpotts

"Somewhere, something incredible is waiting to be known.

Carl Sagan

Abstract

The majority of information gained in astrophysics is deduced from the analysis and interpretation of electromagnetic radiation received with ground or space based telescopes. Analyzing the radiation received from astrophysical objects provides us information about the source, but also about the medium in between the source and the observer. This makes radiative transfer analysis one of the most fundamental techniques in astrophysics. Up to now, radiative transfer approaches often have been limited either in the number of dimensions or in the applied geometry. But high spatially resolved images obtained at different wavelengths for example with the Very Large Array (VLA), the Herschel Space Observatory, and now the Atacama Large Millimeter Array (ALMA), reveal the complex nature of both the structure and the dynamics. Hence, when trying to analyze such complex structures and dynamics with simple (spherical) models, misleading results could occur. This requires detailed three dimensional radiative simulations, which are now computationally feasible.

In my work I have developed a framework called PANDORA that combines existing three dimensional radiative transfer codes (RADMC-3D for a self-consistent determination of the dust temperature and LIME for non-LTE line modeling) with a post-processing routine (using MIRIAD) and optimization algorithms (MAGIX).

I have employed PANDORA to model the thermal dust and free-free continuum as well as selected molecular lines of the intensively studied high-mass star-forming region Sagittarius B2 (Sgr B2). This prominent giant molecular cloud is the most massive region with ongoing star formation in the Galaxy. It is located at a distance of 8.5 pc (Reid et al. 2014), close to the Galactic supermassive black hole. The whole complex contains a total gas mass of 10^7 $M_\odot$, distributed in a large envelope of $\sim$ 22 pc in radius (Lis & Goldsmith 1989). The high densities ($> 10^5$ cm^{-3}) and temperatures ($\sim$ 50-70 K) in Sgr B2, together with its proximity to the Galactic Center make Sgr B2 an interesting environment of extreme star formation, different to typical star forming regions in the Galactic disk, but similar to active galactic centers that dominate star formation throughout the Universe at high redshifts.

Despite the large mass reservoir, star formation seems to be mainly occurring in the two hot molecular cores Sgr B2(N) and Sgr B2(M). These two sites of active star formation are located at the center of the envelope occupying an area of around 2 pc in radius. They contain at least 50 high-mass stars with spectral types ranging from O5 to B0, and constitute one of the best laboratories for the search of new chemical species in the Universe.

I successfully reconstructed a very likely three-dimensional dust density distribution, recovering continuum structures spanning two orders of magnitude in frequency (ν = 10 GHz – 1 THz) and four orders of magnitude in spatial scales (0.02 – 45 pc). Covering a wide range in frequencies at all spatial scales is crucial to successfully constrain the many free parameters and obtain a meaningful model. Some of the main highlights of this work are: (i) The density field of Sgr B2 can be reasonably well fit by a superposition of spherical symmetric density cores with Plummer-like profiles of varying

index . (ii) To reproduce the spectral energy distribution, I have to locate Sgr B2(N) along the line-of-sight behind the plane containing Sgr B2(M). (iii) The derived star formation efficiency are significantly different for both cores. For Sgr B2(N) it is rather low (5%), while for Sgr B2(M) the SFE is very high (50%). This indicates that most of the gas in Sgr B2(M) has already been converted to stars or dispersed.

In addition to the continuum studies, I have investigated the line-of-sight velocity field towards Sgr B2(M) using PANDORA.

Zusammenfassung

Ein Großteil der Informationen in der Astrophysik wird aus der Analyse und Interpretation der elektromagnetischen Strahlung astronomischer Objekte, welche von bodengebundenen oder Weltraumteleskopen detektiert wird, gewonnen. Die Analyse dieser Strahlung erlaubt Erkenntnisgewinn über die strahlende Quelle selbst, aber auch über das Medium zwischen der Quelle und dem Beobachter. Dies macht Strahlungstransportanalysen zu einer der fundamentalsten und wichtigsten Techniken der Astrophysik. Die meisten Strahlungstransportanalysen sind jedoch bisher zumeist entweder in der Anzahl der Dimensionen oder der angewandten Geometrie limitiert. Hochauflösende Beobachtungen bei allen Wellenlängen, beispielsweise mit dem Very Large Array (VLA), dem Herschel Space Observatory oder dem Atacama Large Millimeter Array (ALMA) enthüllen jedoch die komplexe Beschaffenheit sowohl der Struktur als auch der Dynamik astronomischer Objekte. Demzufolge kann es zu fatalen Resultaten führen, würde man versuchen solch komplexe Strukturen und Dynamiken mit einfachen (sphärischen) Modellen zu analysieren. Dies erfordert vielmehr detaillierte dreidimensionale Strahlungstransportsimulationen, welche heutzutage leichtungstechnisch möglich sind.

Im Rahmen dieser Doktorarbeit habe ich ein multifunktionales Programm names PANDORA entwickelt, welches die bereits existierenden dreidimensionalen Strahlungstransportprogramme RADMC-3D (ermöglicht eine selbst-konsistente Berechnung der Staubtemperatur) und LIME (ermöglicht non-LTE Berechnungen) mit einer Nachbearbeitungs- und Optimierungsroutine verbindet. Die Nachbearbeitung stellt die Vergleichbarkeit der Simulation mit Beobachtungskarten sicher. Dies erfolgt unter Verwendung von MIRIAD. Für die Optimierung wird MAGIX verwendet. PANDORA sorgt für eine reibungslose Kommunikation zwischen allen beteiligten Programmen.

Im zweiten Teil der Arbeit habe ich anschliessend PANDORA verwendet um die thermische Staub- und frei-frei Strahlung sowie ausgewählte molekulare Spektrallinien der außergewöhnlichen, massereichen Sternentstehungsregion Sagittarius B2 (Sgr B2) zu modellieren. Diese berühmte Molekülwolke ist die massereichste Region mit aktiver Sternentstehung in unserer Galaxie. Sgr B2 befindet sich in Projektion nah dem Galaktischen Zentrum in einer Entfernung von 8.5 kpc (Reid et al. 2014) zur Erde. Die Molekülwolke beinhaltet eine Gasmasse von 10^7 $M_\odot$, verteilt innerhalb eines Radiuses von 22.5 pc (Lis & Goldsmith 1989). Die hohen Dichten ($> 10^5$ cm^{-3}) und Temperaturen ($\sim 50 - 70$ K) im Inneren der Wolke zusammen mit der Nähe zum supermassereichem Schwarzen

Loch im Zentrum der Milchstraße machen Sgr B2 zu einer außergewöhnlichen Quelle.

Trotz des immensen Gasreservoirs scheint die Sternentstehung hauptsächlich auf die beiden heißen molekularen Kerne Sgr B2(N) und Sgr B2(M) beschränkt zu sein. Diese beiden Regionen aktiver Sternentstehung befinden sich in den inneren 2 pc der Molekülwolke. Zusammen beinhalten beide Kerne bereits mehr als 50 massereiche Sterne mit Spektralklassen zwischen O5 und B0. In meiner Arbeit rekonstruiere ich erfolgreich eine mögliche dreidimensionale Dichteverteilung. Basierend auf dieser Dichteverteilung können die über einen Frequenzbereich von zwei Grßenordnungen (ν = 10 GHz – 1 THz) und auf räumlichen Skalen von vier Grßenordnungen (0.02 – 45 pc) beobachteten Kontinuumstrukturen reprodziert werden. Um ein aussagekräftiges Model zu erstellen ist es besonders wichtig Beobachtungskarten zu verwenden, die einen möglichst großen Frequenzbereich auf allen räumlichen Skalen abdecken. Einige Kernresultate dieser Arbeit sind: (i) Das Dichtefeld von Sgr B2 kann mit einer Superposition von sphärisch symmetrischen Komponenten rekonstruiert werden. Diese Komponenten besitzen ein Plummer ähnliches Profil mit variablen Exponenten. (ii) Um die spektrale Energieverteilung zu reproduzieren ist es nötig Sgr B2(N) entlang der Sichtlinie hinter die Ebene welche Sgr B2(M) beinhaltet zu verschieben. (iii) Die berechnete Effizienz mit der die beiden Kerne Sterne produzieren unterscheidet sich signifikant. Für Sgr B2(N) beträgt sie 5 %, für Sgr B2(M) hingegen beträgt sie 50 %. Dies impliziert, dass Sgr B2(M) bereits einen Grossteil seiner Gasmasse entweder in Sterne umgeformt oder aber zerstreut hat.

Zusätzlich zur Bestimmung der Dichteverteilung habe ich mit Hilfe von PANDORA das Geschwindigkeitsfeld entlang der Sichtlinie in Richtung von Sgr B2(M) untersucht.

Act I – Pandora

Appendices

1. Motivation

Young massive clusters (YMCs) are massive ($M_* \sim 10^4 - 10^6\,M_\odot$) clusters which can be found in both starbursting, e.g. M82, and interacting galaxies, e.g. Antennae (for a review see Portegies Zwart et al. 2010). YMCs are suggested to be the modern day precursors to globular clusters. So understanding their formation may provide a handle on the formation of globular clusters at high redshifts. But at present only little is known about the initial conditions of YMCs. One of the least understood aspects is the initial assembly of cluster stars. To improve our insight into the assembly of YMCs, their substructure, i.e. massive clumps and cores, needs to be investigated. But since the size scale of this substructure is on the order of sub-parsec up to a few parsec at most, it is difficult to resolve the substructure, especially considering the typical distance of the usually distant hosting galaxies. For example, resolving a 1 pc sized clump in M82, which is located at a distance of 3.5 Mpc, requires a resolution of $\lesssim 0.05''$. This is the resolution only Atacama Large Millimeter Array (ALMA) can achieve in its very extended configurations.

Naturally a much better place to study the substructure of YMCs is our Galaxy. The Milky Way is known to host at least two star clusters close to the Galactic center which are at the lower end of the mass range of YMCs: Arches ($M_{\rm phot} \sim 2\times10^4\,M_\odot$, Espinoza et al. 2009) and Quintuplet ($M_{\rm phot} \sim 6\times10^4\,M_\odot$, Figer et al. 1999).

A promising candidate for a site where a YMC is currently forming is Sagittarius B2 (Sgr B2). It is the most massive and dense region of active star formation in the local group, but its distance of only 8.5 kpc (Reid et al. 2014) makes its core structure resolvable and thus accessible to investigate the early formation process of a YMC. Furthermore its proximity to the Galactic Center makes Sgr B2 an environment of extreme star formation, acting as a bridge for our knowledge between the typical star forming regions in the Galactic disk and the more violent and extreme active galactic centers that dominate star formation

throughout the Universe at high redshifts.

Sgr B2 has a large gas mass reservoir of M $\sim 10^6$ M$_\odot$ within 5 pc radius. Assuming a star formation efficiency of only 10 – 30 % (C. J. Lada & E. A. Lada 2003) and an Salpeter-like initial mass function, one would expect this region to produce a star cluster containing a stellar mass of 1 – 3 $\times 10^5$ M$_\odot$, which would exceed the Arches and Quintuplet masses and would be in the mid mass range for YMCs. Sgr B2 is currently forming at least two high mass clusters, Sgr B2(N) and Sgr B2(M). These clusters are located at the center of the cloud within a 2 pc radius and contain the highest concentration of hyper- and ultra-compact HII regions in the Galaxy. Their current stellar masses are estimated to be 2×10^3 M$_\odot$ (Sgr B2(N)) and 2×10^4 M$_\odot$ (Sgr B2 (M)).

High-mass protoclusters such as Sgr B2 are difficult to study since they are crowded, multi-layered regions. To overcome this obstacle, I have developed the radiative transfer tool kit PANDORA to model the three-dimensional structure of astrophysical objects, especially regions that are as complex and crowded as Sgr B2. This tool allows to account for example for line-of-sight positioning of different cores.

In this thesis, I study the massive star forming region Sgr B2 using the three-dimensional radiative transfer framework PANDORA.

1.1 Goal of the thesis

The goal of this thesis is two-fold. First, a three-dimensional radiative transfer framework is created, which should fulfill several requirements.

- **Pipeline:** The framework is expected to perform the entire process of radiative transfer end-to-end. This means that in addition to setting up and performing the radiative transfer simulations, the framework is expected to also perform the post-processing of the synthetic data and the comparison with corresponding observational data.
- **Flexibility:** The framework is supposed to be as flexible as possible. The physically motivated model setup (density structure, velocity field etc) is expected to be modular. This means, similar to a LEGO® system, different building blocks can be put together to form the source model.
- **User friendliness:** Performing the radiative transfer process end-to-end involves many different steps and consequently encompasses a plethora of setup parameters. This leads to a complex setup system. But the framework is expected to maintain user friendliness. It should be as simple to use as possible.

Second, I employ this three-dimensional radiative transfer framework to investigate the exceptional high-mass star forming region Sgr B2. I aim to derive its physical and kinematic structure in order to constrain the current status quo of this source.

1.2 Outline of the thesis

This thesis is split into four parts: Prologue, Pandora, Sagittarius B2, and Epilogue.

In the **Prologue** I provide the reader with an extended motivation of this thesis (Chapter 1) and an introduction to the two major topics of this work, namely star formation and radiative transfer (Chapter 2). In the second part — **Pandora** — I focus on the radiative transfer toolkit PANDORA that I developed in the framework of this thesis. I will explain the setup of PANDORA and its internal working in Chapter 3. A few test cases are then illustrated and discussed in Chapter 4. In the third part — **Sagittarius B2** — I will first summarize the observational data employed in the course of the radiative transfer modeling (Chapter 5). Results from fitting of the multi-scale, multi-frequency continuum data are given in Chapter 6. These provide insights on the physical structure, i.e. the density and stellar distribution of Sgr B2. Chapter 7 provides the results from molecular line fitting, which give insights into the kinematics and chemistry of this region. The **Epilogue** then concludes this thesis with a summary of the presented work and provides an outlook to future applications and improvements.

In this chapter, I will first provide an overview of our current understanding of the life cycle of interstellar matter, which includes the formation process of stars (Section 2.1). This will show that star formation is a multi-scale process. Many different physical processes (gravity, turbulence, magnetic fields) act on many different scales, causing a molecular cloud to collapse and eventually to undergo star (cluster) formation. A very famous star forming region amongst observational astronomers is the so called Sagittarius B2 (Sgr B2) molecular cloud. This cloud is situated in the vicinity of the Galactic center. Before explaining this region in more detail (Section 2.3), I will put it into context and describe the environment it is embedded in, which is the so call Central Molecular Zone (CMZ) of our Galaxy (Section 2.2). Since one of the main goals of this thesis is to derive physical properties of Sgr B2 by the means of 3-dimensional radiative transfer simulations, an introduction of the basics of radiative transfer is provided in Section 2.4.

2.1 Life cycle of interstellar matter

Stars, especially high-mass stars[1] ($M_* \gtrsim 8\,M_\odot$), are a very important constituent of the Universe. They determine the structure of galaxies and influence their evolution. Furthermore, they enrich the Universe chemically, by synthesizing elements heavier than H, He, and Li, which are already present since the Big Bang. For example, according to Morgan & Anders (1980), the main constituents of our Earth are iron (32 %), oxygen (30 %), silicon (15 %), and magnesium (14 %). These are all elements that had to be produced before the Earth was formed. In addition, the formation of planets is linked to the formation of stars. All of this makes star formation, i.e. the conversion of gas into stars, one of the most important processes in galaxies.

[1] Please note: Throughout this thesis, I will use the terms massive star and high-mass star interchangeably.

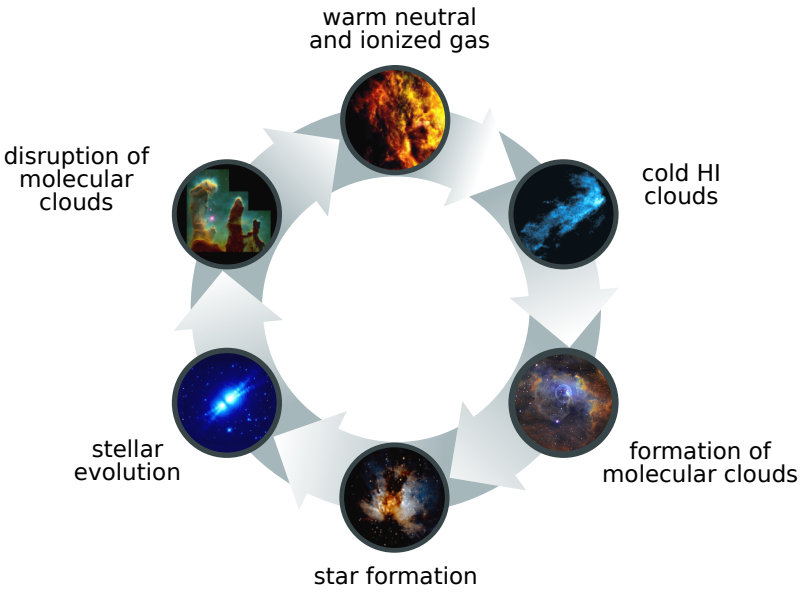

Figure 2.1: Schematic of the life cycle of matter.

In a very simplified picture, star formation encompasses the generation of local over-densities within a mass reservoir of molecular gas, which collapse and turn into stars. But as simple as it sounds, this collapse process not only involves many stages during which different physical processes are involved, but also covers spatial scales ranging from galaxies and giant molecular clouds (GMCs) (100 – 1000 pc) down to dense cores and proto-stellar systems (< 0.1 pc).

In this section, I will briefly summarize the current understanding of the life cycle of interstellar matter, as depicted in Fig. 2.1. This cycle starts with the formation of GMCs out of the diffuse interstellar medium (ISM) (see Sections 2.1.1 and 2.1.2). The densest regions within a GMC then become self-gravitating. This marks the starting point of star formation, as these regions collapse and form dense cores (see Section 2.1.3). The cores collapse further and eventually build clusters of stars (see Section 2.1.4). Once massive stars ($M \gtrsim 8\,M_\odot$) have formed, they will ultimately destruct their parental GMC (see Section 2.1.5) and the majority of the gas is returned to the diffuse ISM, restarting the cycle.

Recent review articles are available covering different aspects of the life cycle of interstellar matter, e.g. on the formation of GMCs (Dobbs et al. 2014), their filamentary structure (André et al. 2014; Molinari et al. 2014), the star formation process itself (e.g. McKee & Ostriker 2007; Klessen 2011) or the formation of massive stars (Beuther et al. 2007; Zinnecker & Yorke 2007; Tan et al. 2014).

Nomenclature

I am adopting the nomenclature used in Zhang et al. (2009): A *cloud* is an entity of molecular gas with a size of $d_{\rm cloud} = 10 - 100$ pc, a molecular *clump* is an entity with a size of $d_{\rm clump} \lesssim 1$ pc forming massive stars together with lower mass stars, a *dense core* is an entity with a size of $d_{\rm core} = 0.01 - 0.1$ pc forming a single or a small group of stars, and a *condensation* is an entity with a size of $d_{\rm condensation} \lesssim 0.01$ pc.

Table 2.1: Physical properties of molecular clouds and cores. [a]

	molecular cloud	cluster forming clump	protostellar cores
Size [pc]	2 – 20	0.1 – 1.0	0.01 – 0.1
Density [cm^{-3}]	10^2 – 10^4	10^3 – 10^5	$> 10^5$
Mass [$M_\odot$]	10^2 – 10^4	10 – 10^3	0.1 – 10
Temperature [K]	10 – 30	10 – 20	7 - 12
Line width [km s^{-1}]	1 – 10	0.3 – 3.0	0.2 – 0.5
Column density [g cm^{-2}]	0.03	0.03 – 1.0	0.3 – 3
Crossing time [Myr]	2 – 10	$\lesssim 1$	0.1 – 0.5
Free-fall time [Myr]	0.3 – 3.0	0.1 – 1.0	$\lesssim 0.1$

[a] Adapted from Klessen (2011), Cernicharo (1991), and Bergin & Tafalla (2007)

2.1.1 The interstellar medium

The ISM includes all baryonic matter that is gravitationally bound to galaxies, except for stars. Its main constituents are dust and gas. Gravitationally unbound dust and gas which are mainly located in the voids between galaxies are part of the so-call intergalactic medium (IGM).

Although the ISM only contributes $\sim$ 10 – 15% to the total baryonic mass of the Galaxy, it makes up most of its volume. The majority of the mass is concentrated in a thin disk with a diameter of $\sim$ 20 – 30 kpc, but a vertical scale height of only $\sim$ 400 – 600 pc. An extensive review on the ISM has been compiled by Ferrière (2001). A brief overview and introduction to the Galaxy and its CMZ is given in Section 2.2.

The dust in the ISM plays an important role. The typical gas-to-dust ratio is on the order of 100 (Hildebrand 1983), but it can be higher in certain regions (Parkin et al. 2012). Recent analytic results of the Planck mission (Planck Collaboration et al. 2014) show that the temperature of the interstellar dust ranges between 10 – 30 K. The main constituents of dust grains are graphites, silicates, or water ice (Field 1975). Using dust extinction curves, Mathis et al. (1977) investigated the size distribution of these grains and found a power-law distribution $N(a)da \propto a^{-3.5}da$ of the grain radius a for the wavelength range 0.005 – 1 µm. An update of this distribution is provided by (Casuso & Beckman 2010). The lower wavelength range is dominated by polycyclic aromatic hydrocarbons (PAHs) (Leger & Puget 1984; Lebouteiller et al. 2011). They build the connection between dust grains and organic macro-molecules. Although dust makes up only a fraction of the mass in the ISM, it has characteristics important for star formation. Under Galactic conditions, the main path to produce molecular hydrogen from atomic hydrogen takes place on dust grains (for a review on grain surface chemistry, see Herbst et al. 2005). Moreover, dust helps to shield the molecules from UV radiation, which would otherwise photo-dissociate and, thus, destroy them. Dust grains themselves can also be destroyed. This releases molecules that were attached to their surface into the gas phase (Seab 1987; Van Loo et al. 2013). Therefore, they also serve as a reservoir of molecules.

The gas phase of the ISM is mainly made up of hydrogen, helium and a little bit of lithium, which

Table 2.2: Physical properties of the phases of the ISM. [a]

Phase	State of Hydrogen	T [K]	n_H [cm^{-3}][b]	heating	cooling
hot ionized medium (HIM)	HII [c]	$\gtrsim 10^{5.5}$	~ 0.004	shock heated	adiabatic expansion, X-ray emission
warm ionized medium (WIM)	HII [c]	10^4	$0.2 - 10^4$	photoelectrons from H, He	optical line emission, free-free emission, fine-structure line emission
warm atomic medium (WNM)	HI [c]	~ 5000	0.6	photoelectrons from dust	optical line emission, fine structure line emission
cold atomic medium (CNM)	HI [c]	~ 100	30	photoelectrons from dust	fine structure line emission
molecular gas	H_2 [c]	10 – 50	$> 10^6$	photoelectrons from dust, cosmic rays (partially)	fine structure line emission, CO line emission

[a] Adapted from Draine (2011) and Wooden et al. (2004)

[b] The density of the molecular gas is given as the density of H_2.

[c] HI refers to atomic hydrogen, HII refers to ionized hydrogen, and H_2 refers to molecular hydrogen.

have been created shortly after the Big Bang. Heavier elements containing more than three protons have been created later-on by nucleosynthesis in stars and in supernovae explosions.

Based on the temperature of the gas, one distinguishes several different phases. Draine (2011) provides an overview of this classification (see Table 2.2 for a summary). The phases are the hot ionized medium (HIM), the warm ionized medium (WIM), the cold neutral medium (CNM), the warm neutral medium (WNM), and the molecular gas. The molecular gas is the densest and coldest part of the ISM. This phase is the most important one for the process of star formation. The neutral atomic phase, which consists of neutral hydrogen, is warmer and more diffuse than the molecular gas phase. It is split into two phases (CNM, WNM), which can co-exist in pressure equilibrium (Field et al. 1969; Wolfire et al. 1995). A fraction of the WNM can be ionized, either by X-rays or cosmic rays. The transition between the WNM and the CNM is induced by shock fronts, which are thermally fragmented and bistable (Koyama & Inutsuka 2002). From this, the CNM inherits its fragmented nature, as is seen in many simulations (e.g. Heitsch et al. 2005). The HIM on the other hand is shock-heated by the blastwaves created from supernova explosions.

I will briefly explain the current understanding of the formation of molecular clouds from the (diffuse) molecular gas in the next subsection.

2.1.2 Giant molecular clouds

A recent and detailed overview of the formation of GMCs is given in Dobbs et al. (2014). Two major obstacles have to be overcome to form a GMC. In the first step, high density (mainly atomic) gas needs to be accumulated, which is then converted to molecular gas in the second step. Three processes influence the formation of molecular clouds: turbulence, gravity, and magnetic fields.

The physical origin of turbulence is, however, not yet fully understood. Terrestrial flows, e.g. the flow of water in oceans, are commonly described using incompressible turbulence. Opposed to that, the ISM is characterized by supersonic, compressible (and magnetized) turbulence. For a thorough review on ISM turbulence see Elmegreen & Scalo (2004) and Scalo & Elmegreen (2004). Such supersonic flows in highly compressible gas can create strong density fluctuations. There are many possible driving sources for turbulence, ranging from large scale, i.e. injected from the outside to small scale origin, i.e. driven by the clouds themselves (see e.g. Klessen & Hennebelle 2010; Vázquez-Semadeni et al. 2009; Peters et al. 2008; Ibáñez-Mejıa et al. 2016).

In the regions where dense gas has accumulated to higher densities, hydrogen is mainly present in the form of HI and carbon in the form of CII. The main observable defining a GMC however is CO[2], so the transition from the atomic gas to the molecular gas needs to be considered. The ratio of the FUV radiation and the gas density controls the abundance of H_2. Thus in a dense gas, where the FUV radiation is attenuated, H_2 becomes dominant (van Dishoeck & Black 1986; Black & van Dishoeck 1987; Sternberg 1988; Wolfire et al. 2010).

Characteristics of GMCs

GMCs have three major characteristics (see Larson 1994, and references therein): First, they are embedded in more widely distributed atomic gas, which provides shielding against the interstellar UV radiation. Second, they are transient structures. They do not survive for more than 10^7 years without changing significantly. Third, they are highly irregular, usually showing filamentary, i.e. coherent and elongated[3], structures. Recent high resolution observations revealed that the entire ISM is highly filamentary (e.g. Molinari et al. 2010a; Schneider et al. 2010). For more information on the filamentary structure of GMCs see André et al. (2014).

2.1.3 Dense cores

Supersonic turbulence is ubiquitously observed in molecular clouds. As described in the previous section, the generated molecular cloud structure is highly transient and inhomogeneous (Klessen 2011). The filamentary structure found within the GMCs are shock-compressed density fluctuations, along which fragmentation occurs, leading to the formation of dense cores (André et al. 2014, and references therein).

From the observations of many star formation regions, the distribution of dense cores has been derived in the past, e.g. for ρ-Oph (Motte et al. 1998; Johnstone et al. 2000) or more recently for Aquila (Könyves

[2]Hydrogen lacks a permanent dipole moment, thus it is very hard to observe. CO, the second most abundant molecular in the universe, has a dipole moment and is thus easily observable.

[3]I will adopt the nomenclature from André et al. (2014), where filaments are structures with aspect ratios of 5 – 10.

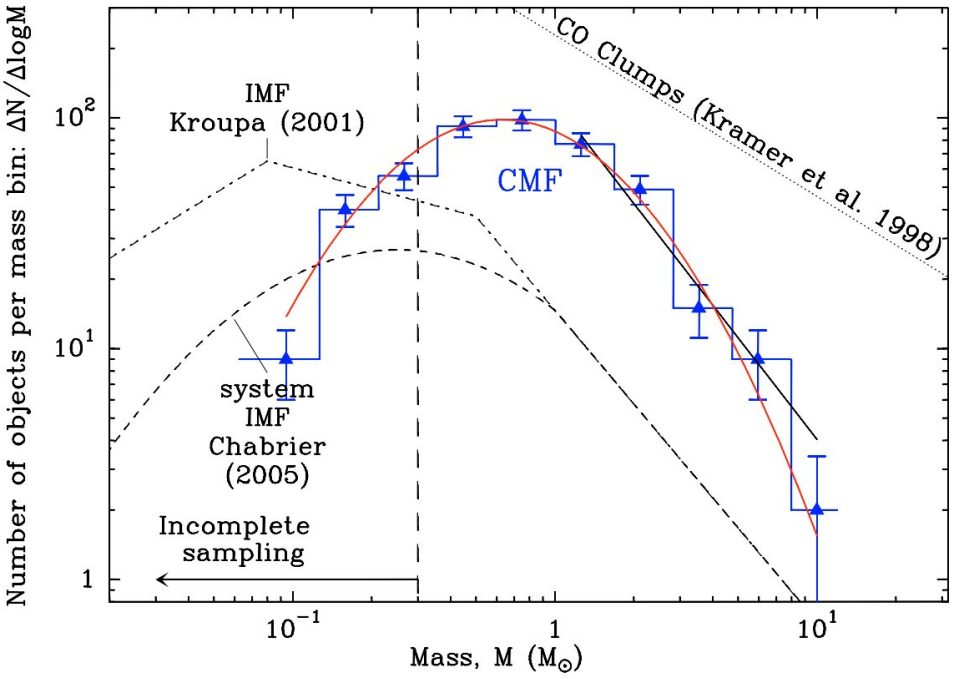

Figure 2.2: Offset between the core mass function and the initial mass function. This figure is taken from Könyves et al. (2010).

et al. 2010). They all determined the number of dense cores in these regions and derived their physical properties, including their mass. From this information, one can derive the distribution of the core masses, i.e. the core mass function (CMF), which is usually given by a probability density function (PDF). Figure 2.2 shows an example of such a resulting CMF obtained by Könyves et al. (2010) from the star-forming region Aquila. The CMF can be fitted with a log-normal distribution. An extensive overview of the CMF, including theories of its origins and caveats concerning its determination are given in Offner et al. (2014).

I will now give a brief overview of the properties of dense cores. This is divided into five key aspects: density, thermal, kinematical, chemical and magnetic field structure. Extensive summaries are provided by Bergin & Tafalla (2007) and Klessen (2011).

Density structure

There are several methods to determine the density structure of prestellar cores. This is done by either analyzing the mm/sub-mm dust continuum emission, the dust absorption against the bright mid-IR background or the dust emission/absorption using near-IR extinction maps. The density profiles are flatter than r^{-1} within radii smaller than 2500 – 5000 au and typical central densities in the range of 10^5 – 10^6 cm^{-3} (e.g. Ward-Thompson et al. 1999). This implies that the density profiles require a central flattening. A common approach to describe these cores is by using a truncated isothermal (Bonner-Ebert) sphere (Ebert 1955; Bonnor 1956) or a Plummer-like profile (Plummer 1911). Both profiles provide good fits to the observational data (e.g. Bacmann et al. 2001; Qin et al. 2011).

Thermal structure

The gas and dust temperature of the cores are influenced by various heating and cooling processes. The gas and the dust have to be thermally coupled via collisions at densities $> 10^5$ cm^{-3}, i.e. at the core centers (Goldsmith 2001). In the envelope of the cores, i.e. at lower densities, the gas and dust temperatures do not necessarily have to be coupled. Hence it is important to derive both temperatures separately.

Large-scale studies of the dust temperature indicate that the dust is colder, $T_{dust,core} \sim 8 - 12$ K, in starless cores compared to its immediate vicinity, $T_{dust,envelope} \sim 15 - 20$ K, (Ward-Thompson et al. 2002). This inverted temperature profile is due to the fact that the core is illuminated by the interstellar radiation field against which the inner part of the core is shielded by the surrounding layers. This is consistent with dust radiative transfer modeling (e.g. Langer et al. 2005).

The gas temperature is usually inferred from the level excitation of simple molecules, like CO and NH_3 (N. J. Evans I. 1999). It is commonly believed that the gas in prestellar cores is mainly heated by cosmic ray ionization, while its cooling is mainly due to molecular line radiation (Goldsmith & Langer 1978).

Kinematical structure

Contrary to the highly turbulent velocity field of the parental molecular cloud, dense cores exhibit low internal velocities. Starless cores in molecular clouds like Taurus or Perseus have spectral linewidths close to the thermal linewidth when observed at low angular resolution (for a discussion of line broadening mechanisms, see Section 2.4.3). Infall motion has been detected in some cores. Observationally infall motion is inferred from optically thick, self-absorbed lines (e.g. from molecules like CO, HCO^+). The low-excitation foreground material absorbs part of the background emission and produces a blue-shifted spectral line profile (N. Evans 2003, see Section 2.4.3 for a more detailed explanation).

Chemical structure

Different molecules trace different physical conditions. Thus, integrated line intensity maps of various molecules can look significantly different for the same core. For example, the nitrogen-hydrogen bearing molecule N_2H^+ is known to be a so called late-depleter. It can be found in very cold environments, where carbon bearing molecules like CO and CS are already frozen out onto dust grains. Thus, integrated line intensity map would show that N_2H^+ follows more closely the dust emission, while, for example, $C^{18}O$ emission appears to be more ring-like around the maximum of the dust emission (Caselli et al. 1999; Tafalla et al. 2002). So on one hand, the freeze-out of many molecules makes it hard to probe physical conditions in the core. But on the other hand, modeling the chemical evolution can provide us with important parameters. The age of a prestellar core can, for example, be determined from the level of CS depletion. The deficit of CS in the envelope, on the other hand, provides insights to the strength of the external UV radiation field (Bergin & Tafalla 2007).

Magnetic field structure

Magnetic fields are observed on all scales throughout the interstellar gas (e.g. Crutcher et al. 2003). Their importance for star formation however remains controversial (Klessen 2011). Recent numerical

simulations have revealed that magnetic fields, even when they are weak, have a noticeable dynamical effect. The magnetic field can alter core fragmentation (e.g. Peters et al. 2011), change the coupling between stellar feedback processes and their parent clouds (e.g. Nakamura & Z.-Y. Li 2007), or slow down the entire evolution (e.g. Heitsch et al. 2001).

2.1.4 Star formation

As mentioned before, some of these dense cores exceed the critical mass for gravitational contraction. They become Jeans unstable, collapse further and build protostars. These protostars continue to accrete mass from the infalling envelope until they either have exhausted the available gas reservoir or stellar feedback effects dominate and remove their parental gas cocoon. Based on the timescales over which protostars form, one distinguishes between low- and high-mass star formation.

Time scales

The timescale for collapse is given by the free-fall time $t_{\rm ff}$ (Shu et al. 1987):

$$t_{\rm ff} = \sqrt{\frac{3\pi}{32\,\mathrm{G}\,\rho}}, \tag{2.1}$$

where G is the gravitational constant and ρ is the average mass density. Typical molecular clouds have a free-fall time of $t_{\rm ff} \lesssim 5 \times 10^6$ years. This provides a lower limit on the timescale for stellar evolution. The contraction of a mass of gas due to self-gravity causes the gravitational potential energy to be converted to heat. The Kelvin-Helmholtz timescale $t_{\rm KH}$ is the timescale on which this process happens

$$t_{\rm KH} = \frac{\mathrm{G}\,M_*^2}{R_*\,L_*}, \tag{2.2}$$

where M_*, R_*, and L_* denote the mass, radius and luminosity of the star, respectively. Stars with $M_* > 8$ $\mathrm{M}_\odot$, have a Kelvin-Helmholtz timescale that is shorter than the free-fall time ($t_{\rm KH} < t_{\rm ff}$). This means that fusion already ignites while the collapse is still ongoing.

Initial mass function

As for the distribution of the core masses within a star-forming region, one can also infer the mass distribution of the stars at the point when they enter the main sequence. This distribution is called the initial mass function (IMF). It has first been described by Salpeter (1955). It has the characteristic form:

$$\xi(m)\Delta m = \xi_0\, m^{-2.35}\,\Delta(m), \tag{2.3}$$

where $\xi(m)\Delta m$ refers to the number of stars within the mass range $[m, m+\Delta m]$. Over the past decades, this function has only changed in the description of the low-mass regime and surprisingly still holds for the high-mass regime. Due to improved measurements of the low-mass regime, Kroupa (2001) was able to improve the IMF by introducing a segmented description that includes a turnover at lower masses (see dashed-dotted line in Fig. 2.2). Another modification has been provided by Chabrier (2003), who describes the IMF using a smooth function (see dashed line in Fig. 2.2).

Low-mass star formation

For low-mass star formation an evolutionary has been established over time (Shu et al. 1987; van Dishoeck & Blake 1998), which is observationally divided in four distinct clases based on their spectral energy distribution (SED) (compare with right column in Fig. 2.3).

- **Class 0:** Collapse is raising the temperature and luminosity of the core. The SED is described by a single blackbody that peaks at wavelengths $> 150\,\mu m$.
- **Class 1:** The accretion phase proceeds, which causes the luminosity and temperature to raise further and the peak of the SED consequently moves to the far-IR ($\sim 100\,\mu m$). The infalling material is shaped to an accretion disk around the central object due to the remaining angular momentum. The SED is doubly peaked, due to (i) a blackbody component originating in the accretion disk (50 – 100 K) and (ii) a component originating in the disk (200 – 400 K).
- **Class 2:** Winds and outflows have swept away most of the natal cloud. The dusty disk is exposed. The peak of the SED is shifted to the near-IR (at $\sim 2\,\mu m$). This pre-main-sequence core is often visible in the optical and identified as an T-Tauri star.
- **Class 3:** The SED of these objects peaks in the near-IR, optical. These objects are visible as stars.

High-mass star formation

Two major formation scenarios are currently still under debate. Their major difference concerns the assembly of molecular mass to form massive protostars. For a review see Zinnecker & Yorke (2007).

- **Competitive accretion scenario:** In this scenario, protostars form in clusters in the same molecular cloud, mainly along density enhancements such as filaments. But since all protostars form from the same reservoir of molecular gas, they have to compete for it. They can gain mass for example via accretion or by merging (the rich get richer). Typically the most massive stars form in the center of the cluster. This scenario is supported observationally by the fact that massive stars are found in clusters rather than in isolation.
- **Monolithic collapse scenario:** This is basically a scaled up version of the low-mass star formation scenario. Theoretical works show that the cavity created by the jet and the outflow may allow the radiation generated by the protostellar object to escape without affection the accretion process of gas, which happens via the disk.

Stages of high-mass star formation include (i) cold collapsing core (also known as a infrared dark cloud), (ii) hot molecular core, and (iii) (hyper-compact and ultra-compact) HII region (see Fig. 2.4). The stages (ii) and (iii) are significantly different from low-mass star formation.

- **Hot molecular cores** are considered to be one of the very early signposts of high-mass star formation. They are compact (size $\leq 0.1\,pc$), dense ($n \geq 10^7\,cm^{-3}$) objects with a relatively hot ($T_{gas} \gtrsim 100\,K$). They exhibit a rich chemistry with a plethora of complex organic molecules (COMs), e.g. CH_3CN, CH_3OCHO. Interestingly similar, but less dense, objects are found around low-mass. These are called hot corinos (see Ceccarelli 2004, for a review).
- **Hyper- and ultra-compact HII regions:** Since high-mass stars are so massive, they already ignite fusion while they are still in the accretion phase. This leads to stellar feedback effects. Stars

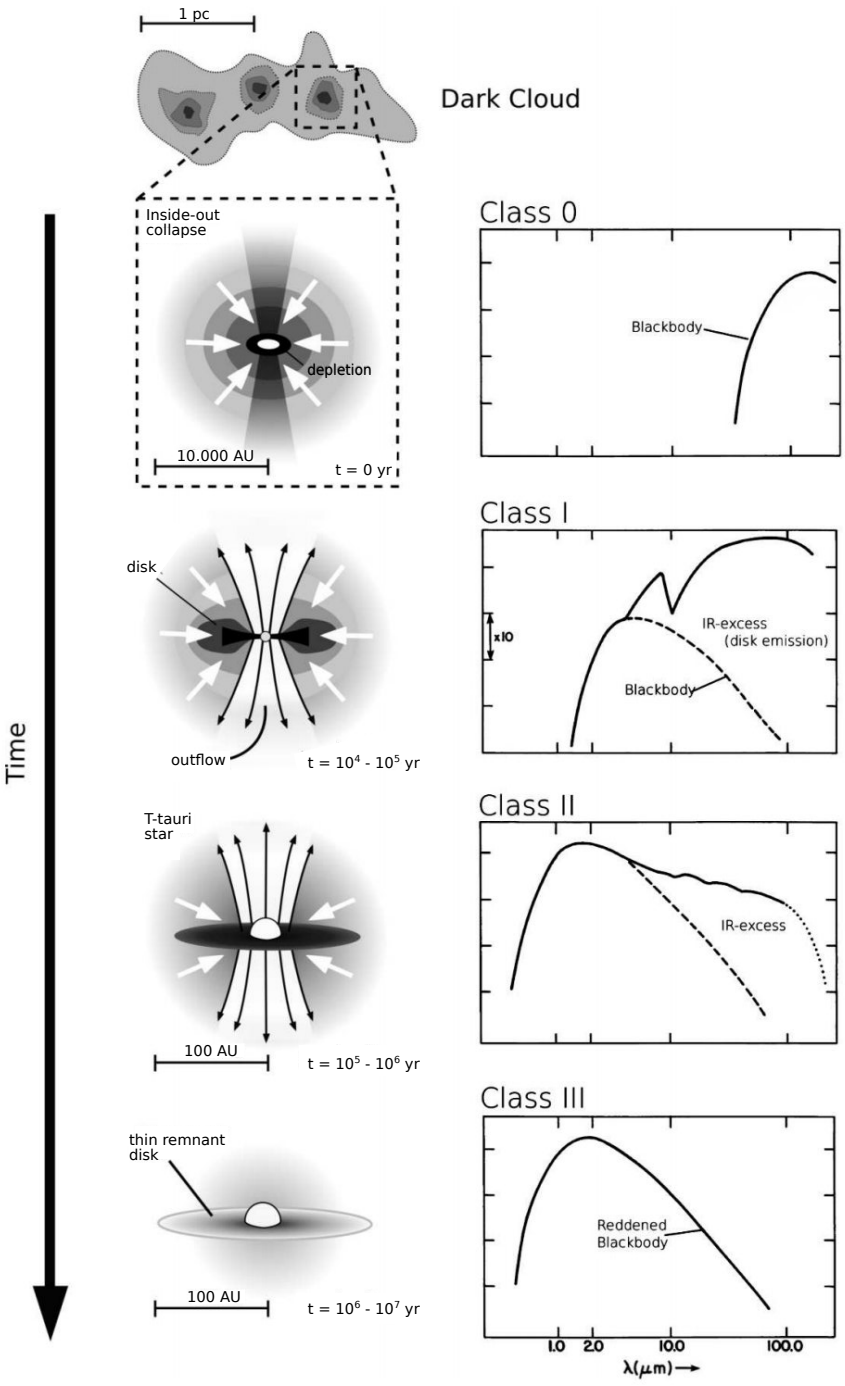

Figure 2.3: Schematic view of the evolutionary sequence of low-mass star formation . A dense core undergoes inside-out collapse, forming a central protostellar object. The residual angular momentum causes the core material to spin into a circumstellar disk. Accretion via the disk causes bipolar outflows and collimated jets. After 10^7 years, the circumstellar material is exhausted and the accretion stops. Image credit: Adaptation from C. J. Lada & Wilking (1984) and van Dishoeck & Blake (1998) by Cormac Purcell.

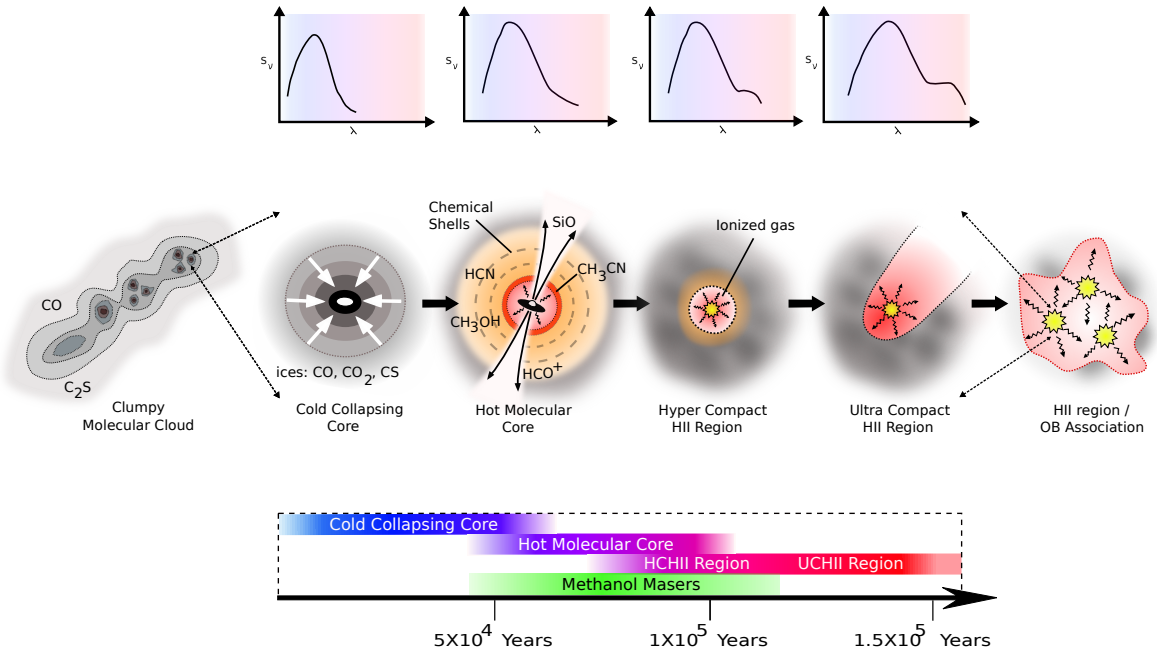

Figure 2.4: Schematic view of the early phases of high-mass star formation. Starting with a clumpy molecular cloud (left), we zoom in to a single core. The four different phases are depicted are shown in the middle row. The image on the right shows the resulting cluster. The top row illustrates the different SED associated with each stage and the bottom row indicates the different time scales involved. Image credit: Cormac Purcell.

of spectral type B3 or earlier are capable to produce the necessary ionizing flux ($h\nu > 13.6\,\mathrm{eV}$). The UV radiation of the high-mass stars ionizes the surrounding medium and creates HII regions. According to their sizes, these regions are called hyper- (size $< 0.05\,\mathrm{pc}$, density $> 10^6\,\mathrm{cm}^{-3}$), and ultra-compact (size $< 0.1\,\mathrm{pc}$, density $> 10^4\,\mathrm{cm}^{-3}$) HII regions (Kurtz 2005). Observed HII regions rarely show ideal spherical symmetry. More often they are found in all kinds of shapes, ranging from cometary, shell-like, core-halo like to irregular. They are best detected by observation at the radio-wavelength due to their characteristic spectrum.

Young massive clusters

YMCs are massive ($M \sim 10^4 - 10^6\,M_\odot$) and dense (radius of a few pc) clusters which can be found in both starbursts and interacting galaxies (for a review see Portegies Zwart et al. 2010). YMCs are suggested to be the modern day precursors to globular clusters. But at present only little is known about their initial conditions. One of the least understood aspects of their formation is the initial assembly of cluster stars. Do they form in a central condensation, or via merging of several small cluster?

2.1.5 Disruption of giant molecular clouds

Before they can turn a significant fraction of their gas mass into stars, GMCs are disrupted. The questions of why and how this happens are tightly linked to the question of how turbulence is generated (see

Figure 2.5: Night sky over the ALMA telescopes in the Atacama desert in Chile. Image credit S. Guisard/ESO.

Section 2.1.2). Each of the mechanisms invoked to explain turbulence and the formation of GMCs also imposes requirements of how GMCs must disrupt.

Stellar feedback mechanisms and photoionization (long-term events) as well as supernovae (short-term event) seem to be the most promising mechanisms to explain GMCs disruption. Studies from A. Whitworth (e.g. 1979) and Matzner (2002) long suggested that photoionization should be the primary mechanism disrupting molecular clouds. The ability of photoionization to disrupt a GMC with a mass of $\lesssim 10^5\,M_\odot$ is also verified in numerical simulations from Dale et al. (e.g. 2012). Supernovae, the other mechanism, are potentially very effective, but they need to be studied further.

2.1.6 Technical advances

Tremendous progress has been made to decipher the life cycle of interstellar matter, which is tightly linked to the star formation processes, due to technical advances, both observationally and theoretically. Observationally, the advent of many state-of-the-art telescopes equipped with improved receivers, e.g. the Herschel Space Observatory, the upgraded VLA, ALMA (see Fig. 2.5), provide high-fidelity images and datacubes which ultimately improve or even allow for the first time the determination of physical properties on all scales (e.g. ALMA Partnership et al. 2015). With this generation of telescopes it is already or will be possible very soon to perform high-fidelity, multi-scale, multi-transition surveys that simultaneously sample star forming cores and their natal clouds very efficiently. This will provide not only detailed insights into the physical conditions as well as the gas kinematics, but also will enable scientists to efficiently study a statistically significant amount of star forming regions. Ideally these observations will rule out some of the proposed formation processes of e.g. GMCs.

Advances in the computational performance of supercomputers, e.g. JUQUEEN, hosted at the Forschungszentrum Jülich, or SuperMUC, hosted at the Leibniz Supercomputing Centre in Garching (see Fig. 2.6), allow numerical simulations to include complex physics and even chemistry (e.g. Walch et al. 2015). The increase in computational capabilities, also allows to eventually connect large scale simulations, i.e. galactic simulations, which currently, due to their low resolution inadequately sample the internal cloud structure, cloud motions and shocks, with small scale simulations, which on the other hand

Figure 2.6: SuperMUC. Image credit MMM/LRZ.

miss the large scale dynamics such as spiral shocks, cloud-cloud collisions. So simulations capturing all physical scales on which star formation occurs, i.e. from the largest cloud-scales of $\sim 100\,\mathrm{pc}$ down to the smallest core-scales of $< 0.1\,\mathrm{pc}$ will provide a clear picture of the formation and evolution of GMCs, dense cores and all mechanisms involved in the formation of stars.

Many different methods, be it for the analysis of observational data or the setup of numerical simulations, have been developed in the past. It is also important to perform consistency checks between these methods. Furthermore, a non-negligible amount of effort should focus on interconnecting theory and observation. For example synthetic observations of simulations could provide insights on what to search for observationally (see e.g. the efforts of R. J. Smith et al. 2013; Chira et al. 2014; Seifried et al. 2016).

2.1.7 Key points

Here I summarize a few of the key points (in no particular order):

- The life cycle of matter connects molecular, atomic, and ionized phases of the ISM (Ferrière 2001).
- Star formation is a crucial process in this perpetual life cycle.
- Stars seem to form in clusters rather than in isolation (e.g. C. J. Lada & E. A. Lada 2003).
- Fusion is ignited in high-mass stars before their collapse has completed.

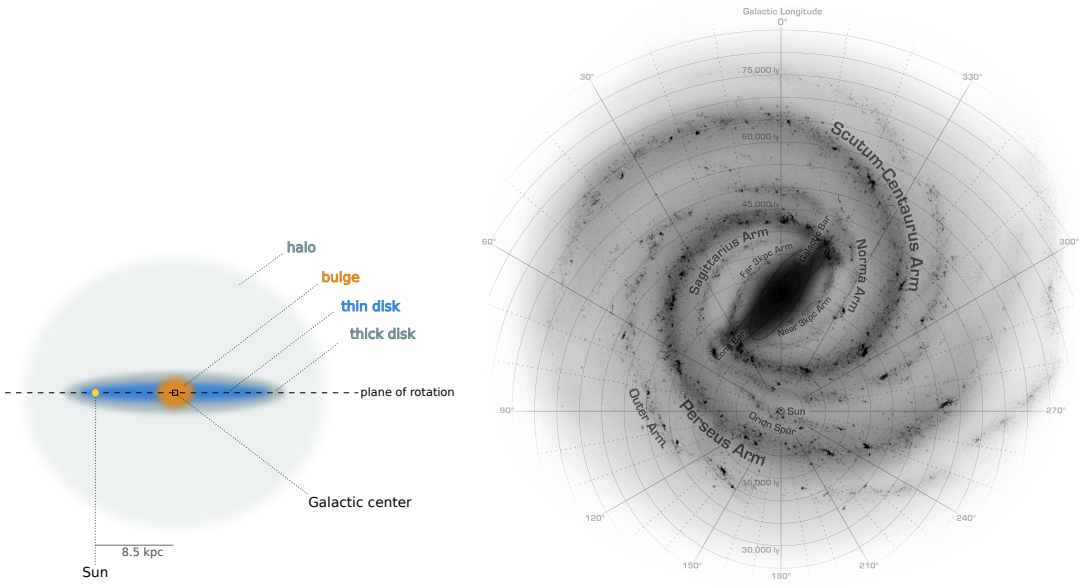

Figure 2.7: Top: Schematic edge-on view of the Milky Way. Bottom: Artist impression of the face-on view of the Milky Way. Image Credit: R. Hurt / SSC-Caltech.

2.2 The Central Molecular Zone of the Milky Way

Our vantage point within the Galaxy hampers our possibilities to accurately deduce the structure and extent of the Milky Way. There is observational evidence that it consists of at least four major constituents: a bulge, a thin disk, a thick disk and a halo. It has a estimated diameter of $\gtrsim 50$ pc (see Fig. 2.7). The Galactic plane has been subject to many surveys at different wavelengths (see Fig. 2.8) spanning a wide range of spatial and spectral resolutions. These surveys highlight the different appearance of the Galactic plane. For example, in the sub-millimeter and infrared, a broad emission band is visible along the entire plane. This emission is mainly due to interstellar dust which is heated by the starlight it absorbs. In the optical, most parts of the Galactic plane are invisible. They are hidden behind the aforementioned interstellar dust. In the gamma ray regime individual sources, e.g. supernova remnants, are visible.

The majority ($\sim 80\,\%$) of the dense ($n \gtrsim 10^3$ cm^{-3}) molecular gas of the Milky Way is situated in the inner $\sim 200 - 500$ pc of the Galactic center (Morris & Serabyn 1996). This region is called the Central Molecular Zone (CMZ). It is very unusual in that it has high molecular gas densities, large velocity dispersions (15 – 50 km/s), high temperatures (50 – 120 K, Ginsburg et al. 2016), and a rich chemistry. A collection of multi-wavelength continuum images of the CMZ is displayed in Appendix B.1. The dense gas is distributed asymmetrically with respect to $l = 0°$. About 3/4 of the gas is situated at positive Galactic longitudes and local standard of rest (LSR) velocities.

Three different models to explain the gas kinematics of the CMZ are currently under debate: (i) the 'two arm model' from Sawada et al. (2004, e.g.), (ii) the 'closed elliptical orbit model' from Molinari et al. (2011), and (iii) the 'open stream(s) model' from Kruijssen et al. (2015). An overview of these different models is shown in Fig. 2.9.

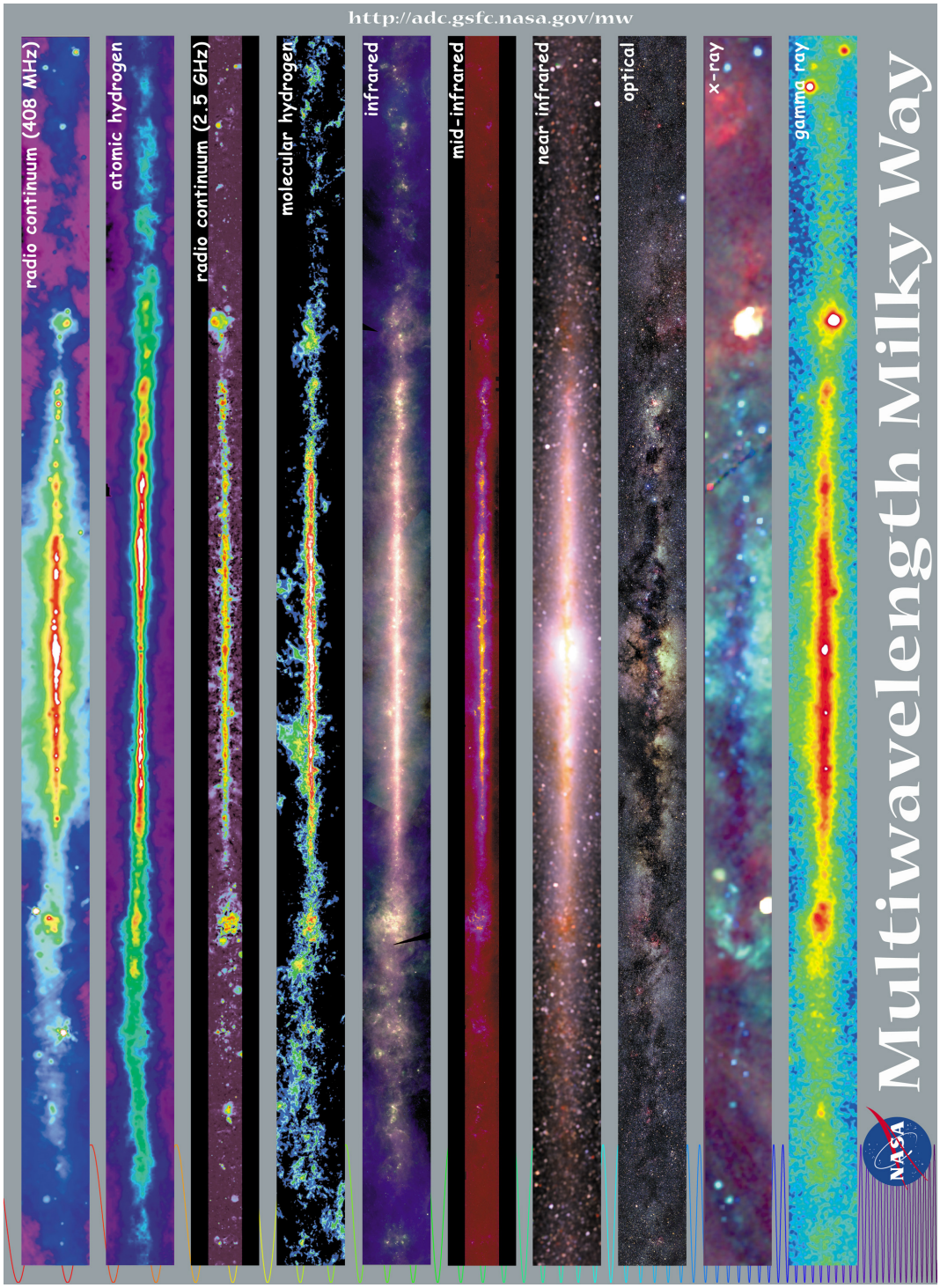

Figure 2.8: The Galactic plane seen at different wavelengths. The images are centered on the Galactic center. Image credit NASA.

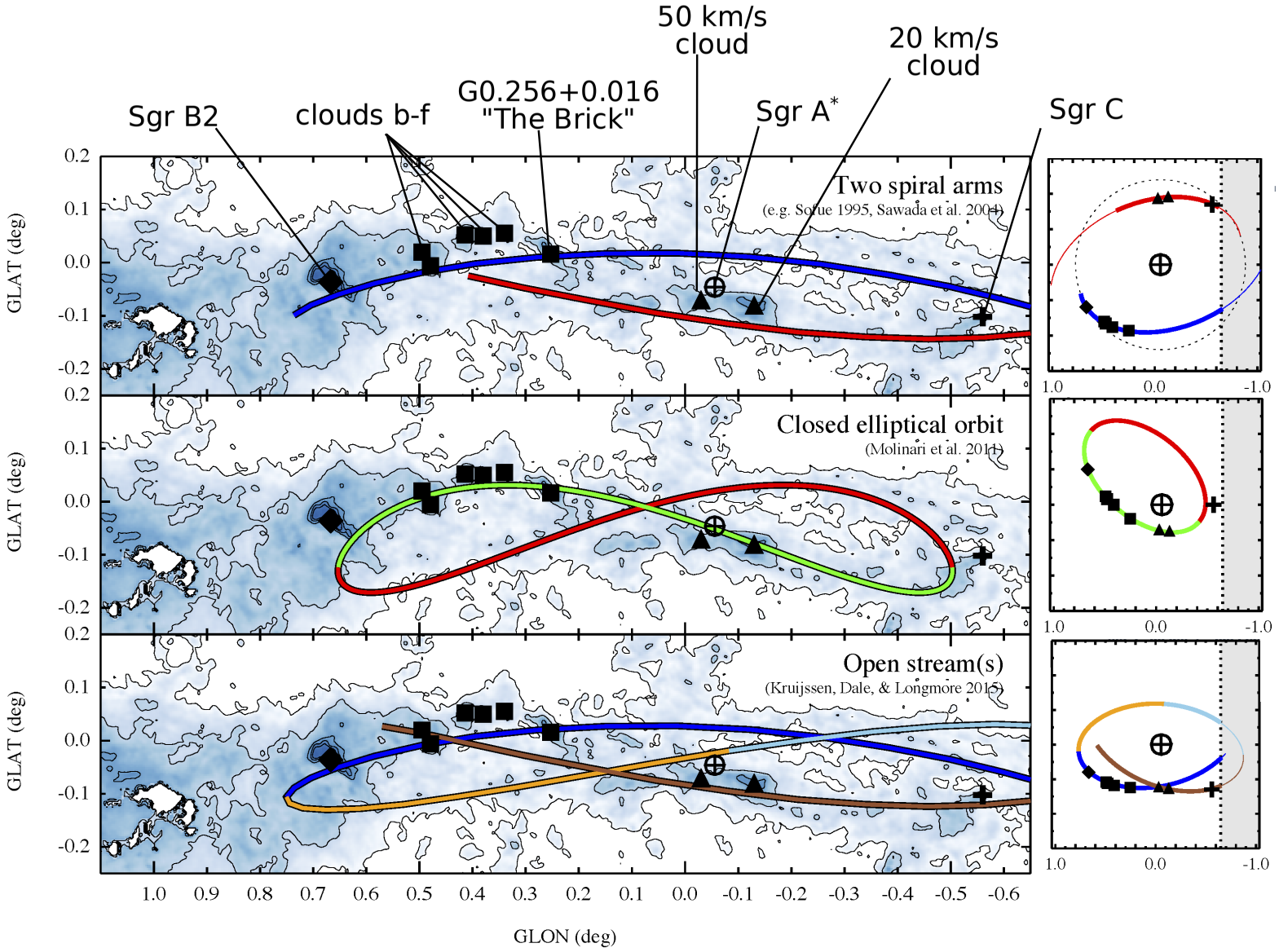

Figure 2.9: Left: All three models of the 3D structure of the CMZ overlaid on a molecular hydrogen column density map of the CMZ (Battersby et al. in prep.). Right: Top-down view of the corresponding model. The observer is located at the bottom of each figure. Figures taken from Henshaw et al. (2016).

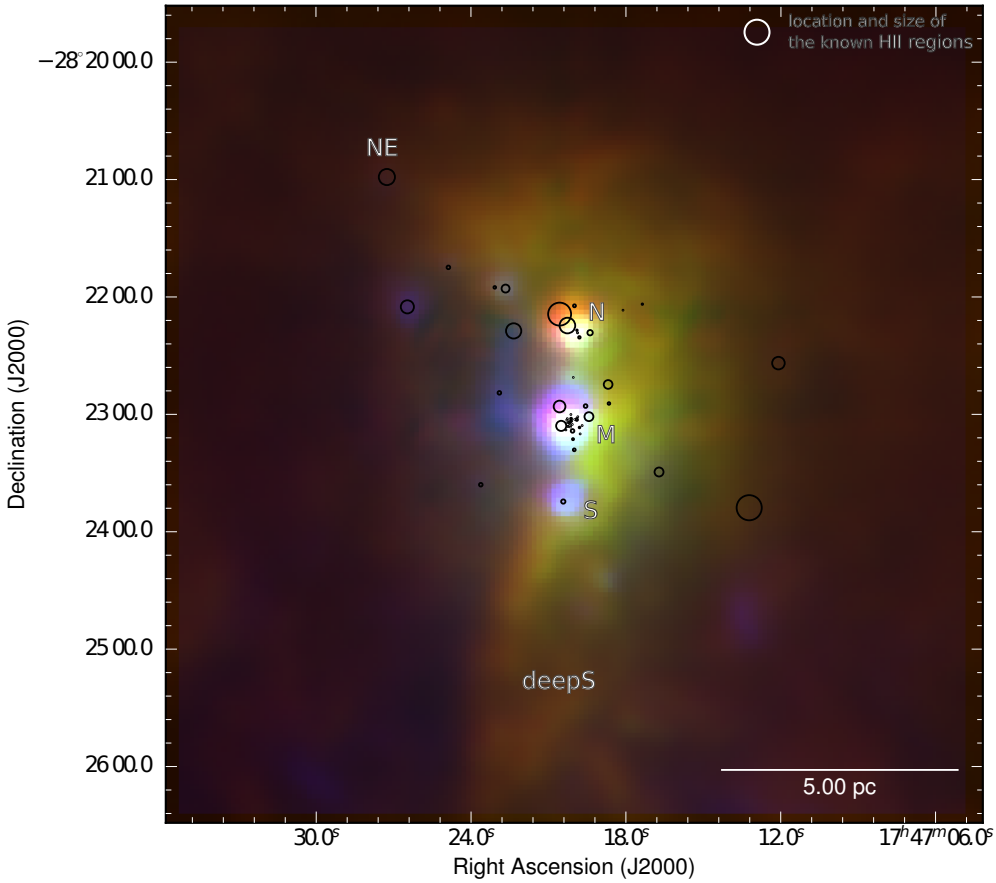

Figure 2.10: Three color composite map of the large-scale structure of Sgr B2. Red: JCMT - SCUBA 850 µm, green: CSO – Sharc II 350 µm, blue: Herschel – PACS 70 µm. The black circles mark the extent of the HII regions.

2.3 Sagittarius B2

Sgr B2 is one of the most massive molecular clouds in the Galaxy. It is located at a distance of 8.34±0.16 kpc (Reid et al. 2014)[4] and has a projected distance of 107 pc (or 43.4′) from Sgr A*, the compact radio source associated with the supermassive black hole located at the Galactic Center.

Hüttemeister et al. (1993) distinguish three different parts in Sgr B2: (i) a low density envelope, (ii) a moderate density region extended around (iii) local hot cores, which are the most compact, densest molecular regions (see Fig. 2.11). The envelope measures 38 pc (or 15.4′) in diameter (Scoville et al. 1975, corrected for distance) and has a gas mass of $7 \times 10^6\,M_\odot$ (Goldsmith et al. 1990). The average H_2 density $n(H_2) \sim 10^3\,cm^{-3}$, and H_2 column density $N(H_2) \sim 10^{23}\,cm^{-2}$, are relatively low compared to the central part of the region. The moderate density region extends over 2.5 pc × 5.0 pc around the

[4]Throughout this thesis, I will assume a distance to Sgr B2 of 8.5 kpc.

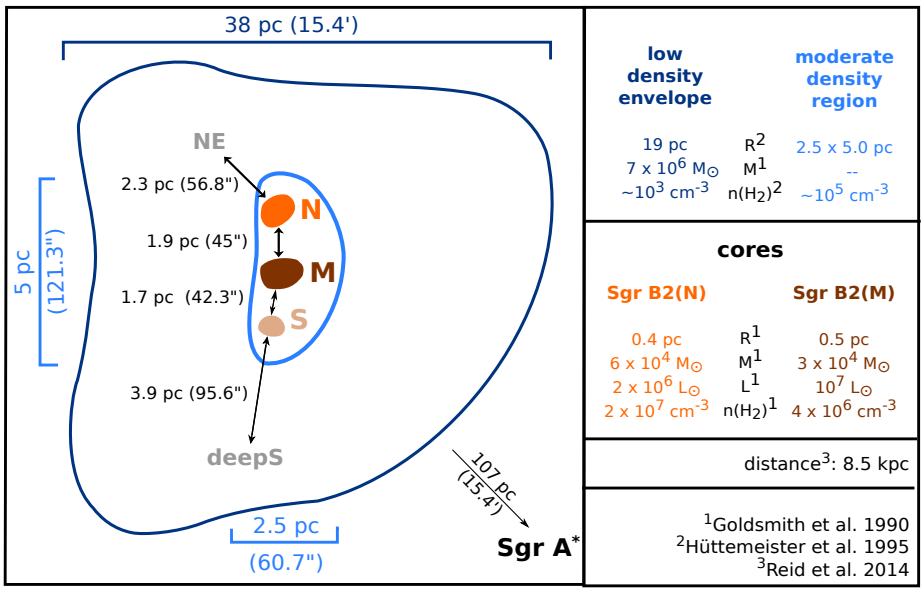

Figure 2.11: Sketch of the Sgr B2 region, adapted from Hüttemeister et al. (1995).

local hotspots. Its density and H_2 column density are higher, $n(H_2) \sim 10^5\,cm^{-3}$ and $N(H_2) \sim 10^{24}\,cm^{-2}$. Embedded in this intermediate region are the local hot cores of which at least three are sites of active star formation (Gordon et al. 1993). Due to their approximate north-south alignment in an equatorial coordinate system, they are historically named: Sgr B2(N)(orth), Sgr B2(M)(ain), and Sgr B2(S)(outh). In projection, Sgr B2(M) is located 1.9 pc (or 45″) south of Sgr B2(N) and Sgr B2(S) is located 1.7 pc (or 42.3″) south of Sgr B2(M), see Fig. 2.11. These cores have sizes of ~ 0.5 pc, H_2 densities of $\sim 10^7\,cm^{-3}$, and column densities of $10^{25}\,cm^{-2}$ (Hüttemeister et al. 1995). Different works, e.g. Goldsmith et al. (1990) and Etxaluze et al. (2013), have derived the gas mass of the two cores Sgr B2(N) and SgrB2 (M) in the ranges of $6 - 25 \times 10^4\,M_\odot$ and $3 - 23 \times 10^4\,M_\odot$, respectively. However, they used different radii (0.4 – 1.6 pc), which makes a comparison of the results impossible.

Sgr B2(N) and Sgr B2(M) are sites of active massive star formation and comprise a plethora of (ultra-compact) HII regions, X-ray sources associated with HII regions, X-ray sources with no radio or IR counterparts (Takagi, Murakami & Koyama 2002), dense cores, embedded protostars, and molecular masers (Goicoechea et al. 2004). More than 70 HII regions have been detected in the whole Sgr B2 cloud complex (see Fig. 2.10; Mehringer et al. 1993; Gaume et al. 1995; De Pree et al. 1998).

2.4 Radiative Transfer

Radiation transfer deals with the propagation of radiation which consists of quantized particles called photons, through absorbing and emitting media. Each photon has four basic properties: (i) the direction from which it emanates, (ii) the time of its arrival, (iii) its polarization, and (iv) its associated energy E, which in turn gives it its frequency / wavelength. The simultaneous knowledge of the arrival time and the energy however is limited by the uncertainty principle.

Radiation transfer is fairly simple if there is no matter present that the radiation could interact with. In this case, the intensity will, in any direction, remain constant along a ray in that direction. The majority of the complications is caused by the interaction of the radiation with a medium.

This interaction adds photons to a ray or removes them from the ray. In radiative transfer calculations one usually assumes that light propagates so fast that one can ignore the light travel time effects, i.e. all photons travel through the medium on a time scale that is much shorter than any changes happening to the medium. The radiation can thus be regarded as a steady-state flow of photons.

The basics of radiative transfer are covered in many good introductory textbooks, such as Rybicki & Lightman (1986), Draine (2011), and Ward-Thompson & A. P. Whitworth (2011).

2.4.1 The equation of radiative transfer and its formal solution

Let us consider a ray consisting of photons of frequency ν. This ray travels a length L through a medium. Photons from the ray can be absorbed or scattered to another direction by the matter present in the medium, which effectively removes the photons from the ray. The matter can also emit photons or scatter other photons in the direction of the ray, thus it effectively adds photons to the ray.

The change of intensity of radiation as it passes through a medium is described by the radiative transfer equation. Neglecting scattering, this equation is

$$\frac{dI_\nu}{ds} = -\kappa_\nu I_\nu + \varepsilon_\nu, \tag{2.4}$$

where I_ν is the specific intensity of the radiation, κ_ν is the absorption coefficient and ε_ν is the emission coefficient of the medium. The first term on the right hand side defines the attenution of the intensity, while the second term described the increase in intensity. By defining the optical depth $d\tau = \kappa_\nu\, ds$[5] as an independent variable and the source function $S = \varepsilon_\nu/\kappa_\nu$, which described the properties of the medium, Eq. (2.4) becomes

$$\frac{dI_\nu}{d\tau_\nu} = -I_\nu + S_\nu. \tag{2.5}$$

In thermodynamic equilibrium, the intensity is uniform, i.e. $I_\nu/d\tau_\nu = 0$, and given by the Planck formula, $B_\nu(T)$.

$$I_\nu = S_\nu = B_\nu(T) = \frac{\varepsilon_\nu}{\kappa_\nu} \qquad \text{(in thermodynamic equilibrium)} \tag{2.6}$$

[5] Note, some authors adopt the definition of radiation propagating in the direction of decreasing optical depth.

Formal integration of Eq. (2.5) yields the general solution of the equation of radiative transfer:

$$I_\nu(\tau_\nu) = I_\nu(0)\, e^{-\tau_\nu} + \int_0^{\tau_\nu} e^{-(\tau_\nu - \tau')}\, S_\nu\, d\tau' \tag{2.7}$$

The intensity of the detected radiation is hence the sum of the attenuated radiation from the source itself (first term on the right hand side) and the self attenuated radiation emitted by the medium (second term on the right hand side).

In an uniform medium, i.e. $\varepsilon_\nu(\tau_\nu) = \varepsilon_\nu^0$ and $S_\nu(\tau_\nu) = S_\nu^0$, the general solution given in Eq. (2.7) simplifies to

$$I_\nu(\tau_\nu) = I_\nu(0)e^{-\tau_\nu} + S_\nu^0\left(1 - e^{-\tau_\nu}\right) \approx \begin{cases} I_\nu(0)e^{-\tau_\nu} & \text{background intensity dominates} \\ S_\nu^0\left(1 - e^{-\tau_\nu}\right) & \text{emission from the medium dominates} \end{cases} \tag{2.8}$$

We can simplify the second case in Eq. (2.8) even further assuming two different cases for the optical depth

$$I_\nu(\tau_\nu) \approx S_\nu^0\left(1 - e^{-\tau_\nu}\right) \approx \begin{cases} S_\nu^0 \tau_\nu & \text{optically thin, i.e. } \tau_\nu \ll 1 \\ S_\nu^0 & \text{optically thick, i.e. } \tau_\nu \gg 1 \end{cases} \tag{2.9}$$

2.4.2 Continuum emission

In the case of continuum radiation, which is emitted by the dust, the background radiation field is usually negligible. Furthermore, if the emitting dust is at a single temperature, we can replace S_ν^0 in Eq. (2.8) with the Planck function $B_\nu(T_{\rm dust})$, yielding

$$I_\nu(\tau_\nu) = B_\nu(T_{\rm dust})\left(1 - e^{-\tau_\nu}\right) \tag{2.10}$$

$$= \frac{2h\nu^3}{c^2}\left[\exp\left(\frac{h\nu}{kT_{\rm dust}}\right) - 1\right]^{-1}\left(1 - e^{-\tau_\nu}\right), \tag{2.11}$$

where $T_{\rm dust}$ is the dust temperature. If the intensity of a specific astrophysical object is measured at many different frequencies, Eq. (2.11) can be invoked to determine the dust temperature and dust optical depth of this object. This is often called a modified blackbody function or a greybody function.

2.4.3 Line radiation

Let us assume we have a gas composed of molecules (or atoms or ions) of a species X together with a collider that has a number density $u_{\rm collider}$ and continuum radiation, which has an energy density u_{ν_0}. For simplicity, we further assume that the species X is a two level system, with the states labeled l and u with statistical weights g_l and g_u and having energies E_l and E_u, respectively, where $E_l < E_u$ and the energy difference is given by $\Delta E = E_u - E_l = h\nu_0$.

Emission and absorption processes – transfer of populations

The energy levels of a molecule are in statistical equilibrium when the rate of transitions populating a given energy level is balanced by the rate of transitions depopulating that energy level. In the two-level system, the statistical equilibrium equation reads

$$n_{X,l} R_{lu} = n_{X,u} R_{ul}, \tag{2.12}$$

where $n_{X,l}$ and n_{X_u} are the number densities of particles of species X in the lower and upper energy level, respectively, and R_{lu} and R_{ul} are the upward or downward transition rates between the two energy levels, respectively. There is a variety of processes that transfer the populations from one level to another:

$$A_{ul} \quad \text{(spontaneous radiative de-excitation)} \tag{2.13}$$

$$B_{lu}\, u_{\nu_0} \quad \text{(stimulated radiative excitation)} \tag{2.14}$$

$$B_{ul}\, u_{\nu_0} \quad \text{(stimulated radiative de-excitation)} \tag{2.15}$$

$$C_{lu}(T)\, n_{\text{collider}} \quad \text{(collisional excitation)} \tag{2.16}$$

$$C_{ul}(T)\, n_{\text{collider}} \quad \text{(collisional de-excitation)} \tag{2.17}$$

A_{ul}, B_{ul}, and B_{lu} are called the Einstein coefficients. $C_{ul}(T)$ and $C_{lu}(T)$ are the temperature dependent collisional coefficients of the collider in question. Typical colliders are H_2, H, He and free electrons.

Putting everything together yields

$$n_{X,l}\left(B_{lu}\, u_{\nu_0} + C_{lu}(T)\, n_{\text{collider}}\right) = n_{X,u}\left(A_{ul} + B_{ul}\, u_{\nu_0} + C_{ul}(T)\, n_{\text{collider}}\right) \tag{2.18}$$

This balance must hold at all temperatures and all densities.

Level populations

Assuming thermodynamic equilibrium, the relative populations of both levels is given by the Boltzmann equation

$$\frac{n_{X,u}}{n_{X,l}} = \frac{g_u \exp\left(\frac{-E_u}{kT}\right)}{g_l \exp\left(\frac{-E_l}{kT}\right)} \tag{2.19}$$

$$= \frac{g_u}{g_l} \exp\left(\frac{-(E_u - E_l)}{kT}\right). \tag{2.20}$$

Using $\Delta E = E_u - E_l = h\nu_0$ yields

$$\frac{n_{X,u}}{n_{X,l}} = \frac{g_u}{g_l} \exp\left(-\frac{h\nu_0}{kT}\right), \tag{2.21}$$

where g_l and g_u are the statistical weights of the lower and upper level, respectively, and E_l and E_u are their respective energy levels.

The fraction of particles in any level i is given by

$$\frac{n_{X,i}}{n_X} = \frac{g_i \exp\left[\frac{-E_i}{kT}\right]}{Z_X(T)} \tag{2.22}$$

where $Z_X(T)$ is the partition function (german: Zustandssumme) of species X. It is given by

$$Z_X(T) = \sum_{\text{all levels i}} \left(g_i \exp\left[\frac{E_i}{kT}\right] \right) \tag{2.23}$$

Relations between the radiative and collisional coefficients

In (local) thermodynamic equilibrium, the relative level populations are given by Eq. (2.21). The energy density of the continuum radiation field is furthermore given by

$$u_{\nu_0} = \frac{4\pi B_{\nu_0}(T)}{c}, \tag{2.24}$$

which in local thermodynamic equilibrium equals the Planck function

$$u_{\nu_0} = \frac{8\pi h \nu_0^3}{c^3} \left[\exp\left(\frac{h\nu_0}{kT}\right) - 1 \right]^{-1}. \tag{2.25}$$

As discussed in Section 2.4.3, the rate at which populations are transferred upwards must balance the rate at which populations are balanced downwards. As aforementioned this balance must hold at all temperatures and all densities. The introduced coefficients A_{ul}, B_{ul}, B_{lu}, $C_{ul}(T)$ and $C_{lu}(T)$ are intrinsic properties of the particles, i.e. they remain the same irrespective the density of the surrounding material. Thus, while keeping the temperature fixed at an arbitrary value and increasing the density only we can show that the collisional terms in Eq. (2.18) must balance independently due to their squared dependence on the density

$$n_{X,u} C_{ul}(T) = n_{X,l} C_{lu}(T). \tag{2.26}$$

Replacing the number densities of the upper and lower level using Eq. (2.21) yields

$$C_{ul}(T) = \frac{g_i}{g_j} \exp\left[\frac{h\nu_0}{kT}\right] C_{lu}(T). \tag{2.27}$$

But also the radiative terms must balance separately. We obtain

$$A_{ul} + \frac{8\pi h \nu_0^3}{c^3} \left[\exp\left(\frac{h\nu_0}{kT}\right) - 1 \right]^{-1} B_{ul} = \frac{n_{X,l}}{n_{X,u}} \frac{8\pi h \nu_0^3}{c^3} \left[\exp\left(\frac{h\nu_0}{kT}\right) - 1 \right]^{-1} B_{lu}. \tag{2.28}$$

Again replacing the number densities of the upper and lower level using Eq. (2.21) gives

$$A_{ul} + \frac{8\pi h \nu_0^3}{c^3} \left[\exp\left(\frac{h\nu_0}{kT}\right) - 1 \right]^{-1} B_{ul} = \frac{g_u}{g_l} \exp\left(-\frac{h\nu_0}{kT}\right) \frac{8\pi h \nu_0^3}{c^3} \left[\exp\left(\frac{h\nu_0}{kT}\right) - 1 \right]^{-1} B_{lu}. \tag{2.29}$$

Multiplying both sides by the term in square brackets then yields

$$A_{ul} \left[\exp\left(\frac{h\nu_0}{kT}\right) - 1 \right] + \frac{8\pi h \nu_0^3}{c^3} B_{ul} = \frac{g_l}{g_u} \exp\left(\frac{h\nu_0}{kT}\right) \frac{8\pi h \nu_0^3}{c^3} B_{lu}. \tag{2.30}$$

In Eq. (2.30), the temperature-dependent as well as the temperature-independent terms must each balance separately, since these terms can be made arbitrarily large (small) by simply decreasing (increasing) the temperature. This yields

$$B_{lu} = \frac{g_u}{g_l} \frac{c^3}{8\pi h \nu_0^3} A_{ul} \tag{2.31}$$

and

$$B_{ul} = \frac{c^3}{8\pi h \nu_0^3} A_{ul} \tag{2.32}$$

Inserting Eq. (2.32) in Eq. (2.31) yields

$$B_{lu} = \frac{g_u}{g_l} B_{ul} \tag{2.33}$$

Equations (2.27), (2.31) and (2.33) are also known as the Einstein relations. They make our life easier, since with measuring (and/or quantum-mechanically calculating) two coefficients, namely one collision coefficient and the Einstein A coefficient (which is not an easy thing to do, especially at low temperatures), all other coefficients can be easily calculated.

Einstein A coefficients, together with the transition frequencies, are measured and tabulated for many transitions of many species. They are stored in publicly available databases such as Cologne Database of Molecular Spectroscopy (CDMS)[6], the JPL catalogue[7]. Collisional rates for some species and some colliders are available covering a limited temperature range. These rates are stored in databases like BASECOL [8].

The Virtual Atomic and Molecular Data Centre (VAMDC) project[9] is a fairly recent effort to connect all existing databases together. This includes the CDMS database, the JPL database, but also for example BASECOL.

LTE vs. non-LTE conditions

The local thermodynamic equilibrium basically means that due to e.g. collisions, the Boltzmann distribution of the level population is established, but the radiation field is not in equilibrium with the particles.

A useful quantity to check if LTE conditions hold, is the so called critical density, which is commonly defined as

$$n_{\text{crit}} \sim \frac{A_{ul}}{C_{ul}}, \tag{2.34}$$

[6] http://cdms.ph1.uni-koeln.de/cdms/portal
[7] https://spec.jpl.nasa.gov/
[8] http://basecol.obspm.fr/
[9] www.vamdc.eu

assuming the intensity I_ν is very low so that absorption and stimulated emission processes are negligible. If the density is lower than the critical density $n_{\rm crit}$, collisions happen too infrequently and the level populations are not given by the Boltzmann distribution. If the density exceeds the critical density, collisions dominates and the energy levels are populated following the Boltzmann distribution. The level populations approach their equilibrium value and the line is thermalized.

Absorption and emission coefficients

The absorption coefficient, κ_ν, is the fractional loss of intensity per unit length,

$$\kappa_\nu = \frac{dI_\nu}{ds}\frac{1}{I_\nu}, \tag{2.35}$$

where the loss of intensity is given by

$$\frac{dI_\nu}{ds} = h\nu_0 \left(n_{X,l} B_{lu} I_\nu - n_{X,u} B_{ul} I_\nu\right) \frac{1}{4\pi}\phi(\nu_0), \tag{2.36}$$

where $\phi(\nu_0)$ is a normalized line profile function, which is usually represented using a Gaussian function. Inserting Eq. (2.36) in Eq. (2.35) yields

$$\kappa_\nu = h\nu_0 \left(n_{X,l} B_{lu} - n_{X,u} B_{ul}\right) \frac{1}{4\pi}\phi(\nu_0). \tag{2.37}$$

Rearranging Eq. (2.37) and inserting Eq. (2.32) yields

$$\kappa_\nu = \frac{c^2}{8\pi\nu^2}\frac{g_u}{g_l}A_{ul}\left(1 - \frac{g_l}{g_u}\frac{n_{X,u}}{n_{X,l}}\right)\phi(\nu_0). \tag{2.38}$$

The emission coefficient, ε_ν, is the energy emitted per time per volume per solid angle per unit frequency,

$$\varepsilon_\nu = h\nu_0 A_{ul} n_{X,u} \frac{1}{4\pi}\phi(\nu_0), \tag{2.39}$$

Line width

Spectral lines are not infinitely narrow. They are broadened by processes that can be categorized as microscopic and macroscopic depending whether the length scales they occur on is smaller or larger than the photon mean free path. Microscopic processes operate on atomic or molecular scale. They change the line strength (profile function). Macroscopic processes involve the redistribution of absorption to different wavelengths. Here the overall strength remains unchanged, e.g. rotational broadening of stellar absorption lines.

Microscopic processes include natural line broadening, thermal doppler broadening, microturbulent broadening.

(i) Natural line broadening Natural broadening is intrinsic to the transition. The emitting particles have a finite life-time in the upper level. At low densities, the mean life-time in the upper level is given by the Einstein A coefficient for spontaneous radiative de-excitation $\Delta t \sim A_{ul}^{-1}$. The Heisenberg uncertainty principle imposes a limit on the accuracy of energy ΔE and time Δt, $\Delta E \Delta t \geq \frac{h}{4\pi}$. The natural line width is roughly the Einstein A coefficient and thus very small.

(ii) Thermal line broadening is due to random thermal noise of the atoms. The velocities of the individual molecules have a Maxwellian distribution. Their average velocity is proportional to $v \propto \sqrt{\frac{T}{m}}$. This causes a thermal line width of $\Delta v = \sqrt{\frac{kT}{m}}$. This is usually on the order of a few tens km s^{-1}.

(iii) Microturbulent broadening This is a collective term of other processes acting on length scale smaller then the photon mean free path. Basically these are non-thermal motions,

$$v^2_{\text{linewidth}} = v^2_{\text{th}} + v^2_{\text{turb}}. \tag{2.40}$$

(iv) Systematic motions In addition to the so chaotic and undirected turbulent motion, systematic motions for example due to infall, rotation, outflows, cause additional line broadening.

Line shapes

Spectral line shapes depend on the line-of-sight distribution of temperature and opacity. In a medium of low optical depth, the spectral line has a Gaussian shape, provided there is only a single velocity component along the line-of-sight. Whether the line if observed in emission or in absorption is determined by the background intensity. In a optically thick medium, the opacity τ exceeds unity first at the maximum of the line profile function $\phi(\nu_0)$. This means that regions closer to the observer are traced at the line center, while regions further away are seen at frequencies having a larger offset from ν_0. Self-absorption, i.e. a dip in the spectral line at the center of the line, is observed if the foreground material is colder than the background material. As already mentioned, $\phi(\nu_0$ is also affected by velocity components along the line-of-sight. For example, infall motion can lead to an asymmetric self-absorption line shape, where the blue side is stronger than the red side. See Fig. 2.12 for an illustration and explanation.

2.4.4 Key points

- The absorption coefficient, α_ν, is the fractional loss of intensity per unit length. This includes stimulated emission.
- The emission coefficient, ε_ν, is the energy emitted per unit time per unit volume per unit solid angle per unit frequency.
- The optical depth, τ_ν, determines the transparency of a medium. This ranges between being opaque ($\tau_\nu > 1$) and transparent ($\tau_\nu < 1$).
- The source function, S_ν, includes all characteristics of the medium in between the source and the observer.
- Kirchhoff's law establishes the equality between the source function and Planck's function in thermal equilibrium ($S_\nu = B_\nu(T)$).
- The radiative transfer equation for a homogeneous cloud in thermal equilibrium is

$$I_\nu = I_0 e^{-\tau_\nu} + (1 - e^{-\tau_\nu}) B_\nu$$

.

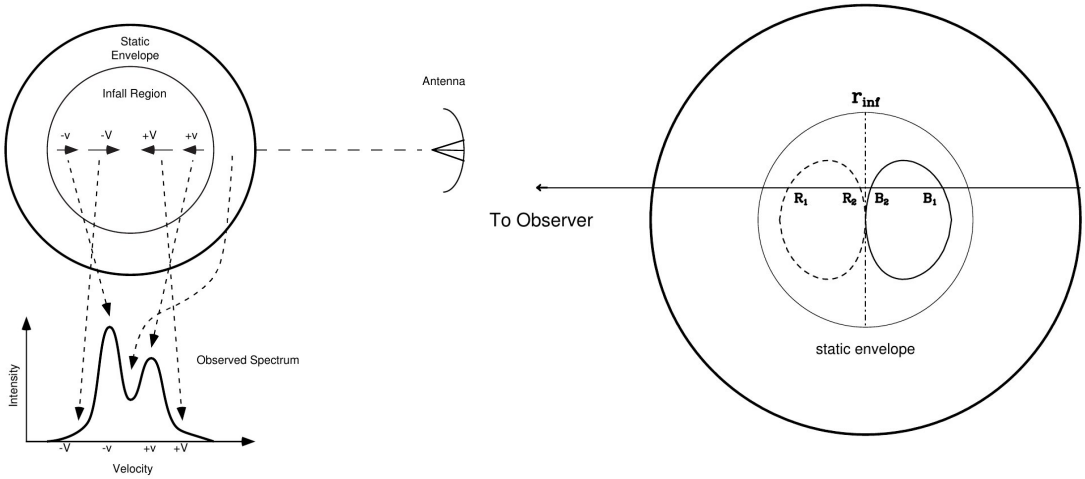

Figure 2.12: Schematic view of the generation of an infall line profile. **Left**: The static envelope produces the absorption dip, the blue peak originates from the gas in the back of the core traveling towards the observer, the red peaks originates from the gas in front of the core that moves away from the observer. Please also note, the faster relative velocities towards the center of the core produce line wings. However, these are observationally often confused by outflow motions, which also produce wide wings in the spectral line profile.**Right:** This is a schematic explanation of the observed asymmetry of optically thick, high excitation lines. The ovals are loci of constant line-of-sight velocity. Each line-of-sight intersects these loci at two points, as indicated by the vertical line pointing towards the observer. The point closer to the center of the core have higher excitation, thus $T_{ex}(R2) > T_{ex}(R1)$ and $T_{ex}(B2) > T_{ex}(B1)$. Thus R1 will obscure the brighter R2, whereas the brighter B2 lies in front of B1. This results in a asymmetric line profile, with the blue peak being stronger than the red peak. Figures taken from N. Evans (2003).

3. Pandora in a nutshell

Apart from in-situ measurements in the Solar System, all information gained in astrophysics is mainly deduced from the analysis and interpretation of electromagnetic radiation received with ground or space based telescopes. So analyzing the radiation received from astrophysical objects provides us information about the source, but also about the medium in between the object and the observer. This makes radiative transfer analysis one of the most fundamental techniques in astrophysics.

Up to now, radiative transfer approaches often have been limited either in the number of dimensions or in the applied geometry. However, high spatially resolved images obtained at different wavelengths e.g. with the VLA, the Herschel Space Observatory, and now ALMA, reveal the complex nature of both the structure and the dynamics. Hence, when trying to simulate such complex structures and dynamics with simple (spherical) models, misleading results could occur. This requires detailed three dimensional radiative simulations, which are now computationally feasible.

As summarized by Steinacker et al. (2013), three-dimensional dust radiative transfer calculations are essential to make progress in many fields of astronomy. Dust grains modify the radiation field in many objects such as protoplanetary disks, evolved stars, reflection nebulae, supernova remnants, molecular clouds, the interstellar medium, galaxies, galactic nuclei, and the high-redshift universe.

First I will quickly introduce the workflow of PANDORA (Section 3.1). Then I will explain various aspects of PANDORA in more detail: The model setup (Sections 3.2 to 3.4), the grid setup (Section 3.5), radiative transfer simulation (Section 3.6), the post-processing (Section 3.7), model evaluation (Section 3.8), error estimation (Section 3.9), and the visualization (Section 3.10).

3.1 Introduction

When doing multi-dimensional (radiative transfer) simulations many steps have to be taken into account. Figure 3.1 illustrates this. Everything starts with the setup of the physical structure and the corresponding model setup parameters followed by the discretization of the problem at hand (i.e. the selection of an appropriate grid structure). Based on this input, dedicated radiative transfer programs then solve the radiative transfer equation and calculate continuum and line intensity maps. To then compare the model prediction with observations obtained from ground- and space-based telescopes, post-processing is necessary. Ideally these steps are then combined with a model optimizer, which takes the results and, based on for example a χ^2 method, optimizes the input model structure parameters. Judging the quality of the optimized parameters requires a proper error estimation. In addition, specially when dealing with a plethora of different images at many wavelengths or data cubes of many transitions, it has proven useful to include an automated plotting routine. These steps can be separated into the following blocks:

- Block 1: **Model setup** (see Sections 3.2 to 3.4)
- Block 2: **Grid selection** (see Section 3.5)
- Block 3: **Radiative transfer** (see Section 3.6)
- Block 4: **Post-processing** (see Section 3.7)
- Block 5: **Evaluation** (see Section 3.8)
- Block 6: **Error estimation** (see Section 3.9)
- Block 7: **Visualization** (see Section 3.10)

Although in theory these steps all sound very easy and straight forward, the devil is in the details and the full scheme has rarely been applied in astrophysical analysis (Steinacker et al. 2013). Full three-dimensional continuum radiative transfer modeling has so far been performed for disks, and ρ Oph D (Steinacker et al. 2005). So to facilitate the process of full three-dimensional radiative transfer modeling including the steps mentioned above I have designed a framework called PANDORA based on initial work of Rainer Rolffs (Rolffs 2011).

PANDORA consists of different modules written in python and it generally follows a philosophy of flexibility. It tries to avoid reinventing the wheel whenever possible, thus it employs already existing codes for individual working steps. For example, PANDORA makes use of the radiative transfer programs RADMC-3D[1], developed by C. Dullemond (Dullemond 2012), and LIME[2], developed by Ch. Brinch and the LIME development team (Brinch & Hogerheijde 2010). Both allow the setup of full three-dimensional models. For the post-processing PANDORA uses MIRIAD[3] (Sault et al. 1995), a well established data calibration and imaging tool kit among observational astrophysicist mainly because all post-processing of the observational data used in this thesis has been done with MIRIAD as well. PANDORA is also partially linked to the model optimization program MAGIX[4], which is developed by Th. Möller and the

[1] http://www.ita.uni-heidelberg.de/~dullemond/software/radmc-3d/

[2] https://github.com/lime-rt/lime

[3] Several adaptations for different telescopes are available, for example for the Submillimeter Array (SMA). https://www.cfa.harvard.edu/sma/miriad/

[4] https://www.astro.uni-koeln.de/projects/schilke/MAGIX

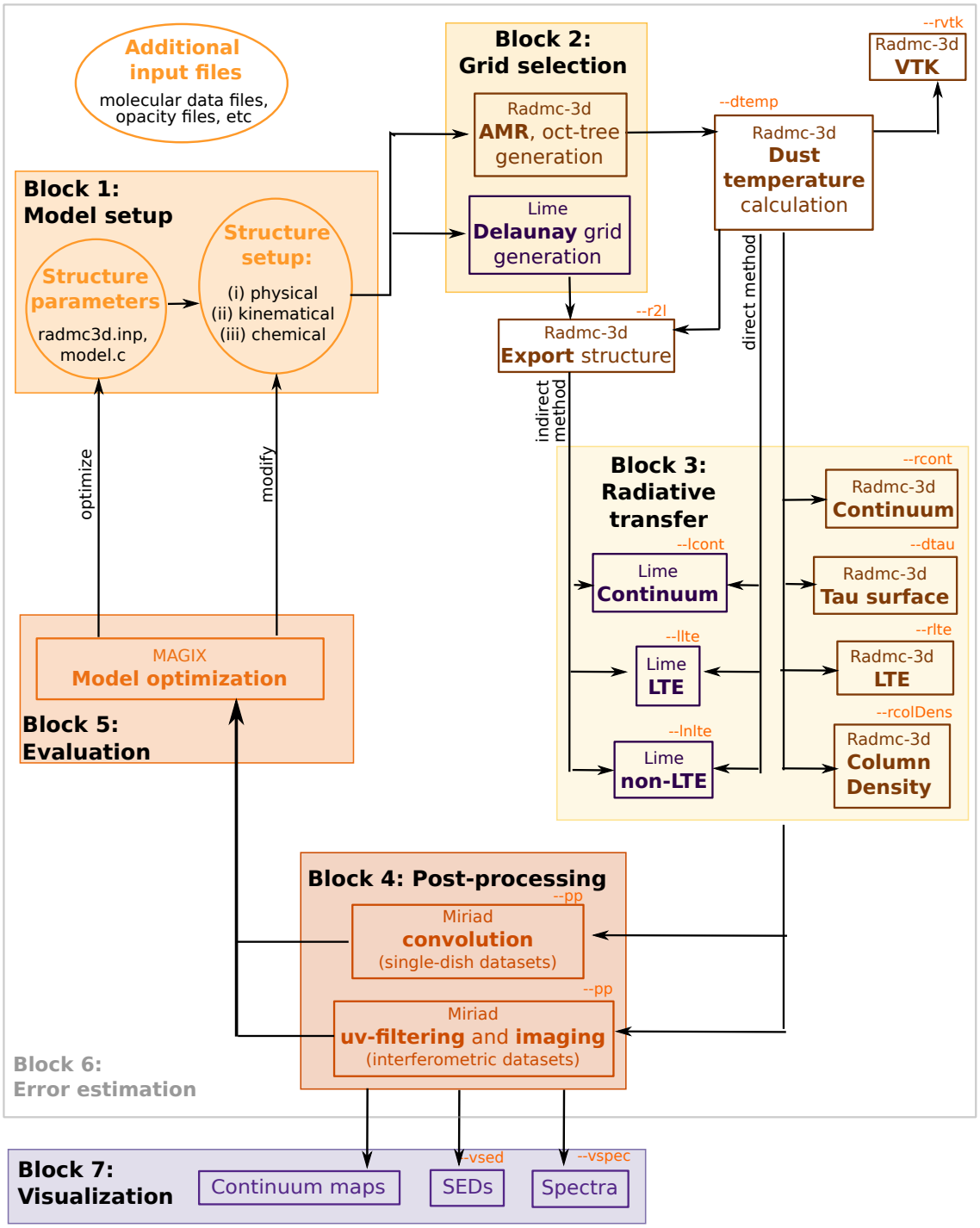

Figure 3.1: Overview of the workflow of the PANDORA framework. The seven major blocks of full radiative transfer analysis are labelled.

CATS team (Möller et al. 2013). MAGIX contains a plethora of well established optimization algorithms to efficiently investigate the model parameter space. Since PANDORA is build in a modular fashion, more and / or different programs can be included as alternatives to the above mentioned programs. This means that, e.g., in addition to MIRIAD, PANDORA could be coupled to CASA[5], a data calibration and imaging suite used for the processing of ALMA data. Furthermore (magneto-)hydrodynamical software (e.g. FLASH[6], RAMSES[7], PLUTO[8]) could be linked to PANDORA, enabling an efficient radiative transfer and post-processing of numerical simulations. Additionally, by coupling PANDORA with astrochemical programs, chemistry is included self-consistently in the simulations. In the case of SAPTARSY (Choudhury et al. 2015), this has already been done.

In the next sections, I am going to explain these seven blocks in more detail. While doing so, I will also explain the setup and inner working of PANDORA. I will start by explaining the model setup, which is divided in three sub-blocks. First I will explain how the physical structure is set up, then I will concentrate on the kinematic setup and introduce the parameterization of the velocity field and last I will introduce the chemical setup, i.e. the setup the molecular densities.

As we will see later-on, the number of free parameters can become very large, which is why it is very important from the beginning to consistently constrain setup parameters whenever possible. RADMC-3D for example offers the possibility to calculate the dust temperature self-consistently. This makes RADMC-3D our first choice of interest, when it comes to simulating the dust emission.

3.2 Model setup: Physical structure

Four major components define the physical structure. To perform full radiative transfer simulations, we need to know the density distribution of the dust (sub-millimeter), the electrons and the ions (free-free). We furthermore nee to know the location of the heating source, i.e. the stars, to be able to calculate the dust temperature self-consistently. The model setup in PANDORA is designed like a LEGO® system, i.e. many different structures are defined and can be put together modularly by the user according to the source-specific needs.

3.2.1 Dust density

The overall density structure is obtained by the superposition of the density profiles of all dust cores, i.e. in overlap regions, the density simply adds up. In each cell j, the density is determined as

$$n_j = \sum_{i=1}^{N} n_{i,j}(\boldsymbol{r}) \tag{3.1}$$

where i is the index of the dust cores and N is the number of cores. Following Qin et al. (2011), I use a modified Plummer-like profile to model the SMA dust density cores as well as the large-scale envelopes.

[5] https://casa.nrao.edu/
[6] http://flash.uchicago.edu/site/
[7] http://irfu.cea.fr/Phocea/Vie_des_labos/Ast/ast_sstechnique.php?id_ast=904
[8] http://plutocode.ph.unito.it/

For a subset of my models, I find it useful to introduce elongated density structures. They are defined as follows:

$$n_i(\boldsymbol{r}) = \frac{n_c}{(1+|\boldsymbol{r}|^2)^{\eta/2}}, \tag{3.2}$$

where n_c is the central density given in H_2 cm^{-3} and $\boldsymbol{r}$ is given by the Euclidean norm, including scaling factors

$$|\boldsymbol{r}| = \sqrt{\left(\frac{r_x}{r_{0,x}}\right)^2 + \left(\frac{r_y}{r_{0,y}}\right)^2 + \left(\frac{r_z}{r_{0,z}}\right)^2}. \tag{3.3}$$

Here, $r_{x,y,z}$ are the components of r and $r_{0,x}$, $r_{0,y}$, and $r_{0,z}$ set the size of the cluster core in each of the three principal axes. A spherical symmetric distribution is obtained by setting $r_0 = r_{0,x} = r_{0,y} = r_{0,z}$. The density distribution is flat inside the radius r_0 and approaches a power-law with an exponent η at $r \gg r_0$.

So to define a dust core, the user needs to provide the center coordinates, the displacement along the z-axis with respect to the reference position, in units of au, the central density n_0, in units of H_2 per cm^3, the turnover radii $r_{0,x}$, $r_{0,y}$, $r_{0,z}$, all three in units of au, and the exponent η.

3.2.2 Electron and ion density

In the model setup, I consider HII regions as non-expanding Strömgren spheres, i.e. as fully ionized, spherical regions of uniform electron density without dust.

To define an HII region in PANDORA, the user needs to provide the center coordinates, the displacement along the z-axis with respect to the model reference position, in units of au, the electron density in units of electrons per cm^3, the radius of the HII region, in units of au, and the Zero-Age-Main-Sequence (ZAMS) type of the embedded star.

Assuming optical thin emission, the number electron density n_e can be calculated using the following formula:

$$\left(\frac{n_e}{\mathrm{cm}^{-3}}\right) = 2.576 \times 10^6 \left(\frac{F_\nu}{\mathrm{Jy}}\right)^{0.5} \left(\frac{T_e}{\mathrm{K}}\right)^{0.175} \left(\frac{\nu}{\mathrm{GHz}}\right)^{0.05} \left(\frac{\theta_{\mathrm{source}}}{\mathrm{arcsec}}\right)^{-1.5} \left(\frac{D}{\mathrm{pc}}\right)^{-0.5}, \tag{3.4}$$

where F_ν is the flux density of the HII region, T_e is the electron temperature, ν is the frequency, θ_{source} is the angular diameter of the HII region, and D is the distance to the source. A derivation of this formula can be found in the appendix A.1.

One note of caution is in order. The formulas given above are only valid under the optical thin assumption. Deriving the number electron density at a certain frequency from the observed flux density assuming optical thin emission will underestimate the number electron density if the HII region is actually optically thick. This underestimate will then lead to the intensity of the (optically thick) HII region being underpredicted by the simulation compared to the observed data at this frequency. To account for this discrepancy, one should compare the synthetic intensities obtained from the model setup with the

observed intensities. From the deviation of the intensity levels, one can identify the HII regions which must be optically thick, if they are resolved. This then allows to iteratively adjust the flux density values and recalculate the number electron density n_e until a reasonably good match between the observed and synthetic intensities is obtained.

3.2.3 Heating sources

RADMC-3D provides several methods to include luminous sources. I choose the option to manually specify the individual luminous sources and assume that all stars are point sources, i.e. their radius is not taken into account. I use a two-step approach. In the first step I account for observed early-type high-mass stars by including known HII regions detected in a region. This usually accounts for stars down to the B0 spectral type and sets the lower limit of the stellar mass detected by observing HII regions, M_1. In the second step I take later spectral types, i.e. stars which cannot produce HII regions detectable with current observations, with stellar masses between 0.01 $M_\odot$ and M_1, into account.

High-mass stars

We assume that each HII region is ionized by a single star. From Section 3.2.2, we already know how to include an HII region in the model. To specify the embedded star, we add another column to the structure file and specify the ZAMS type of the star.

The ZAMS type can be derived from the number of ionizing photons $\dot{N}_i$, which are given by the following formula:

$$\left(\frac{\dot{N}_i}{s^{-1}}\right) = 4.771 \times 10^{42} \times \left(\frac{F_\nu}{Jy}\right) \left(\frac{T_e}{K}\right)^{-0.45} \left(\frac{\nu}{GHz}\right)^{0.1} \left(\frac{D}{pc}\right)^2 \tag{3.5}$$

Here F_ν is the flux density of the HII region, T_e is the electron temperature, ν is the frequency, and D is the distance to the source. Typical values of the electron temperature are between 8000 – 12000 K. A derivation of this formula can be found in the appendix A.1.

From the ZAMS type PANDORA obtains the luminosity and temperature of the star using look-up tables, e.g. Vacca et al. (1996, Table 5). PANDORA furthermore uses the RADMC-3D option to assume simple blackbody spectra for each star, by specifying its blackbody temperature.

Low- and intermediate mass stars

PANDORA provides the possibility to account for (mostly unobservable) low- and intermediate mass stars. For this it includes a star sprinkling algorithm, which in short works as follows: Based on the gravitational potential, the algorithm randomly determines positions for the new stars, following the procedure explained in the appendix of Aarseth et al. (1974). Then a luminosity which is randomly drawn from the IMF of Kroupa (2001), is assigned to each star. It is currently only possible to specify spherical symmetric star clusters. However, PANDORA differentiates between two kind of clusters, any number of local clusters and a single global cluster. Local clusters are non-intersecting with each other. They are embedded in the single global cluster.

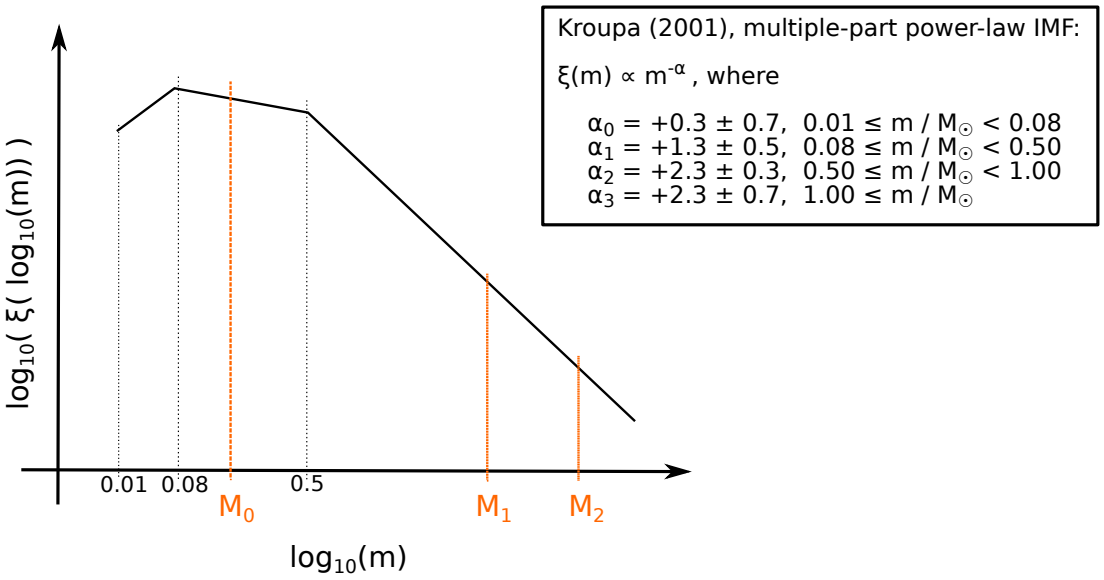

Figure 3.2: Sketch of Kroupa's IMF showing our approach.

The user specifies for each local star cluster the center coordinates, the displacement along the z-axis with respect to the reference position, in units of au, and the radius of the cluster, also in units of au.

For each local star cluster, PANDORA then calculates the fraction $f_{\rm HM}$ of the stars in the high mass regime (i.e. between M_1 and M_2; $M_1 < M_2$) to the mass of all stars (i.e. between M_0 and M_2; $M_0 < M_1 < M_2$) using Kroupa's IMF. This is schematically indicated in Fig. 3.2. The lowest mass boundary M_0 is provided by the user. The mass boundary M_1 can be either provided by the user or by setting it equal to the mass boundary M_0, PANDORA automatically uses the mass boundary set by the high-mass stars that were distributed within the cluster in the first step described above. The total stellar mass of the cluster $M_{\rm cluster}$ is then calculated from the ratio of the sum of the stellar mass of all high-mass stars distributed between M_1 and M_2 to the ratio $f_{\rm HM}$. The star sprinkling algorithm then randomly draws stars between M_0 and M_1 from the IMF until the total stellar mass of the cluster, $M_{\rm cluster}$, is reached.

After the stars are sprinkled separately within each of these local clusters, the star-sprinkling procedure is repeated once more for the global cluster. The user specifies the radius of that cluster and its mass boundaries in the same fashion as for the local clusters. The algorithm determines all stars located explicitly in the global cluster (high-mass stars located in a local cluster are excluded) and calculates their total stellar mass. The algorithm then calculates the total stellar mass of the global cluster (excluding the local star clusters). If it is larger than the total stellar mass of the high-mass stars, stars are sprinkled everywhere except in the local star clusters until the calculated total stellar mass of the global cluster is reached.

PANDORA then converts the stellar mass M to luminosity L using the parameterized mass-luminosity

relation from Griffiths et al. (1988):

$$\log_{10}\left(\frac{L}{L_\odot}\right) = \begin{cases} 0.006 + 4.16\log_{10}\left(\frac{M}{M_\odot}\right), & 0.682 < \log_{10}\left(\frac{M}{M_\odot}\right) < 0.461 \\ 0.370 + 3.51\log_{10}\left(\frac{M}{M_\odot}\right), & \log_{10}\left(\frac{M}{M_\odot}\right) > 0.461 \end{cases} \tag{3.6}$$

Griffiths et al. (1988) provide two sets of boundaries. One is non-continuous but has a better χ^2 value whereas the other set, which we choose to use, provides a continuous behaviour of the mass-to-luminosity relation while having a slightly worse χ^2 value.

PANDORA only includes luminosity in terms of ZAMS luminosity. The total luminosity determined in the literature, however, includes contributions from accretion luminosity, as well as from high-mass stars without an HII region (Hosokawa & Omukai 2009). The luminosity calculated with this approach is thus a lower limit. We determine the corresponding effective temperatures of the stars using the fundamental stellar parameters (spectral type, luminosity, effective temperature) compiled by Straizys & Kuriliene (1981). Since we need to provide an effective temperature for each star, the limitation of the tabulated data sets the lower mass limits of the star clusters to $0.2\,M_\odot$ despite the IMF having a lower mass boundary of $0.01\,M_\odot$.

Please note, that in its current implementation, PANDORA only consider stars as heating sources (see Section 3.2.3). Other types of heating, e.g. cosmic ray heating or coupling with the turbulently heated gas, are currently not considered.

3.2.4 Temperature

As already mentioned, the dust temperature is calculated self-consistently by RADMC-3D using the Monte Carlo method of Bjorkman & Wood (2001). So strictly speaking the dust temperature is not a free parameter and does not need any parameterization and thus no mentioning here. However to better understand the subsequent sections focusing on the velocity field and the chemical setup it is worth briefly explaining the derivation of the dust temperature here.

Initially, all cells have a dust temperature equal to zero. To determine the dust temperature, RADMC-3D first identifies all sources of luminosity, i.e., the total amount of energy available. This amount is divided into photon packages, which are separately emitted by the individual stars one after another. As the photon packages move through the grid, they interact with the dust present (scattering, absorption) causing them to change their direction or wavelength. In the case of absorption, the photon package is immediately re-emitted in a different direction with another wavelength according to Bjorkman & Wood (2001). However, the luminosity fraction each photon package represents remains the same. Whenever a photon package enters a cell, it increases the energy of that cell and thus also increases the temperature of the dust. Photon packages never get lost, they can only escape the model through the outer edge of the grid. After the last photon package has escaped the grid, the dust temperature is obtained. In summary the dust temperature of each cell is basically the sum of the energy fractions of each photon package passing through the cell. In total we use 10 million photon packages.

The calculated temperature is an equilibrium dust temperature, since it is assumed that the amount of energy each dust grain acquires and re-radiates stays the same. For most cases, this is presumably a very good approximation, because the heating and cooling timescales for dust grains are typically very short, compared to any time-dependent dynamics of the system (Choudhury et al. 2015). Thus transiently heated small grains are not important within the wavelength range considered here.

Furthermore, PANDORA provides the possibility to use the Modified Random Walk (MRW) method that is implemented in RADMC-3D in the simplified form described in Robitaille (2010). This method prevents a photon package from getting trapped in high-density regions by predicting where the photon will go next. This allows RADMC-3D to make one single large step of the photon package, saving the computation time for the otherwise necessary hundreds or thousands of absorption or scattering events.

3.2.5 Additional building blocks

There are several cases, where the density structure is not well described using a superposition of (elongated) spherical symmetric clumps. Two examples are outflows and filaments. PANDORA thus includes some simplistic ways of introducing density variations by defining outflow or filamentary structures.

Furthermore, until now, there is no self-consistent calculation of the gas temperature in RADMC-3D. So PANDORA globally assumes that the gas temperature equals the dust temperature. However, this is often not a good assumption. Which is why PANDORA also contains a few handles to modify the gas temperature field locally if need be.

Density related: Filaments

A filament is made up of many individual filamentary components. Each component is represented by a spherical symmetric cylinder, which is defined by its start and end points (right ascension and declination in x and y direction, respectively and the displacement along the z axis in units of au), a radius, and a length, both given in units of au.

Density and temperature related: Outflows

Outflows are very simplistically represented by cones. This setup can and should be improved if modeling an outflow is the goal of using PANDORA. Zernickel (2015) used this basic functionality to improve his model of the star forming region NGC6334. Figure 3.3 shows the geometry of the outflow setup. An outflow cone is defined by the coordinates of the starting point (right ascension, declination in x and y direction, respectively, and the displacement along the z axis in units of au), a length given in units of au, half the opening angle, given in degree and the orientation of the cone, given by the azimuthal angle θ, and the elevation angle φ, both given in degree. The azimuthal angle can take values from 0 up to 360 degrees, the elevation angle can take value from 0 up to 180 degrees. Within the outflow cone, the density is set to a user defined value, given in H_2 cm^{-3}, and a gas temperature, given in units of Kelvin.

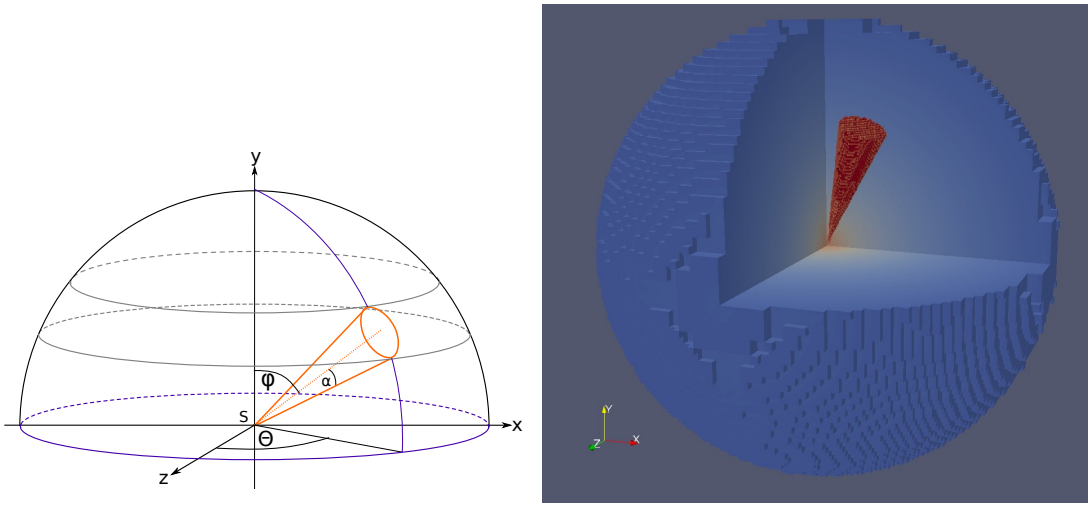

Figure 3.3: Left: Geometry of the outflow setup. An outflow is represented by a cone. θ is the azimuthal angle, φ is the elevation angle, and α is the half open angle of the outflow. The length of the outflow is indicated by the dotted orange line. Right: Sample outflow cone in dark red. The cone is oriented such that the tip of the cone coincides with the model center. The azimuth angle is 60 degree, the elevation angle 25 degree. The outflow has a length of 10000 au and a density of 10^6 H_2 cm^{-3}. The surrounding core has a turnover radius of 1000 au and a center density of 10^4 H_2 cm^{-3}. The orientation of the coordinate system is indicated in the bottom left corner.

Temperature related: shocks

A shock region defines a sphere within which a user-defined gas temperature. This element has been added to provide the possibility to raise the gas temperature over the gas temperature in, e.g. very dense regions, where the gas temperature could be elevated due to shocks. Thus the naming choice. Such a shock structure is defined by the location of the sphere's center (right ascension and declination for the x an y direction, displacement along the z-axis in units of au), the radius of the sphere in units of au, and the gas temperature in units of Kelvin.

Temperature related: shells

De Vicente et al. (1997) reported the detection of a ring-like structure in Sgr B2. Within this ring, the gas temperature is significantly higher than in- or outside the ring. To account for this, PANDORA includes the possibility to define shells. They are given by the location of the shell center (right ascension and declination for the x an y direction, displacement along the z-axis in units of au), the inner and the outer radius of the shell, given in units of au, and the gas temperature in units of Kelvin.

3.3 Model setup: Kinematic structure

3.3.1 Velocity field

The gas velocity field is a combination of a global and a local setup. The user can specify a source velocity, which is then set as the global velocity along the line-of-sight for the source of interest. Locally, the user can then furthermore specify the velocity components for each core separately. Observationally we will not be able to obtain information about the velocity components along the x an y axis, they are added for sake of completeness. In astronomy, infall and expansion motions are very common. As a first approach one often assumes the free-fall velocity for infall motion. Rolffs et al. (2010) find the free-fall infall velocity overestimates the infall velocity. In PANDORA the velocity field is parameterized. For each density core c, the user can thus specify the velocity components along the three major axes, $\vec{v}_c$, as well as a radial velocity component $\vec{v}_{r,c}$, all in units of km/s. Rotation is currently not considered, but can be included easily. The overall velocity field is then calculated by density weighting the contribution from each density gradient

$$\vec{v} = \frac{\sum_{c=1}^{N} n_c \left(\vec{v}_c + \vec{v}_{r,c} \frac{\vec{r}_c}{|\vec{r}_c|} \right)}{\sum_{c=1}^{N} n_c}, \tag{3.7}$$

where the sums go over the indices c for density component and n is the density.

3.3.2 Line width

As discussed in Section 2.4.3, physical processes acting on length scales shorter than the photon mean free path lead to a broadening of spectral lines. We distinguish two major contributors: thermal line broadening and microturbulent line broadening. The thermal line broadening is taken into account by the radiative transfer programs and calculated from the gas temperature. Since the microturbulent line broadening is a collective term for other physical processes apart from thermal broadening, it is treated as one broadening component and the user can specify the full-width at half-maximum (FWHM) that is due to microturbulent line broadening. In the current implementation, this is value is set globally. Local modifications could be implemented, but are currently not available.

3.4 Model setup: Chemical structure

3.4.1 Molecular abundance

As the velocity field, the chemical structure can be set globally and locally. For each molecular species, the user wants to model, PANDORA needs to know the molecular abundance. The abundance is given with respect to H_2. However, molecular abundances are not only linked to the density of H_2. They are also temperature dependent. To account for this, PANDORA includes the possibility to provide different abundances for different temperature regimes. In the current setup, it is only possible to provide one set of

jump temperatures. If the user needs several different jump temperatures for different molecules, these molecules would have to be modeled separately.

For each dust core, the user can then locally modify the molecular densities by providing a scaling factor.

3.5 Grid discretisation

3.5.1 Grid

As dicussed in the introduction, star formation covers a large range of spatial scales of at least four orders of magnitude. The largest entities, i.e. molecular clouds, cover spatial scales of $10 - 100\,\mathrm{pc}$ (see Section 2.1), while condensations have sizes of $< 0.01\,\mathrm{pc}$. To properly investigate the physical, kinematic and chemical structure, PANDORA needs to be able to recover this large dynamic range in spatial resolution. However, if we were to attempt this with a cartesian grid, i.e. a grid where the elements are unit cubes, this would require tens to hundreds of billions of cells. This is not only computationally unfeasible but also unnecessary, for example when the density distribution is flat.

PANDORA thus uses the adaptive mesh refinement technique (originally presented by Berger & Oliger 1984; Berger & Colella 1989) to locally increase the spatial resolution of the numerical radiative transfer simulation. The initial grid consists of N^3 cells. It employs the RADMC-3D option to include a tree-based AMR method (Khokhlov 1998, and references therein). This means that, on a cell-by-cell basis, parent cells are refined into children cells resulting in a recursive tree structure. The resulting grid provides high resolution where needed based on the refinement criteria.

In PANDORA, two criteria are used to check if a cell needs to be refined: (i) the presence of a dust core center or HII region within the cell and (ii) the dust density distribution within the cell. When covering a large dynamical range starting with an initial grid of a few cells per dimension, it is crucial to make sure that small clumps are recognized by the refinement routine. Thus as long as the cell size is larger than twice the radius of a dust core, this cell is refined if the core center is located within the cell. A cell is also refined into eight sub-cells if the density gradient is larger than a threshold:

$$\frac{|n_{\mathrm{center}} - n_i|}{n_{\mathrm{center}}} > \epsilon, \tag{3.8}$$

where n_{center} is the density at the cell center and n_i is the density at the reference position with the cell, and ϵ is the allowed maximum density difference.

During the work on this thesis, I have tried several strategies to calculate the density gradient. The first simply checks the gradient towards the corners and the facets of the cell, i.e. for each cell 14 gradients are checked. Let's call this routine the *corner-facet gradient refinement*. The second routine checks the density gradient using randomly sampled point located on the surface of a sphere within the cell. This sphere has a radius which is the distance between the current cell center and the child cell center, i.e. $\sqrt{3}\,\mathrm{cellsize}/4$. The number of points that are sampled is derived for each cell based on the surface area of the sphere weighted by the refinement criteria. Let's call this routine the *spherical gradient refinement*.

The user can specify the number of initial cells per dimension (N), and the half size of the entire model in units of parsec. For the refinement, the user needs to specify the threshold of the density gradient (ϵ), and the minimum cell size. In addition to this, the user also has to specify the number of maximum cells in the grid. This step unfortunately is needed to calculate the amount of memory needed by RADMC-3D.

In Section 4.1.2, I will discuss and illustrate the difference of these two strategies of grid refinement for a spherical symmetric clump.

3.5.2 Coordinate system

We use a positively right-handed cartesian coordinate system. This means that the x-axis points west on the sky, the y-axis points to the north and the z-axis points towards the observer. The origin of this system is located at the center of the model.

3.6 Radiative transfer simulations

As mentioned in the previous section the main aim of PANDORA is to provide an easy to use modeling framework that combines all steps of modeling. So it avoids to re-invent the wheel over and over again and instead incorporates many already available astronomical software. However in order to avoid just using these software packages as a black-box, I will explain their main features and behind-the-hook capabilities. Many of these programs have very extensive manuals and references to these are given in the subsequent subsections.

3.6.1 RADMC-3D

RADMC-3D is a three-dimensional radiative transfer program developed by Cornelis Dullemond in Heidelberg (Dullemond 2012)[9]. It is the successor of the one and two dimensional RADMC code. Compared to RADMC, RADMC-3D is a new code implementation and offers many advanced capabilities.

It takes heating sources into consideration and based on this calculates the dust temperature self-consistently. It allows to run continuum and line modeling. RADMC-3D is written in Fortran90 and allows the user to setup their own models in a non-invasive way, i.e. via a separate subroutine. PANDORA employs this option as it is the only way to use the adaptive mesh refinement (AMR) module routines provided by RADMC-3D. Furthermore setting up a model internally is more efficient since it is not required to read in from large input files. This allows to quickly build large models.

Unless explicitly stated differently, all models presented in this thesis have been recomputed with RADMC-3D version 0.39.

3.6.2 LIME

LIME is a three-dimensional radiative transfer program developed by Christian Brinch and since 2015 by the LIME development team (Brinch & Hogerheijde 2010). It is available on github[10]. LIME is able to

[9] http://www.ita.uni-heidelberg.de/~dullemond/software/radmc-3d/

[10] https://github.com/lime-rt/lime

take any three-dimensional density distribution, temperature and velocity field (based on a Delaunay grid) and calculates molecular radiative processed.

3.7 Post-processing

To compare the synthetic maps with observations, telescope-dependent post-processing is necessary. This means, that in the case of single-dish observations the synthetic map needs to be (at least) convolved with the beam of the telescope. If the telescope is known to have, e.g. a non-negligible error beam, then ideally this should be included as well. The latter, PANDORA is currently not able to handle automatically. PANDORA can also deal with interferometric observations. We fold the simulated maps with the uv-coverage of the observation. The imaging is then performed for both maps (synthetic and observed) with the same imaging parameters.For that first uv-filtering is performed. Final maps are then produced for the respective telescopes at various wavelengths in intensity units (Jy/beam).

3.7.1 Miriad

For both cases, I employ the data reduction package MIRIAD (Sault et al. 1995). This is a radio interferometry data-reduction package developed for several interferometers (e.g. SMA). It provides a plethora of tasks to calibrate raw telescope data, image and analyze the data. PANDORA makes use of the imaging capabilities.

3.8 Model optimization and evaluation

Three-dimensional modeling intrinsically has many free parameters. The density structure and velocity field of a single core is described by 13 parameters. HII regions are defined by 5 parameters. This can quickly amount to hundreds of free parameters, many of them degenerate.

Concerning the position along the line-of-sight we unfortunately only have limited constraints available for certain sources to fix the three-dimensional structure on all scales. For optically thin radiation, there is no information on the line-of-sight structure. Optically thick radiation comes from a photospheric surface where the opacity exceeds unity. Thus, maps from different wavelengths, with different opacities tracing different radii, can give some constraints on the relative positions of sources along the line-of-sight, but in general it is not possible to fix the absolute positions along the line-of-sight. The more observational data is available the better the full three-dimensional structure could be deduced.

Exploring the complete parameter space of all remaining free parameters is prohibitive in terms of computing time. Thus, PANDORA uses a hybrid approach to constrain all parameters. First, a good guess is derived by varying parameters by hand, and judging the quality visually (χ^2-by-eye). This will enable the user to fix certain parameters, e.g. the exponent of the density profile, the presence of stellar heating source/star clusters and the displacement in right ascension and declination. PANDORA then employes the model optimizer MAGIX (Möller et al. 2013) to iteratively search for the best solution, i.e. the parameter set with the lowest reduced χ^2 value. However, this is currently only set up for continuum data.

3.8.1 Magix

MAGIX is a model optimizer software developed by Th. Möller and the CATS team (Möller et al. 2013). It functions as a wrapper around existing codes and contains an iterating engine to automatically minimize deviations of a model result from available observational data. Thus is allows to explore the parameter space and aims at finding the set of parameter values that best fits observational data. In addition it also provides an error estimate (see Section 3.9).

3.9 Error estimation

This section is in here for the sake of completeness. The current routine does not yet include any error estimation. Two parts would need a separate error estimation algorithm. (i) The radiative transfer codes employed should provide an error estimate of the model in order to determine the quality of their results and (ii) the optimization routine, i.e. varying different parameters to find a suitable match, also need to provide an error estimate.

The second part is in principle provided by MAGIX. To perform a proper error estimation, the parameter space needs to be exploited sufficiently, requiring many function calls. But the employed algorithm for this task is limited to single-core processing which makes it rather inefficient, especially if a single function call is already time-consuming. Thus the employed algorithm for this task is currently under revision and subject to improvement.

3.10 Visualization

For user convenience, PANDORA also includes the visualization of the results. It plots continuum maps along their observational counterparts and includes a user specified comparison of both maps (simple difference map, fidelity map). It can also extract flux densities from continuum maps and plot the SED. This is possible for maps convolved with a fixed beamsize and maps convolved with a fixed telescope dish diameter. It extracts spectra at all given positions and plots them together with the observational data. Spectra from other directories can be included for comparison reasons.

To check and verify that the framework produced proper results, I have set up a few test cases. The simplest one is a spherical symmetric clump (Section 4.1). This will be followed by some tests regarding the model for Sgr B2 (Section 4.2).

4.1 Single spherical symmetric dust core

4.1.1 Model setup

The model consists of a single spherical symmetric core located at the center of the grid. The heating is provided by a single star of spectral type O8. The grid is kept small to ensure a quick computation time. For example the computation of the dust temperature should only take a few minutes. The model parameters are summarized in Table 4.1

4.1.2 Results

Grid refinement

Computationally, the corner-facet gradient refinement is expected to be fast, as it only probes 14 density gradients per cell. But probing only 14 different directions might cause the grid to miss density gradients. The spherical gradient refinement thus probes randomly up N points on the surface of the sphere. N is determined by the surface area of the sphere normalized by the minimum cell size and the density gradient.

Table 4.1: Summary of the model parameters for the spherical symmetric clump test case.

parameter	notation	value
density structure		
central density	n_c	10^6 H_2 cm^{-3}
radius	r	2000 au
exponent	η	2.5
heating		
central heating source	ZAMS-type	O8
stellar parameter reference		Vacca et al. (1996)
star cluster		none
grid setup		
number initial cells		11
grid size		0.2 pc
minimum cell size		50 au
maximum density difference		10 %
number photon packages		10^7
molecular setup		
molecule		HCO^+
transition		5-4
abundance	χ	10^{-9}
microturbulence	fwhm	5.0 km/s
data cube setup		
number of pixels		47
pixel size		0.1″
number of channels		201
channel width		0.2 km/s
velocity fields		
source velocity	v_s	0.0 and 20.0 km s^{-1}
velocity component along the line-of-sight	v_z	0.0 and 5.0 km s^{-1}
radial velocity	v_r	-4.0, 0.0 and 4.0 km s^{-1}
RADMC-3D to LIME method		direct

[1] $r = r_x = r_y = r_z$

If the gradient is weak, the refinement is very slow.

$$N = \frac{3}{4}\pi \left(\frac{x_{\text{cell}}}{x_{\text{min}}\, n_{\text{grad}}} \right)^2 \tag{4.1}$$

In this spherical symmetric test case, modifying the refinement routine caused a significant save of grid cells. The corner-facet gradient refinement generates a grid that consists of 621720 cells. It took about one minute to generate this grid. On the other hand the spherical gradient refinement generates a grid that consists of only 122025 cells. This is a factor of 5.1 less cells in the spherical refinement. But it took about 30 minutes to generate the grid. The saving in terms of total number of grid cells is due to the corner-facet gradient refinement probing the same density gradient threshold over different length scales as opposed to the spherical gradient refinement, which is probing the density gradient over the same (shorter) scale length. As can be seen from Fig. 4.1, the corner-facet methods generates a multi-pole like grid structure, whereas the spherical method results as expected in a spherical grid structure.

As already indicated, both methods have their advantages and disadvantages. The corner-facet gradient refinement produces more cells, thus needing more memory. But is saves computational time during the generation process. So if memory is not a problem and the density is still being iterated on, this grid refinement routine might be the better choice. The spherical gradient refinement on the other hand takes more time to generate the grid, but it uses less cells and is thus lighter on the memory. So if the density structure is already fixed and the user works on fitting molecular lines, this refinement might be the choice.

Mass distribution

To verify that the density profile is calculated properly, I plot the density profile from the model together with the analytical solution (see Fig. 4.2). Furthermore, I calculate the cumulative mass and plot the dust temperature. The model setup works as expected.

Velocity field

The next thing to test is the setup of the velocity field. In addition, I want to verify that RADMC-3D and LIME produce the same results. The source velocity v_s was set to either 0.0 km/s (see Fig. 4.3), and to 20.0 km/s (see Fig. 4.4). I expect the spectral lines to be centered on this velocity but otherwise remain unchanged.

For each source velocity I set the velocity of the core component to either 0.0 km/s (see top row in Figs. 4.3 and 4.4), and to 5.0 km/s (see bottom row in Figs. 4.3 and 4.4). By setting the velocity component along the line-of-sight of the core to 5 km/s, I expect the spectral line to be shifted by 5 km/s, relative to the source velocity.

For each source velocity and each velocity component along the line-of-sight, I set the radial velocity component to either -4.0 km/s (see left column in Figs. 4.3 and 4.4), 0.0 km/s (see middle column in Figs. 4.3 and 4.4), and to 4.0 km/s (see right column in Figs. 4.3 and 4.4). The line profile should now show different asymmetries. A negative radial velocity represents infall motion and results in a blue-shifted

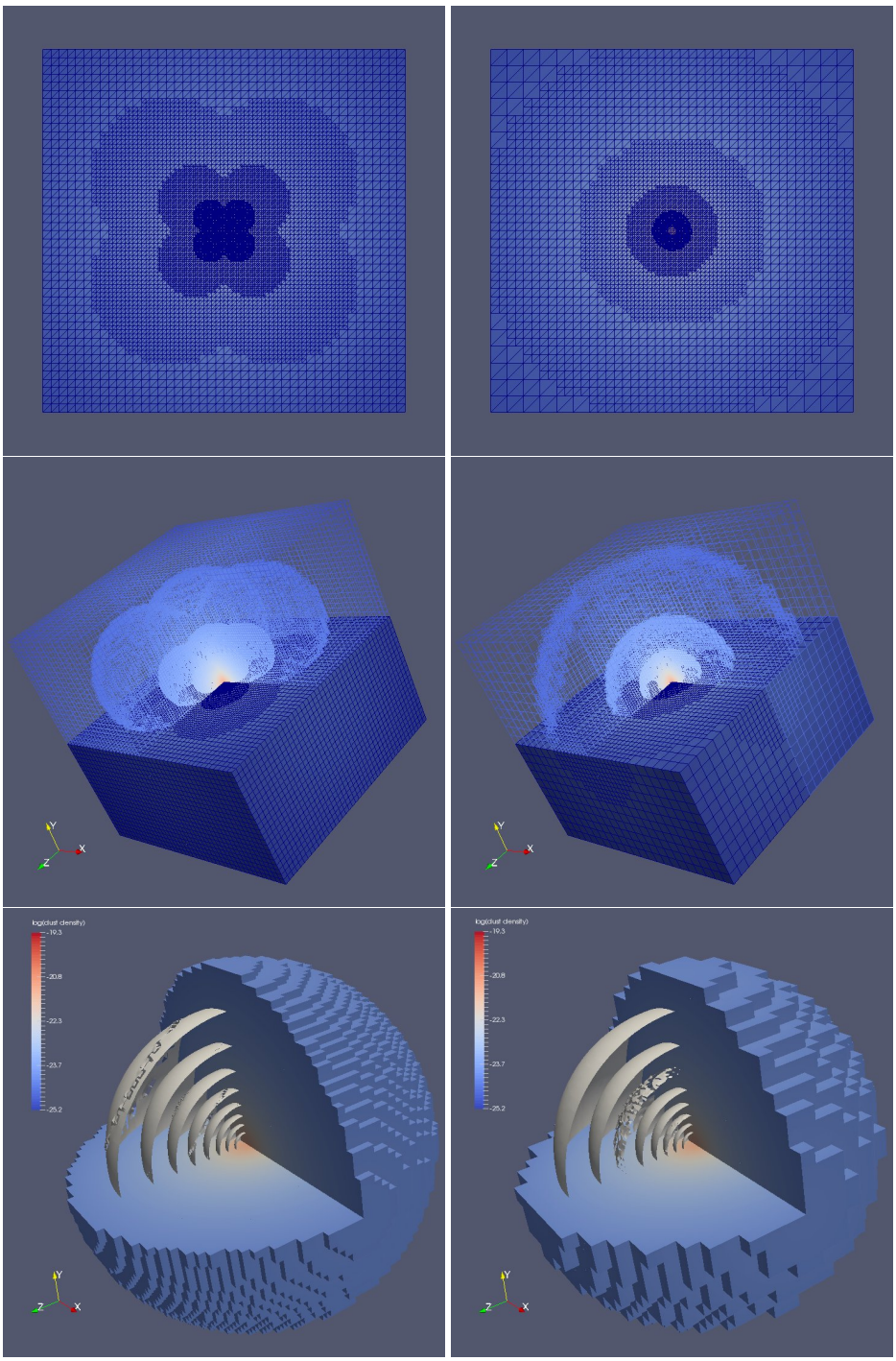

Figure 4.1: Examples of different refinement strategies. Left: Refinement according to density gradient between cell center and corners/facets. Right: Refinement according to density gradient between cell center and point on surface of a sphere that has the diameter of the cell. Top row: Displayed is the z=0 plane. Middle row: Displayed is the entire cube where the (+, +, +)-octant is cut out and the upper half is visualized using a wireframe structure. Bottom row: Displayed is the dust density distribution. This is a zoomed-in view.

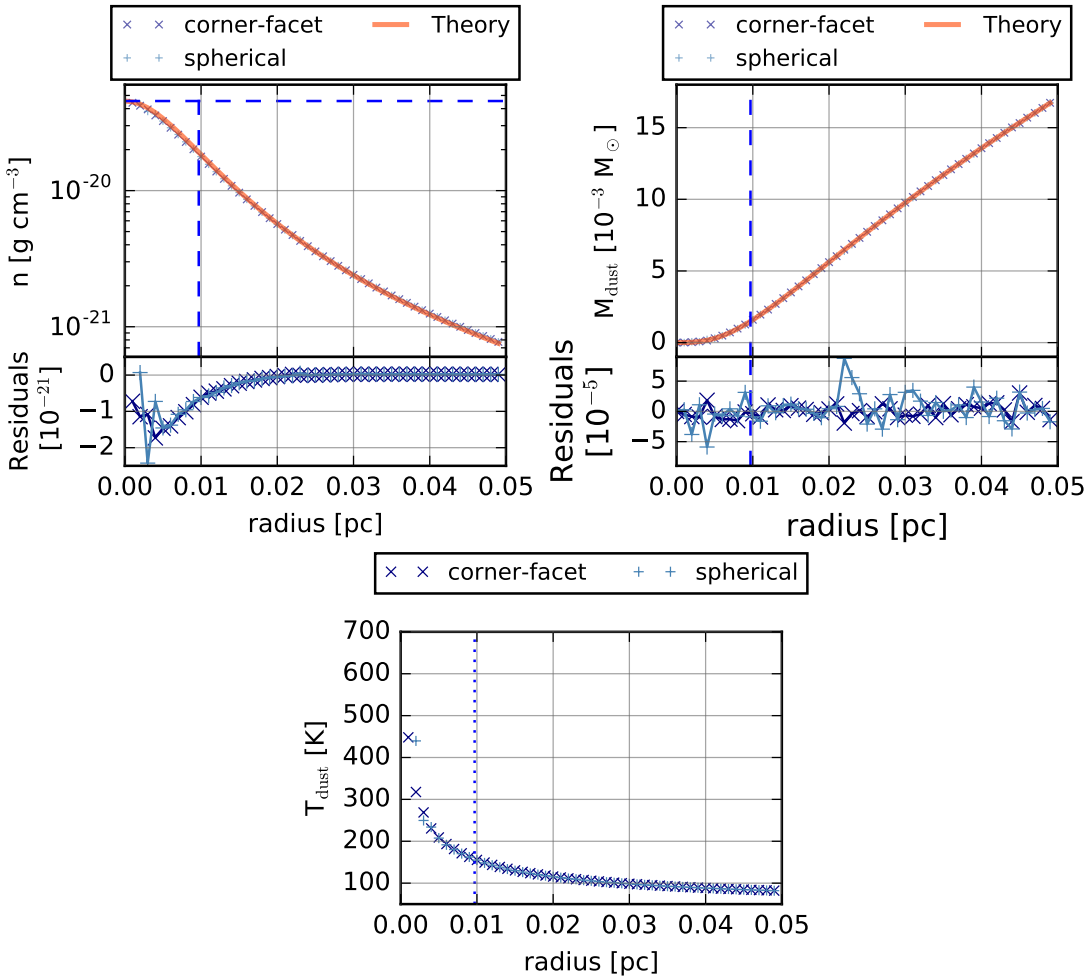

Figure 4.2: Spherical symmetric core. Top left: Density distribution. Top right: Cumulative dust mass. Bottom: Calculated dust temperature.

asymmetry, i.e. the blue peak is stronger than the red peak. A positive radial velocity represents expansion motion and results in a red-shifted asymmetry.

As can be seen from all spectra (Figs. 4.3 and 4.4), the shapes of the spectral lines are predicted as expected. The comparison of the spectral lines produced by RADMC-3D and LIME are in good agreement.

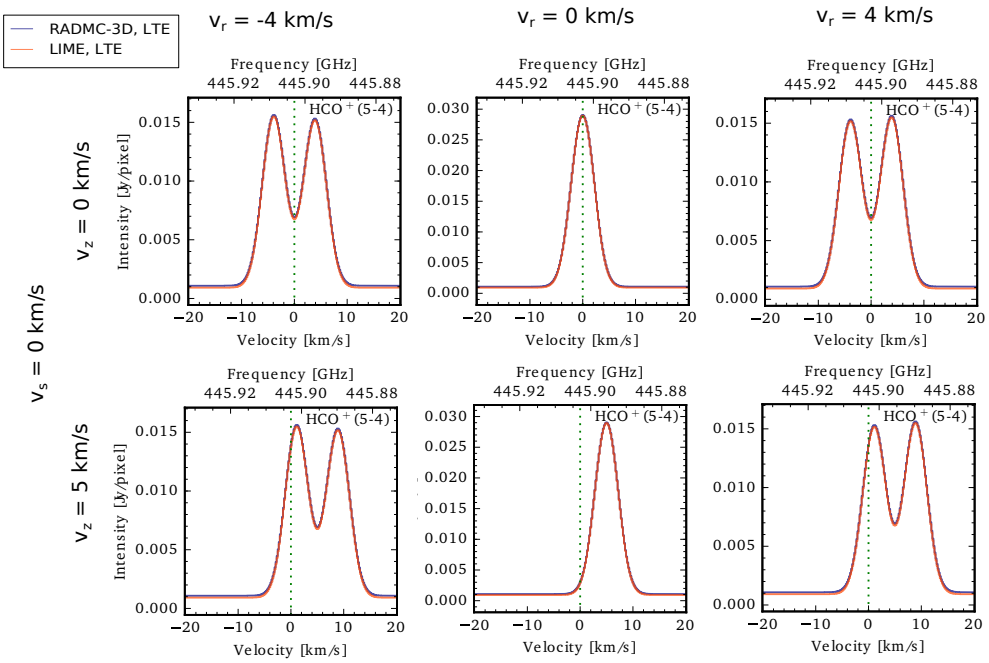

Figure 4.3: Comparison of spectra for a spherical symmetric core with different setups of the velocity field. The source velocity is set to 0 km/s. First row: Velocity of the core along the line-of-sight (v_z) equals 0 km/s. Bottom row: Velocity of the core along the line-of-sight (v_z) equals 5 km/s. From left to right: The radial velocity of the core varies between -4 km/s, 0 km/s, and 4 km/s, respectively. The source velocity is indicated by the vertical dotted green line.

4.2 Towards modeling Sagittarius B2

Ultimately, I want use PANDORA to model the high-mass star forming region Sgr B2 (see Section 4.2.3). Sgr B2 is a molecular cloud containing a plethora of HII regions, and exhibiting a complex dust distribution. reproduced by a superposition of many HII regions and dense cores. To verify that the choice of grid parameters was okay, I've performed several tests, which I will summarize here.

I have tested the influence of the parameters influencing the grid refinement and the dust temperature calculation. These parameters are the grid refinement gradient ϵ, the number of photon packages, and the modified random walk method.

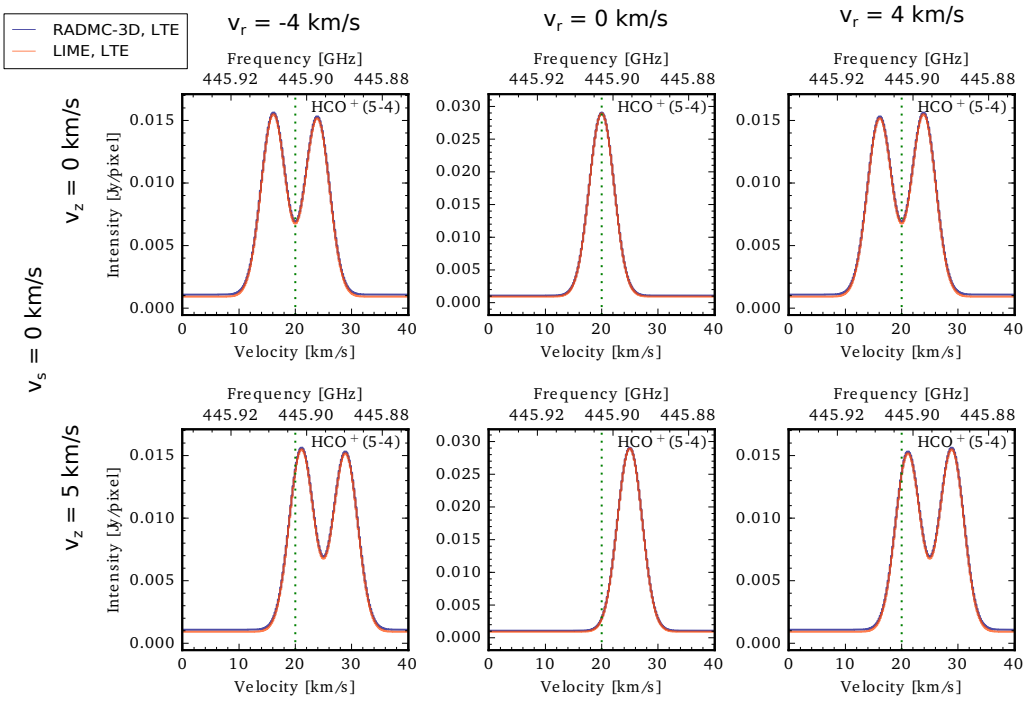

Figure 4.4: Same as Fig. 4.3 but for a source velocity of 20 km/s.

4.2.1 Grid refinement

Figure 4.5 shows the influence of different gradients ϵ, 10 % and 5 %, on the column density. The 10 % gradient model generated a grid of $\sim$ 68 million cells, while the 5 % generated a grid with $\sim$ 100 million cells. When comparing the maps it becomes obvious that both gradients sample the density distribution equally well. Naturally, the 5 % model produces a smoother dust column density map, especially in the column density range of 3–5$\times 10^5$ H_2 cm^{-2}.

4.2.2 Dust temperature

Figure 4.6 shows the influence of different gradients, number of photon packages, and the MRW method being turned on or off, on the dust temperature calculation. As a rule of thumb, the more the density gradient is decreased, i.e. the more accurately one samples the density structure, the mode photon packages should be employed to calculate the dust temperature. The difference introduced by using the MRW is on the order of a few Kelvin at most.

4.2.3 Comparison of 45 pc and 3 pc grid

The model of Sgr B2 covers spatial scales up to 45 pc. As we will see in Chapter 6, the smallest structures we need to recover with the model are 100 au. These are four orders of magnitude in spatial scales. The resulting cube contains more then 60 million cells. When doing spectral line radiative transfer, this will

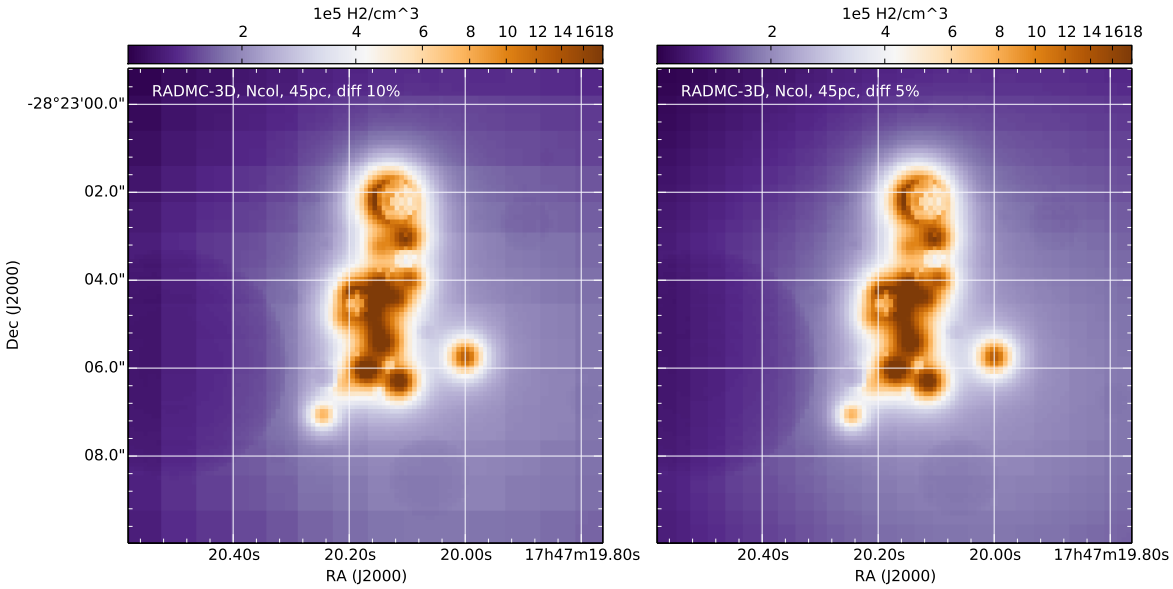

Figure 4.5: Column density map of 45 pc cube for two different density gradients ϵ of 10 % (left) and 5 % (right).

require a lot of memory. However, certain molecular lines are only excited in the hottest and densest regions. But due to the AMR refinement, we cannot simply cutout a sub-cube from the full cube. As a first approach, we simply generated a new grid with the smaller cube size of 3 pc. This encompasses all of the high-mass stars and most of the distributed low- and intermediate mass stars as well as the hot cores. So the heating on small scales should only be little affected.

Temperature maps

In Fig. 4.8 the dust temperature maps for density gradients of 10 % is displayed. These maps show that the average dust temperature in a 3 pc box along the line-of-sight varies by at most $\pm$ 3 K.

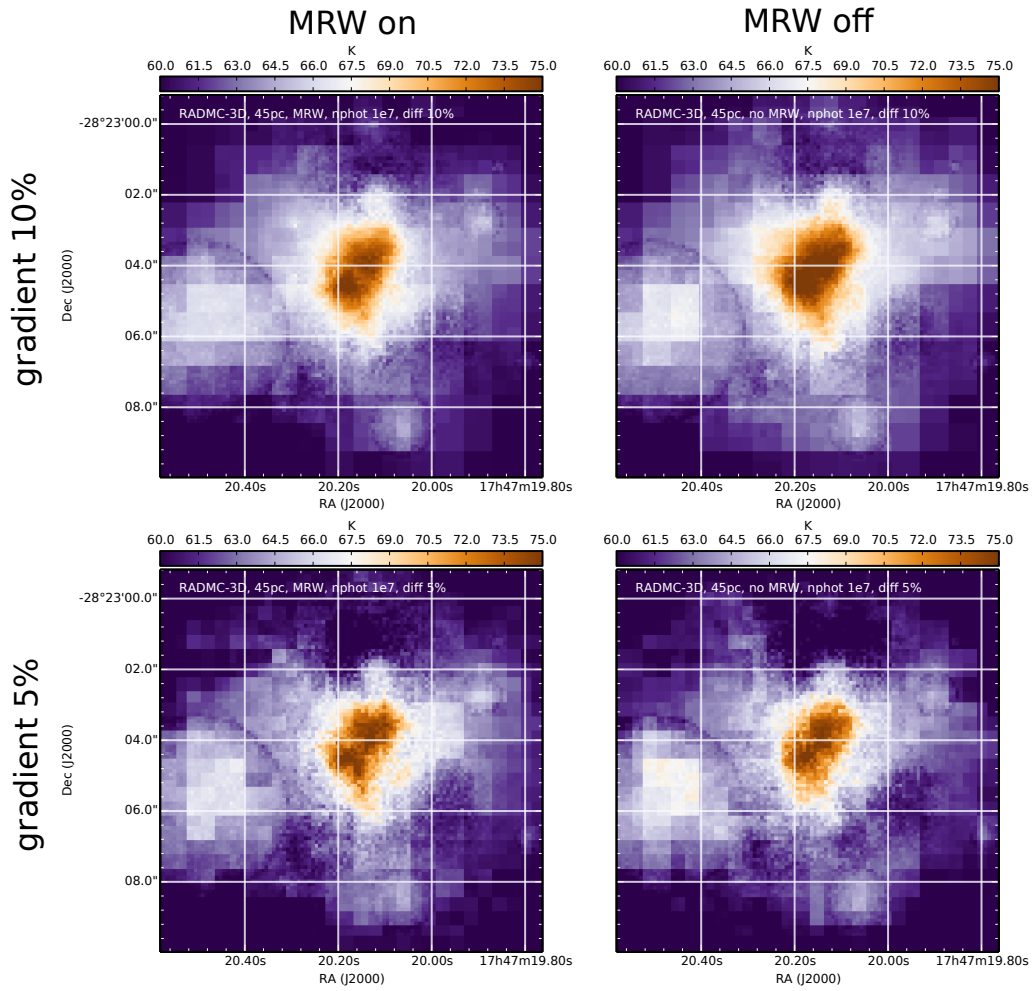

Figure 4.6: Dust temperature maps of the 45 pc cube. 10^7 photon packages where used during calculation. Top row: Density gradient ϵ set to 10 %. Bottom row: Density gradient ϵ set to 5 %. Left column: The MRW method was employed. Right column: The MRW method was switched off.

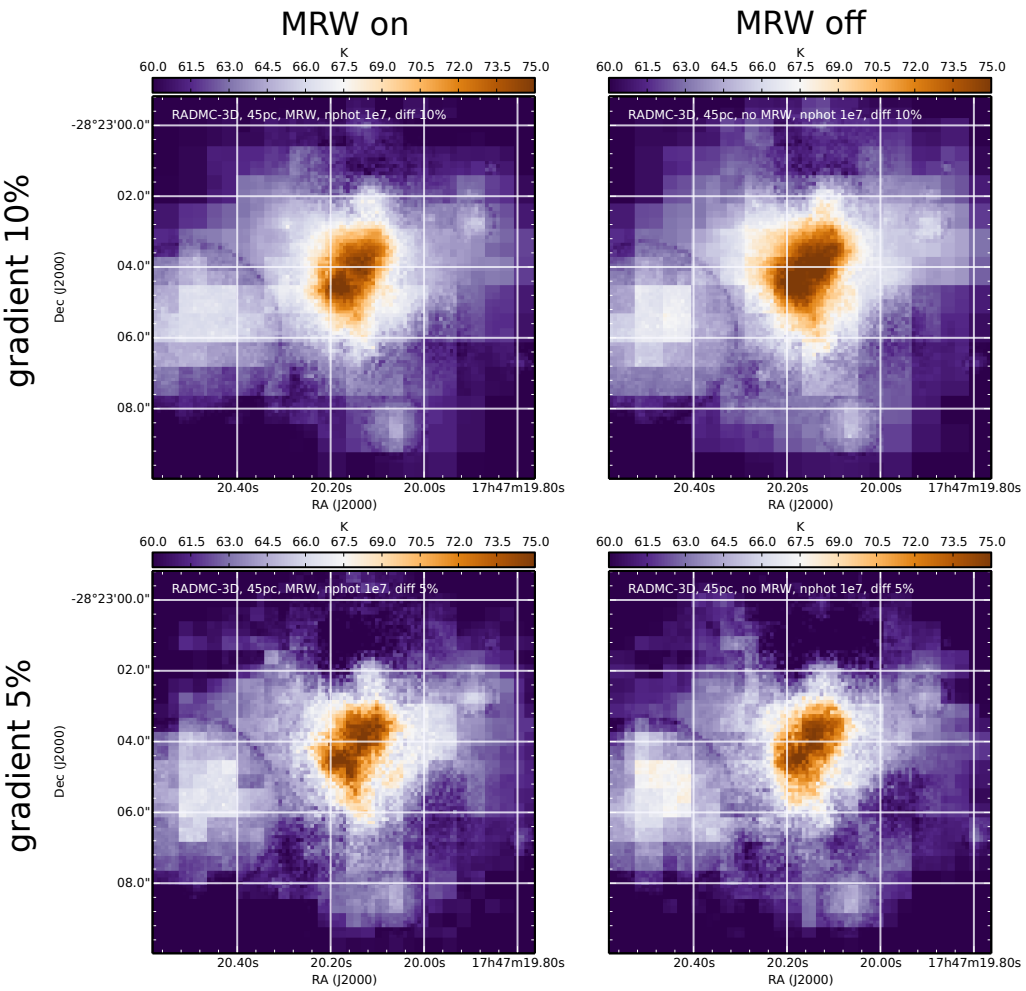

Figure 4.7: Same as Fig. 4.6, but using 10^9 photon packages.

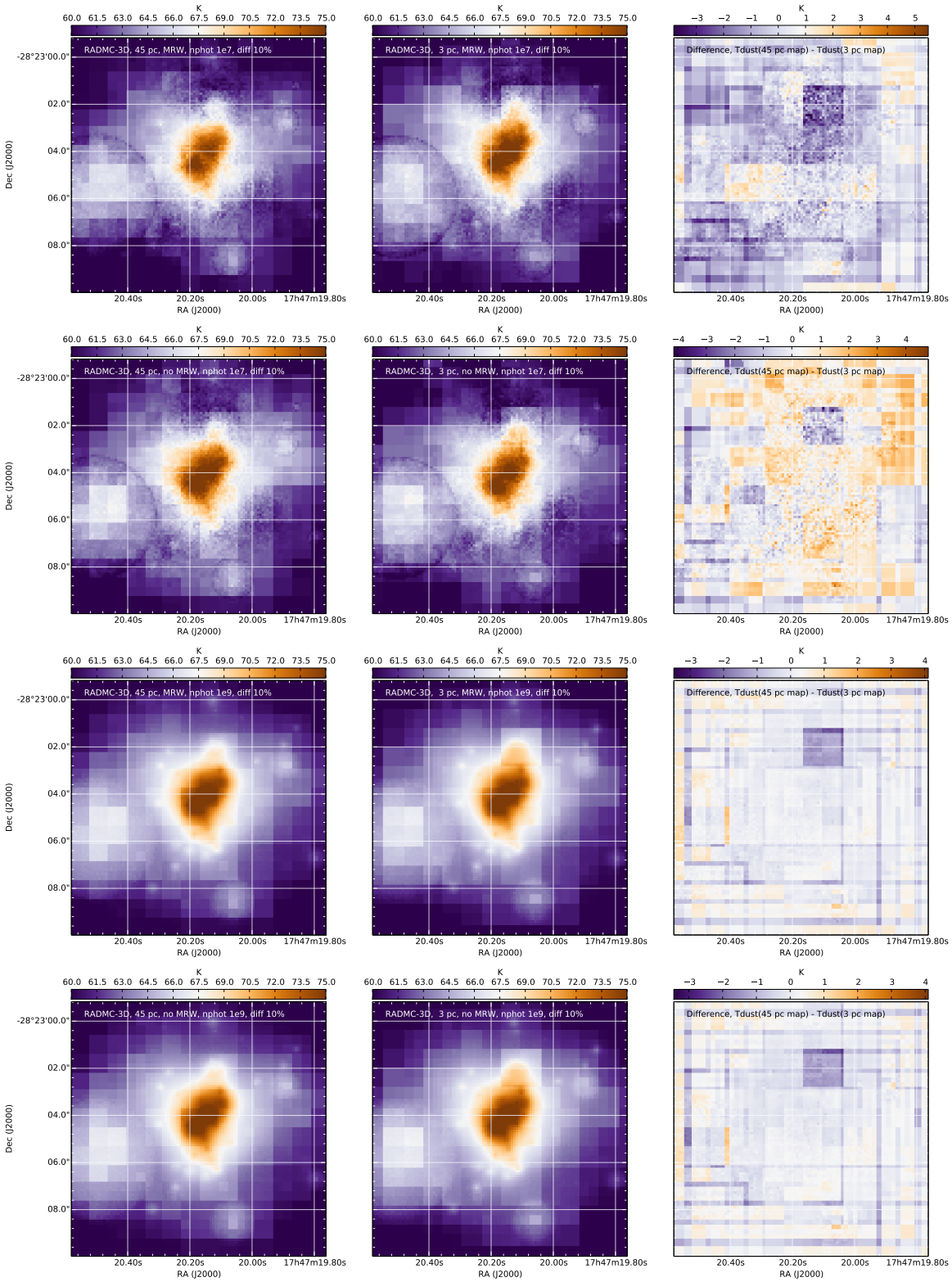

Figure 4.8: Dust temperature comparison between the 45 pc cube (left column, same maps as shown in the top row of Figs. 4.6 and 4.7) and the 3 pc cube (middle column) for a density gradient of 10 %. The difference is plotted in the right column. Again, the number of photon packages has been varied and the modified random walk has been turned on and off.

5. Observational data and data reduction

This chapter is based on Schmiedeke et al. (2016, sec. 2).

Multiwavelength, multiscale data is crucial to properly constrain the structure of Sgr B2. Towards the hot cores Sgr B2(N) and Sgr B2(M), the Herschel / HIFI spectral surveys provide the continuum information from the sub-mm up to the far-infrared regime (Section 5.1). High-resolution interferometric maps towards both hot cores obtained with the Submillimeter Array (SMA) and the Very Large Array (VLA) provide the necessary spatial resolution on small scales (Sections 5.2 and 5.3). To cover the large-scale structure, we use dust continuum maps obtained within the surveys ATLASGAL and HiGAL, described in detail below (Sections 5.4 and 5.5). A summary of the data employed in this thesis is presented in Table 5.1. Figure 5.1 provides an overview of the employed datasets and the spatial scales they cover.

5.1 Herschel / HIFI

Within the Herschel / HIFI guaranteed time key project HEXOS (Herschel / HIFI observations of EXtraOrdinary Sources; Bergin et al. 2010) full line surveys of Sgr B2(N) towards $\alpha_{J2000} = 17^h47^m19.88^s$, $\delta_{J2000} = -28°22'18.4''$ and Sgr B2(M) towards $\alpha_{J2000} = 17^h47^m20.35^s$, δ_{J2000} = -28°23′3.0″, covering the frequency ranges of 480 – 1250 GHz and 1410 – 1910 GHz have been obtained. The corresponding half-power beam widths of these observations are 44.9 – 17.2″ and 15.3 – 11.3″, respectively.

The calibration of the data has been performed using HIPE version 10.0 (Roelfsema et al. 2012). The resulting double-sideband (DSB) spectra were then reduced using the GILDAS CLASS[1] package.

[1] http://www.iram.fr/IRAMFR/GILDAS

Table 5.1: Summary of observational data used to determine the physical structure.

Telescope	ν [GHz]	λ [μm]	resolution [$''$]	center coordinates RA, DEC (J2000) [17:47:s, -28:m:s]	map size [a] [$''$]	incl. sources
large-scale						
VLA	23.1	13000	0.27×0.23 [1]	20.166, 23:04.76	143	Sgr B2
APEX [2]	345	870	19.2	19.943, 23:01.62	1100 [3]	Sgr B2
Herschel [4]	600	500	42.5	19.639, 22:57.77	1100 [3]	Sgr B2
	857	350	30.3	19.791, 22:59.68	1100 [3]	Sgr B2
	1200	250	23.4	19.939, 23:01.64	1100 [3]	Sgr B2
Herschel [5]	4283	70	10.4	20.046, 23:02.89	1100 [3]	Sgr B2
small-scale						
VLA	40.8	7000	0.15×0.10 [6]	19.902, 22:17.8	24	Sgr B2(N)
			0.15×0.10 [6]	20.202, 23:05.3		Sgr B2(M)
	40.8	7000	0.049×0.079 [7]	20.115 23:04.0	10	Sgr B2(M)
SMA	342	874	0.37×0.22 [8]	19.883, 23:18.4	16	Sgr B2(N)
			0.37×0.22 [8]	20.158, 23:05.0		Sgr B2(M)
single pointing						
Herschel [9]	480 – 1250	625 – 240	44.9 – 17.2	19.88, 22:18.4	—	Sgr B2(N)
				20.35, 23:03.0	—	Sgr B2(M)
	1410 – 1910	213 – 157	15.3 – 11.3	19.88, 22:18.4	—	Sgr B2(N)
				20.35, 23:03.0	—	Sgr B2(M)

[a] All maps are square maps, so x = y.

[1] The VLA was in the DnCnBnA hybrid array configuration.

[2] LABOCA instrument. This map has been combined with the Planck map.

[3] The coverage of these maps is beyond the extent of Sgr B2. We have thus extracted cutouts.

[4] SPIRE instrument.

[5] PACS instrument.

[6] The VLA was in the BnA hybrid array configuration.

[7] The VLA was in the A array configuration.

[8] The SMA was in the compact and in the very extended array configuration. Both data sets have been combined.

[9] HIFI instrument.

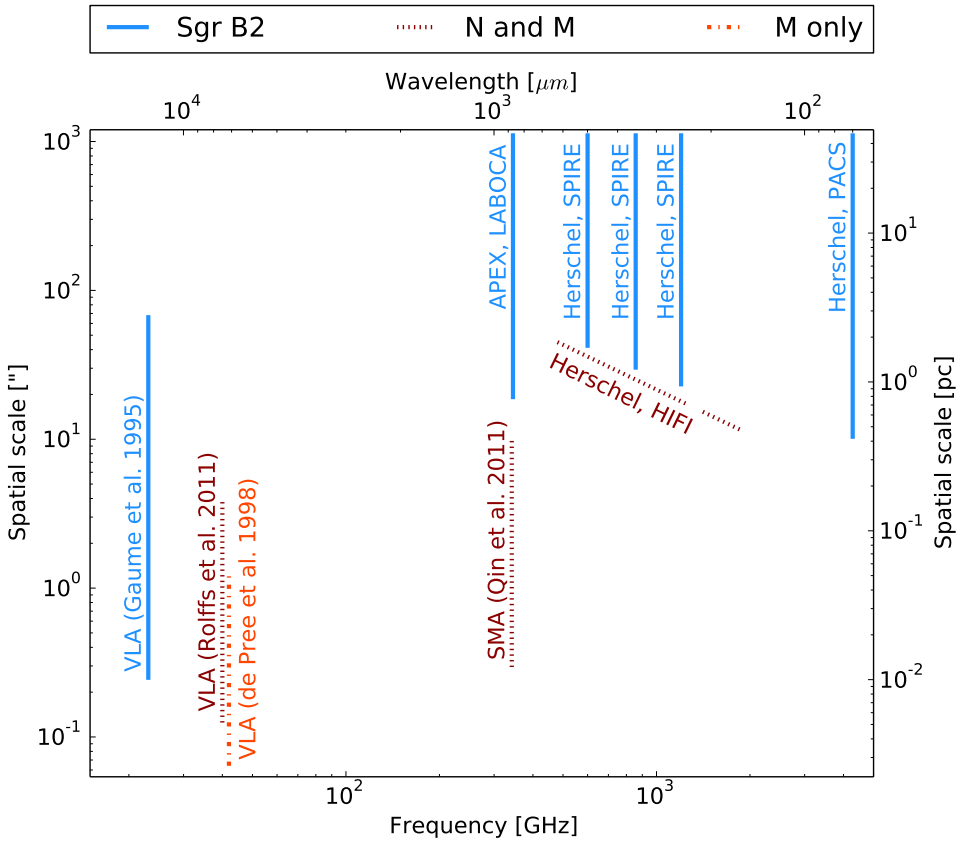

Figure 5.1: Covered spatial scales versus frequency of the different data employed in this study.

The basic data reduction steps included removal of spurious features or otherwise unusable parts of the spectra. The continuum emission was subtracted from the DSB scans by mostly zero-th, first- or more rarely second-degree polynomial fitting.The continuum-subtracted DSB data were deconvolved (sideband separation through pure χ^2 minimization; Comito & Schilke 2002) to provide an equivalent single-sideband (SSB) spectrum for each HIFI band.

Since a single full HIFI line survey is actually made up of 14 independent line surveys with seven different local oscillators (HIFI LO bands 1a through 7b), inconsistencies in the continuum level between HIFI bands were expected and indeed observed. A linear least squares fit of the subtracted continuum values as a function of local oscillator (LO) frequency provided a reliable — because unaffected by spectral features — parametrization of the continuum variation across each HIFI band, which was then folded back into each continuum-subtracted SSB spectrum.

The overall continuum was then rendered self-consistent in two steps. First, to achieve a zero-continuum level for the observed saturated absorption features, an additive factor was applied to each band. This is based on the absorption of molecules with a high dipole moment. These molecules are located in foreground, i.e. low density, clouds along the line-of-sight towards Sgr B2. Thus they will have a very low excitation temperature. Second, to achieve consistent continuum values in overlapping regions between the bands, a multiplicative factor was apllied.

For Sgr B2(N), the additive factors range between -1.08 and 0.48 K, with a median of 0.05 K; the multiplicative factors range between 0.82 and 1.42, with a median of 1.00. For Sgr B2(M), the additive factors range between -0.87 and +0.34 K, with a median of 0.28 K; the multiplicative factors range between 0.86 and 1.42, with a median of 1.03.

5.2 Submillimeter Array (SMA)

High resolution, interferometric maps have been obtained towards Sgr B2(N) and (M) at 345 GHz using the SMA in two array configurations, the compact configuration and the very extended configuration. The observations were performed on June 11, 2010 using seven antennas and on July 11, 2010 using eight antennas. The phase tracking centers were $\alpha_{J2000} = 17^h47^m19.883^s$, $\delta_{J2000} = -28°22'18.4''$ for Sgr B2(N) and $\alpha_{J2000} = 17^h47^m20.158^s$, $\delta_{J2000} = -28°23'5.0''$ for Sgr B2(M). The data reduction and continuum results are described in detail in Qin et al. (2011). They estimate the absolute flux scale to be accurate to within 20%. Both sources were observed in double-sideband mode, and covered rest frequencies from 342.2 to 346.2 GHz and from 354.2 to 358.2 GHz. The line-free channels have been used to reconstruct the continuum image. I have re-imaged the continuum maps with almost uniform weighting, resulting in a beam of $0.37'' \times 0.22''$, position angle (hereafter: PA) = 17.8 ° with a rms of $\sim$ 26 mJy/beam.

5.3 Very Large Array (VLA)

To constrain the location and physical parameters of the HII regions in Sgr B2, I use several different data sets obtained with the VLA.

5.3.1 Gaume et al. (1995) map at 1.3 cm covering Sgr B2

Gaume et al. (1995) observed Sgr B2 with the VLA in three configurations, BnA, CnB, and DnC, between February 1989 and October 1989 (project AG0287). The central pointing position is $\alpha_{J2000} = 17^h47^m20.166^s$, $\delta_{J2000} = -28°23'4.76''$. The data set and its calibration is described in detail in Gaume et al. (1995). I use an image of the combined DnCnBnA data, resulting in a beam of $0.27'' \times 0.23''$ (HPBW), PA = 70 °, with an rms of $\sim$ 0.38 mJy/beam.

5.3.2 Rolffs et al. (2011a) maps at 7 mm covering Sgr B2(N) and Sgr B2(M)

Sgr B2 has been observed with the VLA in the BnA hybrid configuration at 40.7669 GHz, corresponding to 7.5 mm (project AR687). The phase tracking centers were $\alpha_{J2000} = 17^h47^m19.902^s$, $\delta_{J2000} = -28°22'17.8''$ for Sgr B2(N) and $\alpha_{J2000} = 17^h47^m20.202^s$, $\delta_{J2000} = -28°23'5.3''$ for Sgr B2(M). Sgr B2(M) was observed on 2009 January 31, and Sgr B2(N) on February 1. The data set and its calibration is described in detail in Rolffs et al. (2011a). The continuum was fitted using line-free channels. I have re-imaged the continuum map with almost uniform weighting, resulting in a beam of $0.15'' \times 0.10''$ (HPBW), PA = 52.8 °, with a rms of $\sim$ 0.9 mJy/beam.

5.3.3 De Pree et al. (1998) map at 7 mm covering Sgr B2(M)

De Pree et al. (1998) observed Sgr B2(M) with the VLA using the A configuration on 1996 December 12, and 1997 January 17 (project AF0302). The central pointing position is $\alpha_{J2000} = 17^h47^m20.115^s$, $\delta_{J2000} = -28°23'4.02''$. The data set and its calibration is described in detail in De Pree et al. (1998). The image we used has a spatial resolution of $0.049'' \times 0.079''$ (HPBW), PA = $11°$, with a rms of $\sim$ 0.5 mJy/beam.

5.4 APEX / ATLASGAL project

The APEX Telescope Large Area Survey of the Galaxy (ATLASGAL), presented in Schuller et al. (2009), covers the full inner Galactic Plane at 870 µm with a resolution of $19.2''$ and a rms below 70 mJy/beam. Using the on-the-fly mapping technique, each position of the inner Galatic plane has been mapped twice with different scanning directions to avoid striping. The pointing accuracy is of the order of $4''$ and the flux calibration uncertainty is lower than 15 %. A detailed description of the data reduction is given in Csengeri et al. (2014). The maps were recently cross-calibrated using the data of the Planck mission and the large-scale structure that is filtered out during the processing of the LABOCA data has been added back into the map (Csengeri et al. 2016). I use this improved map in the following study.

5.5 Herschel / HiGAL project

The Herschel Infrared Galactic Plane Survey (Hi-GAL) presented in Molinari et al. (2010b), provides photometric mid-IR observations at 70 µm and 160 µm using the Photodetector Array Camera & Spectrometer (PACS), Poglitsch et al. (2010), and sub-millimeter observations at 250 µm, 350 µm, and 500 µm using the Spectral and Photometric Imaging Receiver (SPIRE), Griffin et al. (2010). Sgr B2 was observed as part of the Field 0 observations covering the Galactic Center (OD 481; obsids 1342204102, 1342204103). The observations were carried out in PACS/SPIRE parallel mode with a fast scanning speed of $60'' \text{ s}^{-1}$. The data reduction is described in detail in Traficante et al. (2011). This dataset was cross-calibrated using the data of the Planck mission on the long-wavelength side and the data from the IRAS mission on the short wavelength side. The angular resolutions at the five wavelengths, listed by increasing wavelength, are $10.4''$, $13.6''$, $23.4''$, $30.3''$, and $42.5''$ (Traficante et al. 2011). I note that the 160 µm PACS map is saturated towards Sgr B2(M) and N and is thus not used in our study.

This chapter is based on Schmiedeke et al. (2016, sec. 4).

Within the scope of this thesis, I focus the analysis on the regions for which a wealth of data is available, namely Sgr B2(N), Sgr B2(M), and partly Sgr B2(S). I included Sgr B2(NE) and Sgr B2(deepS) in the model. However, I did not attempt to fit these components, since the available dataset is scarce.

I want to recover the large dynamic range in spatial resolution from 38 pc, i.e. the diameter of the envelope (Scoville et al. 1975, corrected for distance) down to 100 au (small scale structure around the hot cores and HII regions). If I would attempt this with a cartesian grid, 800 billion cells would be required. This is not only computationally unfeasible but also unnecessary in regions, where e.g the density distribution is flat. I am employing the AMR technique to efficiently sample Sgr B2. Based on the given density structure, the grid is refined to level 13, i.e. at least one initial cell has been refined 13 times. This results in a minimum cell size of 100 au and in total ∼68 million final cells. See Section 3.5 for more information.

First I will explain the constrained electron and ion density based on the distribution of HII regions (Section 6.1). Then I will describe the determination of the large- and small-scale density structure (Section 6.2). This is followed by a description of the stellar clusters (Section 6.3). In Section 6.4 I will analyze and interpret the obtained model structure. This includes a discussion of the star formation efficiency (Section 6.4.1), the column density (Section 6.4.2), modified blackbody fitting (Section 6.4.3), and the influence of the convolution beamsize on the dust opacity (Section 6.4.4)

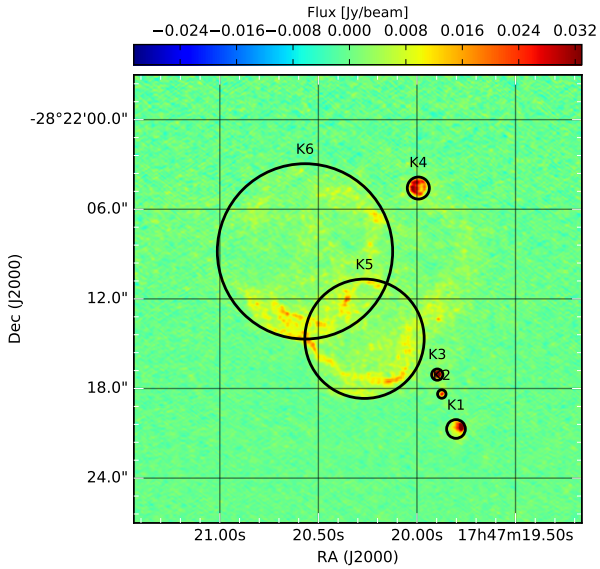

Figure 6.1: Part of the 1.3 cm map from Gaume et al. (1995) covering Sgr B2(N). The circles indicate the extent of the HII regions.

6.1 Electron and ion density

There are more than 70 HII regions detected in Sgr B2 (Mehringer et al. 1993; Gaume et al. 1995; De Pree et al. 1998). I obtained the high-resolution interferometric maps presented in Gaume et al. (1995) and De Pree et al. (1998) and performed the following analysis steps.

HII regions come in many different shapes, which makes them hard to fit with Gaussians. So in order to match them as best as possible with spheres, I masked everything below three times the rms in the continuum maps and by eye inspection adjusted circles to enclose the observed HII regions (see Figs. 6.1 and 6.2). I then integrated the enclosed flux and assuming optical thin emission and a homogeneous, non-expanding HII region, I calculated the number electron density n_e, the emission measure EM, and the number of ionizing photons $\dot{N}_i$ using the following formulas.

$$\left(\frac{EM}{\mathrm{pc\ cm^{-6}}}\right) = 3.217\times10^{7}\left(\frac{F_\nu}{\mathrm{Jy}}\right)\left(\frac{T_e}{\mathrm{K}}\right)^{0.35}\left(\frac{\nu}{\mathrm{GHz}}\right)^{0.1}\left(\frac{\theta_{\mathrm{source}}}{\mathrm{arcsec}}\right)^{-2}, \tag{6.1}$$

$$\left(\frac{n_e}{\mathrm{cm^{-3}}}\right) = 2.576\times10^{6}\left(\frac{F_\nu}{\mathrm{Jy}}\right)^{0.5}\left(\frac{T_e}{\mathrm{K}}\right)^{0.175}\left(\frac{\nu}{\mathrm{GHz}}\right)^{0.05}\left(\frac{\theta_{\mathrm{source}}}{\mathrm{arcsec}}\right)^{-1.5}\left(\frac{D}{\mathrm{pc}}\right)^{-0.5}, \tag{6.2}$$

$$\left(\frac{\dot{N}_i}{\mathrm{s^{-1}}}\right) = 4.771\times10^{42}\times\left(\frac{F_\nu}{\mathrm{Jy}}\right)\left(\frac{T_e}{\mathrm{K}}\right)^{-0.45}\left(\frac{\nu}{\mathrm{GHz}}\right)^{0.1}\left(\frac{D}{\mathrm{pc}}\right)^{2}, \tag{6.3}$$

where F_ν is the flux density of the HII region, T_e is the electron temperature, ν is the frequency, D is the distance to the source, and θ_{source} is the angular diameter of the HII region. A derivation of these formulas can be found in the appendix A.1.

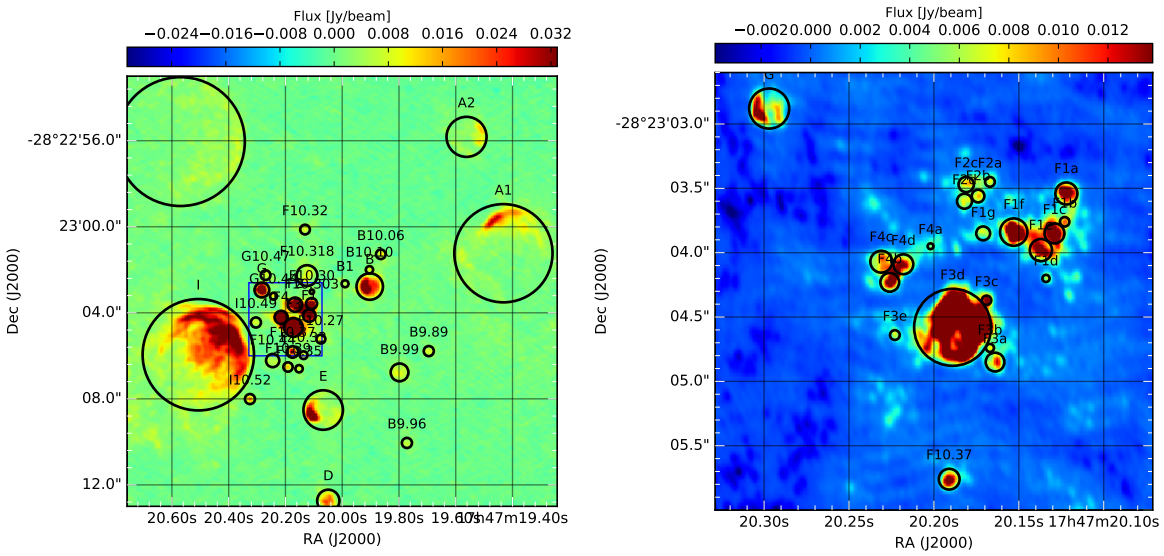

Figure 6.2: Left: Part of the 1.3 cm map from Gaume et al. (1995) covering Sgr B2(M). The circles indicate the extent of the HII regions. The blue box indicates the extent of the map shown on the right. Right: High resolution 7 mm map from De Pree et al. (1998) covering the F-cluster of HII regions in Sgr B2(M).

As the main goal is to model the dust emission, I need to derive the free-free contribution from the HII regions. Hence I did not aim at a very sophisticated model of the HII regions. To improve the model of HII regions, I would have to consider different geometries and a (non-constant) density structure.

The HII regions detected by Mehringer et al. (1993) were included according to the parameters stated therein. However, Mehringer et al. (1993) assumed a source distance of 7.5 kpc. I have thus re-calculated the radii and the parameters stated above for a distance of 8.5 kpc. All parameters, including the radii and the precessed coordinates, are listed in Table C.1.

6.2 Dust density distribution

6.2.1 Large-scale structure

To recover the large scale structure of the envelope, as visible in the ATLASGAL and Hi-GAL intensity maps, I superimpose many density components having profiles with varying exponents (see Sect. Section 3.2.1). While fitting the large-scale dust continuum maps, I noted the following problem. For a model where the density profile for each component is spherically symmetric and all components are located in the z=0 plane (Model A), the 70 µm intensity was always overestimated and the 870 µm intensity was underestimated, especially for the two cores Sgr B2(N) and Sgr B2(M). By moving Sgr B2(N) along the line of sight behind the plane containing Sgr B2(M) as suggested by e.g. Goldsmith et al. (1990) (Model B), the emission from Sgr B2(N) gets attenuated by the envelope of Sgr B2(M) and an improved fit is possible. However, the general trend of the overestimation of the intensity at 70 µm and

underestimation of the intensity at 870 µm remains, especially for Sgr B2(M). This is a sign of the dust column density being underestimated and the luminosity being overestimated. In a first approach, I have reduced this effect by assuming that the envelopes of both, Sgr B2(N) and Sgr B2(M) are elongated along the line-of-sight, i.e. they basically look like a cigar (Model C). I achieve an improved fit by increasing the radii along the line-of-sight by factors of 1.4 and 2.3 for Sgr B2(N) and Sgr B2(M), respectively. At 70 µm the dust becomes optically thick. So by increasing the dust column density along the line-of-sight, the contribution from the stars gets hidden. On the other hand, this approach increases the intensity at 870 µm, because it increases the total dust column density, which is proportional to the intensity of the optically thin 870 µm emission. Another solution would be to decrease the luminosity. The luminosity was calculated assuming a single ionized star in each HII region. However, besides the Lyman continuum emission from the early-type star, additional UV photons could be emitted from accretion shocks in the stellar neighborhood (Cesaroni et al. 2016, submitted) which would lead to assigning an earlier spectral type and thus overestimating the total luminosity. To test this possibility, I have multiplied the luminosity by an arbitrary factor of 0.5 (Model D). While doing so, I needed to increase the density to preserve the 870 µm fluxes. In this approach, there was no need for the elongated envelope, except for Sgr B2(M), where the envelope is still slightly elongated. However, the observational and theoretical evidence of this Lyman continuum overluminosity seems to be mainly given for B-type stars (Sánchez-Monge et al. 2013; M. D. Smith 2014). Thus it is unclear if O-type stars exhibit the same behavior. Furthermore, the effect of dust inside the HII regions has not been assessed. This will be part of future work.

The total number of components in all four models has been kept fixed. All parameters of each component are listed in Table Table C.3. To facilitate the comparison of these different models, I have produced cuts of the intensity along the reversed right ascension axis at the constant declination of the components Sgr B2(NE), (N), (M) and (S). These cuts are shown in Fig. 6.3. These different models show that there is a degeneracy between the dust density, luminosity and the relative location of the different dust density centers and star clusters along the line of sight. So in summary Model A overestimates the 70 µm intensity for both, Sgr B2(N) and Sgr B2(M) while underestimating the intensity for both regions at 870 µm. Model B only improves the discrepancy for Sgr B2(N), but still gives a bad fit for Sgr B2(M). These two models are thus clearly unfavorable to proceed the analysis with them. Model D provides an improved fit, however it remains unclear to which degree the luminosity could be adjusted. I thus choose to use Model C for the following analysis, since it provides a reasonably good fit for Sgr B2(N) and Sgr B2(M) without assuming any modification of the luminosity.

The resulting large-scale single-dish maps of all four models are shown in Figs. 6.4 to 6.7. The first row shows the observed maps, the second row the synthetic maps and the third row is a simple difference map between the observed data and synthetics maps. In the observed maps, the two hot cores Sgr B2(N) and (M) are clearly visible. The extensions to the north-east, i.e. Sgr B2(NE), and the one to the south, i.e. Sgr B2(S), are also distinguishable. In both the observed and the synthetic maps, the intensity of Sgr B2(M) is stronger than Sgr B2(N) except for 870 µm where the opposite is the case. So the model reproduces the general behavior, but is currently incapable to reproduce the absolute intensities. Especially in Sgr B2(M), the model underestimates the flux at 870 µm and slightly overestimates the flux at 70 µm.

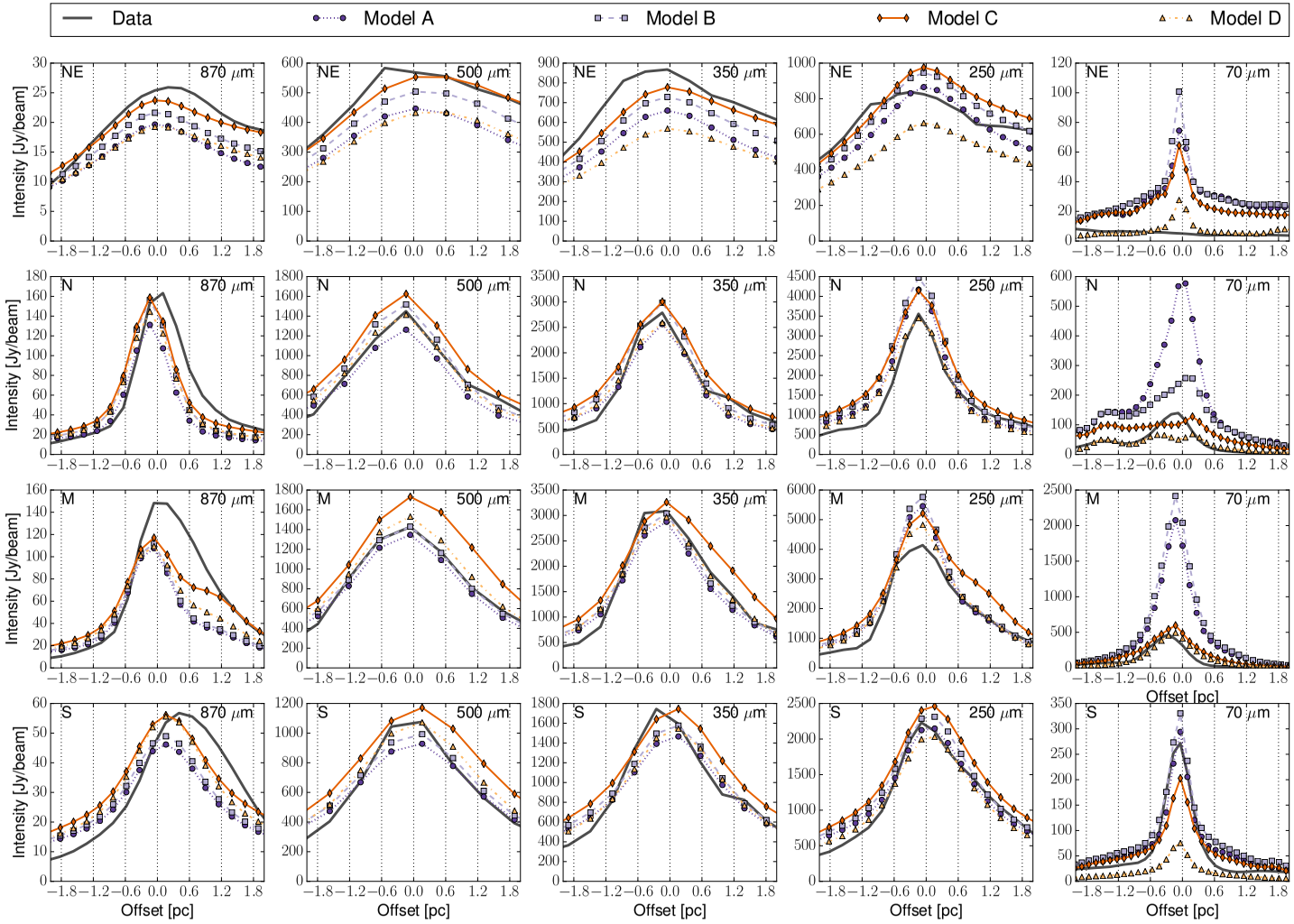

Figure 6.3: Intensity cuts along the reversed right-ascension axis at the constant declination of the envelope components of Sgr B2(NE), Sgr B2(N), Sgr B2(M), and Sgr B2(S) (top to bottom row). The data is plotted in solid black. The wavelength decreases from left to right: 870 μm, 500 μm, 350 μm, 250 μm, and 70 μm.

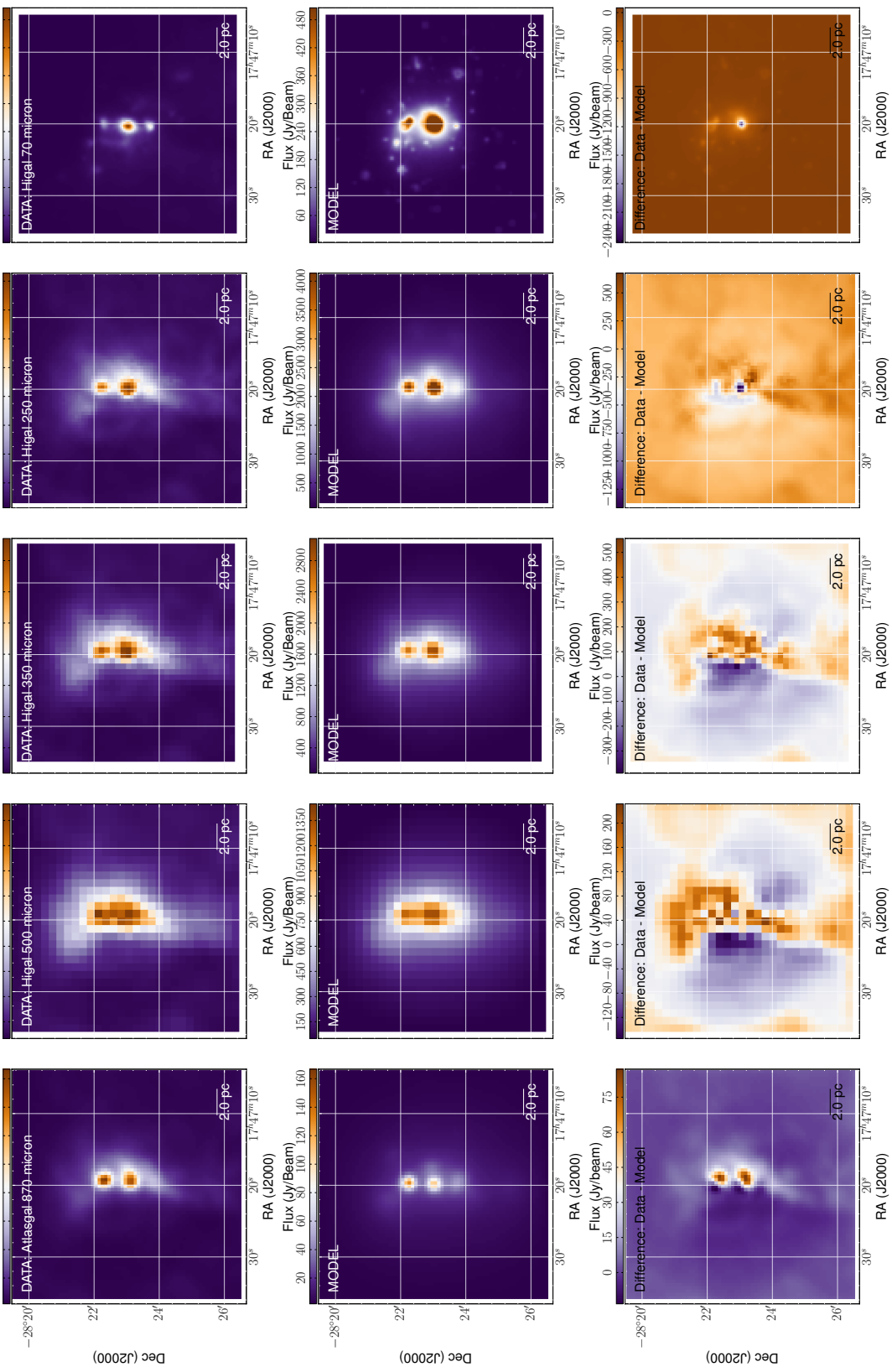

Figure 6.4: Sgr B2, large scale continuum maps (Model A). From left to right: ATLASGAL 870 µm, Hi-GAL 500 µm, 350 µm, 250 , and 70 µm. First row: Data. Second row: Simulation. Third row: Difference between data and simulation.

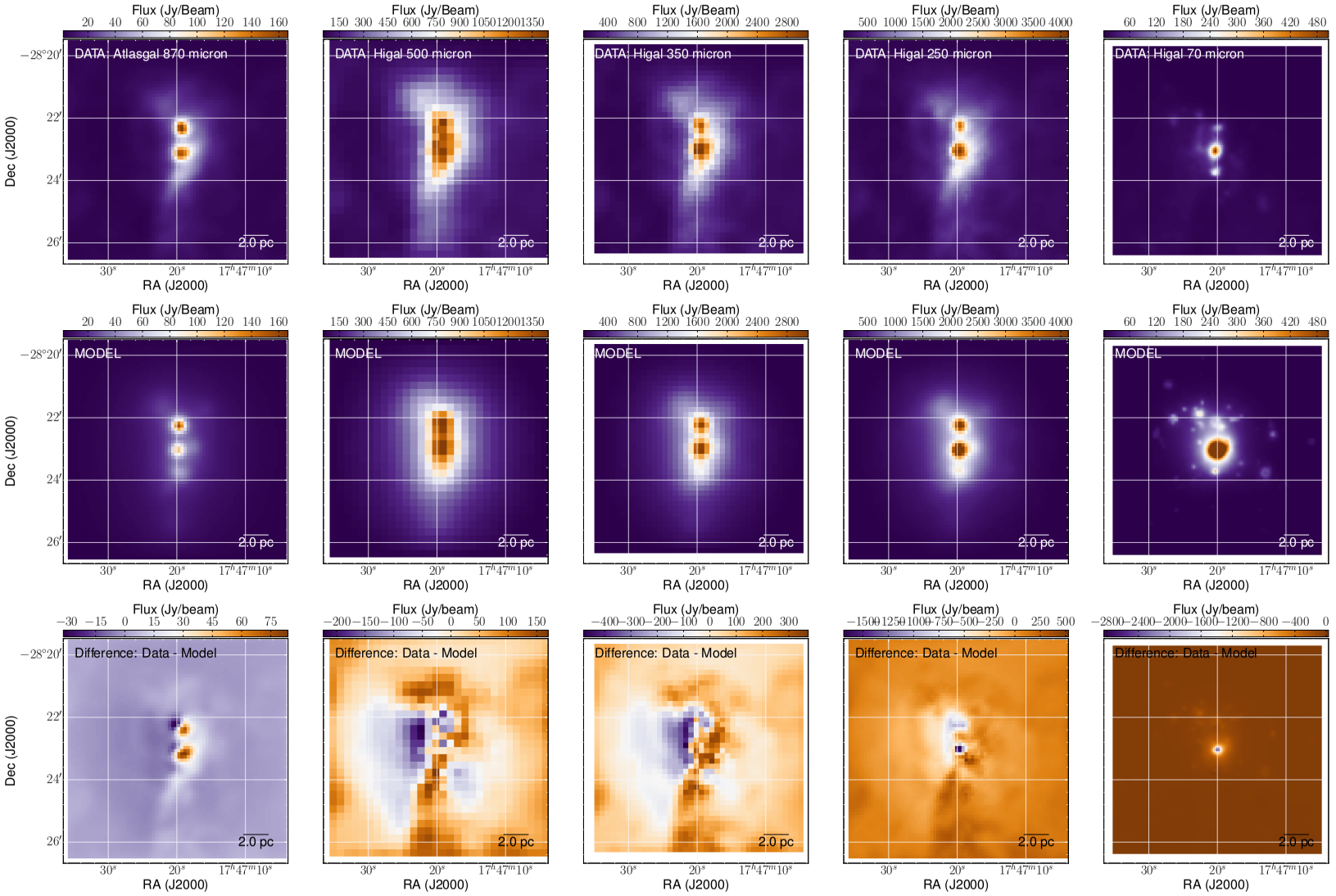

Figure 6.5: Same as Fig. 6.4 but for Model B.

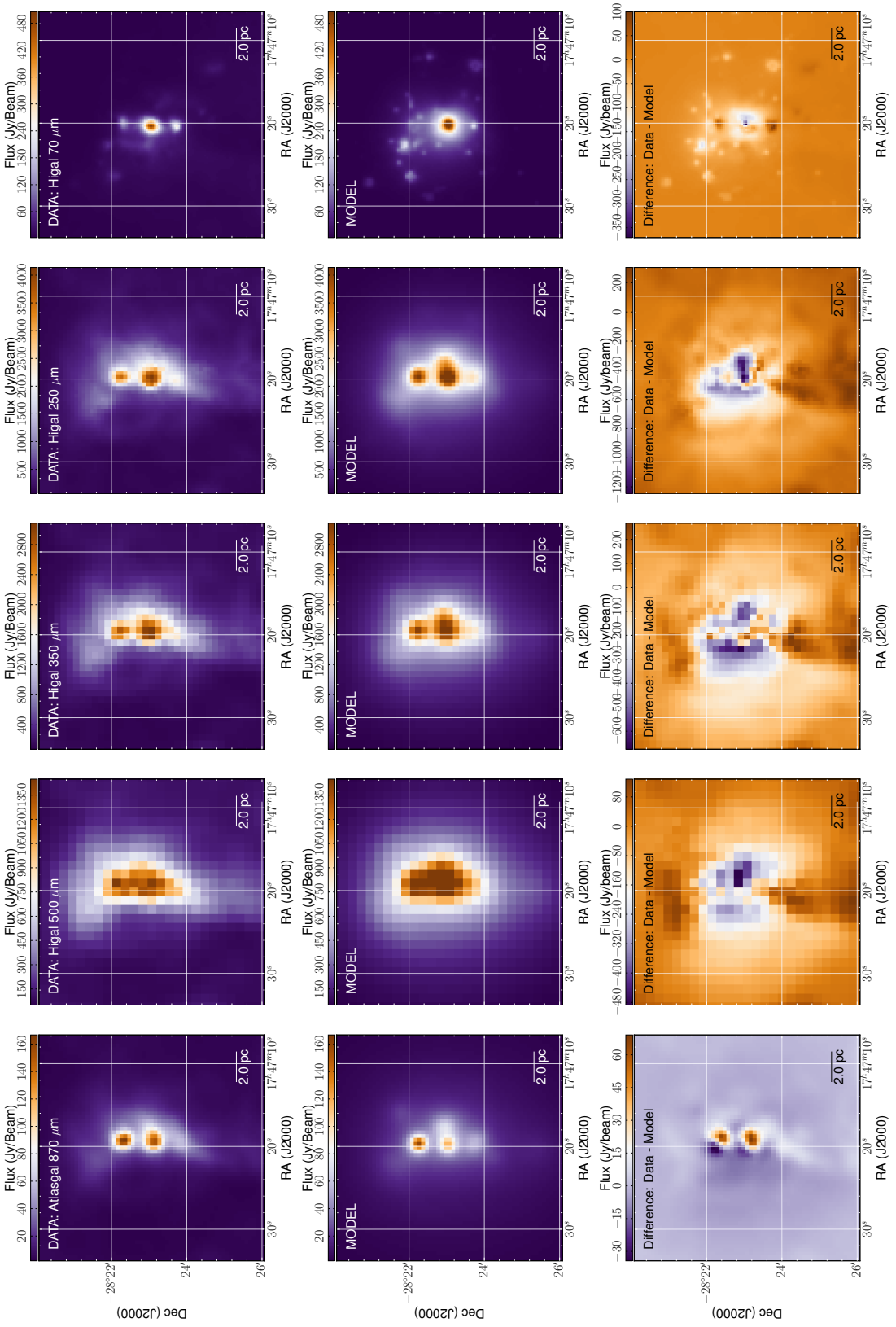

Figure 6.6: Same as Fig. 6.4 but for Model C.

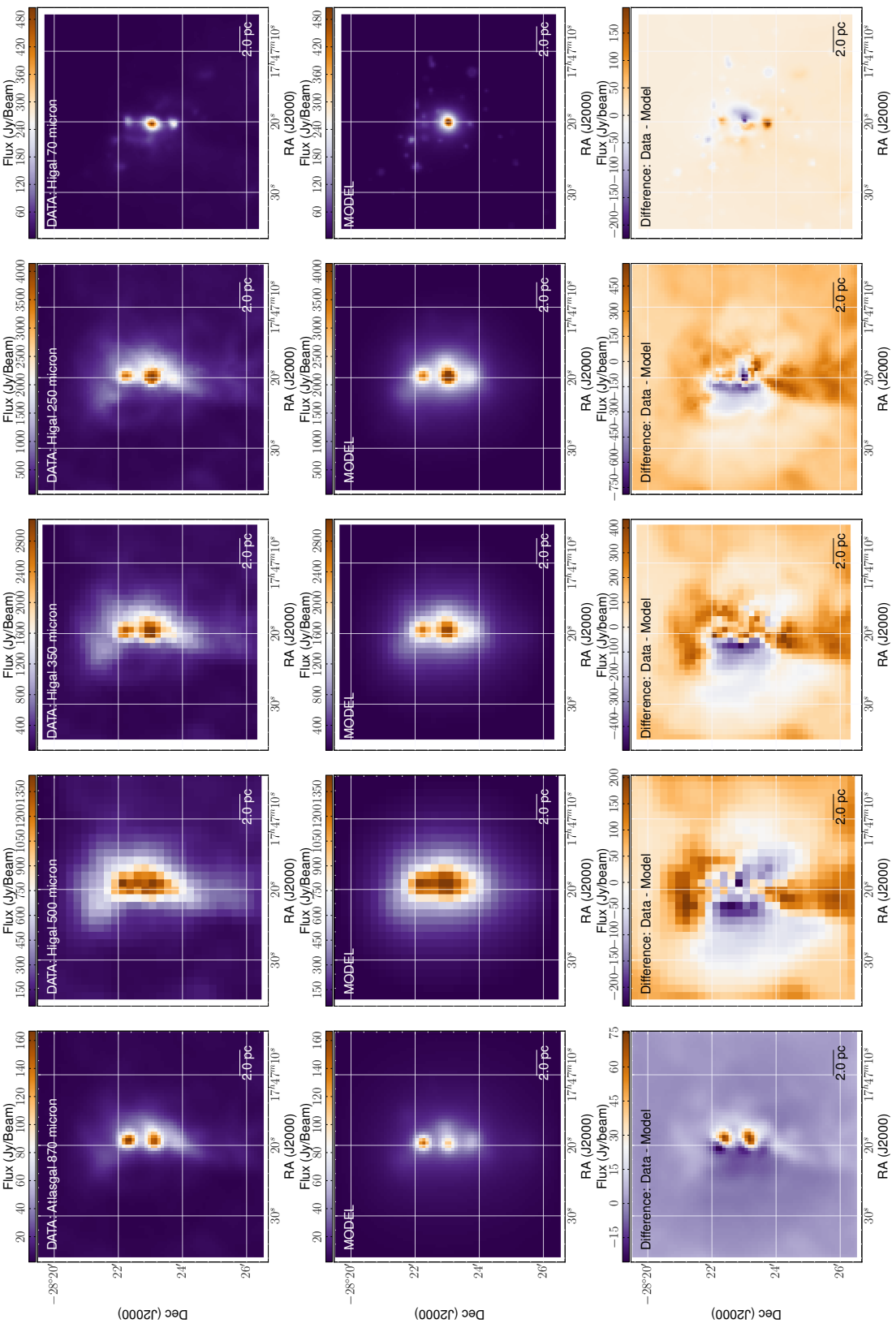

Figure 6.7: Same as Fig. 6.4 but for Model D.

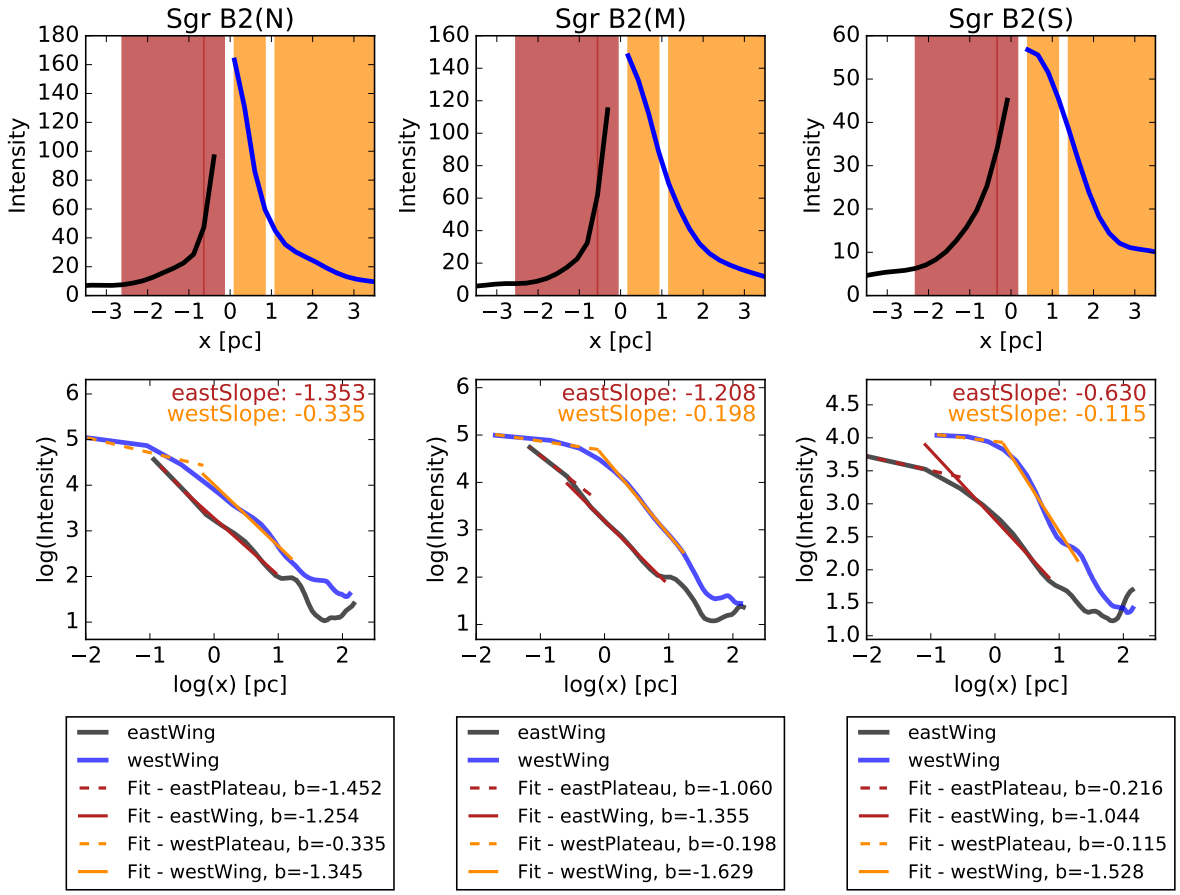

Figure 6.8: Example of the fitted intensity profiles, $I \propto r^{-p}$, of Sgr B2(N), (M), and (S) for the wavelengths of 870 µm.

The observed maps and the intensity cuts (see Figs. 6.3 to 6.7) furthermore show a clear asymmetry, i.e. the profile of the continuum emission has at all wavelengths a slope that is steeper on the east side of the peak than on the west side. To quantify the difference of these slopes, I have fitted the intensity profiles, $I \propto r^{-p}$, of Sgr B2(N), Sgr B2(M) and Sgr B2(S) for the wavelengths 870, 500, 350, and 250 µm. An example of such a fit is displayed in Fig. 6.8 for Sgr B2(N), (M) and (S) based on the 870 µm ATLASGAL map.

For the east side of the peak, I obtain an averaged exponent p of 1.0 and for the west side of the peak I obtain an averaged exponent p of 0.4. Looking at the slopes of the individual sources, I find that the steepness of the west side of the peak remains unchanged with declination, whereas the steepness of the east side of the peak changes significantly with declination. For Sgr B2(N) and Sgr B2(M), the slope p is on average 1.2, whereas it is 0.7 for Sgr B2(S). This asymmetry is impossible to account for using a single spherically symmetric component. If the slope of the intensity profile, i.e. the column density distribution, is p, then the slope of the density profile should be $p+1 (= \eta)$. So based on the fitting of the intensity profile, the east wing should have a density exponent of $\eta \sim 2.0$ and the west wing should have a density exponent of $\eta \sim 1.4$.

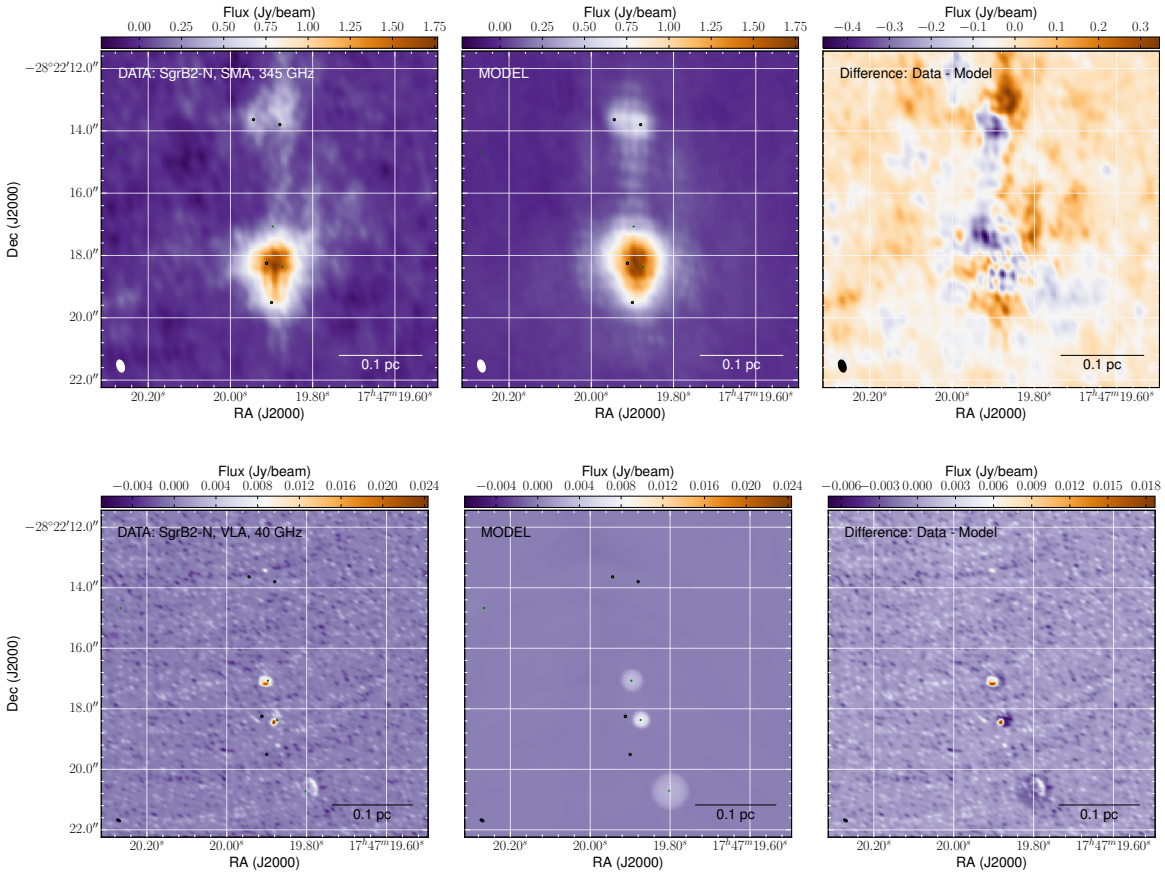

Figure 6.9: Interferometric maps of Sgr B2(N). Top row: SMA dust continuum map at 870 µm (i.e. 345 GHz). Bottom row: VLA free-free continuum map at 7 mm (i.e. 40 GHz). Left column: Observations. Middle column: Synthetic maps. Right column: Difference plot. The field of view is the same for both rows. The green pluses denote the center of the HII regions and the black circles denote the center of the density cores.

In the model, I am able to approximate the asymmetry by using a superposition of two components with different exponents for each clump. The east wing is fitted with a density profile having an exponent of $\eta = 2.5$, whereas the west wing is fitted with a density profile having a lower exponent of $\eta = 1.8$. These exponents are in good agreement with the ones derived from the intensity profile fitting mentioned above. This clearly shows that the assumption of spherically symmetric clumps as basis limits the modeling effort.

In addition, it is noticeable that the peak of the intensity profiles is shifted to the west in the 870 µm ATLASGAL maps compared to all Hi-GAL maps by ≈ 0.2 pc, corresponding to $\approx 5''$. But since this is well within the relative pointing error of the ATLASGAL map (pointing accuracy $\sim 4''$) and the Hi-GAL maps (pointing accuracy $\sim 1''$), I do not attempt to reproduce this shifting of the peak with the model.

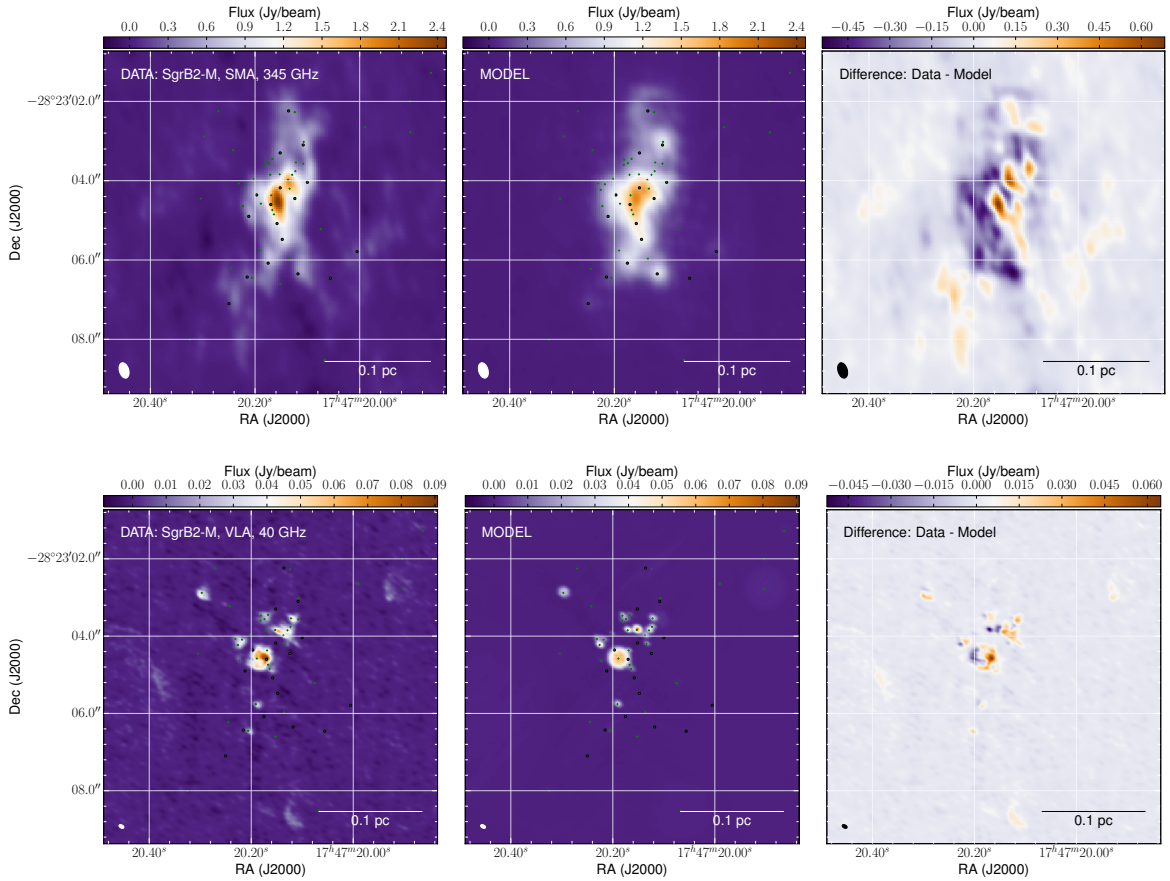

Figure 6.10: Same as Fig. 6.9 for Sgr B2(M).

6.2.2 Small-scale structure

The interferometric maps cover spatial scales up to ~ 0.25 pc. I refer to these spacial scales as the small-scale structure. The resulting maps are shown in Fig. 6.9 for Sgr B2(N) and in Fig. 6.10 for Sgr B2(M). In addition to the intensity maps at different wavelengths, I also show the physical setup of Sgr B2(M) in Fig. 6.11. In this figure, three density isocontours colored using the dust temperature are visualized. To allow a view inside the model, it is cut open along the (x, y, 0)-plane. The bubbles visible there are the HII regions that contain no dust. Their dust surface however gets heated by the UV radiation field from the embedded young stellar object. Dust temperatures as high as 600 K are reached.

For the dust cores I find, similar to Qin et al. (2011, for Sgr B2(N)) and Rolffs et al. (2011b, for the hot molecular core G10.47+0.03), a Plummer exponent of $\eta = 5.0$ reproducing the small-scale density structure well. For a comparison, Ie plot the observed and synthetic azimuthally averaged radial profile of each component in Fig. 6.12. The parameters of all dust cores are listed in Table C.2. For some of the dust cores, I had to include an internal heating source by placing B-type stars at the center of the core. These could be e.g. stars that do (not yet) show signs of an HII region. This is also documented in the above mentioned Table C.2. I also had to shift a few of the many HII regions in Sgr B2(M) behind the

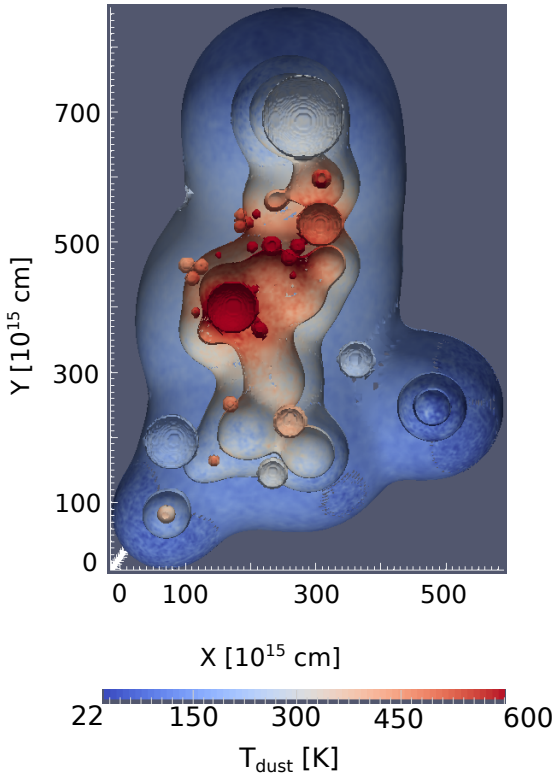

Figure 6.11: Impression of the 3d view of the dust density distribution in Sgr B2(M). Three density isocontours are presented, i.e. at densities of $10^{-17.5}$, 10^{-18}, and 10^{-19} g cm^{-3}. They are colored using the dust temperature. The model is cut open at the model center to allow a view inside. The bubbles are the empty half-shells of the distributed HII regions, which are free of dust. The dust on the surface of these HII regions is heated by the UV radiation field from the young stellar object embedded in the HII region. This dust is thus very hot, exceeding dust temperatures of 600 K (dark red spots). Visible here are mainly the HII regions detected by De Pree et al. (1998, F1a – F4d).

dust components to produce a good fit. Please note that at frequencies higher than 100 GHz only one high resolution dataset is available in this modeling procedure. Thus the resulting density distribution is only one possible solution. Other density distributions, e.g. dust cores with a lower exponent and a smaller radius, might yield similar good fits.

However, when comparing Sgr B2(M) and Sgr B2(N) a clear difference is immediately noticeable. Sgr B2(M) appears to be more fragmented compared to Sgr B2(N), which appears rather monolithic. This has already been noticed by Qin et al. (2011). The model presented here allows, however, to quantify this difference further. I will do this especially in Section 6.4.1.

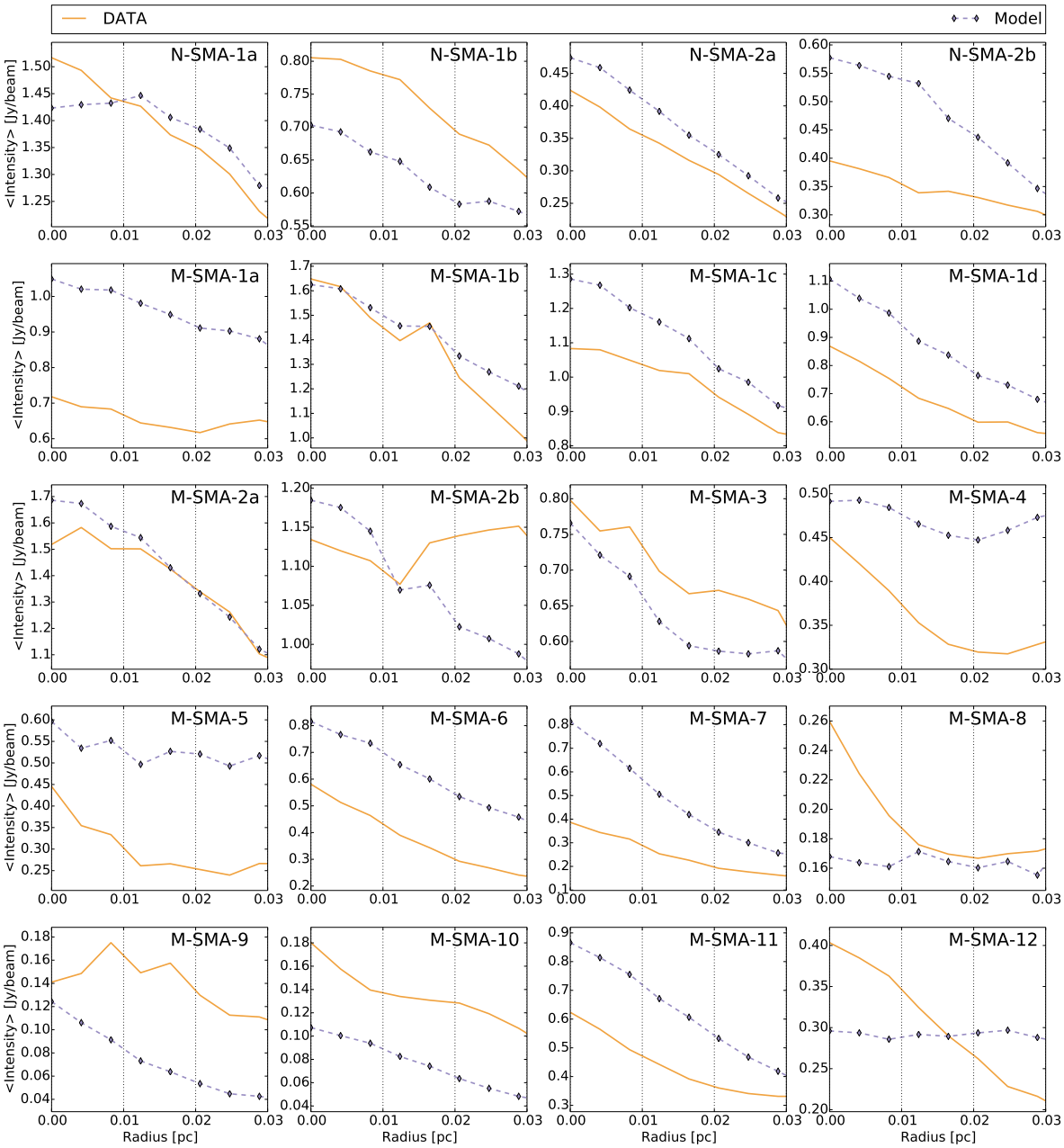

Figure 6.12: Radial profiles of the averaged intensity of the small-scale SMA structure around the position of the small-scale density components listed in Table C.2. For each of the four different models (A – D) described in this paper, the setup of the small-scale structure was fixed. The data is plotted in solid Orange, the model is shown in dashed blue. The identifier of the components are written in the upper right corner of each subplot.

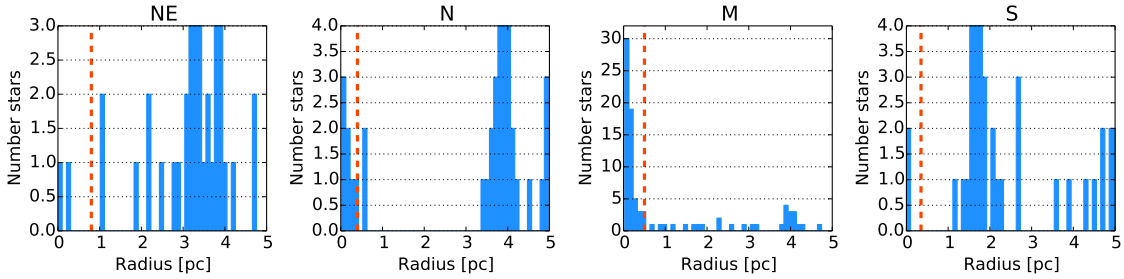

Figure 6.13: Example of the radial histogram of four different cluster regions in Sgr B2. The vertical orange dashed line indicates the cluster radius.

6.3 Stellar distribution

For all four models, I employ the same stellar distribution. I account in total for four stellar clusters: Sgr B2(NE), (N), (M), and (S). The radius of each of these clusters is determined using a radial histogram of all high-mass stars placed int he model based on the observed HII regions (see Fig. 6.13). I use these histograms to determine by-eye the star cluster radii of 0.8, 0.4, 0.5, and 0.35 pc for Sgr B2(NE), (N), (M), and (S), respectively. Within these radii stars are sprinkled separately for each cluster (see Section 3.2.3).

Note, I only consider stars as heating sources (see Section 3.2.3). The calculated dust temperature in the outer parts of the envelope is on average $12 - 15$ K. Modified blackbody fitting of SCUBA data (Pierce-Price et al. 2000) and Herschel data Etxaluze et al. (2013) yields average dust temperature values for Sgr B2 (along the line-of-sight) of ~ 20 K. Apart from line-of-sight effects in the modified blackbody fitting, which do not influence the modeling, part of this discrepancy is most likely due to heating by sources not considered here, e.g. cosmic rays or coupling with the turbulently heated gas.

I then treat Sgr B2 as a cluster itself and continue to sprinkle stars everywhere, except in the previously mentioned star clusters, until the calculated total stellar mass of Sgr B2 is reached. I will call this part the envelope of Sgr B2. The stellar density distribution and the mass distribution of the stellar mass produced with this approach (including the high-mass stars placed by hand) are shown in Fig. 6.14. Instead of plotting a histogram, I use a kernel density estimate. A histogram has several disadvantages. In addition to being unsmooth, it depends on the end points as well as on the widths of the bins. Using a smooth kernel yields a smooth distribution that is independent of the choice of the end points of the bins and only depends on the chosen bandwidth. For the kernel density estimate a bandwidth of 0.217 $M_\odot$ has been calculated in linear space.

The results of applying this star sprinkling algorithm are listed in Table 6.1. For each cluster I list the radius, the number of initial stars, the total number of stars, the enclosed stellar mass, and the luminosity from the initial and all stars, respectively. Where available, I also list luminosities from Lis & Goldsmith (1990) as a reference. Additionally, this table lists the enclosed gas mass for each of the clusters. This is calculated from the dust density distribution assuming a gas-to-dust ratio of 100 (Hildebrand 1983). I derive a stellar luminosity to mass ratio of 90 $L_\odot$ $M_\odot{}^{-1}$, 71 $L_\odot$ $M_\odot{}^{-1}$, 1176 $L_\odot$ $M_\odot{}^{-1}$, and 120 $L_\odot$ $M_\odot{}^{-1}$ for Sgr B2(NE), Sgr B2(N), Sgr B2(M), and Sgr B2(S), respectively.

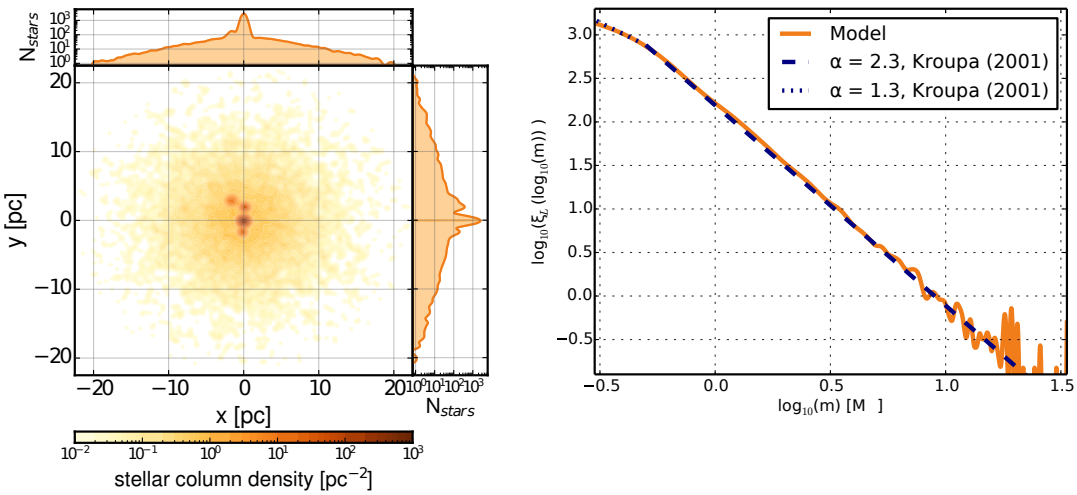

Figure 6.14: Left: Stellar column density map of Sgr B2 (center map). The projected distribution of the stars along the x- and y-axis are shown in the right and top panel, respectively. Right: Mass distribution of the stellar population contained in the Sgr B2 complex, indicated by the orange line. The dotted and dashed blue lines indicate the corresponding segmented IMF from Kroupa 2001.

Table 6.1: Summary of the star clusters.

	radius [pc]	no. stars (initial)	no. stars (all)	M_* [$M_\odot$] (initial)	M_* [10^3 $M_\odot$] (all)	M_{gas} [$M_\odot$]	L [10^6 $L_\odot$] (initial)	L [10^6 $L_\odot$] (all)	L [a] [10^6 $L_\odot$]
Sgr B2(NE)	0.8	2	1282	52	1.2	7777	0.54	0.80	—
Sgr B2(N)	0.4	6	2642	150	2.4	27897	1.38	1.80	1.7
Sgr B2(M)	0.5	60	22705	1295	20.7	9572	7.78	12.10	13.0
Sgr B2(S)	0.35	2	1204	50	1.1	4472	0.45	0.66	—
Envelope	–	19	8929	446	8.0	—	3.32	4.70	—
Sgr B2	22.5	89	36762	1993	33.4	8.0×10^6	13.47	20.06	—

[a] Lis & Goldsmith (1990, their models C)

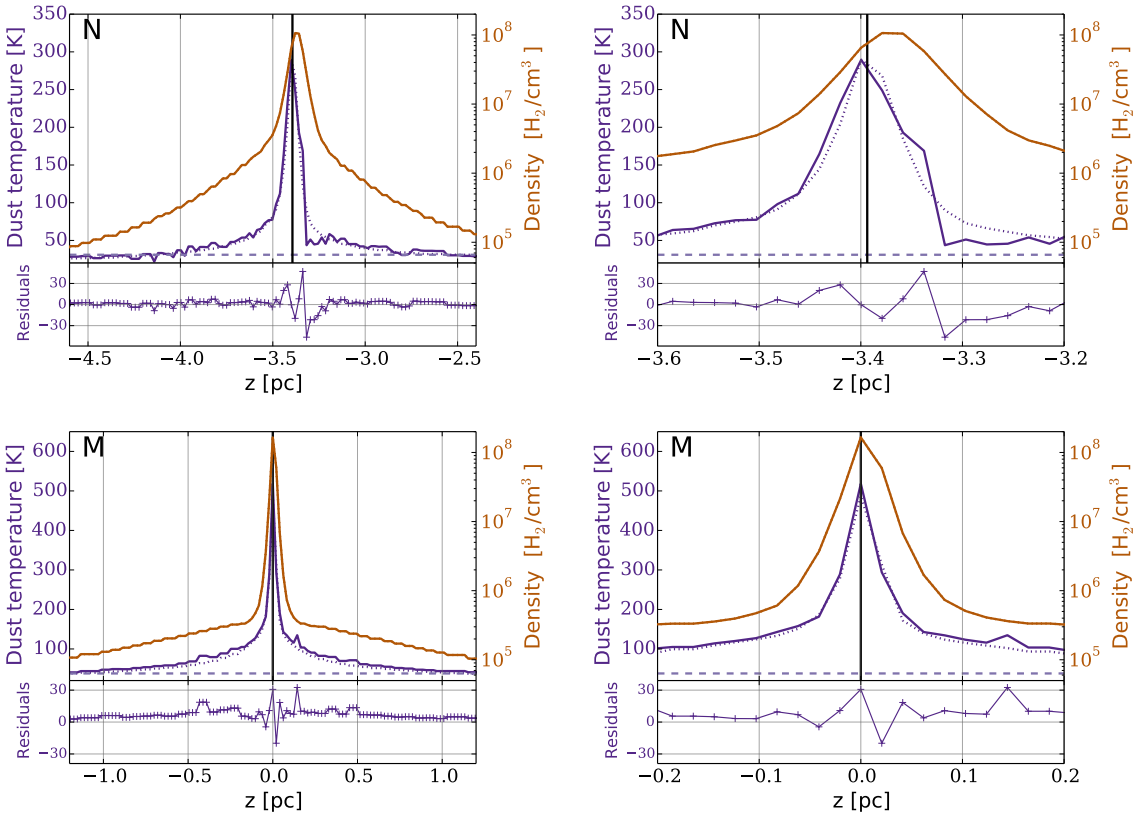

Figure 6.15: Density and dust temperature profile along the line-of-sight towards the two hot cores Sgr B2(N) (top) and Sgr B2(M) (bottom). This is obtained with a pixel resolution of 0.5″. The left panels show the profile along 2 pc around the hot cores, whereas the panels on the right show a zoom-in view of the inner 0.4 pc. The solid lines show the resulting distributions when including the star clusters. In addition, the temperature profile for the same model but without the extrapolated population of low- and intermediate-mass stars (dotted line) is shown. The bottom panel of each plot shows the residuals.

In their appendix, Belloche et al. (2013) also estimate the stellar mass of the entire Sgr B2 region by extrapolating the already distributed stellar mass of all stars embedded in observed ultra-compact HII regions using different IMFs. I apply the same method. However, the total stellar mass presented in this work is an order of magnitude higher than the results estimated by Belloche et al. (2013). This difference is explained by the different initial parameters applied and different conversion tables for spectral type to stellar luminosity used. Belloche et al. (2013) calculate a total stellar mass of 675 $M_\odot$ for the 41 ultra-compact HII regions they account for. Their lowest mass star has a mass of 11 $M_\odot$ using the conversion table from Panagia (1973). Using Kroupa's IMF, they extrapolate a total stellar mass of $\sim$ 3900 $M_\odot$ for the mass range of 0.01 – 120 $M_\odot$. In this study, I account for more than twice the number of HII regions, of which the embedded lowest mass star has a mass of 18 $M_\odot$ using the conversion table from Vacca et al. (1996).

Using the stellar cluster approach, I infer a large population of low- and intermediate mass stars.

These low- and intermediate mass stars contain the major fraction of the stellar mass, but the high-mass stars contribute the major fraction of the luminosity. To evaluate the influence of the additional low- and intermediate mass stars, I performed a simulation excluding these stellar populations. The intensity levels in the large-scale maps are unaffected and I investigate the dust temperature profiles. Fig. 6.15 shows the density and dust temperature profile along the line-of-sight towards the two hot cores. These line-of-sight profiles are obtained within a 0.5 arcsec beam. Differences in dust temperature on the order of 5-40 K (<10%) are only visible on very small scales towards the cores. The envelope temperature is only affected marginally.

6.4 Analysis and interpretation

6.4.1 Star formation efficiency and evolutionary stage

From the model I obtain the three-dimensional distribution of the stellar and gas mass. This allows to investigate the star formation efficiency (hereafter SFE), i.e. the fraction of gas that has been processed into stars. I calculate the SFE using the standard definition (e.g. Myers et al. 1986; Federrath & Klessen 2013):

$$\mathrm{SFE} = \frac{M_*}{M_* + M_{\mathrm{gas}}} \tag{6.4}$$

where M_* is the stellar mass and M_{gas} is the gas mass. Figure 6.16 shows the radial distribution of the stellar and gas mass around all four star clusters: Sgr B2(NE), Sgr B2(N), Sgr B2(M), and Sgr B2(S) as well as the derived radially resolved star formation efficiency. For Sgr B2(M) I derive star formation efficiencies of on average 50 %, for Sgr B2(N) the derived value is 5 % and thus significantly lower. C. J. Lada & E. A. Lada (2003) suggest that the SFE of a cluster increases with time and can reach a maximum value of typically 30 % by the time the cluster emerges from its parental cloud core. This would indicate that Sgr B2(M) has already lost a significant portion of its gas mass through conversion into stars and dispersion. This stellar cluster is emerging from the parental cloud, whereas Sgr B2(N) is still forming stars. This agrees well with the findings by Vogel et al. (1987). For Sgr B2(NE) as well as Sgr B2(S), I calculate rather high average star formation efficiencies of $\sim$ 30 %.

These results have to be taken with caution. The SFE depends on the distributed gas and stellar mass. From the cross cuts in Fig. 6.3, I conclude that the derived gas masses on large scales are reasonable for all clusters. But while the star sprinkling algorithm will always distribute the same amount of stars if the number of initial stars and their mass is unchanged, the volume within which these stars are placed is set by the star cluster radius. Hence a larger cluster radius effectively decreases the stellar mass density thus causing a lower SFE.

However, to interpret these results, I analyse the relationship between the gas mass of the clusters and their total luminosity. This allows to study the evolution of the young stellar objects during the phase when they are still embedded in their parental cloud. I follow the same steps outlined in Molinari et al. (2008) and use their evolutionary tracks[1]. In these evolutionary models, the fast accretion phase is stopped when

[1] Kindly provided by Sergio Molinari.

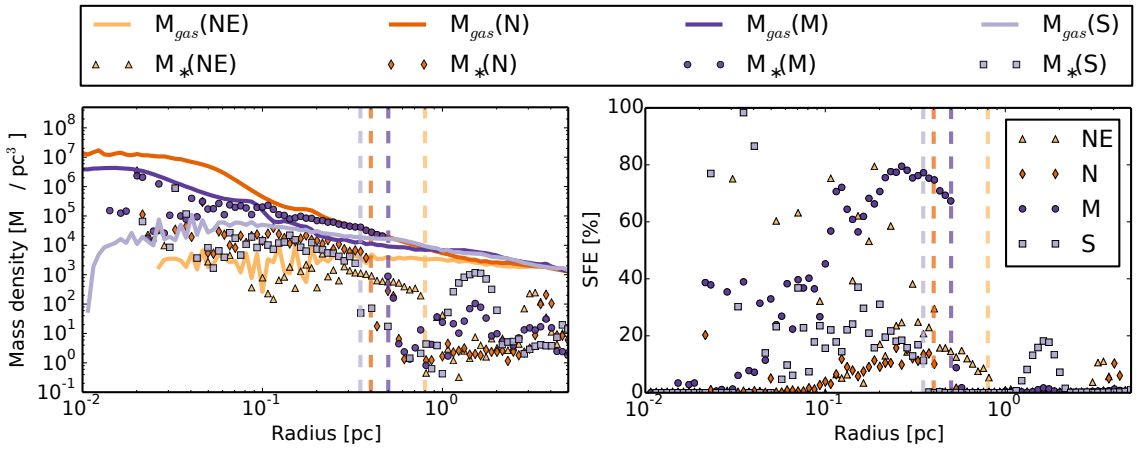

Figure 6.16: Left: Radial distribution of the gas and stellar mass density around Sgr B2(NE), Sgr B2(N), Sgr B2(M) and Sgr B2(S). Right: Calculated star formation efficiency for Sgr B2(NE), Sgr B2(N), Sgr B2(M), and Sgr B2(S). The vertical dashed lines mark the extent of each star cluster. The same colors belong to the same clusters.

the tracks approach the line where HII regions are found (at a few thousands solar masses). To match the order of magnitude provided by the massive clusters studied here, Sergio Molinari had to arbitrarily extend this line. Caution is in order, since these evolutionary models assume that a single massive star is forming, which is clearly not the case for at least Sgr B2(N) and Sgr B2(M). All tracks are presented in Fig. 6.17. The five least massive tracks are the ones presented in Molinari et al. (2008). To obtain the two most massive ones, Sergio Molinari had to stop the accretion when the central star reaches 80 and 220 $M_\odot$, respectively. Based on the instantaneous accretion rates along the tracks, we estimate that in reality the forming star reaches the ZAMS earlier than reaching the HII line. In particular around 50 $M_\odot$ for the first track and 75 $M_\odot$ for the second. The track luminosity where this occurs is around 4.8 $\times 10^5$ $L_\odot$ for the first track and around 10^6 $L_\odot$ for the second track. If I assume a single massive star is forming, then these tracks suggest that Sgr B2(S) should be compatible with HII regions (at least one HII region is observed towards Sgr B2(S)), and Sgr B2(NE) as well as Sgr B2(N) are reaching the ZAMS now. For Sgr B2(M) I do not obtain any useful interpretation. Apart from the fact that a realistic calculation would use a stellar cluster rather than a single star, to reach this relation between gas mass and luminosity in full accretion would require producing a star of a very large mass; or else a star with much larger initial clump mass which would reach the location of M during the ZAMS evolution.

Kruijssen et al. (2015) presented an orbital structure of the CMZ and derived an evolutionary timeline. According to their model, the orbital time between G0.253 (the Brick) and Sgr B2 is $\Delta t = 0.43$ Myr. Given the uncertainties in the ages and the age difference, I can only say that the approximate age is compatible with star formation beginning when Sgr B2 was at the position where G0.253 is now. But the scenario is not able to shed light on the different development stages of the various sources in the region, because on the scales considered by the gaseous streams model all Sgr B2 sources are co-spatial.

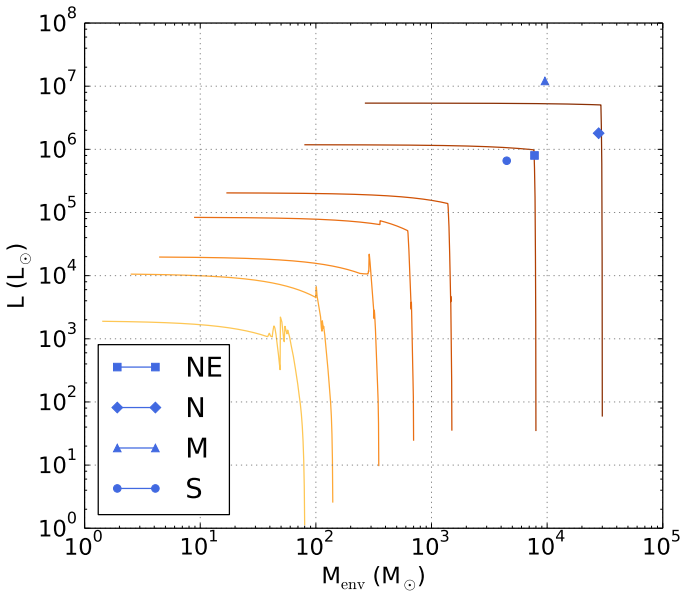

Figure 6.17: Luminosity-mass diagram for the four clusters presented here. The five evolutionary tracks with the lowest initial envelope mass are taken from Molinari et al. (2008). The two highest mass tracks are obtained by extending the evolutionary model from Molinari et al. (2008).

6.4.2 Column density map and probability density function

I convert the dust density to gas density assuming a gas-to-dust ratio of 100 (Hildebrand 1983), and that 73 % of the gas is in H_2 (Cox 2000). An H_2 column density map of the whole cloud complex is then obtained by simply summing up the H_2 density distribution along the line-of-sight. The map of the full model with a resolution of 0.1″ and zoom-ins to Sgr B2(N) and Sgr B2(M) are shown in Fig. 6.18. The HII regions are clearly visible in the zoom-in maps due to their lack of dust.

The propability density function (hereafter: PDF) of the H_2 column density within molecular clouds is commonly used as a tool to investigate the influence of various competing star formation processes within them (see e.g. Kainulainen et al. 2009; Schneider et al. 2013; Federrath & Klessen 2013). Unfortunately observational data covering the intermediate scales of Sgr B2 (see Fig. 5.1) are lacking. This affects the scales from $\sim 10 - 20''$, corresponding to $\sim 0.4 - 0.8$ pc. So while the total flux on these scales is recovered in the Hi-GAL and ATLASGAL maps, its exact distribution is uncertain. I thus refrain from showing the PDF obtained from the H_2 column density map of the model. More observational data is needed.

6.4.3 Fitting the spectral energy distribution (SED) towards N and M

The fit of the SED towards Sgr B2(N) and Sgr B2(M) obtained with HIFI is shown in Fig. 6.19 on the left. The fluxes from the simulated maps are convolved to the frequency-dependent beam of the 3.5 m Herschel telescope. This kind of fitting thus does not suffer from the necessary convolution to the worst spatial

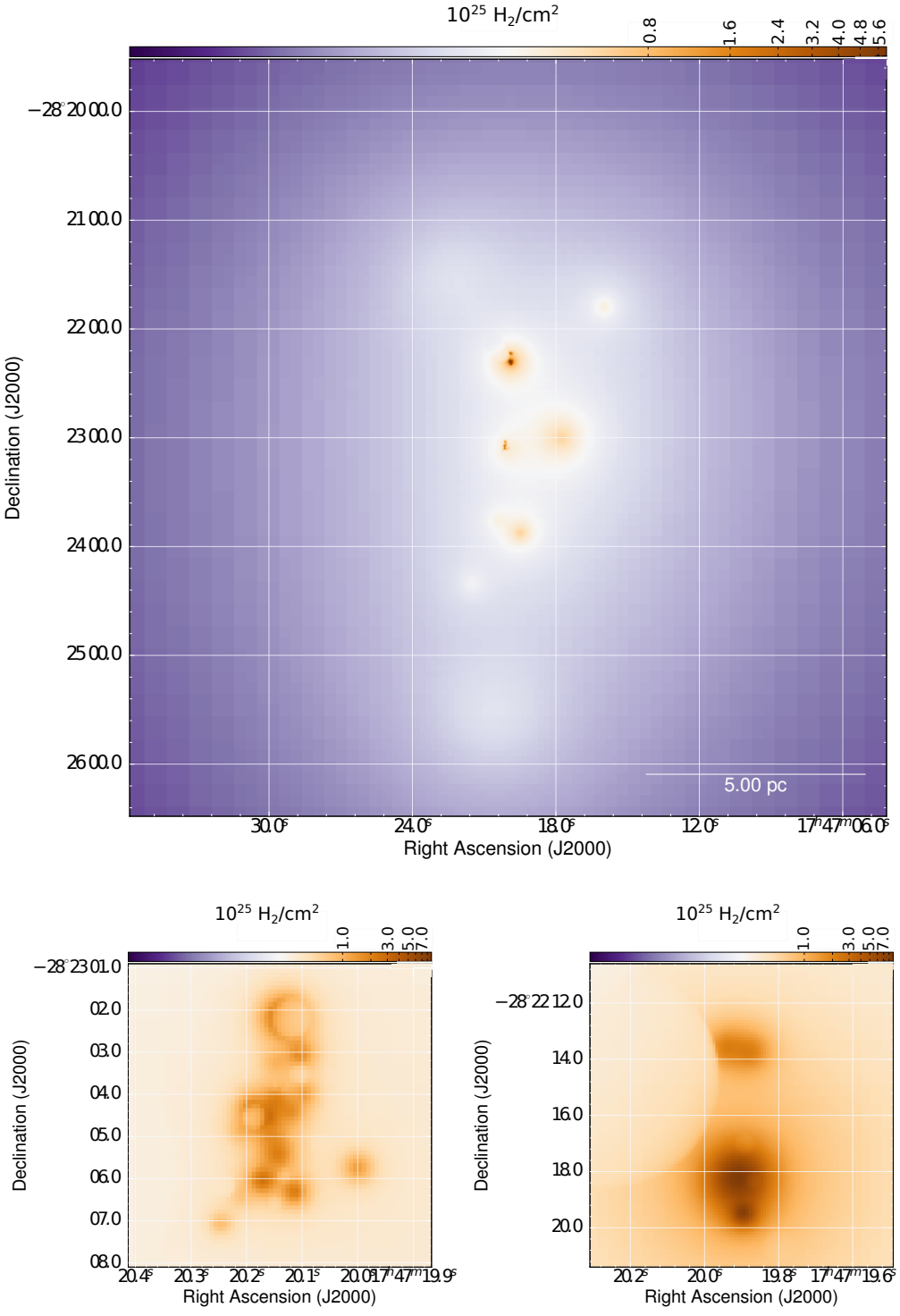

Figure 6.18: Top: Hydrogen column density map of the whole cloud complex. The pixel resolution is 0.5 arcsec. Bottom left: Zoom-in to Sgr B2(M). Bottom right: Zoom-in to Sgr B2(N). The HII regions are visible due to their lack of dust.

resolution required for modified blackbody fitting. For comparison with previous studies towards Sgr B2(M) and Sgr B2(N) (e.g. Goldsmith et al. 1992; Etxaluze et al. 2013), I have convolved the synthetic continuum maps with a beam of 30″ and extracted the flux towards both sources (see Fig. 6.19, right). The agreement between observations and simulation in the ranges, where observational data is available is very good. Please note however that the model is not able to reproduce fluxes at wavelengths shorter than 70 µm.

Full three-dimensional continuum radiative transfer modeling has so far been performed for disks, and ρ Oph D (Steinacker et al. 2005). However, this has to my best knowledge not been attempted for Sgr B2, which limits the possibilities of comparison. So in order to compare the results presented here to the work from other authors working on Sgr B2 (e.g. Lis & Goldsmith 1989; Goldsmith et al. 1990; Etxaluze et al. 2013), I have applied the modified black body fitting technique to the synthetic maps.

The intensity I of a blackbody at frequency ν is given by the Planck function

$$I_\nu = \frac{2h\nu^3}{c^2}\left(e^{\frac{h\nu}{kT}} - 1\right)^{-1}, \tag{6.5}$$

where h is the Planck constant, k is the Boltzmann constant, c is the speed of light in vacuum and T is the temperature of the blackbody. This equation is multiplied by the factor $1 - e^{-\tau}$, where the optical depth τ is given by

$$\tau = \mu_{H_2}\, m_H\, \kappa_\nu\, N(H_2), \tag{6.6}$$

where μ_{H_2} is the mean molecular weight of hydrogen, m_H is the mass of hydrogen, $N(H_2)$ is the hydrogen column density. The dust opacity κ_ν is determined as a continuous function of frequency ν, by fitting a power-law to the dust opacities given by Ossenkopf & Henning (1994):

$$\kappa_\nu = \frac{\kappa_0}{\chi_d}\left(\frac{\nu}{\nu_0}\right)^\beta, \tag{6.7}$$

where κ_0 is the reference dust opacity and χ_d is the gas-to-dust mass ratio.

I have extracted the flux within a beam of 40″ towards the SPIRE FTS pointing positions, given in Etxaluze et al. (2013), i.e. $\alpha_{J2000} = 17^h47^m20.00^s$, $\delta_{J2000} = -28°22'17.44''$ for Sgr B2(N) and $\alpha_{J2000} = 17^h47^m20.30^s$, $\delta_{J2000} = -28°23'4.1''$ for Sgr B2(M).

I employ MAGIX (Möller et al. 2013) using first the Genetic Algorithm to find the global best solution, followed by a Levenberg-Marquardt fit to obtain the local best fits for both cores. The dust temperature T_d, the dust spectral index β and the hydrogen column density $N(H_2)$ where left as free parameters. The mean molecular weight μ_{H_2} is assumed to be 2.8 (Kauffmann et al. 2008), the gas-to-dust mass ratio χ_d is assumed to be 100 (Hildebrand 1983), the reference dust opacity $\kappa_{500\mu m}$ is 1.773 cm^2g^{-1} assuming no grain mantles and no coagulation (Ossenkopf & Henning 1994).

I perform the fit covering the frequency range from 450 GHz to 2.87 THz, i.e. excluding the optically thick regime. The resulting SEDs are shown in Fig. 6.20. The results are summarized in Table 6.2. For Sgr B2(N), I obtain a dust temperature T_d of $\sim$ 31 K, a dust spectral index β of 1.8 and a column density

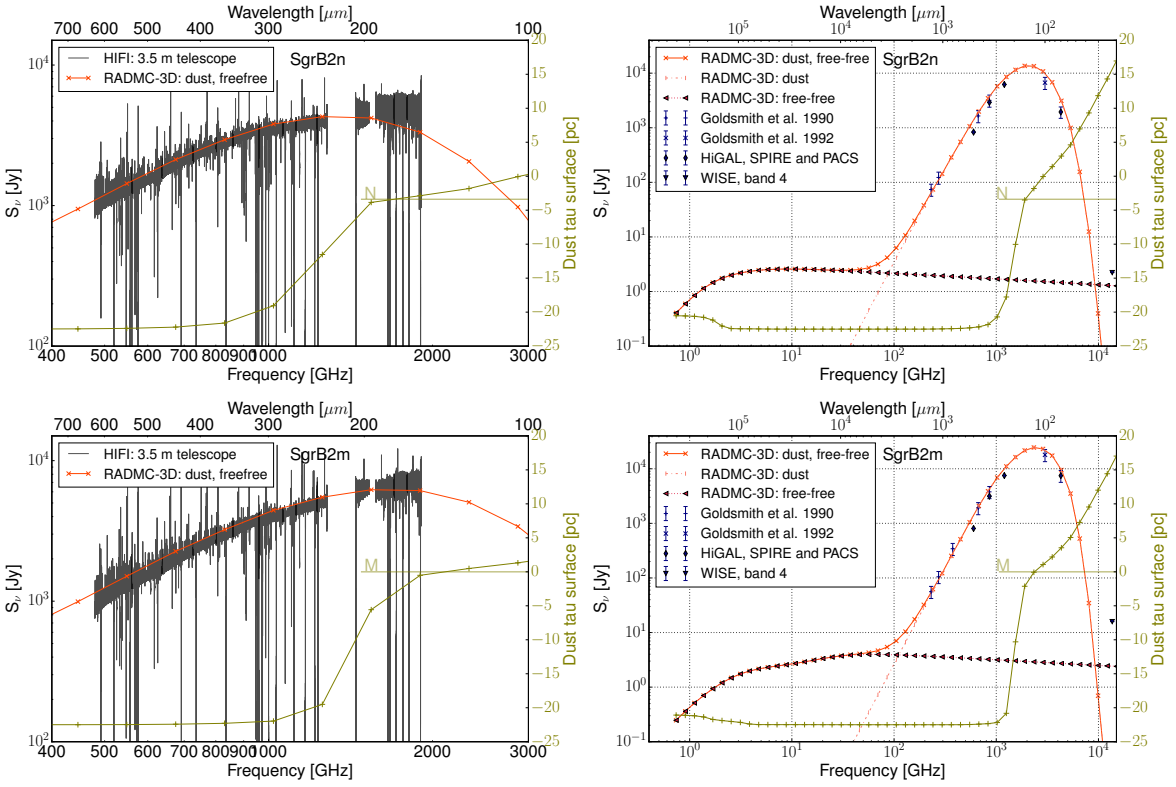

Figure 6.19: **Left:** Spectral energy distribution of the HIFI data (in grey). The data is unsmoothed, what looks like noise are actually individual spectral lines. The best fit towards Sgr B2(M) and N are represented by the solid orange line. The synthetic intensity maps have been convolved to the frequency dependent beam of the 3.5 m Herschel telescope. The fit includes dust and free-free emission. **Right:** Spectral energy distribution plots using a fixed beamsize of 30″. The orange solid line is the RADMC-3D dust and free-free best fit, the orange dotted line represents the free-free contribution, the dashed-dotted line represents the contribution from dust emission. The different dark blue markers represent the observational results from Goldsmith et al. (1990) and Goldsmith et al. (1992), as well as from Hi-GAL and WISE maps. The surface, where the dust optical depth equals one is plotted in olive, the corresponding axis is shown on the right. The z-axis points towards the observer, Sgr B2(M) is located at z = 0 and Sgr B2(N) is located at z = 7×10^5 au. A tau surface datapoint at -22.5 pc indicates that the dust is optically thin at the corresponding frequency.

Table 6.2: Results from modified blackbody fitting of Sgr B2(N) and Sgr B2(M). For each core, I list results from three different approaches.

	SgrB2(N)			Sgr B2(M)		
	T_d [K]	$N(H_2)$ [10^{24} cm^{-2}]	β	T_d [K]	$N(H_2)$ [10^{24} cm^{-2}]	β
3d model[a]	—	2.6	—	—	2.3	—
blackbody fitting[b]	31	2.9	1.8	36	2.5	1.9
Etxaluze et al. (2013)[c]	30	7.0	2.2	37	5.0	2.3

[a] Hydrogen column density in a 40″ beam directly taken from the model. This serves as the reference value.

[b] Results obtained from modified black body fitting described in this subsection.

[c] Results obtained by Etxaluze et al. (2013).

$N(H_2)$ of 2.9×10^{24} cm^{-2}. For Sgr B2(M) I obtain a dust temperature T_d of ~ 36 K, a dust spectral index β of 1.9 and a column density $N(H_2)$ of 2.5×10^{24} cm^{-2}. These values are the averaged values in a 40″ beam and are thus the results for the envelopes of Sgr B2(N) and Sgr B2(M). The fitted dust temperature values correspond to radii of 2.0 and 1.3 pc for Sgr B2(N) and Sgr B2(M), respectively (see Fig. 6.15).

Recently Etxaluze et al. (2013) convolved the Herschel/SPIRE FTS spectral scan maps covering the wavelength range from 194 µm to 671 µm to 40″ and performed modified black body fits towards Sgr B2(N) and Sgr B2(M). They find spectral indices β of 2.2 and 2.3, dust temperatures T_d of 30 K and 37 K, and column densities $N(H_2)$ of 7×10^{24} cm^{-2} and 5×10^{24} cm^{-2} for Sgr B2(N) and Sgr B2(M), respectively. Assuming a distance of 8.5 kpc, a mean molecular weight μ_{H_2} of 2.3, and a dust opacity of $\kappa_{250\mu m}$ of 5.17 cm^2 g^{-1} (A. Li & Draine 2001), they then estimate dust masses of 2500 $M_\odot$ and 2300 $M_\odot$ and luminosities of 1.1×10^6 $L_\odot$ and 5×10^6 $L_\odot$ for Sgr B2(N) and Sgr B2(M), respectively.

The derived dust temperatures from the study presented here and the ones from Etxaluze et al. (2013) agree very well. But I obtain lower dust spectral indices for which I see two reasons. On the one hand our modeling setup is limited such that only a single dust species is considered. On the other hand different datasets are considered in both studies. I include the ATLASGAL 870 µm map, as well as the Hi-GAL 500, 350, 250, and 70 µm maps, all cross-calibrated with Planck data and in the case of the Hi-GAL map also cross-calibrated with IRAS data, whereas Etxaluze et al. (2013) only considered Hi-GAL data. This could introduce differences in the fluxes which may result in different dust spectral indices as well as different column densities. This might also explain why I derive a factor of two difference in the dust column densities.

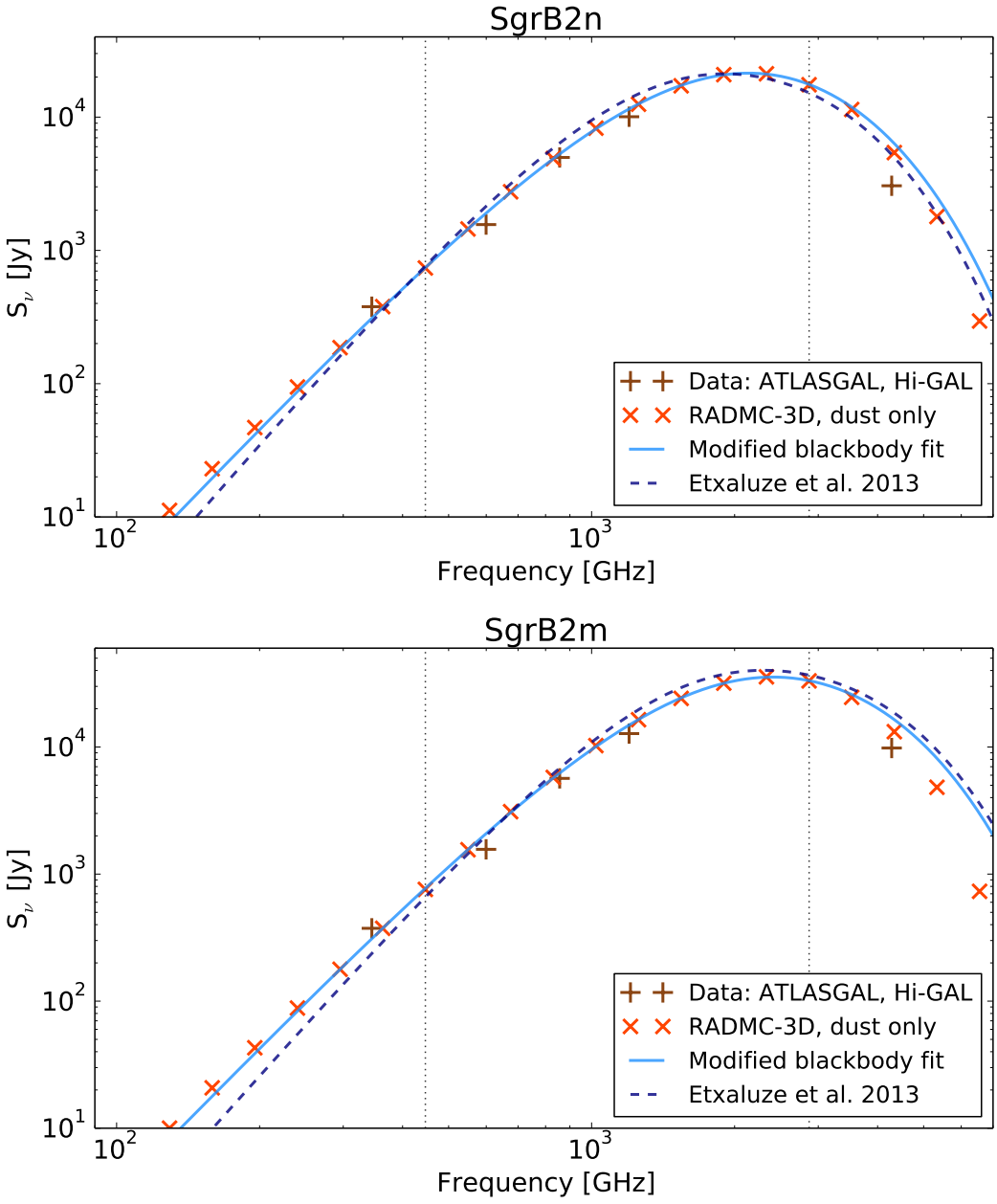

Figure 6.20: Spectral energy distribution from the modified blackbody fitting for a beamsize of 40″. The brown pluses represent the observed flux densities obtained from the ATLASGAL and Hi-GAL maps. The orange markers are the flux densities obtained with RADMC-3D including only dust. The solid blue line is the fitted SED and the dotted blue line is the SED from Etxaluze et al. (2013). Top: Sgr B2(N), bottom: Sgr B2(M).

6.4.4 Optical depth

An important point is the resolution of the observation. Using PANDORA I have calculated high resolution (i.e. the pixel size equals 0.1″) synthetic intensity maps covering the same frequency range as the SED plotted in Fig. 6.19. I have then convolved these images with decreasing beamsizes from 30″ down to 0.5″. I extract the SEDs towards the Herschel/HIFI positions of Sgr B2(N) and Sgr B2(M) as specified above for each beamsize as well as the respective $\tau = 1$ surface at each wavelength. This is shown in Fig. 6.21.

From these two SEDs, it is clearly visible that towards the position of Sgr B2(N) the free-free emission becomes optically thicker for smaller beamsizes. This indicates that an HII region is located along the line-of-sight. Furthermore the dust also becomes optically thick towards Sgr B2(N) with decreasing beamsize, leaving a very narrow frequency range of 100-200 GHz, where the dust is optically thin while still dominating over the free-free emission. The contribution of free-free emission at 100 GHz is in the order of 30 %, which is still a significant fraction of the overall emission at this frequency. For Sgr B2(M) the dust remains optically thin for this specific position up to 600 GHz. However, at 100 GHz, the fraction of free-free emission is in the order of 70 % for Sgr B2(M), indicating that the free-free emission still dominates at this frequency. Looking at the short-frequency range it is interesting to note that the free-free is partly optically thick for intermediate beamsizes, but turns optically thin for small beamsizes. This shows that there is no HII region located along the line-of-sight towards the position of the Herschel/HIFI beam on small scales. Given that there are a lot of HII regions located along the line-of-sight towards Sgr B2(M) this shows that the pointing choice might be crucial for high-resolution observations. It furthermore shows that if instead of a smooth dust density distribution I would assume a clumpy distribution, this clumping would change the photon penetration depth at certain sightlines.

6.5 Modifications

6.5.1 Intermediate scales

In the next chapter, we will see that the continuum level produced by Model C when modeling individual (optically thin) molecular lines, such as $C^{18}O$ is underestimating the observed continuum level. Optically thin molecules can be used to determine the molecular column density along the line-of-sight. Especially optically thin CO isotopologues are commonly used as a tracer of the molecular gas (especially hydrogen). Thus the spectral line observations yield additional constraints on the hydrogen column density along certain lines-of-sight of the intermediate scales, i.e. scales between $\sim 8 - 20''$. By adding an intermediate sized clump to Model C (modified Model C1), the continuum level can be corrected. However, I need to verify that Model C1 still reproduces the continuum structure discussed in this chapter. Figure 6.22 shows that Model C1 still yielding a reasonable fit of the continuum maps.

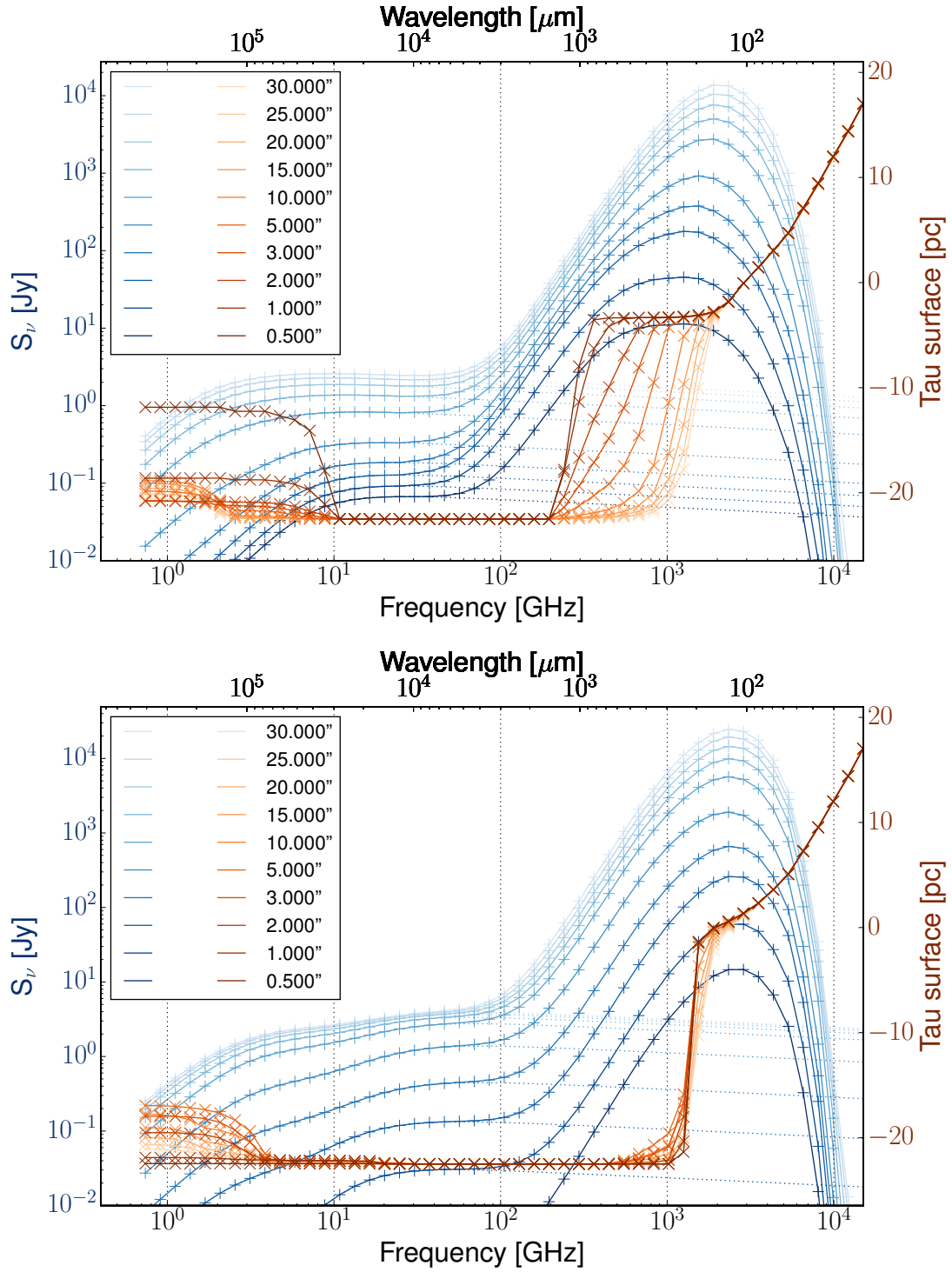

Figure 6.21: Top: Sgr B2(N), bottom: Sgr B2(M). The SED convolved with different beam sizes is plotted in blue. For each beam, the combined dust and free-free emission is indicated with the solid blue line, and the contributions from the free-free emission is indicated with the dotted blue line. The $\tau = 1$ surface, i.e. the place along the line-of-sight where the optical depth τ equals one is plotted in orange. Darker colors indicate a smaller beam size.

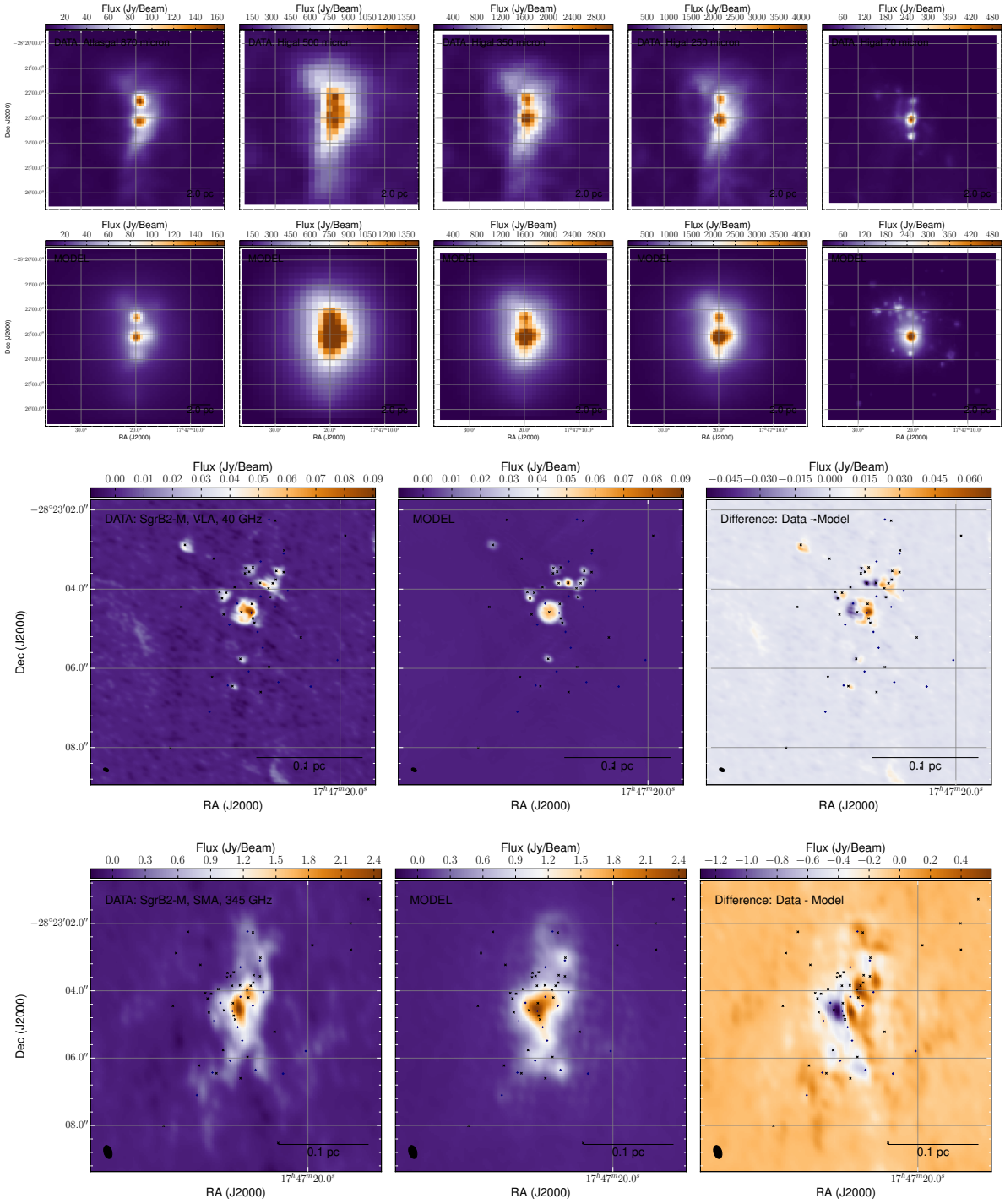

Figure 6.22: Influence of the additional intermediate sized envelope around Sgr B2(M) on the continuum structure presented in Chapter 6.

In the previous chapter, I have described the adaptation of the three-dimensional modeling system for Sgr B2. With the derived model setup, I was able to reconstruct the multi-wavelength continuum emission and could determine important physical parameters, such as density, dust temperature and stellar population.

In the next step, I want to constrain important information of the velocity field and molecular densities. However, there are $\sim$ 190 molecules detected in space[1], so I will not start by modeling just any molecule, but by carefully selecting a set of molecules based on (a) their known properties as tracers of specific conditions, (b) availability of observational data and (c) availability of necessary spectroscopic data, such as transition frequencies, Einstein A coefficients and if full non-LTE simulation is to be performed, also collisional rates.

Condition (c) imposes the hardest constrains. Transition frequencies and Einstein A coefficients are available from databases such as CDMS[2] and JPL molecular database catalog[3]. While there are measured and/or theoretically derived transition frequencies and Einstein A coefficient for all of the $\sim$ 190 molecules detected in space, only a handful have collisional rates. This is because calculating collisional rates is a challenging task. In short it involves two major processes. First the interaction potential between the studied atom/molecule and the collider need to be calculated. This involves quantum chemistry. One of the major difficulties in this step is the description of high exited states. The second step then involves the dynamics of the problem. Using a so called quantum close-coupling approach, accurate collisional cross sections and rate coefficients can be determined. But even if collisional rates are available, ideally they need to cover a larger temperature range which is often not the case.

[1] As of October 2015, 194 molecules have been detected in space (http://www.astro.uni-koeln.de/cdms/molecules).
[2] http://cdms.ph1.uni-koeln.de/cdms/portal/
[3] https://spec.jpl.nasa.gov/

Condition (b) also imposes some constraints. But due to the fact that Sgr B2 is so chemically rich it has drawn plenty of attention from many molecular 'treasure hunters'. Since many interstellar molecules have been first detected towards Sgr B2, there has always been an interest to observe this star forming region. As a consequence there are molecular line data from basically any telescope available (somewhere).

In the following, I present a summary of a typical modeling approach (Section 7.1). I then attempt to model the line-of-sight structure of carbon monoxide (CO), hydrogen cyanide (HCN), formyl cation (HCO^+), and carbon monosulfide (CS) towards Sgr B2(M). This is described in Section 7.2. This will be based on the Herschel/HIFI spectral line survey presented in Section 5.1. I will interpret and summarize the modeling results in Section 7.3.

In addition to determine kinematic and chemical properties, this work presented here also serves as a possible guideline for what molecular modeling setup might be useful to derive certain properties. This might be helpful when applying PANDORA to other sources of interest.

7.1 Modeling strategy

Ideally, the modeling of spectral lines is first done with pointed observation (or a single line-of-sight) of a mapped observation (step A). In the second step (step B) the modeling can then be expanded to maps covering the entire cloud. Within each step, it is useful to break the modeling into several sub-steps.

(I) Use optical thin molecules.
  (a) Optically thin molecules constrain the molecular column density along the line-of-sight.
  (b) Get source velocity from these spectra.
  (c) Adjust the abundance and gas temperatures.

(II) Use optical thick molecules.
  (a) Obtain velocity field information along the line-of-sight.
  (b) Adjust abundance and gas temperatures.

7.2 Modeling individual molecular species

7.2.1 Carbon monoxide, CO

Carbon monoxide is the second most abundant molecule in the Universe. It is widely used as a tracer of molecular gas. Figure 7.1 shows selected transitions of CO and the $C^{18}O$ isotopologue towards Sgr B2(M) from the Herschel/HIFI survey. These transitions indicate several things: (i) the CO lines are wide, indicative of a highly turbulent velocity field, (ii) the $C^{18}O$ transitions peak at the center of the absorption dip of the CO transitions, indicating self-absorption of the main isotopologue, and (iii) the asymmetry of the self-absorbed CO transitions switches with increasing quantum number J from red-shifted to blue-shifted.

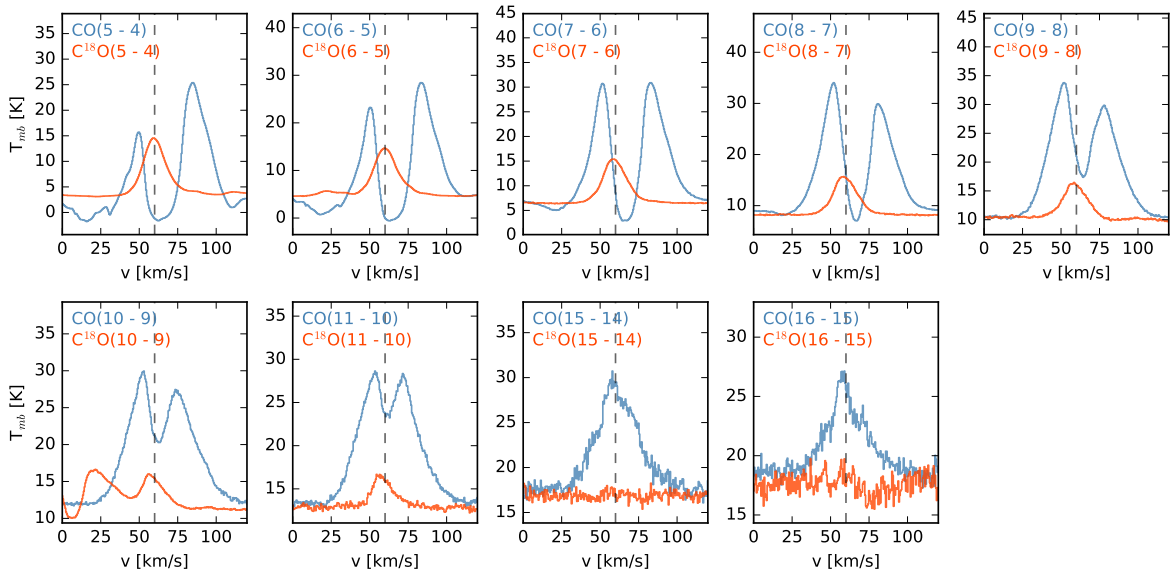

Figure 7.1: Herschel/HIFI spectra of CO (in blue) and $C^{18}O$ (in orange) from the HEXOS survey towards Sgr B2(M).

Optically thin isotopologue: $C^{18}O$

In the local ISM, the $C^{18}O$ isotopologue is a factor of 500 less abundant than the main molecule $C^{16}O$ (Wilson & Rood 1994). Is is optically thin. Optically thin molecules constrain the molecular column density along the line-of-sight. As already mentioned, CO is often used to constrain the hydrogen column density. This isotopologue can thus be used to cross-check the continuum modeling. Multi transitions of these molecules are available towards Sgr B2(M) from the HEXOS survey obtained with the HIFI instrument aboard of Herschel Section 5.1. Since the beam size decreases with increasing frequency, the line survey can even be used to constrain the molecular column density within slabs of the same length (line-of-sight), but with different diameters.

For Sgr B2(M), the continuum levels of the predicted $C^{18}O$ spectra are lower than the observed continuum levels. This indicates that there is a fraction of molecular column density along the line-of-sight missing. This is not contradicting the results from the previous chapter, it merely hints at the imperfection of the observational data, causing ambiguities. By including a intermediate sized clump, I am able to recover the continuum level. After that I modify the molecular abundance, until I obtain a reasonable fit for the low-J transitions. Figure 7.2 shows for five different transitions, from top to bottom, the initial offset of the continuum level (Model C), the correction of the continuum level by including an intermediate sized density component (Model C1), the inclusion of a constant temperature shock component (Model C1 shock1) and the modification of this shock component to use a radius dependent temperature profile (Model C1 shock2).

The normalized populations of the relevant $C^{18}O$ levels are shown in Fig. 7.3. The high-J transitions originate in the inner core region.

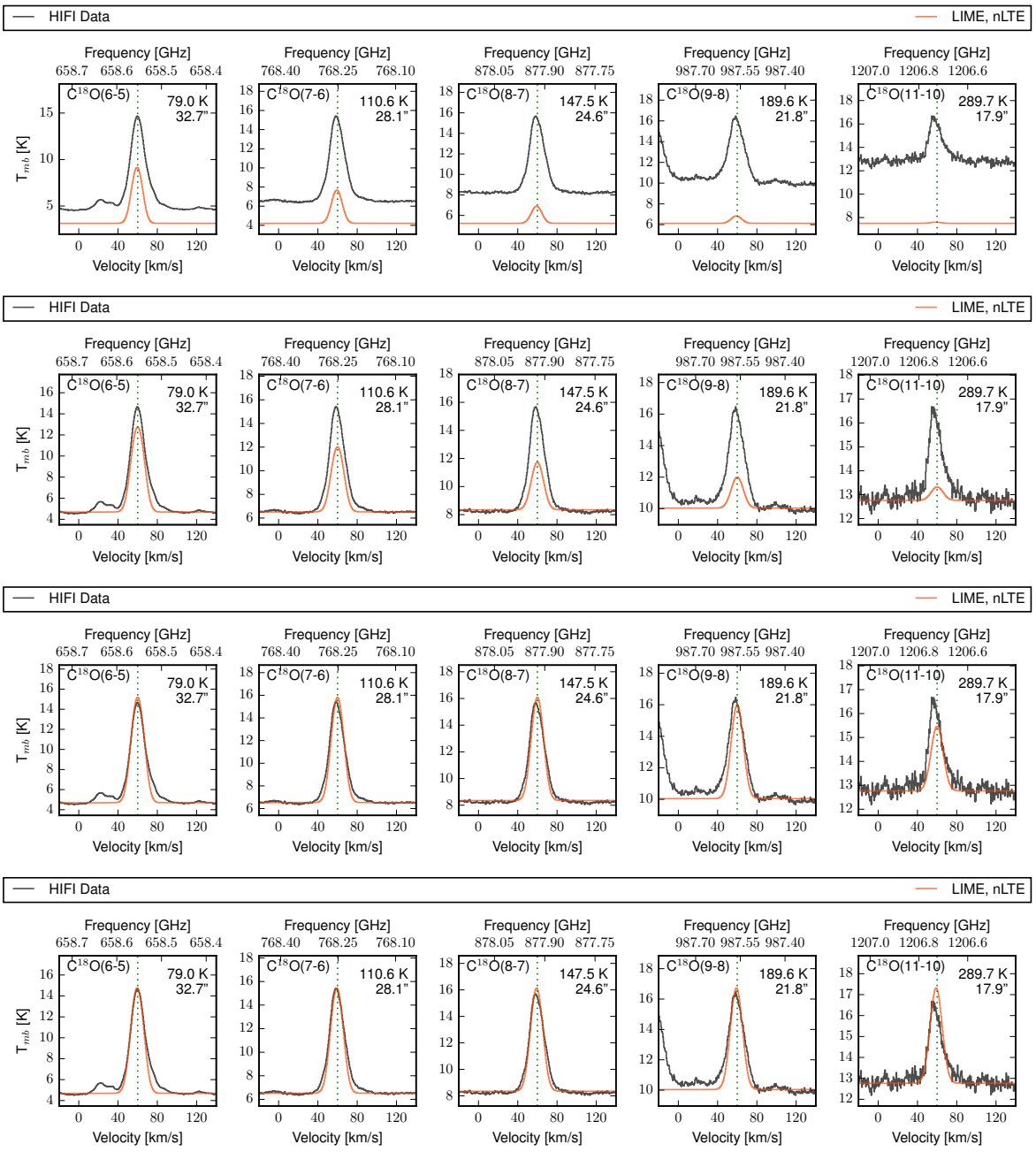

Figure 7.2: $C^{18}O$ spectra of Sgr B2(M). Top: Initial model from structure file obtained in continuum modeling step (Model C). The offset between the observed continuum and the predicted continuum is clearly visible. Second: Match of the continuum level by adding an intermediate sized envelope around Sgr B2(M) (Model C1). Third: A constant temperature shock component has been added to increase the intensity of the high-J transitions (Model C1-shock1). Bottom: The constant temperature shock component has been replaced by a shock component with a temperature gradient (Model C1-shock2).

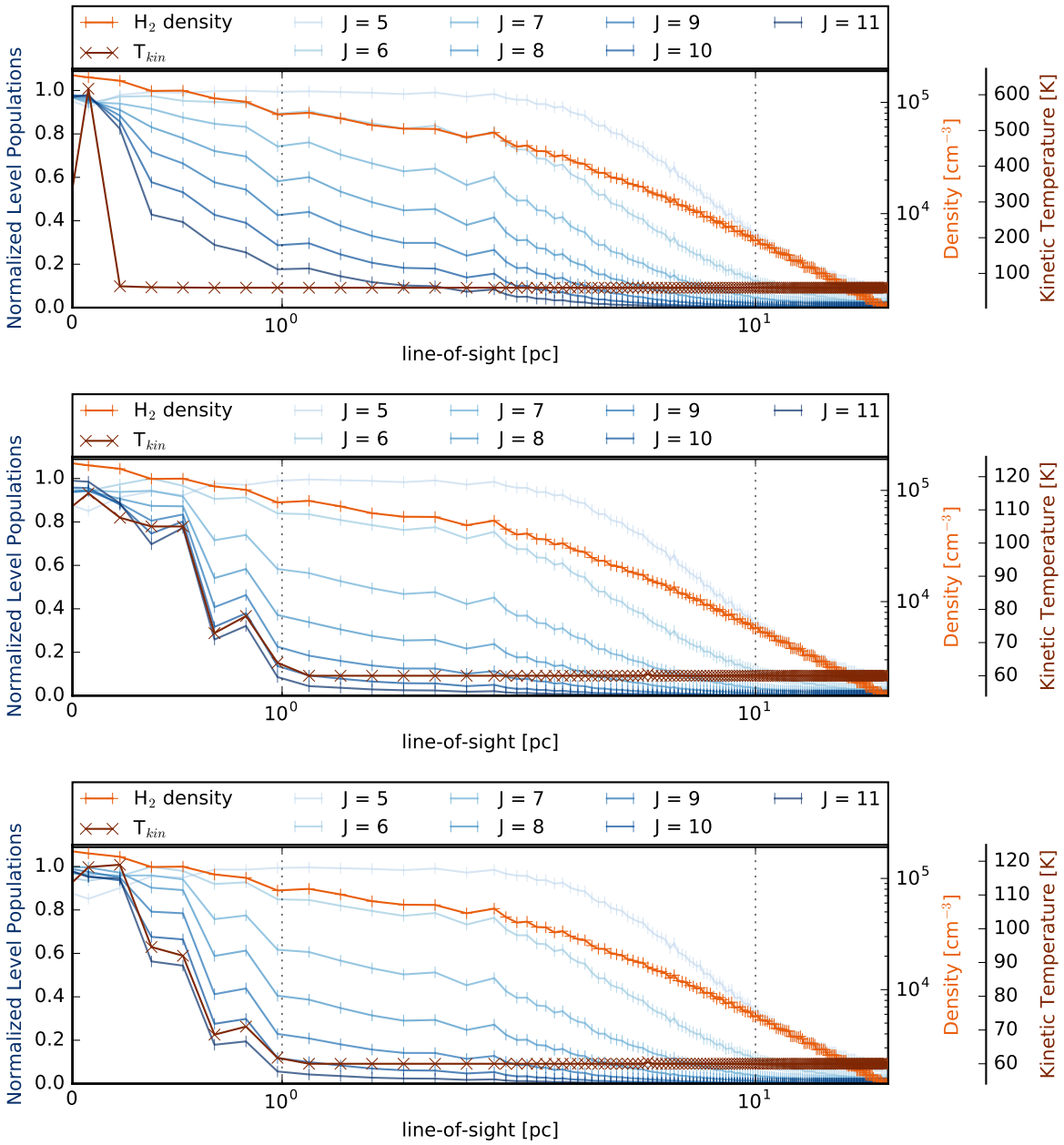

Figure 7.3: Normalized $C^{18}O$ level populations within a 32″ beam along the line-of-sight towards Sgr B2(M). Top: Model C1. Middle: Model C1-shock1. Bottom: Model C1-shock2.

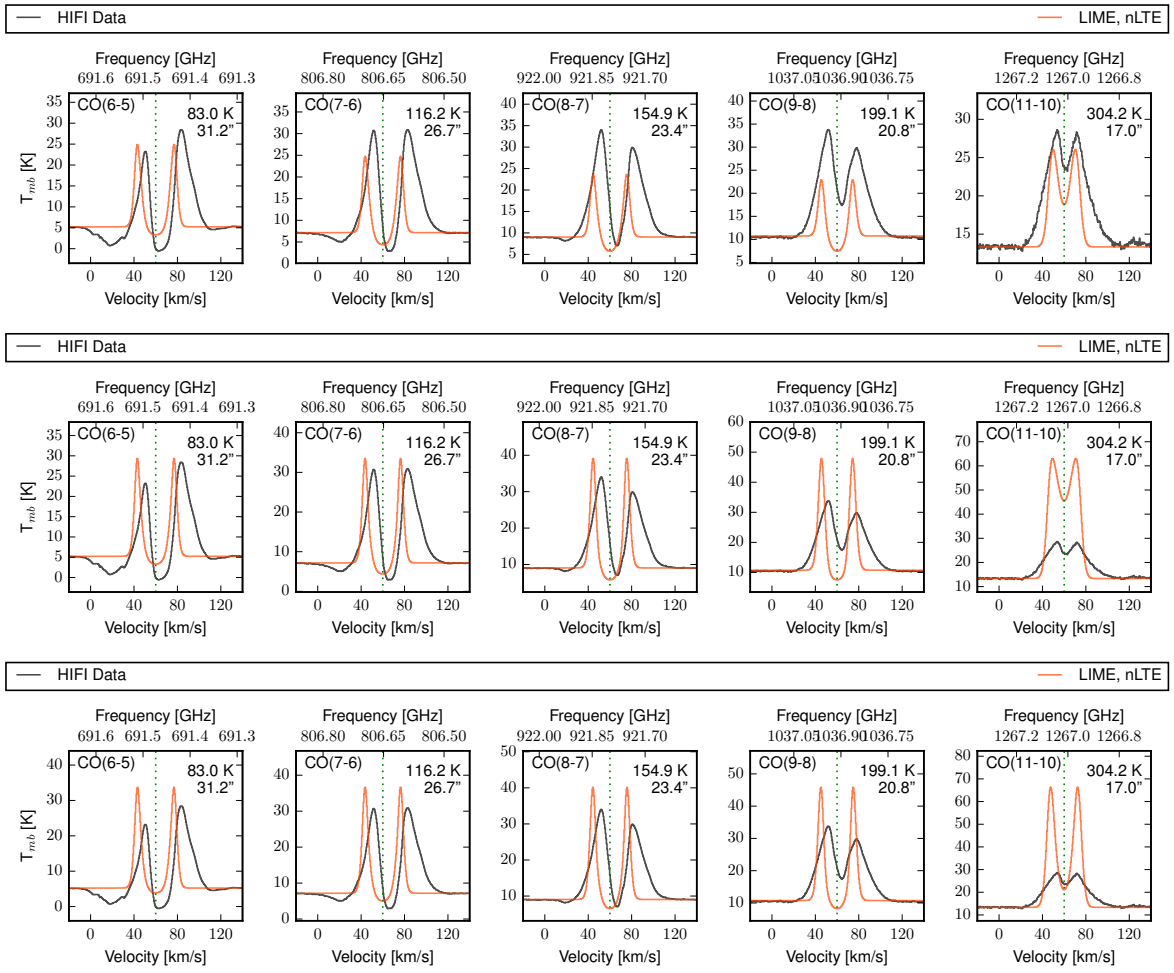

Figure 7.4: CO spectra of Sgr B2(M). Top: Model C1. Middle: Model C1-shock1. Bottom: Model C1-shock2.

Optically thick molecule: CO

The CO(6-5) spectral line has a red-shifted asymmetry, CO(7-6) shows no clear asymmetry at all, and the CO(8-7) and CO(9-8) spectral lines are blue-shifted. The CO(11-10) transition shows no significant asymmetry (see Fig. 7.1). Apart from the last transition, all spectral lines have very pronounced self-absorption dips, originating from the envelope surrounding Sgr B2. Figure 7.4 shows the results when applying Model C1 (top), Model C1-shock1 (middle), and Model C1-shock2. Clearly both shock models overestimate the high-J line intensities. Since no velocity field was applied, the asymmetries are not reproduced as well. The normalized populations of the relevant CO levels are shown in Fig. 7.5. The low-J transitions originate from the outer envelope.

In the next attempt, I add the shell discovered by De Vicente et al. (1997). Figure 7.6 employs a shock-shell combination as well as a modified velocity field. The shift of asymmetry is reproduced by giving the large-scale envelope a radial expansion motion along the line-of-sight and the intermediate

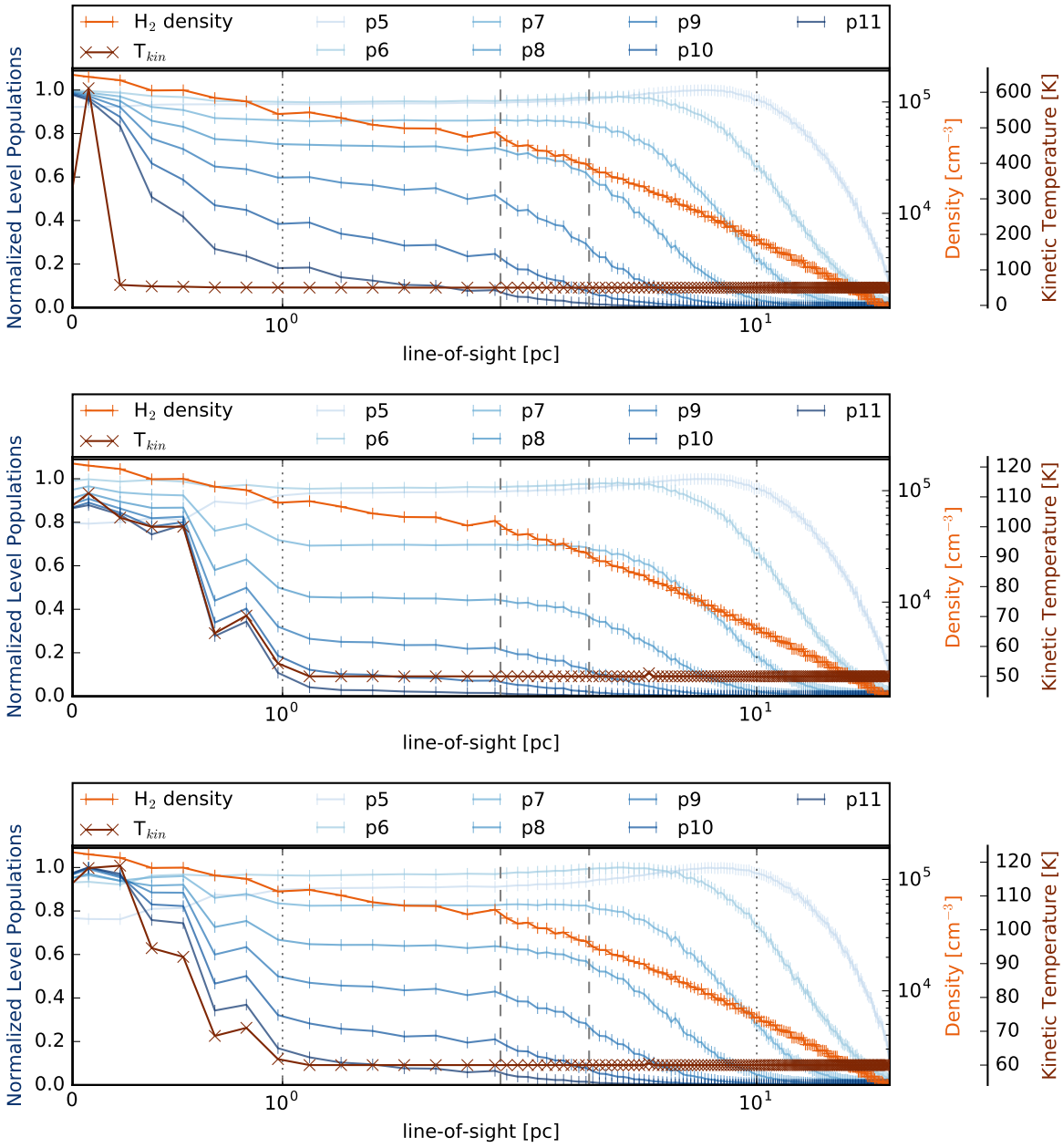

Figure 7.5: Normalized CO level populations within a 32″ beam along the line-of-sight towards Sgr B2(M). Top: Model C1. Middle: Model C1-shock1. Bottom: Model C1-shock2. Both models that include the additional heating in the inner core clearly overestimate the high-J CO transitions.

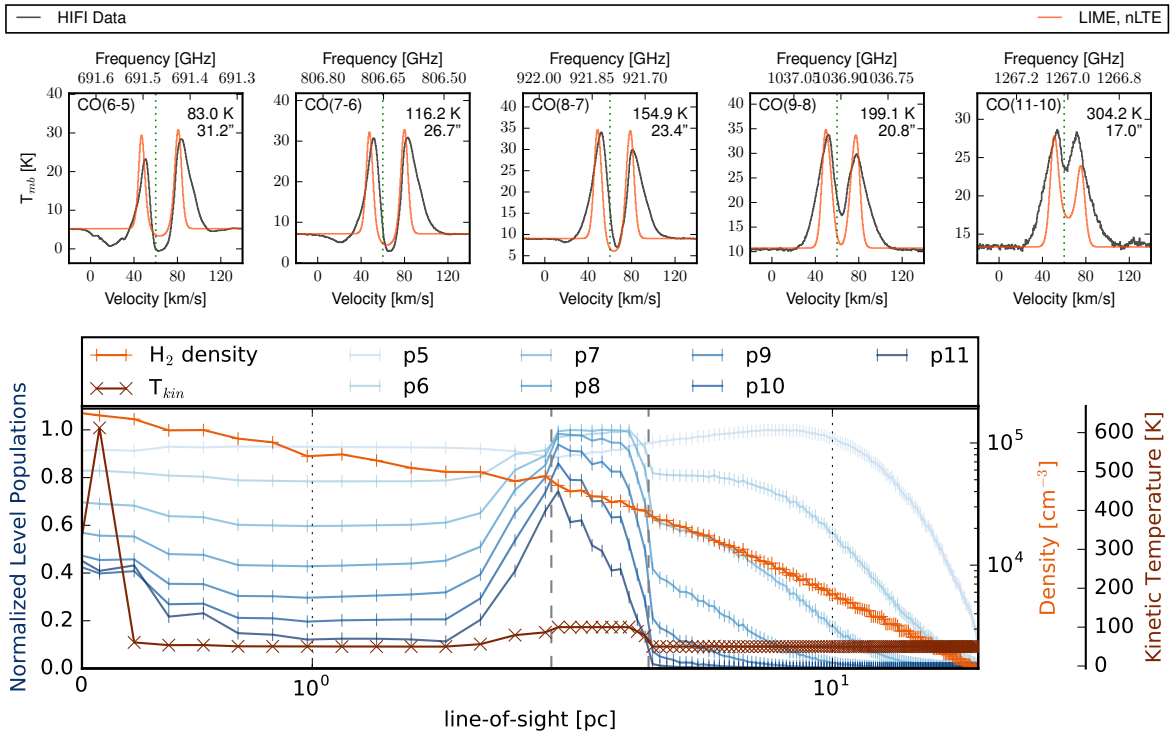

Figure 7.6: Results from a combined shell-shock model with a modified velocity field. Top: CO spectra of Sgr B2(M). Bottom: Normalized CO level populations within a 32″ beam along the line-of-sight towards Sgr B2(M).

sized envelope an infall motion.

7.2.2 Hydrogen cyanide, HCN

Due to its larger dipole moment, the rotational lines of HCN have a higher critical density than CO. These lines thus probe denser gas. Towards Sgr B2(M), the HCN(6-5) HIFI spectral line has a very pronounced blue-shifted asymmetry, HCN(7-6) shows a slight blue-shifted asymmetry, HCN(8-7), HCN(9-8) and HCN(10-9) are all red-shifted (see Fig. 7.7). The $H^{13}CN$ isotopologue also features a double-peaked structure, indicating that this isotopologue might also be optically thick. Using a single spherical symmetric clump, Rolffs et al. (2010) reproduced the shift in asymmetry in the HCN rotational lines by assuming a velocity field that exhibits infall on intermediate scales and expansion on small scales. In an attempt to reproduce this finding, I have given the small scale cores a positive radial velocity of 2 km/s and the intermediate core a negative radial velocity of -2 km/s. The resulting spectra are shown in Fig. 7.8 and the corresponding fractional level populations are shown in Fig. 7.9. The spectra clearly indicate that the expansion motion of the inner cores is too dominant. The infall motion on the intermediate scales is not traced by the current setup.

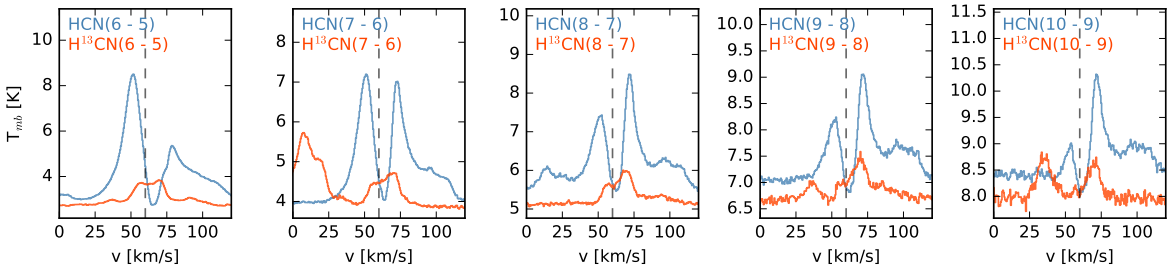

Figure 7.7: Herschel/HIFI spectra of HCN (in blue) and $H^{13}CN$ (in orange) from the HEXOS survey towards Sgr B2(M).

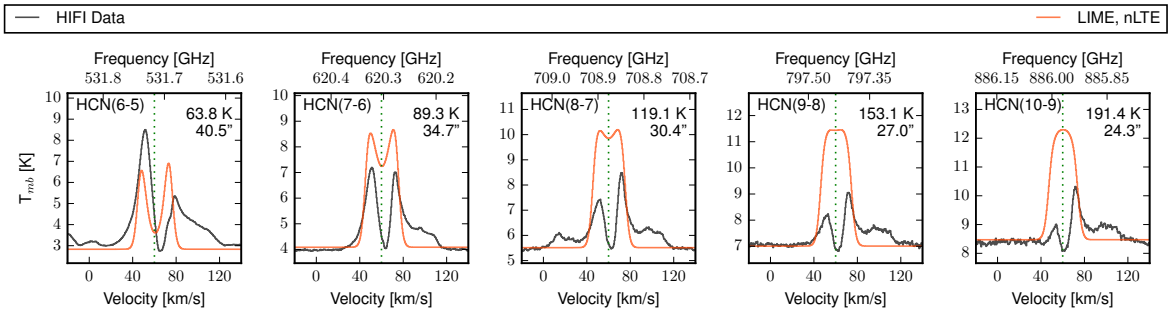

Figure 7.8: HCN spectra of Sgr B2(M). The continuum level is reproduced. The intensities are currently overestimated, the shift in asymmetry is not reproduced yet.

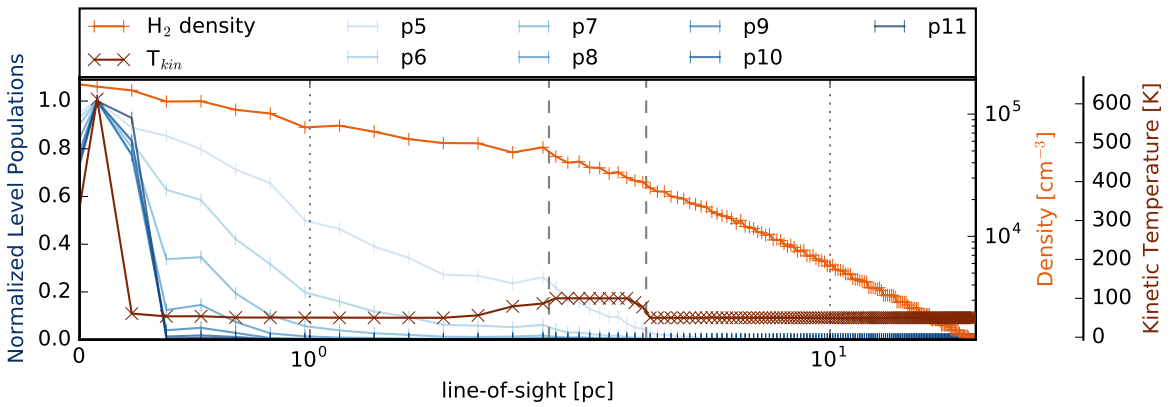

Figure 7.9: HCN level populations within a beam of 32″ along the line-of-sight towards Sgr B2(M).

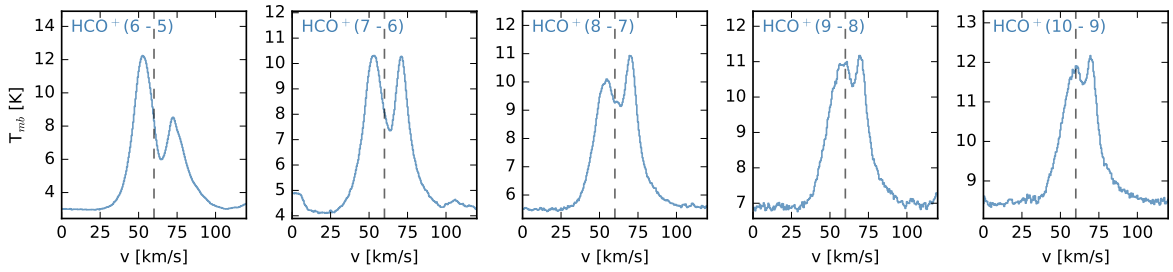

Figure 7.10: Herschel/HIFI spectra of HCO^+ (in blue) from the HEXOS survey towards Sgr B2(M).

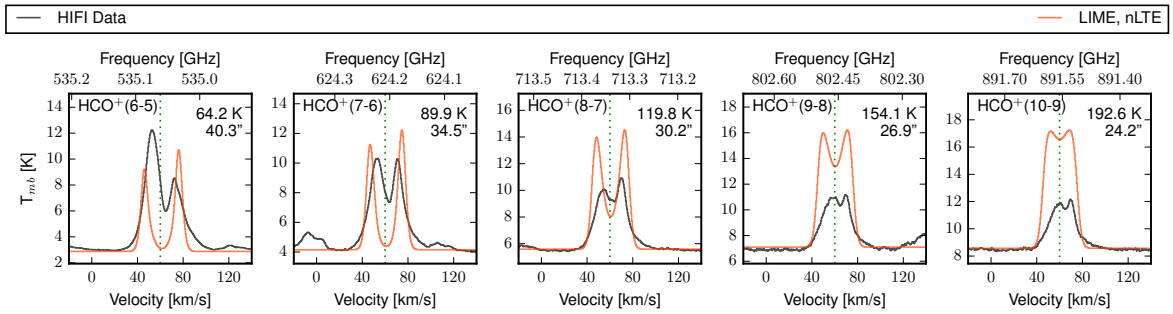

Figure 7.11: HCO^+ spectra of Sgr B2(M). The continuum level is reproduced. The intensities are currently overestimated, the shift in asymmetry is not reproduced yet.

7.2.3 Formyl cation, HCO^+

Similarly to HCN, HCO^+ has a larger dipole moment than CO. Thus the rotational transitions of this molecule have a higher critical density and probes dense gas. The spectra of the transition covered by HIFI towards Sgr B2(M) show a similar behavior as the HCN spectra (see Fig. 7.10). The low-J transitions are blue-shifted, while the higher-J transitions are red-shifted. I used a similar model setup as for HCN. The spectra and the fractional level populations are shown in Figs. 7.11 and 7.12, respectively. The outcome is similar as for HCN.

7.2.4 Carbon monosulfide, CS

Like HCN and HCO^+, CS is a commonly used dense gas tracer. The HIFI spectra as shown in Fig. 7.13. The rotational spectra are Gaussian shaped without any clear asymmetry. The spectra and fractional population levels of a combined shock-shell model is shown in Fig. 7.14. While the model reproduces the low-J transitions, it clearly underestimated the high-J transitions. Thus the abundance profile had been modified (Fig. 7.15). In this model, the low-J transitions are overestimated while the match to the higher-J transitions is improved.

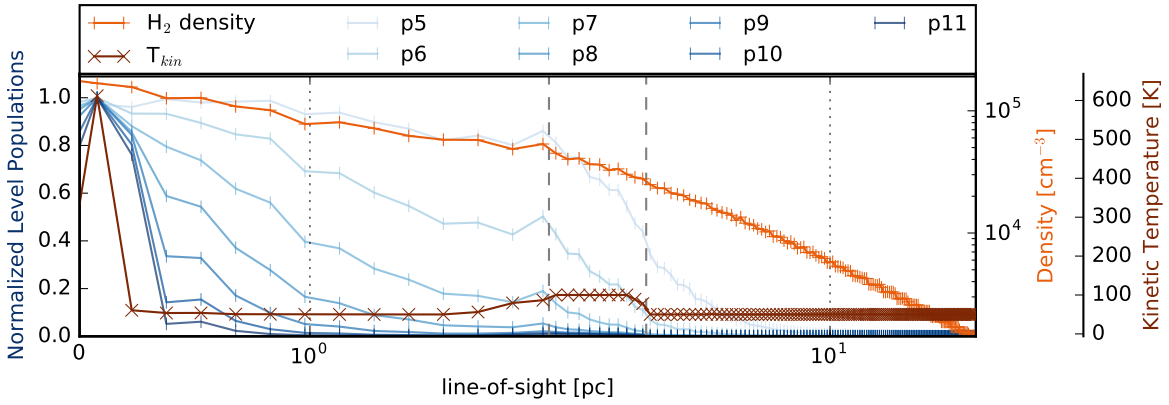

Figure 7.12: HCO^+ level populations within a beam of 32″ along the line-of-sight towards Sgr B2(M).

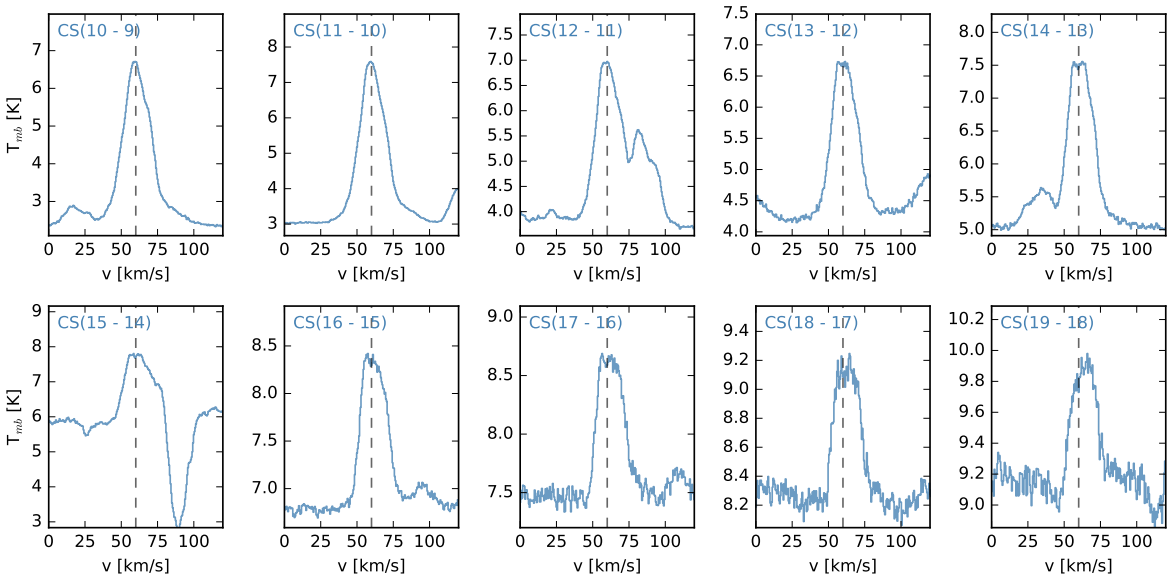

Figure 7.13: Herschel/HIFI spectra of CS (in blue) from the HEXOS survey towards Sgr B2(M).

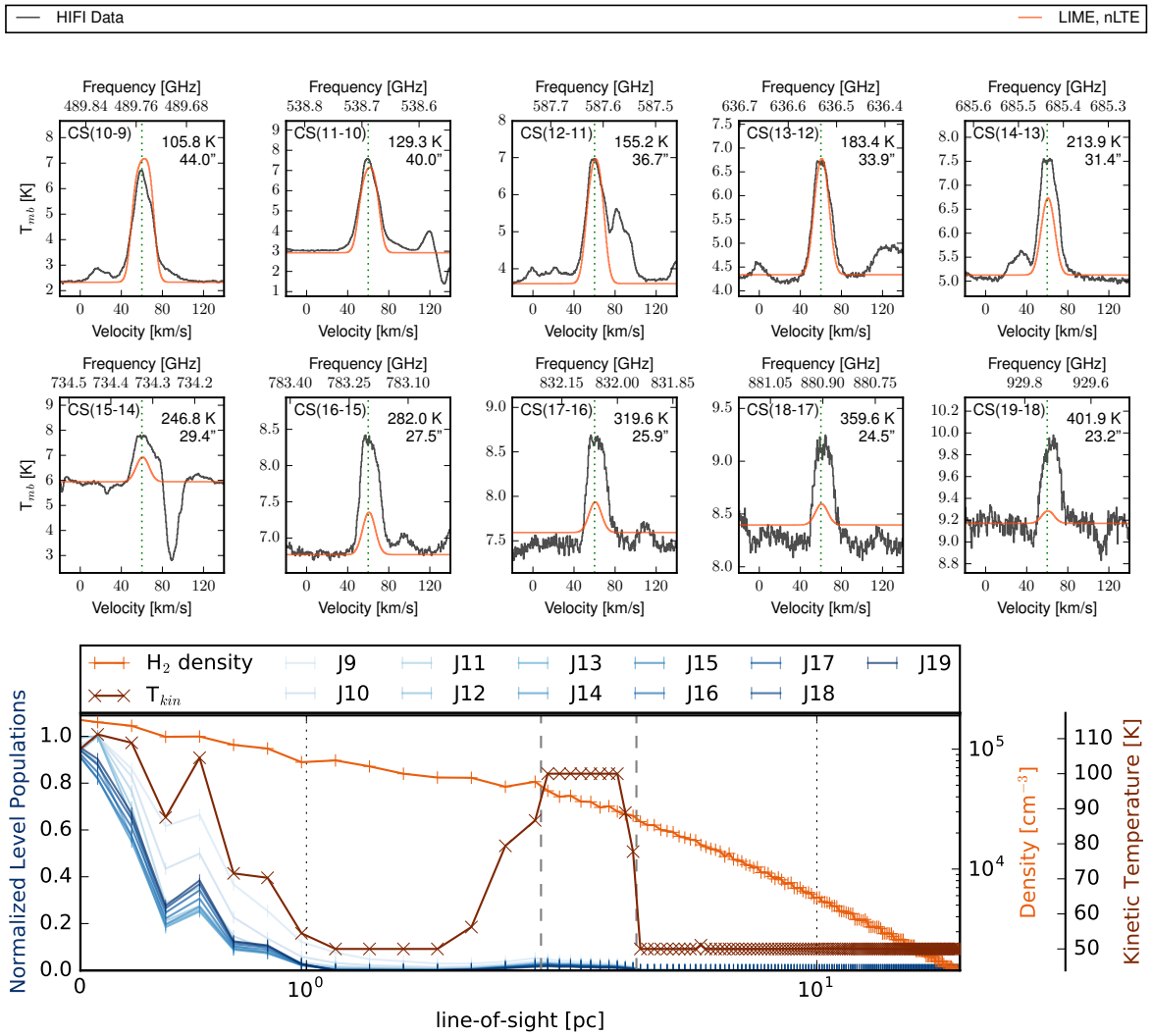

Figure 7.14: Top: CS spectra of Sgr B2(M). The continuum level is reproduced, the intensity of the low-J transitions are reproduced. The intensity of the high-J transitions are underestimated. Bottom: CS level populations within a beam of 32″ along the line-of-sight towards Sgr B2(M).

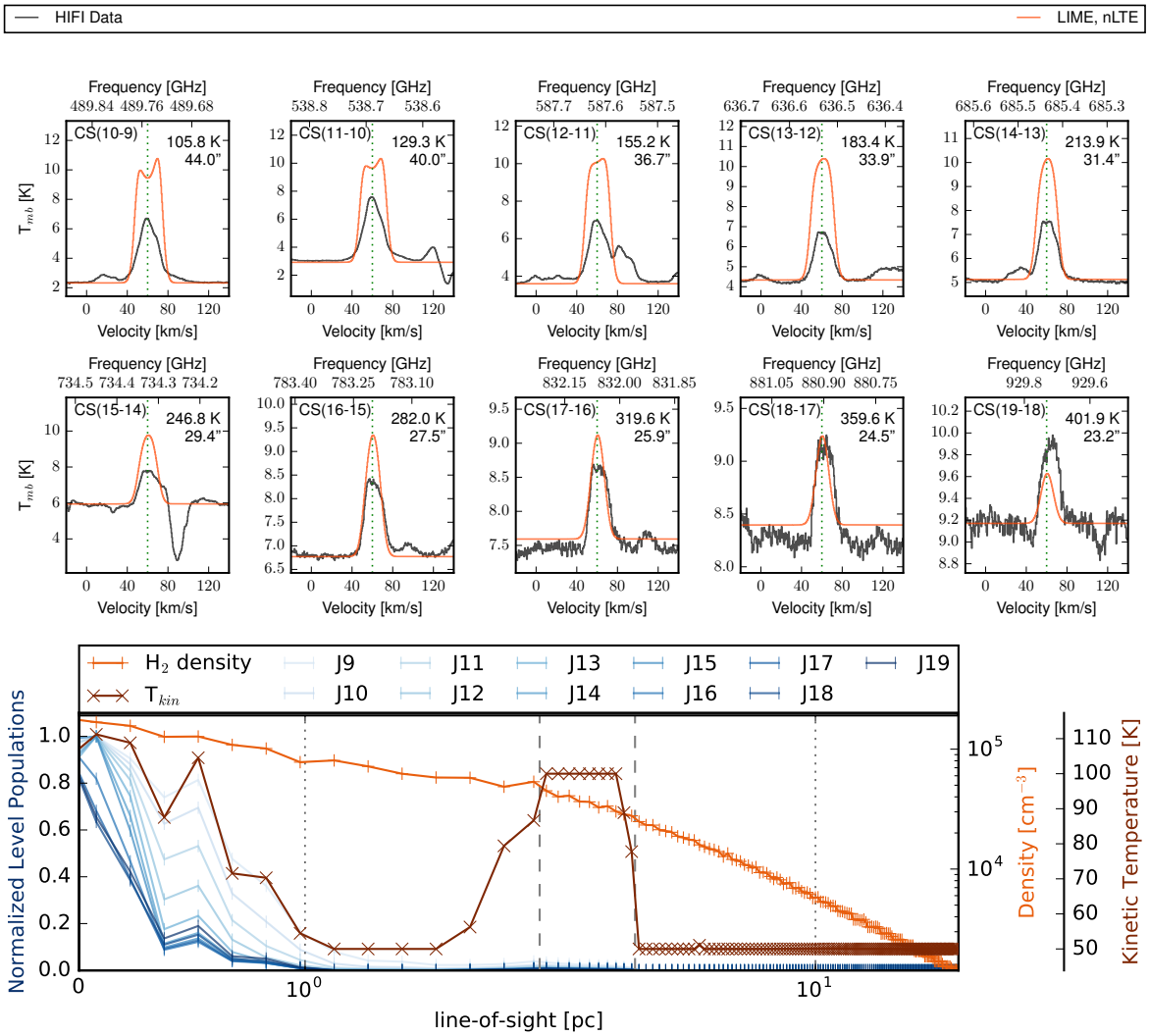

Figure 7.15: Top: CS spectra of Sgr B2(M). The abundance profile has been modified. The intensity of the low-J transitions are now overestimated while the intensity of the higher-J transitions provide a reasonable fit. Bottom: CS level populations within a beam of 32″ along the line-of-sight towards Sgr B2(M).

7.2.5 Summary of the model setups

- **Model C1:**
  - Additional intermediate sized core. Coordinates α_{J2000}= $17^h47^m20.056^s$, δ_{J2000}= $-28°23'6.46''$, $dz = 0$, central density $n = 2 \times 10^6$, radii $r_x = r_y = r_z$ = 30000 au, exponent η = 2.5
- **shock1:**
  - Radius r = 1 pc, centered on HIFI pointing position of Sgr B2(M), temperature T = 150 K
- **shock2:**
  - Radius r = 1 pc, centered on HIFI pointing position of Sgr B2(M), temperature T = 100 K, exponent s = 0.8
- **CO best fit model:**
  - intermediate core: v_z = -2.0 km/s, v_r = -2.5 km/s
  - large-scale envelope: v_z = 8.0 km/s, v_r = 2.5 km/s
  - shock: radius r = 0.5 pc, temperature T = 100 K
  - shell: inner radius r_i = 2.1 pc, outer radius r_o = 3.6 pc, temperature T = 100 K
- **HCN, HCO^+ model:**
  - small scale cores SMA-M-XX: v_r = 2.0 km/s
  - intermediate core: as for CO best fit model
  - shock and shell structure: as for CO best fit model
- **CS model:**
  - shock: radius r = 1 pc, temperature T = 150 K
  - shell: as for CO best fit model

7.3 Results

7.3.1 Velocity field information

I will now discuss the modeling efforts in deriving the velocity field along the line-of-sight towards Sgr B2(M) For this I employed the data from the Herschel/HIFI survey (Section 7.2). The molecules of interest were CO, HCN, HCO^+, and CS. Their spectral lines exhibit a very interesting behavior. From low to high rotational transition number J, the lines, especially of CO, HCN and HCO^+, display a change in asymmetry. Based on the fit of the rotational spectra of these four molecules presented, an initial (tentative) picture of the line-of-sight structure towards Sgr B2(M) can be deduced. The different spectral line asymmetries could be explained, if the outer envelope was expanding, the intermediate scales were infalling and the small scale were expanding again. In this picture, the investigates CO transitions emanate from the outer envelope up to intermediate scales. Here the density is sufficiently high enough, so that the lower rotational levels of the high density tracers such as HCN and HCO^+ are populated.

Unfortunately, a single model reproducing all aspects of the here presented spectral line analysis could not yet been obtained.

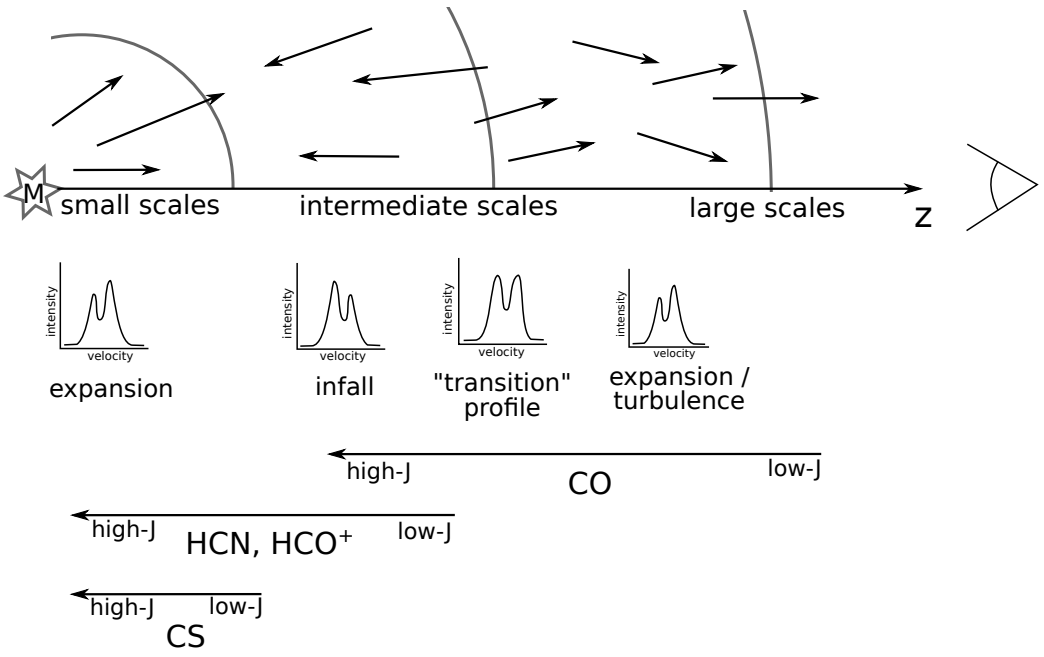

Figure 7.16: Tentative sketch of the line-of-sight velocity field of Sgr B2(M). All values have to be taken with caution.

7.4 Preliminary outlook

Once the velocity field along a few line-of-sights is obtained, one can attempt to model data cubes of the entire Sgr B2 region. Using APEX, Rolf Güsten has recently obtained a CO(6-5) map covering the inner part of Sgr B2. Out of curiosity, I ran PANDORA with the best fit CO model. Figure 7.17 shows integrated intensity maps of the observed and synthetic CO emission. The line-of-sight towards Sgr B2(M) is already promising, but for example the absorption feature towards Sgr B2(N) is not reproduced. This shows that still quite some work has to be done to gain a better understanding of the velocity field of Sgr B2.

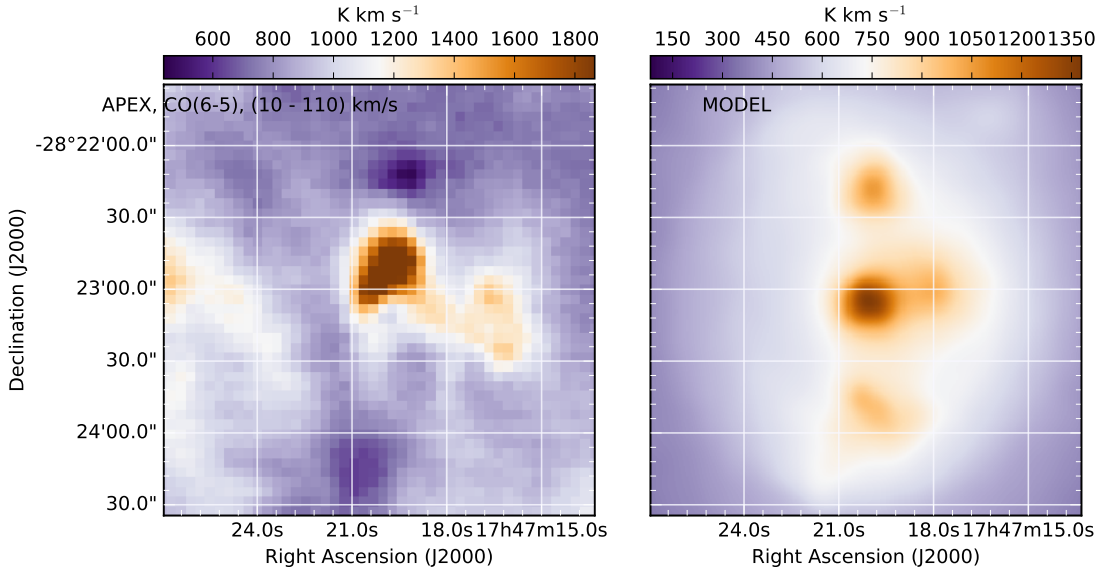

Figure 7.17: Preview of the integrated CO(6-5) map obtained with APEX.

8. Conclusions

To facilitate the process of full three-dimensional radiative transfer modeling including all steps necessary to compare synthetics maps with observational maps, I have designed the PANDORA framework. I successfully apply this framework to reconstruct a possible three dimensional density distribution of Sgr B2, recovering the continuum structures covering a wide frequency range (ν = 40 GHz – 4 THz) on scales from 100 au to 45 pc.

I find that the density field of Sgr B2 can be reasonably well fitted by a superposition of spherical symmetric density cores with Plummer-like profiles. To reproduce the spectral energy distribution, we locate Sgr B2(N) along the line of sight behind the plane containing Sgr B2(M). Sgr B2 comprises a total gas mass of $8.0 \times 10^6\,M_\odot$ within a diameter of 45 pc. This corresponds to an average gas density of $170\,M_\odot\ pc^{-3}$. For Sgr B2(N) we find a stellar mass of $2400\,M_\odot$, a luminosity of $1.8 \times 10^6\,L_\odot$, a H_2 column density of $2.9.7 \times 10^{24}\,cm^{-2}$ in a $40''$ beam. For Sgr B2(M) we derive a stellar mass of $20700\,M_\odot$, a luminosity of $1.2 \times 10^7\,L_\odot$, a H_2 column density of $2.5 \times 10^{24}\,cm^{-2}$ in a $40''$ beam. For Sgr B2(S) we find a stellar mass of $1100\,M_\odot$, a luminosity of $6.6 \times 10^5\ L_\odot$, a H_2 column density of $2.2 \times 10^{24}\,cm^{-2}$ in a $40''$ beam. The derived star formation efficiency is very low for Sgr B2(N), $\sim$5 %, and significantly higher for Sgr B2(M), $\sim$50 %. This indicates that most of the gas in Sgr B2(M) has already been converted to stars or dispersed.

The derived density structure builds the foundation for the modeling of molecular spectral lines. In the second step, I employ PANDORA and attempt to reconstruct the line-of-sight velocity structure towards Sgr B2(M) using different tracers of low, intermediate and high densities. Although I do not yet succeed in obtaining a single model reproducing all spectral lines investigated, I find evidence hinting at a potentially three-layered line-of-sight velocity field: (i) Expansion motion dominates in the outer envelope, (ii) on

intermediate scales, the gas might be infalling towards Sgr B2(M), and (iii) the inner cores show signs of expansion.

The development of the modeling engine PANDORA and its usage to derive the density structure and temperature field of Sgr B2 presented in this thesis opens the stage for a plethora of different applications and improvements. Naturally, the modeling engine PANDORA and its usage to derive the physical structure of an astrophysical are tightly linked. Each new source will pose new requirements and challenges. However, in this outlook I will try to separate the modifications needed to improve PANDORA from the next, e.g. observational steps needed to improve the derived physical structure of Sgr B2.

9.1 Pandora

9.1.1 Functionality

The developed modeling engine PANDORA has many advantages. Let us assume we have a model based on a specific set A of observational data. With the advent of, for example higher resolved, observational data (dataset B), the physical structure can be progressively fine-tuned, since instead of rather modeling dataset B with a new setup, it will be added to dataset A and this will add valuable additional constraints to the physical structure. Thus over time, a consistent library of physical setups for individual sources could be established.

Concerning PANDORA, future work should focus on improving the modeling engine. This includes for example an improved treatment of the optimization, i.e. the link between PANDORA and MAGIX, especially for the spectral line modeling. Furthermore the modeling procedure would gain significantly by adding features to automatically generate an initial guess of the source structure in order to save time spent on an otherwise by-hand adjustment technique. This encompasses the determination of the

density and stellar distribution. Efforts to combine PANDORA with a sophisticated chemical modeling engine are currently undertaken by G. Stéphan. This will allow a self-consistent determination of the molecular abundances. Eventually I would also like to link PANDORA with numerical codes that perform (magneto-)hydro-dynamical simulations (e.g. Flash, Ramses, Pluto).

Here I could imagine two different applications. First one could (a) use PANDORA to simplify and standardize the post-processing of numerical simulations (radiative transfer calculation, convolution etc.) and (b) to use the physical structure obtained for a specific source of interest and use this as a starting point for a numerical simulation to derive the fate of the region. This is not straight forward, but it would nicely link theoretical and observational efforts to gain more insights into specific sources.

9.1.2 Model setup

The physical setup of the model presented in this thesis sets the stage for future improvements. By including the possibility to spatially vary the composition of dust, the influence of different compositions can be tested. The treatment of the HII regions can and should be improved, eventually leading the way to also model radio recombination lines and thus getting access to the ionized gas content. Furthermore the effect of a clumpy density structure can be tested as well as the influence of dusty HII regions.

9.2 Source application

9.2.1 Sagittarius B2

With the current state of telescopes, it is now possible to efficiently map larger portions of the sky with a high resolution. As indicated in Fig. 5.1, maps with high angular resolution of Sgr B2 are missing, especially in the frequency range of 100 – 400 GHz. But they are necessary to improve the setup of the envelope. Currently there is for example only one map available, that resolves dust structures down to ~ 0.01 pc towards Sgr B2(N) and Sgr B2(M). To constrain the dust properties properly, at least another map covering similar scales at a different wavelength is needed. Studying spatial variations of the dust properties on scales smaller than $10''$ in the entire envelope is impossible with the data sets currently available. However, this could be partly achieved by using the Atacama Compact Array (ACA).

The investigation of the dynamics of Sgr B2 need to be continued, leading to the determination of a consistent velocity field. (i) Along the line-of sight towards the hot cores Sgr B2(N) and Sgr B2(M), multi-frequency molecular line data is available. This provides the necessary wide range of transitions of a diversity of molecular species to perform a *molecular line tomography*. Part of this work has already been performed towards Sgr B2(M). But more molecules need to be included to confirm the current conclusions. Eventually this approach should be expanded to include Sgr B2(N). (ii) The two hot cores are embedded in an extended, lower density envelope. Based on the experience gained during step (i) crucial transitions of selected molecules throughout the entire envelope should be modeled. This will provide us with a complete physical state of Sgr B2, including the spatial structures, the dynamics and the properties of the stellar populations.

9.2.2 Other sources

PANDORA follows a philosophy of flexibility. The model setup of the physical structure works like a LEGO system, i.e. different structures (dense cores, filaments, outflows etc) can be combined if needed. Up to now PANDORA has been used to successfully model Sgr B2 (presented in this thesis) and the nearby high-mass star-forming region NGC6334 (presented in Zernickel 2015). It would be insightful to apply the framework methodically to other star-forming regions, for example Orion, other clouds in the CMZ (e.g. G0.253 aka the Brick, Sgr C), and nearby extragalactic sources (e.g. the Magellanic Clouds, which are now resolvable using ALMA). This will enable us to investigate similarities and differences between the sources and thus will provide statistics, ultimately allowing to test star formation theories.

A. Theoretical Background

A.1 HII regions

HII regions are sharply defined regions of photoionised gas. For simplicity we first assume a massive star to be buried in a cloud which consists of purely molecular hydrogen and has a uniform density. The energetic photons ejected from the stellar surface first dissociate the molecular hydrogen (i.e. atomic hydrogen, HI, is generated) and then ionize the atomic hydrogen (i.e. ionized hydrogen, HII, is generated). For the last step photons with energies larger than 13.6 eV are needed. On the other hand, existing electrons and protons may recombine to form atomic hydrogen. For each of dissociation, ionization reactions, a photon is needed. The ionized particles are free, i.e. their energy states are not quantized, thus the free-free radiation is continuous over the spectrum. Since stars only have a fixed amount of photons, they can only ionize a limitied region around the star. If the ionization spreads isotropically, then the ionization fills a volume around the star that is called Strömgren sphere.

We assume an electron density distribution that equals N_e within the radius r_0 of the HII region and is zero elsewhere. We furthermore assume, that the entire HII region is ionized, i.e. the electron density n_e equals the ion density n_i. We can then calculate the emission measure EM as follows

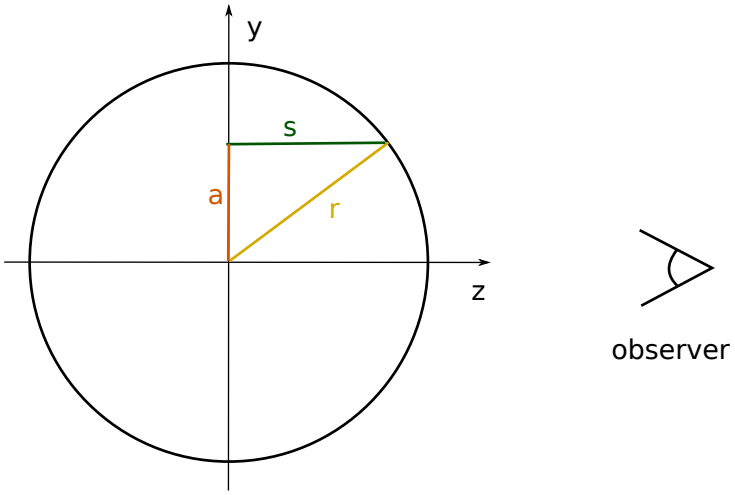

Figure A.1: Sketch of the HII region along the line of sight. The integration path along-the line of sight for the calculation of the emission measure is marked.

$$
\begin{aligned}
EM &= 2\int_0^s n_e n_i \, dz \\
&= 2\int_a^{r_0} N_0^2 \frac{r}{\sqrt{r^2-a^2}} dr \\
&= 2N_0^2 \left[\sqrt{r^2-a^2}\right]_a^{r_0} \\
&= 2N_0^2 \left(\sqrt{r_0^2-a^2} - \sqrt{a^2-a^2}\right) \\
&= 2N_0^2 r_0 \sqrt{1-\frac{a^2}{r_0}} \\
&= 2N_0^2 D\,\theta_0 \sqrt{1-\left(\frac{\theta_a}{\theta_0}\right)^2}
\end{aligned} \tag{A.1}
$$

where D is the distance to the source, θ_0 is the radius of the HII region in angular units, $\psi(a)$ is the remaining angle term, a is the angular position along the line of sight in the x-y plane. Introducing the source size $\theta_{\text{source}} = 2 * \theta_0$, we obtain

$$EM = N_0^2 D\,\theta_{\text{source}} \sqrt{1-\left(\frac{4\theta_a}{\theta_{\text{source}}}\right)^2} \tag{A.2}$$

$$= N_0^2 D\,\theta_{\text{source}}\,\psi(a) \tag{A.3}$$

If we want to calculate the maximum emission measure then we set $a = 0$ and the term $\psi(a)$ vanishes.

$$\left(\frac{EM}{\text{pc cm}^{-6}}\right) = \left(\frac{N_0}{\text{cm}^{-3}}\right)^2 \left(\frac{D}{\text{pc}}\right) \left(\frac{\theta_{\text{source}}}{\text{rad}}\right) \tag{A.4}$$

However, neither the emission measure nor the electron density are known. So we need another equation to solve the system. Integrating the specific intensity I_ν over the angular size of the source Ω_{source} yields the flux density F_ν

$$F_\nu = \int_{\Omega_{\text{source}}} I_\nu d\Omega \tag{A.5}$$

From the radiative transfer section we recall that the general solution of the radiative transfer equation for the specific continuum intensity is

$$\begin{aligned} I_\nu &= I_0\, e^{-\tau_\nu} + \int_0^{\tau_\nu} S_\nu\, e^{-\tau'} d\tau' \\ &= (S_\nu - I_0)\left(1 - e^{-\tau_\nu}\right) \end{aligned} \tag{A.6}$$

where S_ν is the source function of the HII region and I_0 is the background intensity. We assume an HII region with uniform temperature and negligible background temperature, i.e. $I_\nu(0) \ll S_\nu$. The intensity I_ν is then given by

$$I_\nu = S_\nu \left(1 - e^{-\tau_\nu}\right) \tag{A.7}$$

We have to distinguish two cases for the optical depth τ_ν:

$$I_\nu = \begin{cases} S_\nu \tau_\nu & \text{if } \tau_\nu \ll 1 \quad \text{(optical thin)} \\ S_\nu & \text{if } \tau_\nu \gg 1 \quad \text{(optical thick)} \end{cases} \tag{A.8}$$

The source function S_ν for the free-free radiation can be defined using the Planck function B_ν at an electron temperature T_e

$$\begin{aligned} S_\nu &= B_\nu(T_e) \\ &= \frac{2k\nu^3}{c^2} \frac{1}{e^{h\nu/kT_e} - 1} \\ &\approx \frac{2kT_e\nu^2}{c^2} \end{aligned} \tag{A.9}$$

where k is the Boltzman constant, c is the speed of light in vacuum and h is the Planck constant. The last step holds if $h\nu \ll kT$ (Rayleigh-Jeans approximation). The optical path length for free-free emission was derived by Oster (1961). For that the continuum absorption coefficient $\kappa_{\text{ff}}(\nu)$ is needed, however its derivation is challenging. Oster (1961) dicusses the history and problems of calculating the free-free emission coefficient in detail. The calculations require modeling of the electrical interaction between two charged particles, but also the velocity dispersion of the particles. Classically, the encounter of two moving charged particles involves changes in their directions - either toward each other for unlike charges or away from each other for like charges. The acceleration of these direction changes causes radiation (as

shown by the early work of Hertz). In the end Oster (1961) provide the following formula:

$$\tau_{\text{Oster}} = 3.014 \times 10^{-2} \left(\frac{T_e}{\text{K}}\right)^{-1.5} \left(\frac{\nu}{\text{GHz}}\right)^{-2.0} \left(\frac{\text{EM}}{\text{pc cm}^{-6}}\right) \left(ln\left(4.955 \times 10^{-2} \left(\frac{\nu}{\text{GHz}}\right)^{-1}\right) + 1.5\, ln\left(\frac{T_e}{\text{K}}\right)\right) \tag{A.10}$$

An approximation of this equation was given by Altenhoff et al. (1960).

$$\tau_{\text{AMWW}} = 8.235 \times 10^{-2} \left(\frac{T_e}{\text{K}}\right)^{-1.35} \left(\frac{\nu}{\text{GHz}}\right)^{-2.1} \left(\frac{\text{EM}}{\text{pc cm}^{-6}}\right) \tag{A.11}$$

In both equations, the number electron density N_e equals the number ion density N_i. According to Mezger & Henderson (1967), the deviation factor a, defined as

$$a = \frac{\tau_{\text{Oster}}}{\tau_{\text{AMWW}}} \tag{A.12}$$

deviates in the region of interest, i.e. $5 \times 10^3 \leq T_e \leq 1.2 \times 10^4\,\text{K}$ and $100\text{MHz} \leq \nu \leq 35\,\text{GHz}$, less than 10%.

Putting everything together, and assuming optical thin emission, we obtain

$$\begin{aligned}
F_\nu &= I_\nu \Omega_{\text{source}} \\
&= \frac{2kT_e\nu^2}{c^2}\, \tau_\nu\, \Omega_{\text{source}} \\
&= \frac{2k}{c^2} \left(\frac{T_e}{\text{K}}\right) \text{K} \left(\frac{\nu}{\text{GHz}}\right)^2 (\text{GHz})^2\, \tau_\nu\, \Omega_{\text{source}} \\
&= \frac{2k}{c^2} \times 10^{18}\,\text{K Hz}^2 \times 8.235 \times 10^{-2} \left(\frac{T_e}{\text{K}}\right)^{-0.35} \left(\frac{\nu}{\text{GHz}}\right)^{-0.1} \left(\frac{\text{EM}}{\text{pc cm}^{-6}}\right) \Omega_{\text{source}} \\
&= \frac{2k}{c^2} \times 8.235 \times 10^{16}\,\text{K Hz}^2 \left(\frac{T_e}{\text{K}}\right)^{-0.35} \left(\frac{\nu}{\text{GHz}}\right)^{-0.1} \left(\frac{\text{EM}}{\text{pc cm}^{-6}}\right) \Omega_{\text{source}} \\
&= 2.525 \times 10^{-23} \frac{\text{J}\ \cancel{\text{K}}\ \cancel{\text{Hz}^2}\ \cancel{\text{s}^2}}{\cancel{\text{K}}\,\text{m}^2} \left(\frac{T_e}{\text{K}}\right)^{-0.35} \left(\frac{\nu}{\text{GHz}}\right)^{-0.1} \left(\frac{\text{EM}}{\text{pc cm}^{-6}}\right) \Omega_{\text{source}} \\
&= 2.525 \times 10^3 \times \underbrace{\left(10^{-26} \frac{\text{J}}{\text{s m}^2\,\text{Hz}}\right)}_{=1\,\text{Jy}} \left(\frac{T_e}{\text{K}}\right)^{-0.35} \left(\frac{\nu}{\text{GHz}}\right)^{-0.1} \left(\frac{\text{EM}}{\text{pc cm}^{-6}}\right) \Omega_{\text{source}}
\end{aligned}$$

$$\left(\frac{F_\nu}{\text{Jy}}\right) = 2.525 \times 10^3 \left(\frac{T_e}{\text{K}}\right)^{-0.35} \left(\frac{\nu}{\text{GHz}}\right)^{-0.1} \left(\frac{\text{EM}}{\text{pc cm}^{-6}}\right) \Omega_{\text{source}} \tag{A.13}$$

Usually one fits a Gaussian to the data and extracts the flux density and the full width at half maximum

from this fit. If so then the solid angle has to be converted info useful units assuming a Gaussian beam.

$$\begin{aligned}\Omega_{\text{source}} &= \frac{\pi}{4\ln 2}\left(\frac{\theta_s}{\text{rad}}\right)^2 \\ &= \frac{\pi}{4\ln 2}\left(\frac{\theta_s}{\frac{180\text{ deg}}{\pi}\times 60\frac{\text{arcmin}}{\text{deg}}\times 60\frac{\text{arcsec}}{\text{arcmin}}}\right)^2 \\ &= \frac{\pi}{4\ln 2}\left(\frac{\pi}{180\times 60\times 60}\right)^2\left(\frac{\theta_s}{\text{arcsec}}\right)^2 \\ &= 2.66\times 10^{-11}\left(\frac{\theta_s}{\text{arcsec}}\right)^2 \end{aligned} \tag{A.14}$$

However, we simply determine the total flux in a given circular aperture. We calculate the solid angle for the given density distribution as follows:

$$\begin{aligned}\Omega_{\text{source}} &= 2\pi\int_0^{\theta_0}\theta_a\psi(a)\,d\theta_a \\ &= 2\pi\int_0^{\theta_0}\frac{\theta_a}{\theta_0}\sqrt{\theta_0^2-\theta_a^2}\,d\theta_a \\ &= \frac{2\pi}{\theta_0}\left[-\frac{1}{3}\sqrt{\left(\theta_0^2-\theta_a^2\right)^3}\right]_0^{\theta_0} \\ &= \frac{2\pi}{3}\theta_0^2 \\ &= \frac{\pi}{6}\left(\frac{\theta_{\text{source}}}{\text{rad}}\right)^2 \\ &= \frac{\pi}{6}\left(\frac{\pi}{180\times 60\times 60}\right)^2\left(\frac{\theta_{\text{source}}}{\text{arcsec}}\right)^2 \\ &= 1.231\times 10^{-11}\left(\frac{\theta_{\text{source}}}{\text{arcsec}}\right)^2 \end{aligned} \tag{A.15}$$

Now we obtain the following expression for the emission measure for a circular aperture

$$\left(\frac{\text{EM}}{\text{pc cm}^{-6}}\right) = 3.217\times 10^7\left(\frac{F_\nu}{\text{Jy}}\right)\left(\frac{T_e}{\text{K}}\right)^{0.35}\left(\frac{\nu}{\text{GHz}}\right)^{0.1}\left(\frac{\theta_s}{\text{arcsec}}\right)^{-2} \tag{A.16}$$

Combining Eq.A.4 and Eq.A.16, we can derive an expression to calculate the electron density N_0

$$\begin{aligned}\left(\frac{N_0}{\text{cm}^{-3}}\right) &= \left(\frac{EM}{\text{pc cm}^{-6}}\right)^{0.5}\left(\frac{D}{\text{pc}}\right)^{-0.5}\left(\frac{\theta_{\text{source}}}{\text{rad}}\right)^{-0.5} \\ &= \left(\frac{EM}{\text{pc cm}^{-6}}\right)^{0.5}\left(\frac{D}{\text{pc}}\right)^{-0.5}\left(\frac{\pi}{180\times 60\times 60}\right)^{-0.5}\left(\frac{\theta_{\text{source}}}{\text{arcsec}}\right)^{-0.5} \\ &= 454.16\times\left(\frac{EM}{\text{pc cm}^{-6}}\right)^{0.5}\left(\frac{D}{\text{pc}}\right)^{-0.5}\left(\frac{\theta_{\text{source}}}{\text{arcsec}}\right)^{-0.5} \end{aligned} \tag{A.17}$$

This yields

$$\left(\frac{N_0}{\mathrm{cm}^{-3}}\right) = 2.576 \times 10^6 \left(\frac{F_\nu}{\mathrm{Jy}}\right)^{0.5} \left(\frac{T_e}{\mathrm{K}}\right)^{0.175} \left(\frac{\nu}{\mathrm{GHz}}\right)^{0.05} \left(\frac{D}{\mathrm{pc}}\right)^{-0.5} \left(\frac{\theta_s}{\mathrm{arcsec}}\right)^{-1.5} \tag{A.18}$$

We derive the flux of ionizing photons $\dot{N}_i$ by balancing the number of recombinations and photoionizations within the HII region. For a Strömgren sphere this is determined by

$$\left(\frac{\dot{N}_i}{\mathrm{s}^{-1}}\right) = \int n_e n_i (\beta - \beta_1)\, dV \tag{A.19}$$

where β and β_1 are the rate coefficients for recombinations to all levels and to the ground state, respectively. Thus $(\beta - \beta_1)$ provides the recombination coefficient to level two or higher. Rubin (1968) approximate the recombination coefficient given by Seaton (1959) for electron temperatures T_e generally found in HII regions as

$$\left(\frac{\beta - \beta_1}{\mathrm{cm}^3\,\mathrm{s}^{-1}}\right) = 4.1 \times 10^{-10} \left(\frac{T_e}{\mathrm{K}}\right)^{-0.8} \tag{A.20}$$

We will use again the idealization that the HII region is fully ionized, yielding $n_e = n_i = N_0$. We then combine A.19 and A.20 and solve the integral for a spherical symmetric clump. This yields

$$\left(\frac{\dot{N}_i}{\mathrm{s}^{-1}}\right) = \frac{4}{3}\pi \left(\frac{r_0}{\mathrm{cm}}\right)^3 \left(\frac{N_0}{\mathrm{cm}^{-3}}\right)^2 \left(\frac{\beta - \beta_1}{\mathrm{cm}^3\,\mathrm{s}^{-1}}\right) \tag{A.21}$$

the radius r_0 of the HII region can be converted to the angular diameter provided the distance to the HII region is known

$$\left(\frac{r_0}{\mathrm{cm}}\right) = \frac{1}{2}\left(\frac{\theta_s}{\mathrm{rad}}\right)\left(\frac{D}{\mathrm{cm}}\right) \tag{A.22}$$

Putting everything together yields

$$\begin{aligned}
\left(\frac{\dot{N}_i}{\mathrm{s}^{-1}}\right) &= \frac{1}{6}\pi \left(\frac{\theta_s}{\mathrm{rad}}\right)^3 \left(\frac{D}{\mathrm{cm}}\right)^3 \left(\frac{N_0}{\mathrm{cm}^{-3}}\right)^2 \left(\frac{\beta - \beta_1}{\mathrm{cm}^3\,\mathrm{s}^{-1}}\right) \\
&= \frac{1}{6}\pi \left(\frac{\theta_s}{\mathrm{rad}}\right)^3 \times \left(3.086 \times 10^{18}\right)^3 \times \left(\frac{D}{\mathrm{pc}}\right)^3 \left(\frac{N_0}{\mathrm{cm}^{-3}}\right)^2 \left(\frac{\beta - \beta_1}{\mathrm{cm}^3\,\mathrm{s}^{-1}}\right) \\
&= 1.539 \times 10^{55} \left(\frac{\pi}{180 \times 3600}\right)^3 \left(\frac{\theta_s}{\mathrm{arcsec}}\right)^3 \left(\frac{D}{\mathrm{pc}}\right)^3 \left(\frac{N_0}{\mathrm{cm}^{-3}}\right)^2 \left(\frac{\beta - \beta_1}{\mathrm{cm}^3\,\mathrm{s}^{-1}}\right) \\
&= 1.754 \times 10^{39} \left(\frac{\theta_s}{\mathrm{arcsec}}\right)^3 \left(\frac{D}{\mathrm{pc}}\right)^3 \left(\frac{N_0}{\mathrm{cm}^{-3}}\right)^2 \left(\frac{\beta - \beta_1}{\mathrm{cm}^3\,\mathrm{s}^{-1}}\right) \\
&= 7.189 \times 10^{29} \left(\frac{\theta_s}{\mathrm{arcsec}}\right)^3 \left(\frac{D}{\mathrm{pc}}\right)^3 \left(\frac{N_0}{\mathrm{cm}^{-3}}\right)^2 \left(\frac{T_e}{\mathrm{K}}\right)^{-0.8}
\end{aligned} \tag{A.23}$$

This yields

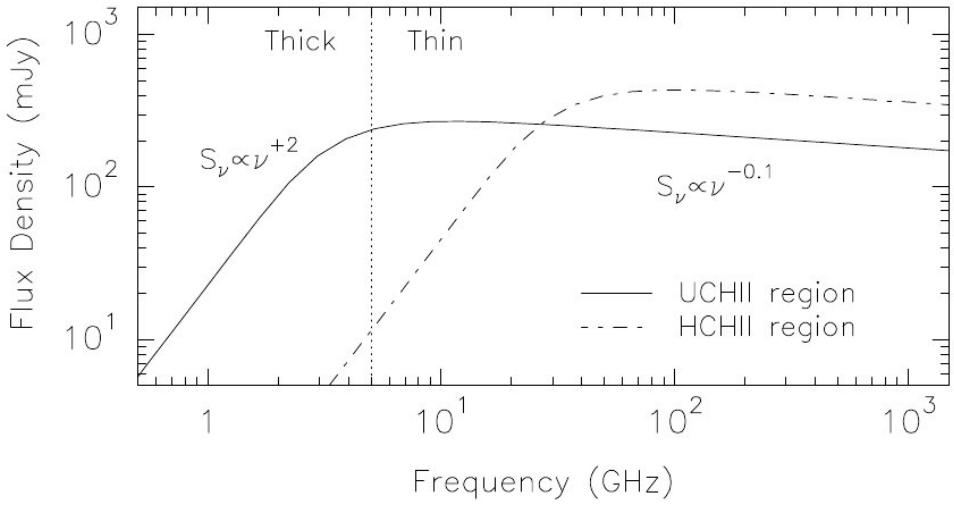

Figure A.2: spherical, homogenous isothermal HII region. Figure taken from Sánchez-Monge (2011).

$$\left(\frac{\dot{N}_i}{\mathrm{s}^{-1}}\right) = 4.771 \times 10^{42} \left(\frac{D}{\mathrm{pc}}\right)^2 \left(\frac{F_\nu}{\mathrm{Jy}}\right) \left(\frac{\nu}{\mathrm{GHz}}\right)^{0.1} \left(\frac{T_e}{\mathrm{K}}\right)^{-0.45} \tag{A.24}$$

B.1 The Central Molecular Zone

Many large-scale continuum surveys have been performed towards the CMZ. To provide a visual impression of the structure of the CMZ, I have obtained available archival data at various wavelengths. Table B.1 presents an overview of the data and their origin. Except for the Herschel SPIRE and PACS maps, I have obtained calibrated archival data. In the case of the Herschel data, I obtained the raw data and calibrated them myself. For most data sets, the coverage of the CMZ was split into several sub maps. I employed the publicly available MONTAGE software[1] to stack these individual maps together. Furthermore this task involved a lot of unit conversion. The calibrated data of different telescopes, even of different instruments aboard the same telescope, are provided in different units. For the radio, sub-mm, and far-infrared regime I decided to use Jy/beam. For each of these maps, the beam size is denoted by an orange circle in the bottom left corner of the map. Due to the large field-of-view and the high resolution of many of these maps, this circle is rather small. For the infrared, ultra-violet and X-ray regime, I decided to stick to the provided units, except for maps given in units of data number (DN), as was the case for the data obtained with the Infrared Array Camera (IRAC) instrument aboard of the Spitzer Space Telescope. I have converted them to units of magnitude according to the documentation.

In the order of operation from long wavelength to short wavelength, here are a few details on the telescopes, their instruments and the data obtained.[2].

[1] http://montage.ipac.caltech.edu/

[2] Please note: I do not claim this list, nor the collected telescope specific information to be complete. This served as an overview for myself during the study of the CMZ and Sgr B2 in particular.

VLA

The Karl G. Jansky Very Large Array (VLA) is an interferometer consisting of 27 antennas, each 25-meter in diameter, located about eighty kilometers west of Socorro, New Mexico. The VLA is operated by National Radio Astronomy Observatory (NRAO). Observations are performed in the centimeter wavelength regime (400 – 0.7 cm, 74 MHz – 50 GHz). The 20 cm map presented here was obtained under project number AL83 (PI: Harvey Liszt). Observations were performed in the compact, hybrid array configuration DnC, yielding a resolution of 30″. The archival data has been processed by Yusef-Zadeh et al. (2004). For more details about the data calibration and imaging, the reader is refered to Yusef-Zadeh et al. (2004).

CSO

The Caltech Submillimeter Observatory (CSO) is a 10.4 m diameter single-dish telescope located on Mauna Kea, Hawai'i. The Bolocam Galactic Plane Survey (BGPS) is a 1.1 mm continuum survey of the Galactic Plane. This survey employed the Bolocam on the CSO. I use the version 2.1 release of the BGPS which is described in detail in Ginsburg et al. (2013). More information as well as the data products can be found here: `http://irsa.ipac.caltech.edu/data/BOLOCAM_GPS/`

Operation of the CSO has been shut down as of September 18, 2016 and the telescope is in the process of being dismantled and removed from Mauna Kea.

APEX

The Atacama Pathfinder Experiment (APEX) is a 12 m diameter single dish telescope located at the Llano de Chajnantor Observatory in the Atacama desert in Chile. It is build and operated by Max Planck Institute for Radio Astronomy (MPIfR), Onsala Space Observatory (OSO), and European Southern Observatory (ESO). The telescope is a modified ALMA prototype antenna. ATLASGAL is an observing programme using the Large APEX Bolocam Camera (LABOCA), a multi-channel bolometer array for continuum observations at APEX, to map the Galactic Plane at 870 μm. More information about ATLASGAL as well as data products are available here: `http://www3.mpifr-bonn.mpg.de/div/atlasgal/`

JCMT

The James Clerk Maxwell Telescope (JCMT) is a 15 m single-dish telescope located close to the summit of Mauna Kea, Hawai'i, right next to the CSO. Operations started in 1987 as a joint collaboration of the United Kingdom, Canada, and the Netherlands. In 2015 the operation of the telescope was taken over by the East Asian Observatory. The JCMT is equipped with both, broadband continuum receivers and high-resolution spectral line receivers. One of these continuum receivers was Submillimetre Common-User Bolometer Array (SCUBA). This receiver was actively used between 1997 and 2003 to observe at 450 and 850 µm. More information can be found here `http://www.eaobservatory.org/jcmt`.

Herschel Space Observatory

The Herschel Space Observatory (hereafter: Herschel) is a European space observatory, constructed and operated by European Space Agency (ESA). It consisted of a 3.5 m sized telescope and operated between

2009 and 2013 in the sub-mm, far-infrared wavelength regime. The observatory carried three instruments: Heterodyne Instrument for the Far-Infrared (HIFI), SPIRE, and PACS. Hi-GAL is a large-scale survey aimed at mapping the entire Galactic plane at four wavelength. The survey employed SPIRE and PACS in parallel mode. More information can be found here http://sci.esa.int/herschel. Data products are available in the Herschel Science Archive (http://archives.esac.esa.int/hsa/whsa/)

MSX

The Midcourse Space Experiment (MSX) is a satellite managed by the Ballistic Missile Defense Organization. It was launched in 1996 and operated until 2008. The satellite carried a 33 cm telescope. Part of the mission was to map the Galactic plane. In addition it also covered areas missed by Infrared Astronomical Satellite (IRAS) and performed follow-up observations of regions that were particularly bright in the IRAS observations. More information is available here http://irsa.ipac.caltech.edu/data/MSX/mission.htm. MSX data products are available here http://irsa.ipac.caltech.edu/Missions/msx.html.

Spitzer Space Telescope

The Spitzer Space Telescope (hereafter: Spitzer) is an infrared space telescope launched in 2003 by National Aeronautics and Space Administration (NASA). IRAC and operating in the wavelength range between 3 and 180 µm. Spitzer carried three instruments: IRAC, Infrared Spectrograph (IRS), and Multiband Imaging Photometer for Spitzer (MIPS). More information on the space mission and its instruments can be found here: http://www.spitzer.caltech.edu/. Data products are publicly available: http://irsa.ipac.caltech.edu/Missions/spitzer.html.

2MASS

The Two Micron All Sky Survey (2MASS) is a ground-based all sky survey in three near infrared bands (1.25 µm - J-Band, 1.65 µm - H-Band, and 2.17 µm - K_S-Band). Observations were carried out between 1997 and 2001. The survey used two highly automated 1.3 m telescopes, one located in the U.S. to cover the Northern Hemisphere and the other in Chile to perform the same observations of the Southern Hemisphere. More information is available here http://www.ipac.caltech.edu/2mass/. Data products can be downloaded here http://irsa.ipac.caltech.edu/Missions/2mass.html.

Galex

The Galaxy Evolution Explorer (GALEX) is an Earth-orbiting space telescope. It operates in the ultraviolet wavelength regime and has a 50 cm sized primary mirror. The telescope operation time was between 2003 and 2012. More information on the mission can be found here http://www.galex.caltech.edu. The data is publicly available and can be downloaded via the following webpage http://galex.stsci.edu/GR6/.

XMM-Newton

The X-ray Multi-Mirror Mission (XMM-Newton) is an X-ray space observatory which was launched in 1999 by the ESA. The primary instrument aboard of the satellite are the three European Photon Imaging Cameras (EPIC). The total field of view of EPIC is 30″ and it operates in the range between 0.15 and 15 keV. Detailed information on the mission can be found here: https://www.cosmos.esa.int/web/xmm-newton

Table B.1: Overview of observational surveys towards the CMZ

Wavelength [μm]	Telescope	Instrument	Reference	Comment
2×10^5	VLA		Yusef-Zadeh et al. (2004)	
10^3	CSO	Bolocam	Ginsburg et al. (2013)	BGPS
870	APEX	LABOCA	Csengeri et al. (2016)	ATLASGAL
850	JCMT	SCUBA	Pierce-Price et al. (2000)	
500	Herschel	SPIRE	Molinari et al. (2010b)	Hi-GAL[a]
450	JCMT	SCUBA	Pierce-Price et al. (2000)	
350	Herschel	SPIRE	Molinari et al. (2010b)	Hi-GAL[a]
250	Herschel	SPIRE	Molinari et al. (2010b)	Hi-GAL[a]
160	Herschel	PACS	Molinari et al. (2010b)	Hi-GAL[a,b]
70	Herschel	PACS	Molinari et al. (2010b)	Hi-GAL[a]
21.3	MSX	SPIRIT III	Price et al. (2001)	
14.65	MSX	SPIRIT III	Price et al. (2001)	
12.13	MSX	SPIRIT III	Price et al. (2001)	
8.28	MSX	SPIRIT III	Price et al. (2001)	
8.0	Spitzer	IRAC	Stolovy et al. (2006)	GALCEN program
5.8	Spitzer	IRAC	Stolovy et al. (2006)	GALCEN program
4.5	Spitzer	IRAC	Stolovy et al. (2006)	GALCEN program
3.6	Spitzer	IRAC	Stolovy et al. (2006)	GALCEN program
2.17	Mt Hopkins & CTIO, Chile		Skrutskie et al. (2006)	2MASS
1.65	Mt Hopkins & CTIO, Chile		Skrutskie et al. (2006)	2MASS
1.25	Mt Hopkins & CTIO, Chile		Skrutskie et al. (2006)	2MASS
0.27 – 0.18	GALEX		GALEX team[c]	
$(6.3 – 2.5) \times 10^{-3}$	XMM-Newton	EPIC	Ponti et al. (2015)	
$(2.5 – 0.6) \times 10^{-3}$	XMM-Newton	EPIC	Ponti et al. (2015)	
$(0.6 – 0.3) \times 10^{-3}$	XMM-Newton	EPIC	Ponti et al. (2015)	
$(0.3 – 0.2) \times 10^{-3}$	XMM-Newton	EPIC	Ponti et al. (2015)	
$(0.2 – 0.1) \times 10^{-3}$	XMM-Newton	EPIC	Ponti et al. (2015)	

[a] Calibrated by myself.

[b] This map is saturated towards Sgr B2.

[c] http://www.galex.caltech.edu/index.html.

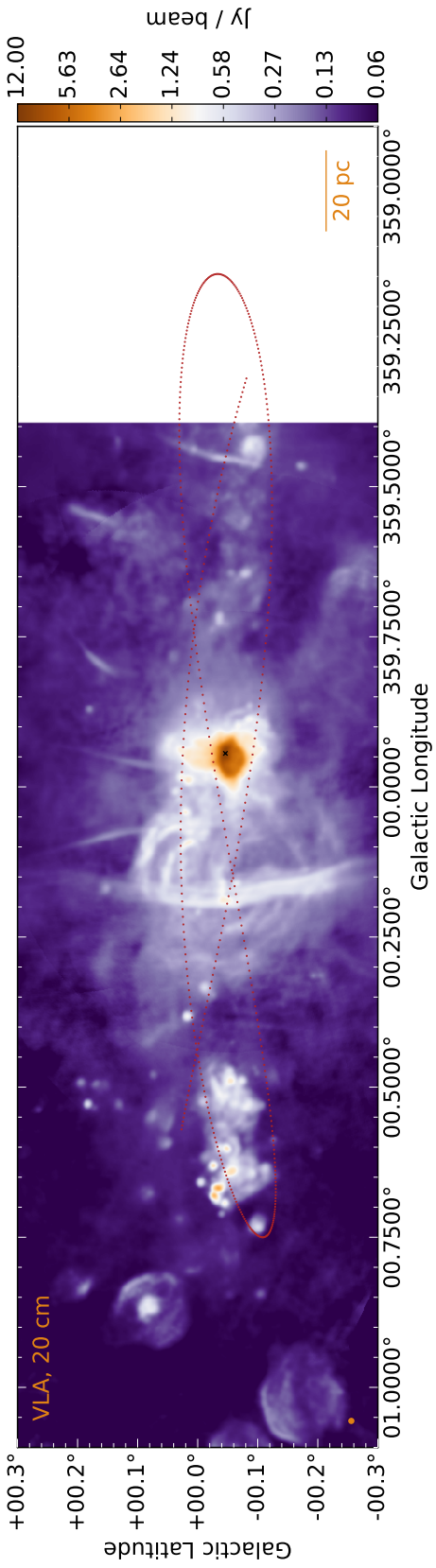
Jy / beam
12.00
5.63
2.64
1.24
0.58
0.27
0.13
0.06
20 pc
VLA, 20 cm
Galactic Latitude
+00.3°
+00.2°
+00.1°
+00.0°
-00.1°
-00.2°
-00.3°
Galactic Longitude
01.0000°
00.7500°
00.5000°
00.2500°
00.0000°
359.7500°
359.5000°
359.2500°
359.0000°

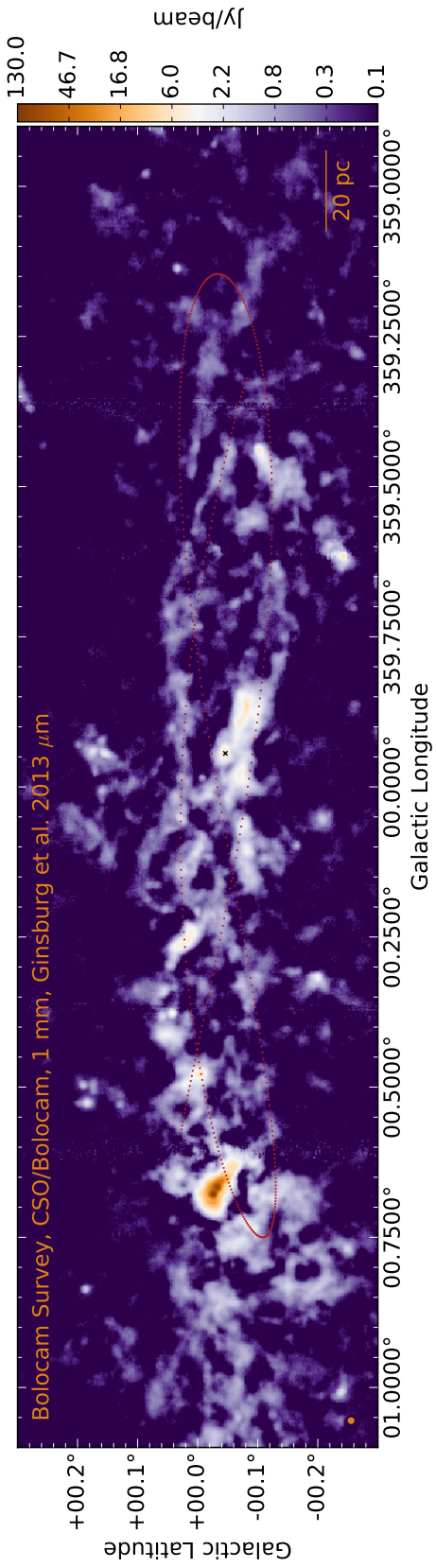
Jy/beam
130.0
46.7
16.8
6.0
2.2
0.8
0.3
0.1
20 pc
Bolocam Survey, CSO/Bolocam, 1 mm, Ginsburg et al. 2013 μm
Galactic Latitude
+00.2°
+00.1°
+00.0°
-00.1°
-00.2°
Galactic Longitude
01.0000°
00.7500°
00.5000°
00.2500°
00.0000°
359.7500°
359.5000°
359.2500°
359.0000°

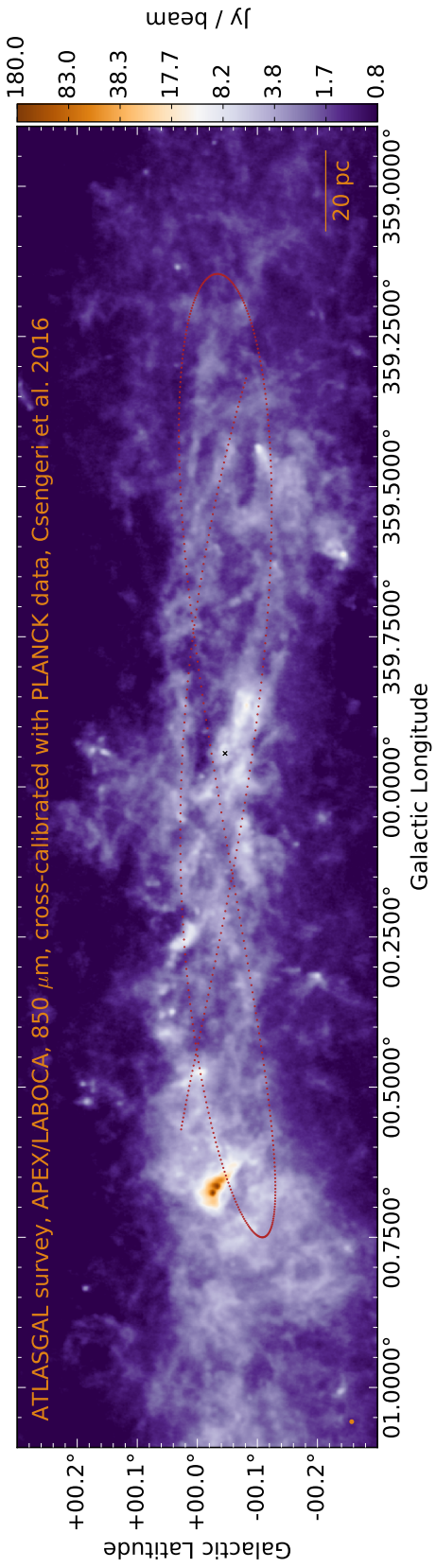
ATLASGAL survey, APEX/LABOCA, 850 μm, cross-calibrated with PLANCK data, Csengeri et al. 2016
20 pc
Jy / beam
180.0
83.0
38.3
17.7
8.2
3.8
1.7
0.8
Galactic Longitude
01.0000°
00.7500°
00.5000°
00.2500°
00.0000°
359.7500°
359.5000°
359.2500°
359.0000°
Galactic Latitude
+00.2°
+00.1°
+00.0°
-00.1°
-00.2°

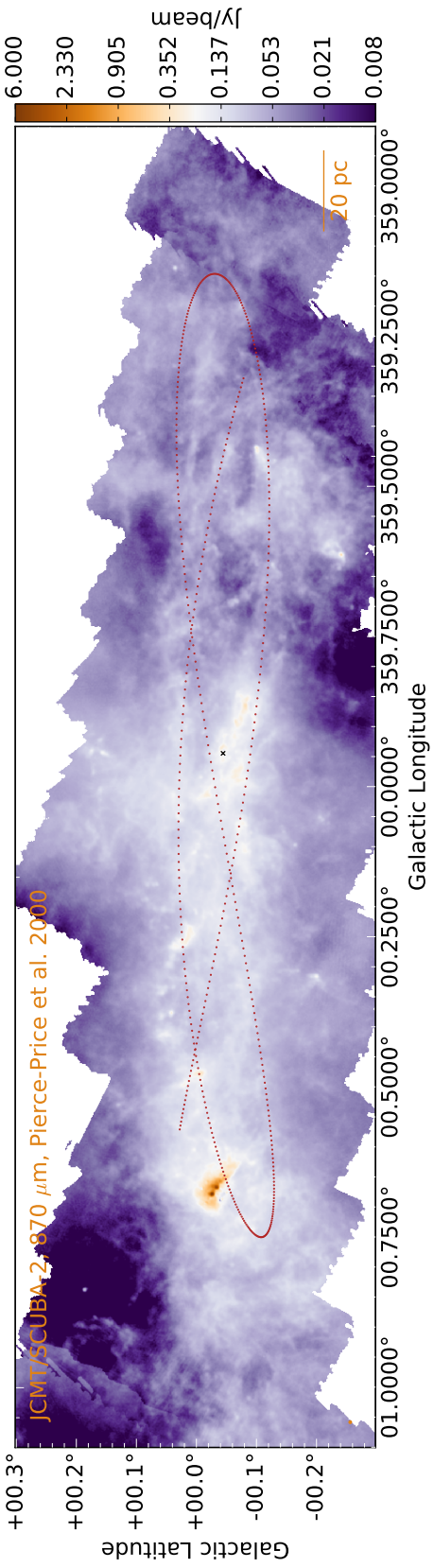
JCMT/SCUBA-2, 870 μm, Pierce-Price et al. 2000
20 pc
Jy/beam
6.000
2.330
0.905
0.352
0.137
0.053
0.021
0.008
Galactic Longitude
01.0000°
00.7500°
00.5000°
00.2500°
00.0000°
359.7500°
359.5000°
359.2500°
359.0000°
Galactic Latitude
+00.3°
+00.2°
+00.1°
+00.0°
-00.1°
-00.2°

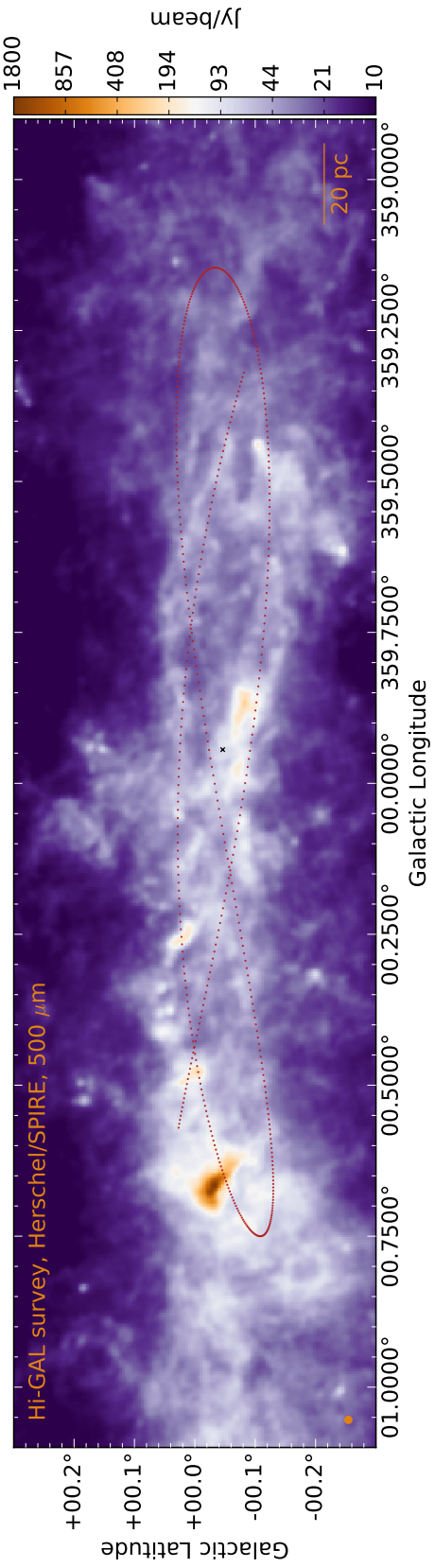
Hi-GAL survey, Herschel/SPIRE, 500 μm
20 pc
Jy/beam
1800
857
408
194
93
44
21
10
Galactic Longitude
Galactic Latitude
01.0000°
00.7500°
00.5000°
00.2500°
00.0000°
359.7500°
359.5000°
359.2500°
359.0000°
+00.2°
+00.1°
+00.0°
-00.1°
-00.2°

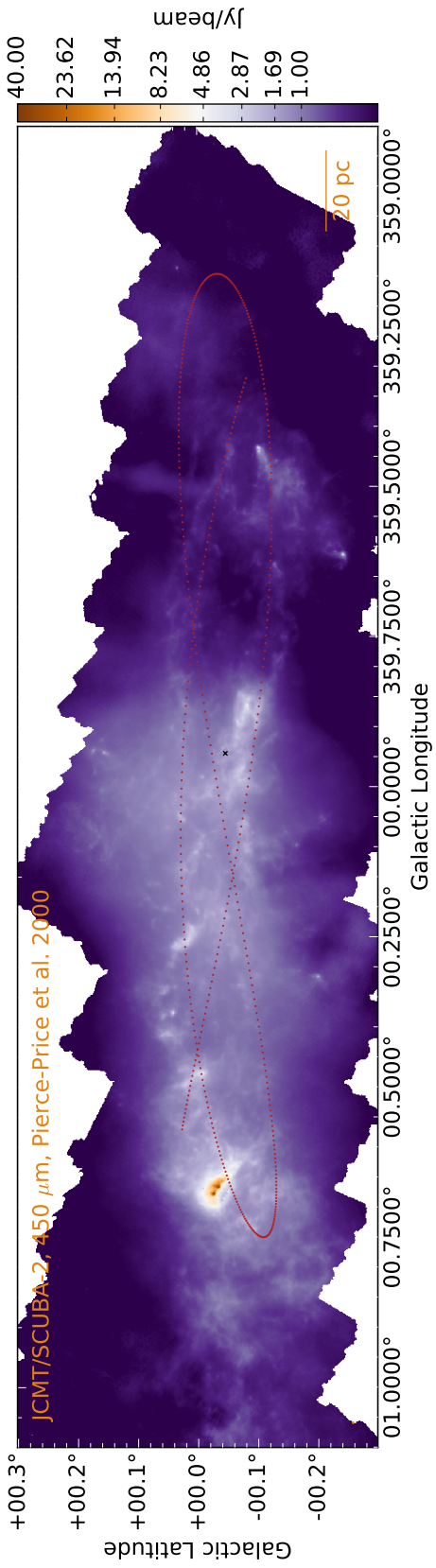
JCMT/SCUBA-2, 450 μm, Pierce-Price et al. 2000
20 pc
Jy/beam
40.00
23.62
13.94
8.23
4.86
2.87
1.69
1.00
Galactic Longitude
Galactic Latitude
01.0000°
00.7500°
00.5000°
00.2500°
00.0000°
359.7500°
359.5000°
359.2500°
359.0000°
+00.3°
+00.2°
+00.1°
+00.0°
-00.1°
-00.2°

Hi-GAL survey, Herschel/SPIRE, 350 μm
20 pc
Jy/beam
3300
1591
767
370
178
86
41
20
Galactic Longitude
01.0000°
00.7500°
00.5000°
00.2500°
00.0000°
359.7500°
359.5000°
359.2500°
359.0000°
Galactic Latitude
+00.2°
+00.1°
+00.0°
-00.1°
-00.2°

Hi-GAL survey, Herschel/SPIRE, 250 μm
20 pc
Jy/beam
4000
1876
880
413
194
91
43
20
Galactic Longitude
01.0000°
00.7500°
00.5000°
00.2500°
00.0000°
359.7500°
359.5000°
359.2500°
359.0000°
Galactic Latitude
+00.2°
+00.1°
+00.0°
-00.1°
-00.2°

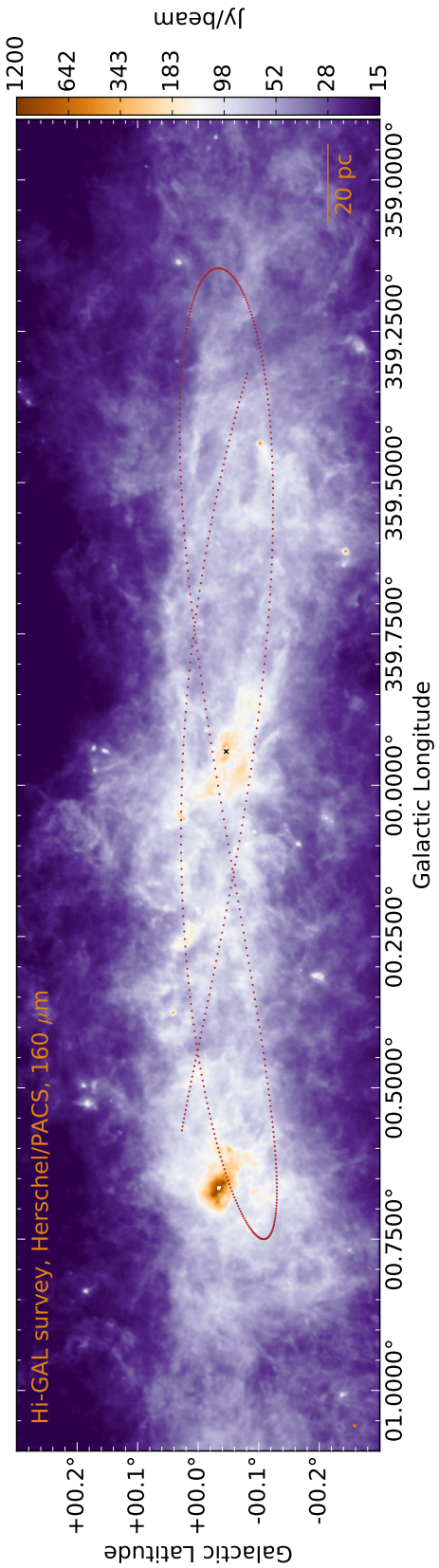
Jy/beam
1200
642
343
183
98
52
28
15
Hi-GAL survey, Herschel/PACS, 160 μm
20 pc
Galactic Latitude
+00.2°
+00.1°
+00.0°
-00.1°
-00.2°
Galactic Longitude
01.0000°
00.7500°
00.5000°
00.2500°
00.0000°
359.7500°
359.5000°
359.2500°
359.0000°

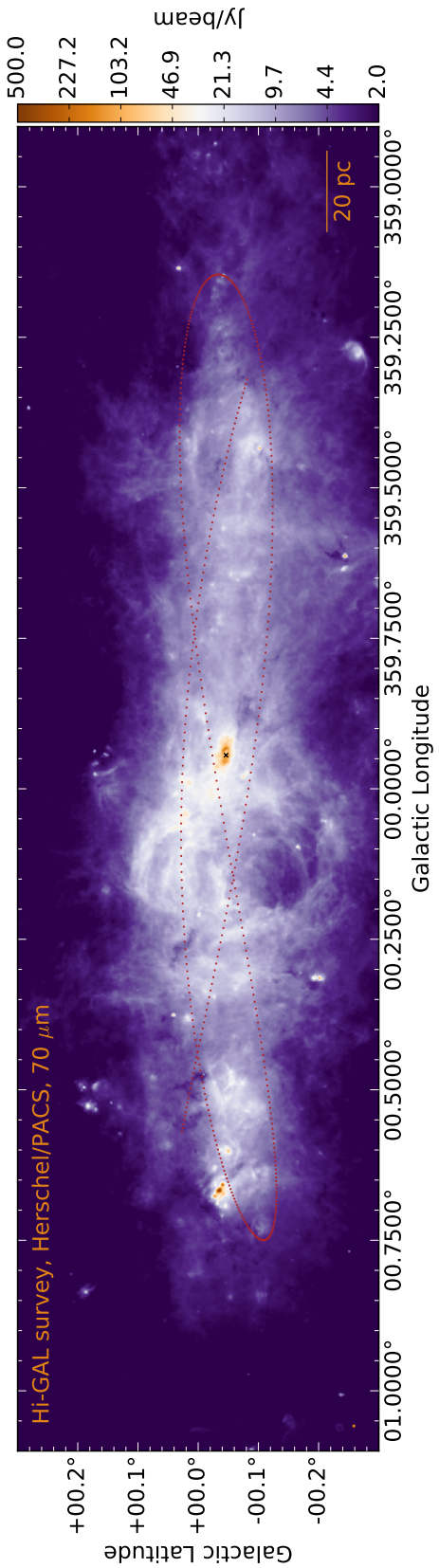
Jy/beam
500.0
227.2
103.2
46.9
21.3
9.7
4.4
2.0
Hi-GAL survey, Herschel/PACS, 70 μm
20 pc
Galactic Latitude
+00.2°
+00.1°
+00.0°
-00.1°
-00.2°
Galactic Longitude
01.0000°
00.7500°
00.5000°
00.2500°
00.0000°
359.7500°
359.5000°
359.2500°
359.0000°

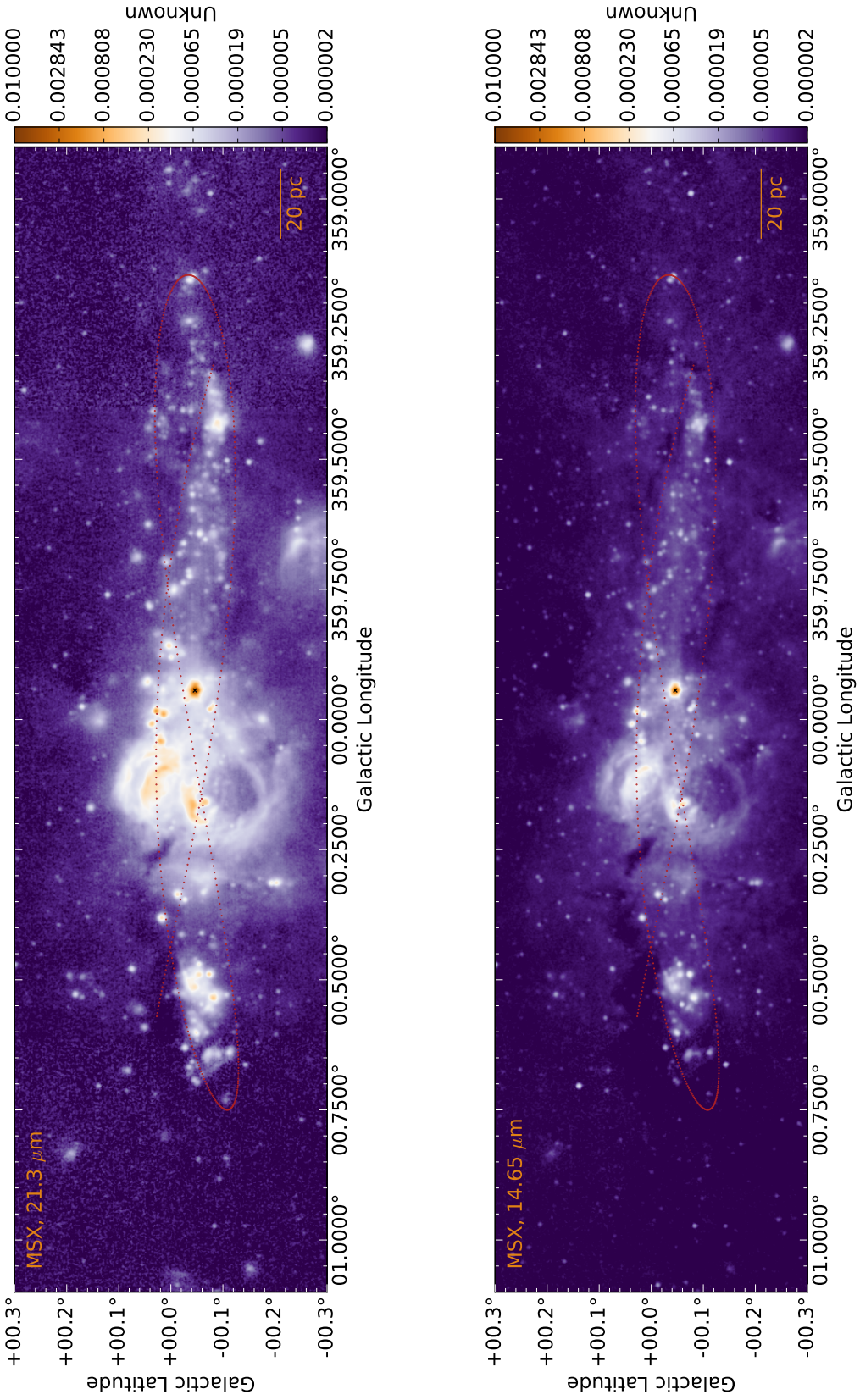
MSX, 21.3 μm
MSX, 14.65 μm
20 pc
Unknown
0.010000
0.002843
0.000808
0.000230
0.000065
0.000019
0.000005
0.000002
Galactic Longitude
Galactic Latitude
01.0000°
00.7500°
00.5000°
00.2500°
00.0000°
359.7500°
359.5000°
359.2500°
359.0000°
+00.3°
+00.2°
+00.1°
+00.0°
-00.1°
-00.2°
-00.3°

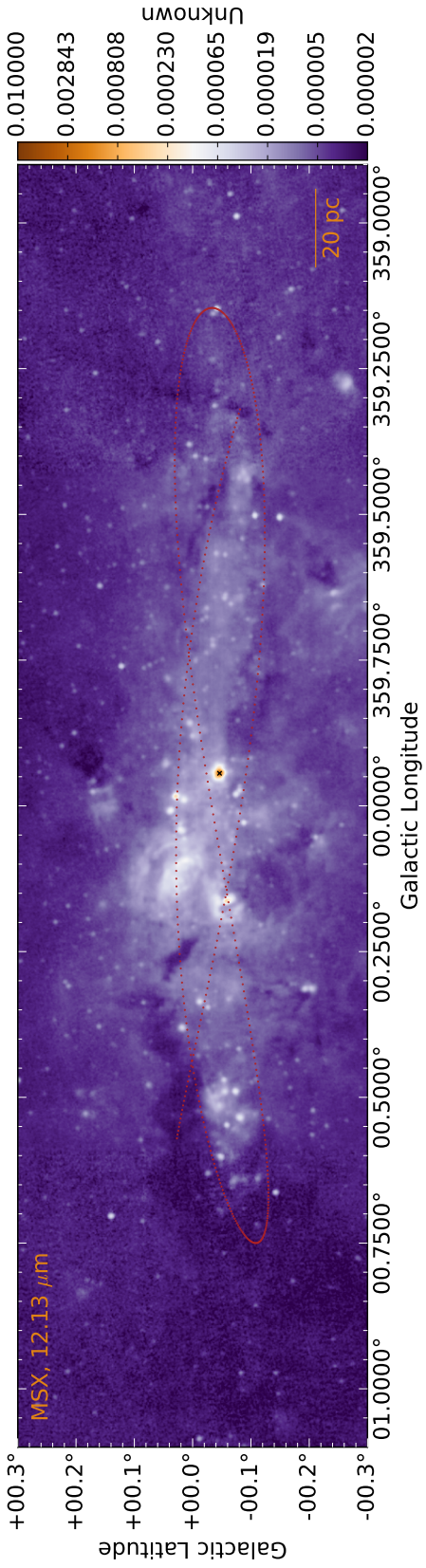
Unknown
0.010000
0.002843
0.000808
0.000230
0.000065
0.000019
0.000005
0.000002
20 pc
MSX, 12.13 μm
Galactic Latitude
+00.3°
+00.2°
+00.1°
+00.0°
-00.1°
-00.2°
-00.3°
Galactic Longitude
01.0000°
00.7500°
00.5000°
00.2500°
00.0000°
359.7500°
359.5000°
359.2500°
359.0000°

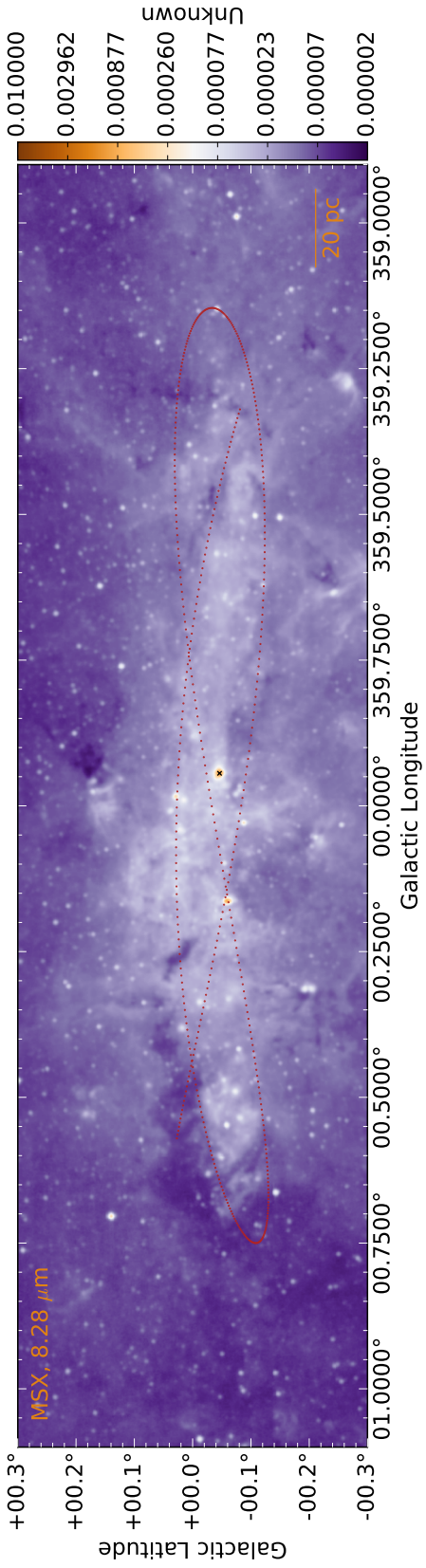
Unknown
0.010000
0.002962
0.000877
0.000260
0.000077
0.000023
0.000007
0.000002
20 pc
MSX, 8.28 μm
Galactic Latitude
+00.3°
+00.2°
+00.1°
+00.0°
-00.1°
-00.2°
-00.3°
Galactic Longitude
01.0000°
00.7500°
00.5000°
00.2500°
00.0000°
359.7500°
359.5000°
359.2500°
359.0000°

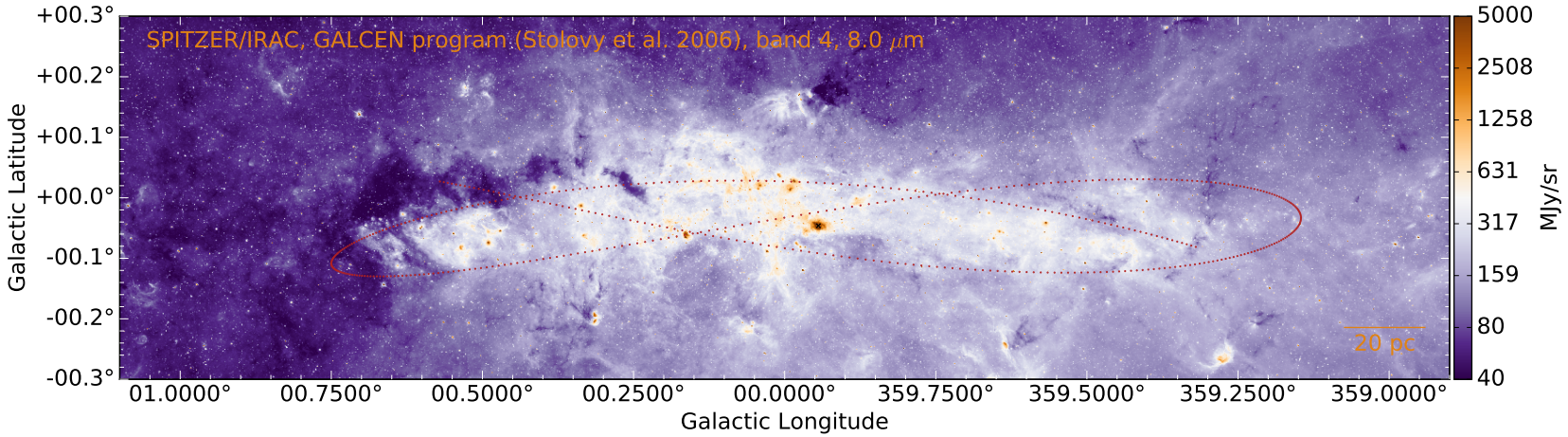
SPITZER/IRAC, GALCEN program (Stolovy et al. 2006), band 4, 8.0 μm
20 pc
Galactic Latitude
+00.3°
+00.2°
+00.1°
+00.0°
-00.1°
-00.2°
-00.3°
Galactic Longitude
01.0000°
00.7500°
00.5000°
00.2500°
00.0000°
359.7500°
359.5000°
359.2500°
359.0000°
5000
2508
1258
631
317
159
80
40
MJy/sr

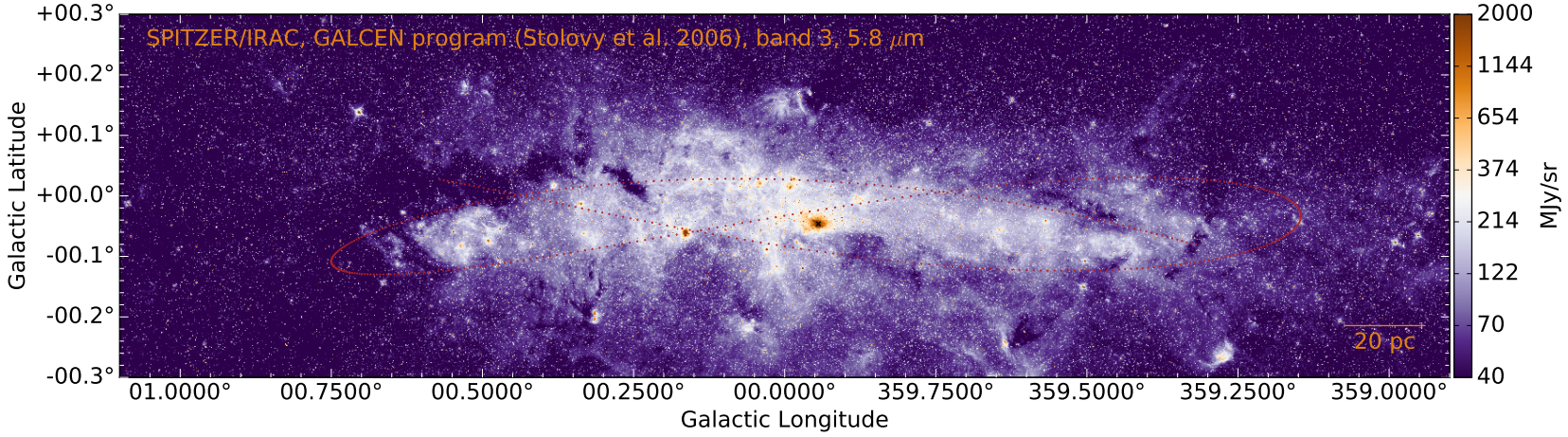
SPITZER/IRAC, GALCEN program (Stolovy et al. 2006), band 3, 5.8 μm
20 pc
Galactic Latitude
+00.3°
+00.2°
+00.1°
+00.0°
-00.1°
-00.2°
-00.3°
Galactic Longitude
01.0000°
00.7500°
00.5000°
00.2500°
00.0000°
359.7500°
359.5000°
359.2500°
359.0000°
2000
1144
654
374
214
122
70
40
MJy/sr

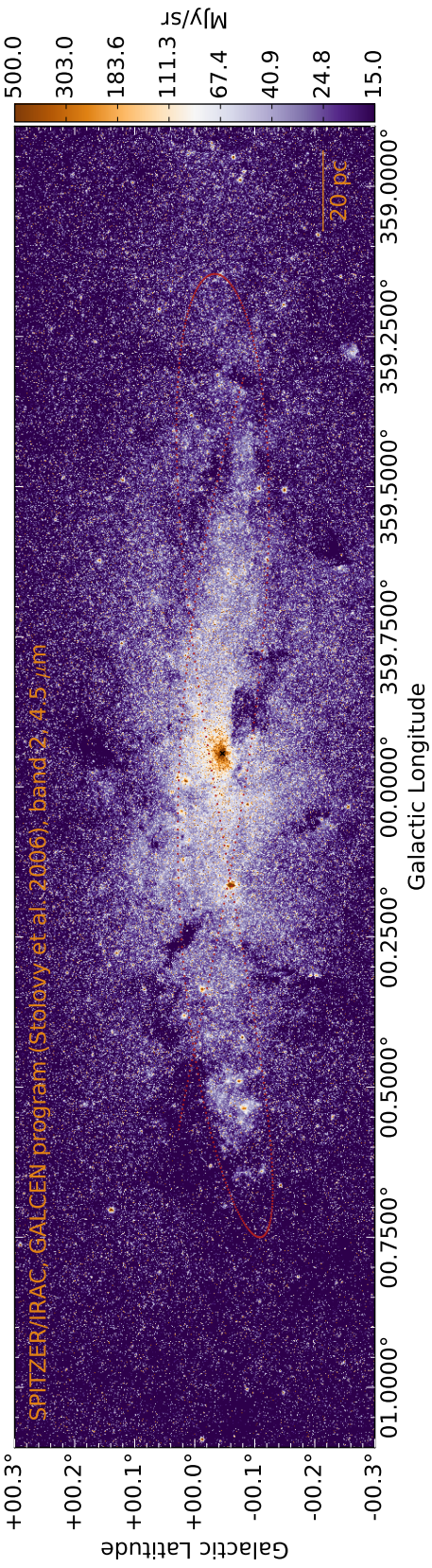
MJy/sr
500.0
303.0
183.6
111.3
67.4
40.9
24.8
15.0
SPITZER/IRAC, GALCEN program (Stolovy et al. 2006), band 2, 4.5 μm
20 pc
Galactic Latitude
+00.3°
+00.2°
+00.1°
+00.0°
-00.1°
-00.2°
-00.3°
Galactic Longitude
01.0000°
00.7500°
00.5000°
00.2500°
00.0000°
359.7500°
359.5000°
359.2500°
359.0000°

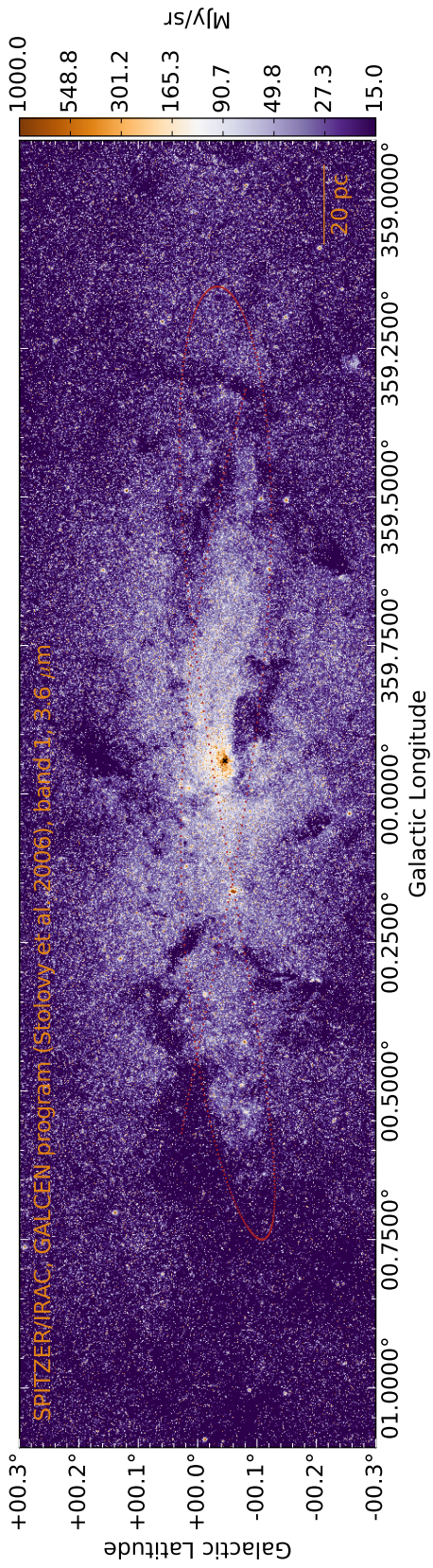
MJy/sr
1000.0
548.8
301.2
165.3
90.7
49.8
27.3
15.0
SPITZER/IRAC, GALCEN program (Stolovy et al. 2006), band 1, 3.6 μm
20 pc
Galactic Latitude
+00.3°
+00.2°
+00.1°
+00.0°
-00.1°
-00.2°
-00.3°
Galactic Longitude
01.0000°
00.7500°
00.5000°
00.2500°
00.0000°
359.7500°
359.5000°
359.2500°
359.0000°

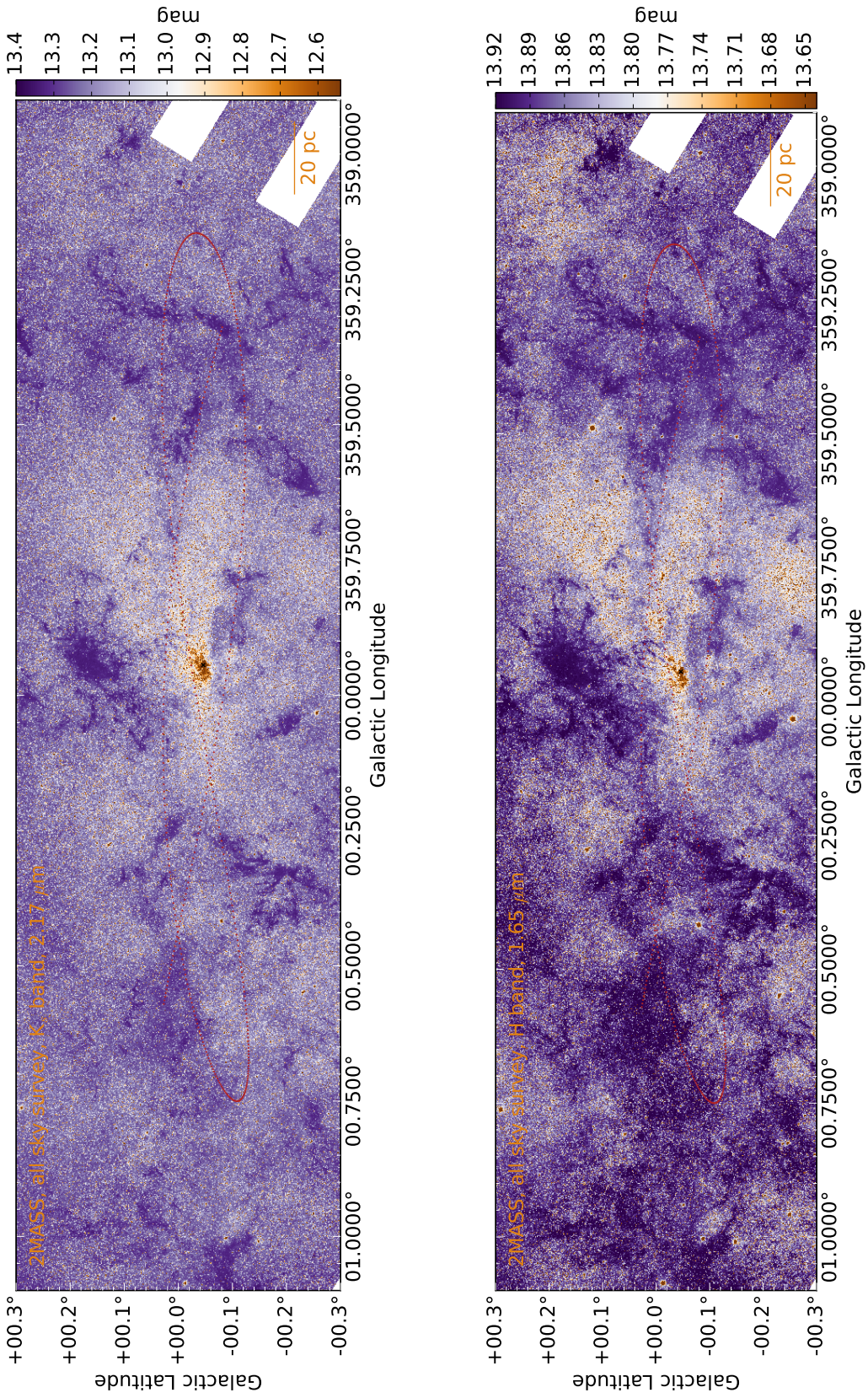
mag
13.4
13.3
13.2
13.1
13.0
12.9
12.8
12.7
12.6
20 pc
2MASS, all sky survey, K_band, 2.17 μm
Galactic Latitude
+00.3°
+00.2°
+00.1°
+00.0°
-00.1°
-00.2°
-00.3°
Galactic Longitude
01.0000°
00.7500°
00.5000°
00.2500°
00.0000°
359.7500°
359.5000°
359.2500°
359.0000°
mag
13.92
13.89
13.86
13.83
13.80
13.77
13.74
13.71
13.68
13.65
20 pc
2MASS, all sky survey, H band, 1.65 μm
Galactic Latitude
+00.3°
+00.2°
+00.1°
+00.0°
-00.1°
-00.2°
-00.3°
Galactic Longitude
01.0000°
00.7500°
00.5000°
00.2500°
00.0000°
359.7500°
359.5000°
359.2500°
359.0000°

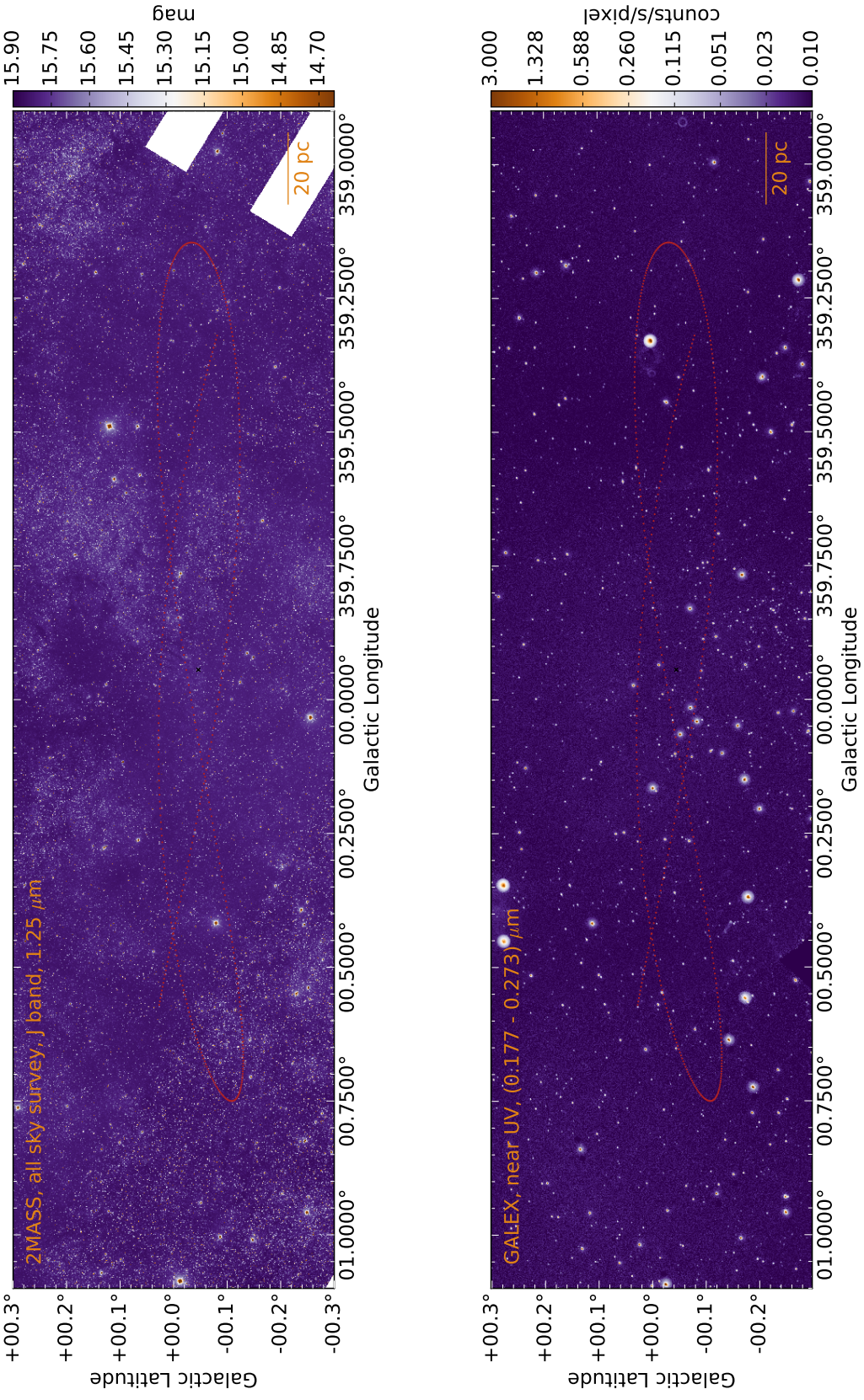
mag
15.90
15.75
15.60
15.45
15.30
15.15
15.00
14.85
14.70
2MASS, all sky survey, J band, 1.25 μm
20 pc
Galactic Latitude
+00.3°
+00.2°
+00.1°
+00.0°
-00.1°
-00.2°
-00.3°
Galactic Longitude
01.0000°
00.7500°
00.5000°
00.2500°
00.0000°
359.7500°
359.5000°
359.2500°
359.0000°
counts/s/pixel
3.000
1.328
0.588
0.260
0.115
0.051
0.023
0.010
GALEX, near UV, (0.177 - 0.273) μm
20 pc
Galactic Latitude
+00.3°
+00.2°
+00.1°
+00.0°
-00.1°
-00.2°
Galactic Longitude
01.0000°
00.7500°
00.5000°
00.2500°
00.0000°
359.7500°
359.5000°
359.2500°
359.0000°

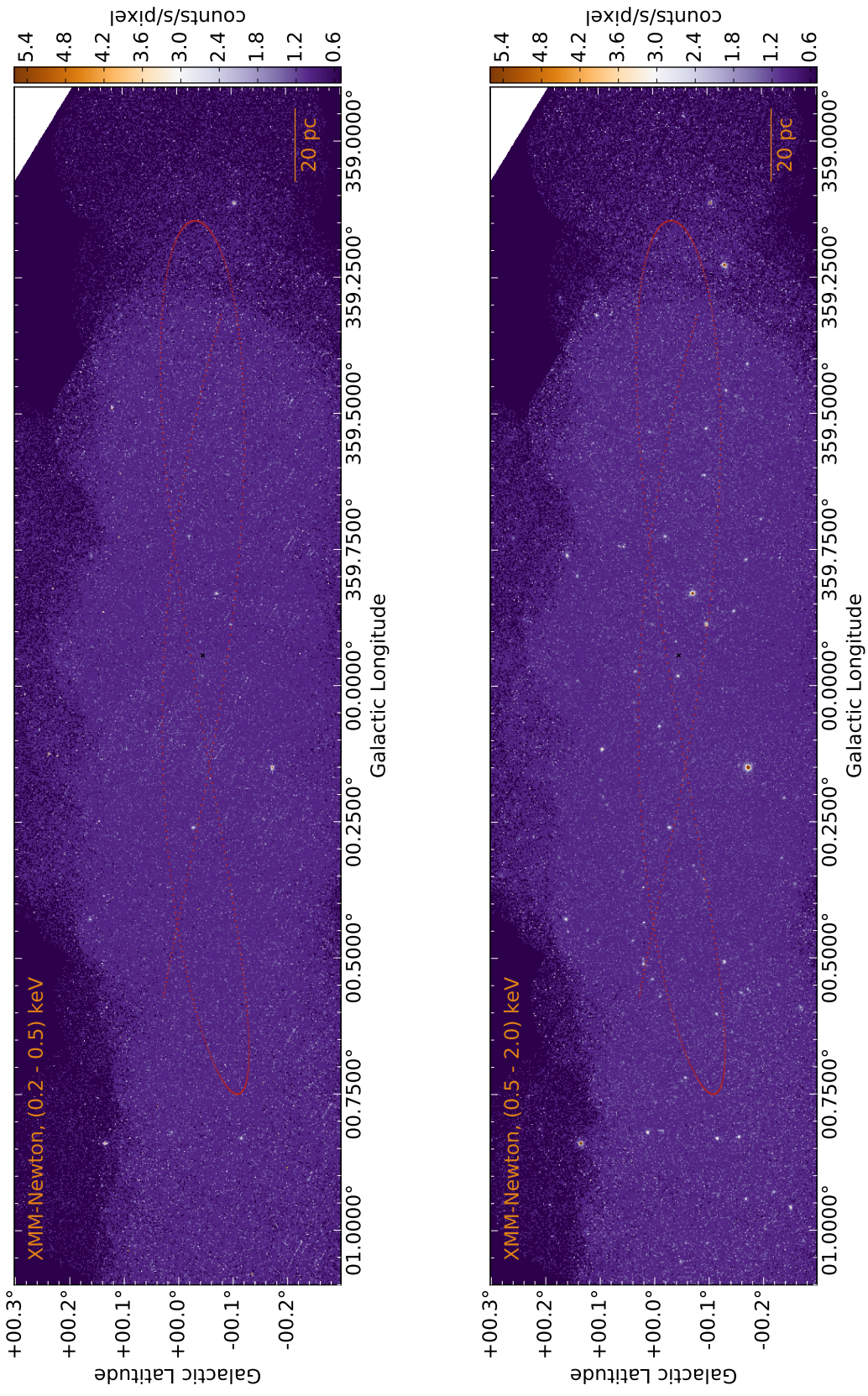
XMM-Newton, (0.2 - 0.5) keV
XMM-Newton, (0.5 - 2.0) keV
20 pc
counts/s/pixel
5.4
4.8
4.2
3.6
3.0
2.4
1.8
1.2
0.6
Galactic Longitude
01.0000°
00.7500°
00.5000°
00.2500°
00.0000°
359.7500°
359.5000°
359.2500°
359.0000°
Galactic Latitude
+00.3°
+00.2°
+00.1°
+00.0°
-00.1°
-00.2°

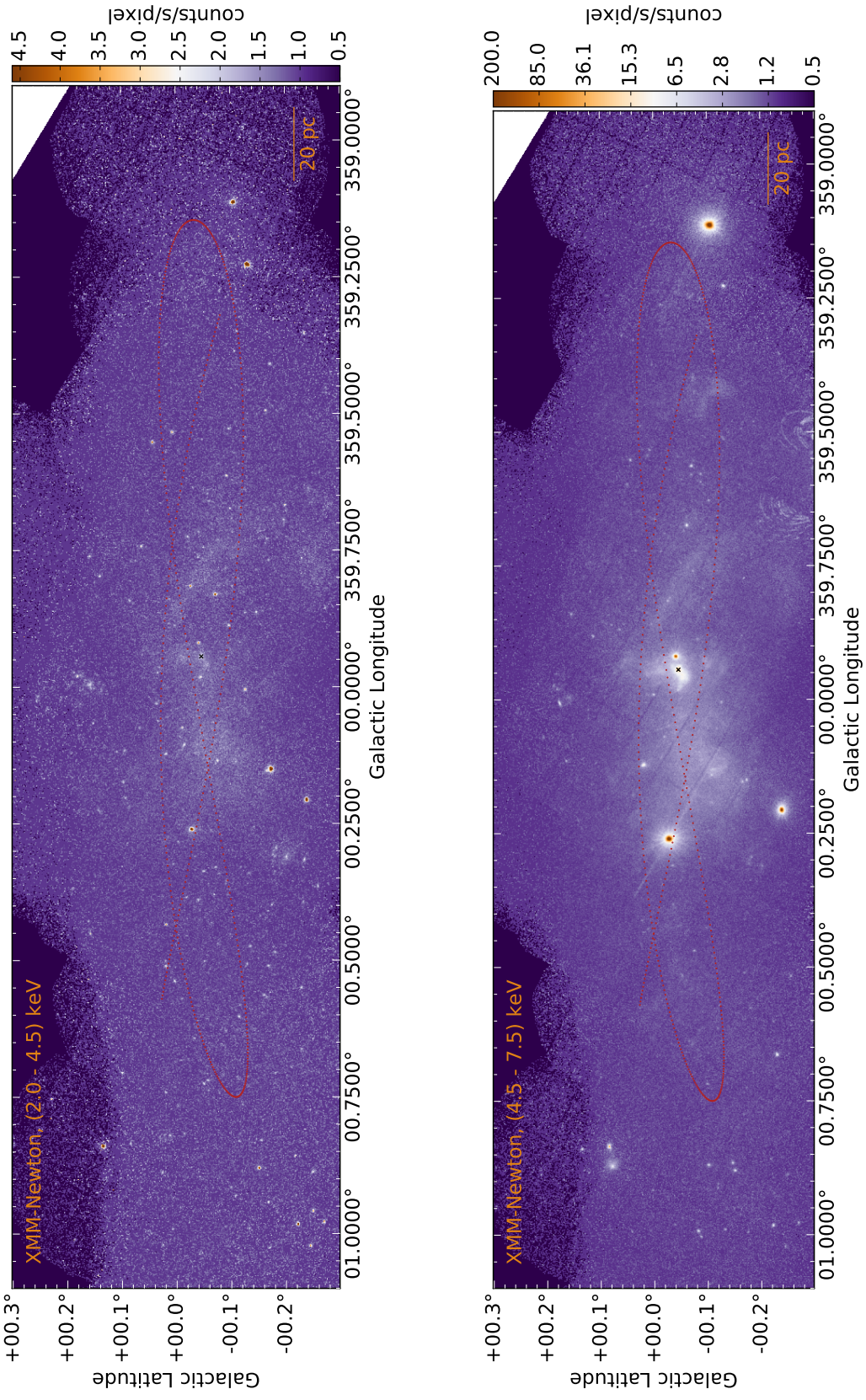
counts/s/pixel
4.5
4.0
3.5
3.0
2.5
2.0
1.5
1.0
0.5
XMM-Newton, (2.0 - 4.5) keV
20 pc
Galactic Latitude
+00.3°
+00.2°
+00.1°
+00.0°
-00.1°
-00.2°
Galactic Longitude
01.0000°
00.7500°
00.5000°
00.2500°
00.0000°
359.7500°
359.5000°
359.2500°
359.0000°
counts/s/pixel
200.0
85.0
36.1
15.3
6.5
2.8
1.2
0.5
XMM-Newton, (4.5 - 7.5) keV
20 pc
Galactic Latitude
+00.3°
+00.2°
+00.1°
+00.0°
-00.1°
-00.2°
Galactic Longitude
01.0000°
00.7500°
00.5000°
00.2500°
00.0000°
359.7500°
359.5000°
359.2500°
359.0000°

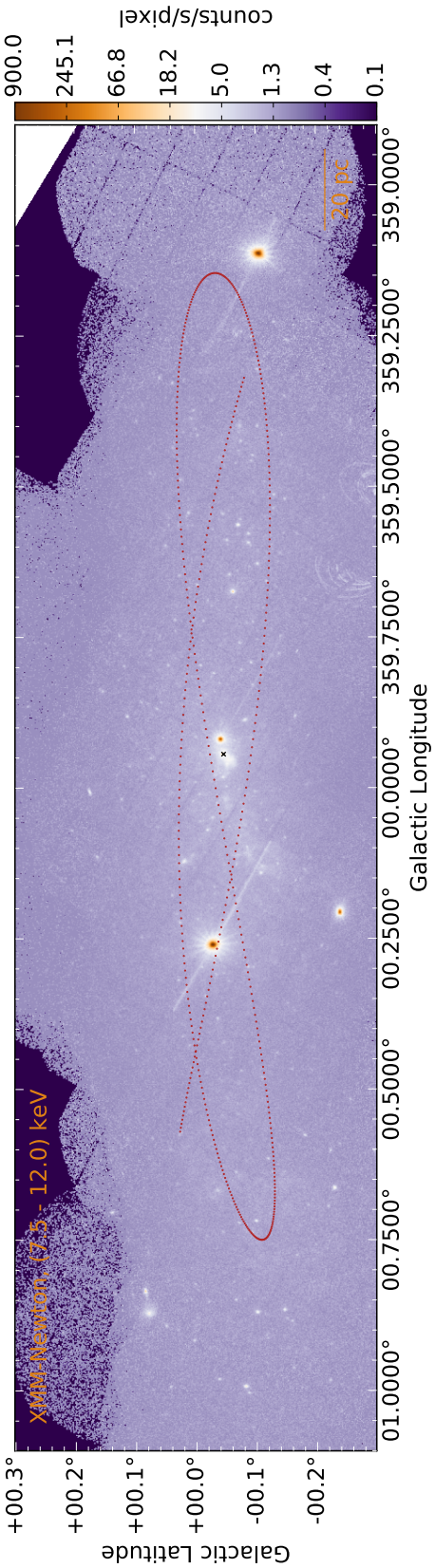
counts/s/pixel
900.0
245.1
66.8
18.2
5.0
1.3
0.4
0.1
20 pc
XMM-Newton (2.5 - 12.0) keV
Galactic Latitude
+00.3°
+00.2°
+00.1°
+00.0°
-00.1°
-00.2°
Galactic Longitude
01.0000°
00.7500°
00.5000°
00.2500°
00.0000°
359.7500°
359.5000°
359.2500°
359.0000°

B.2 Sagittarius B2

A common feature of the maps covering the CMZ in the radio and sub-mm regime is the very bright intensity of the Sgr B2 region. I am here presenting zoom-in maps toward the Sgr B2 region. This overview includes the data specified in Appendix B.1.

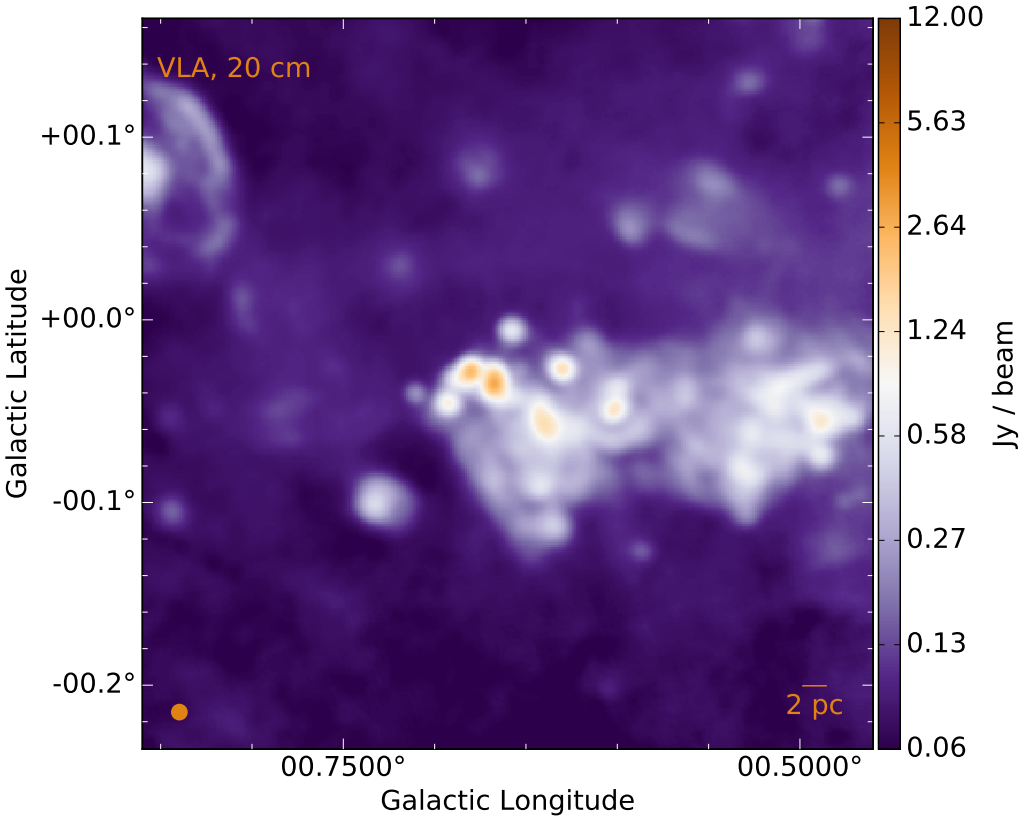
VLA, 20 cm
+00.1°
+00.0°
-00.1°
-00.2°
Galactic Latitude
00.7500°
00.5000°
Galactic Longitude
2 pc
12.00
5.63
2.64
1.24
0.58
0.27
0.13
0.06
Jy / beam

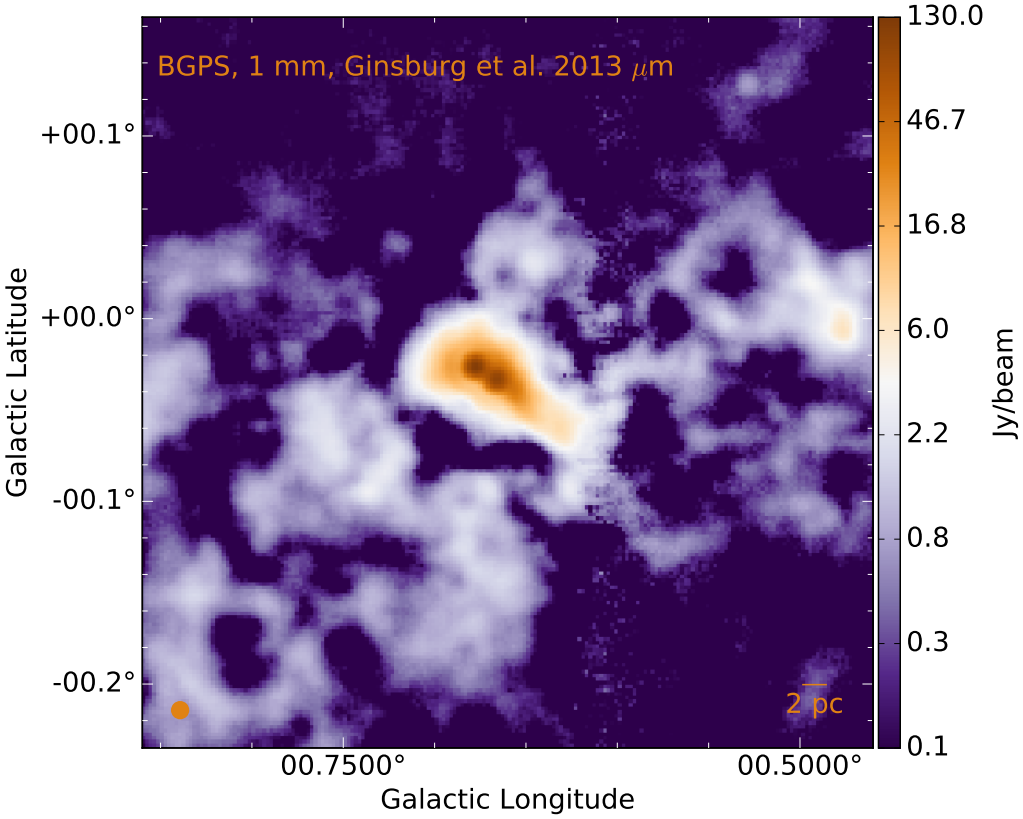
BGPS, 1 mm, Ginsburg et al. 2013 μm
+00.1°
+00.0°
-00.1°
-00.2°
Galactic Latitude
00.7500°
00.5000°
Galactic Longitude
2 pc
130.0
46.7
16.8
6.0
2.2
0.8
0.3
0.1
Jy/beam

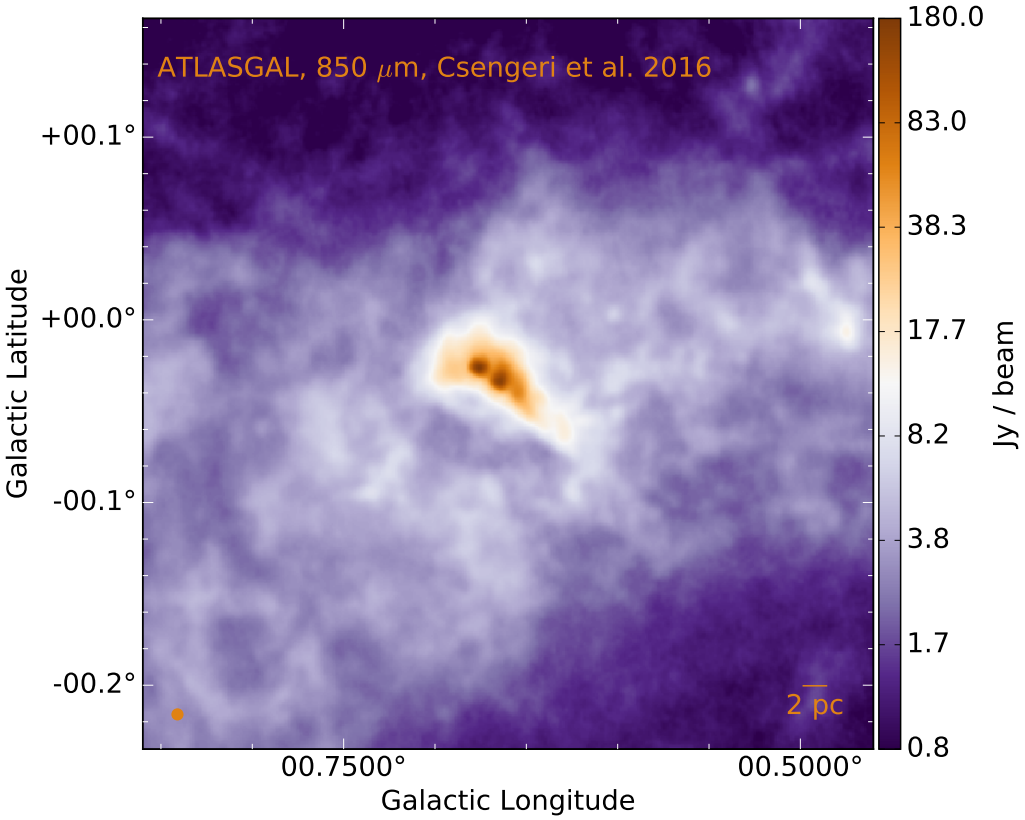
ATLASGAL, 850 μm, Csengeri et al. 2016
+00.1°
+00.0°
-00.1°
-00.2°
Galactic Latitude
00.7500°
00.5000°
Galactic Longitude
2 pc
180.0
83.0
38.3
17.7
8.2
3.8
1.7
0.8
Jy / beam

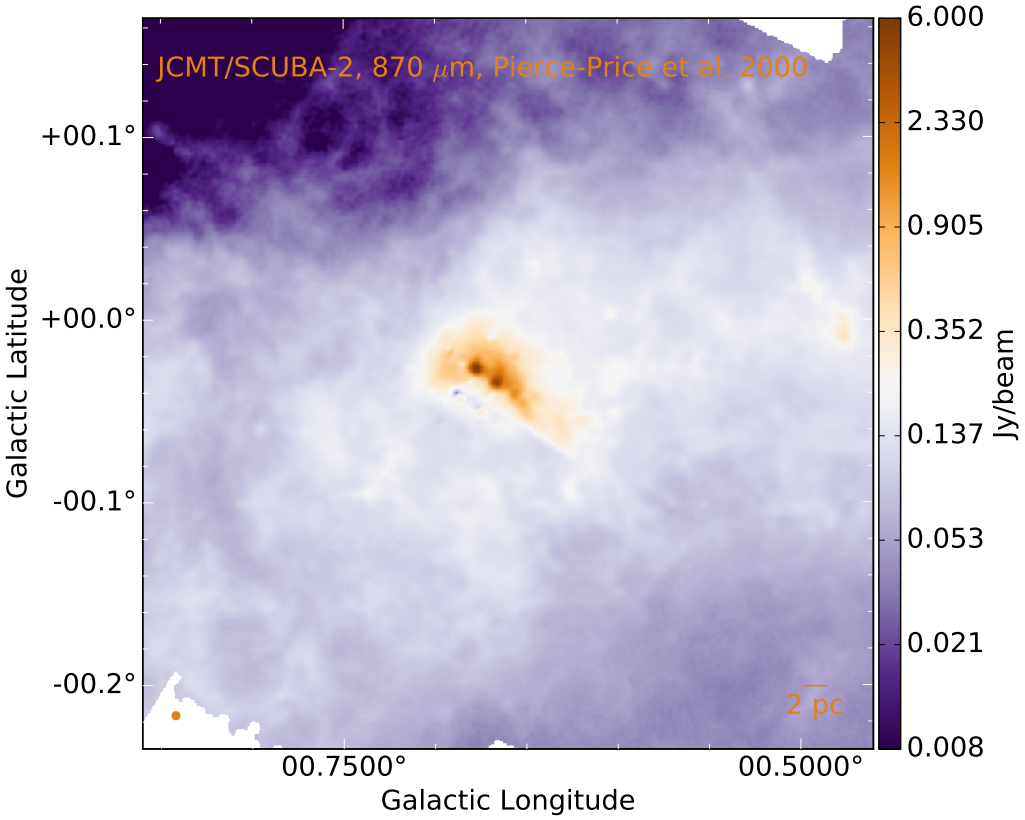
JCMT/SCUBA-2, 870 μm, Pierce-Price et al. 2000
+00.1°
+00.0°
-00.1°
-00.2°
Galactic Latitude
00.7500°
00.5000°
Galactic Longitude
2 pc
6.000
2.330
0.905
0.352
0.137
0.053
0.021
0.008
Jy/beam

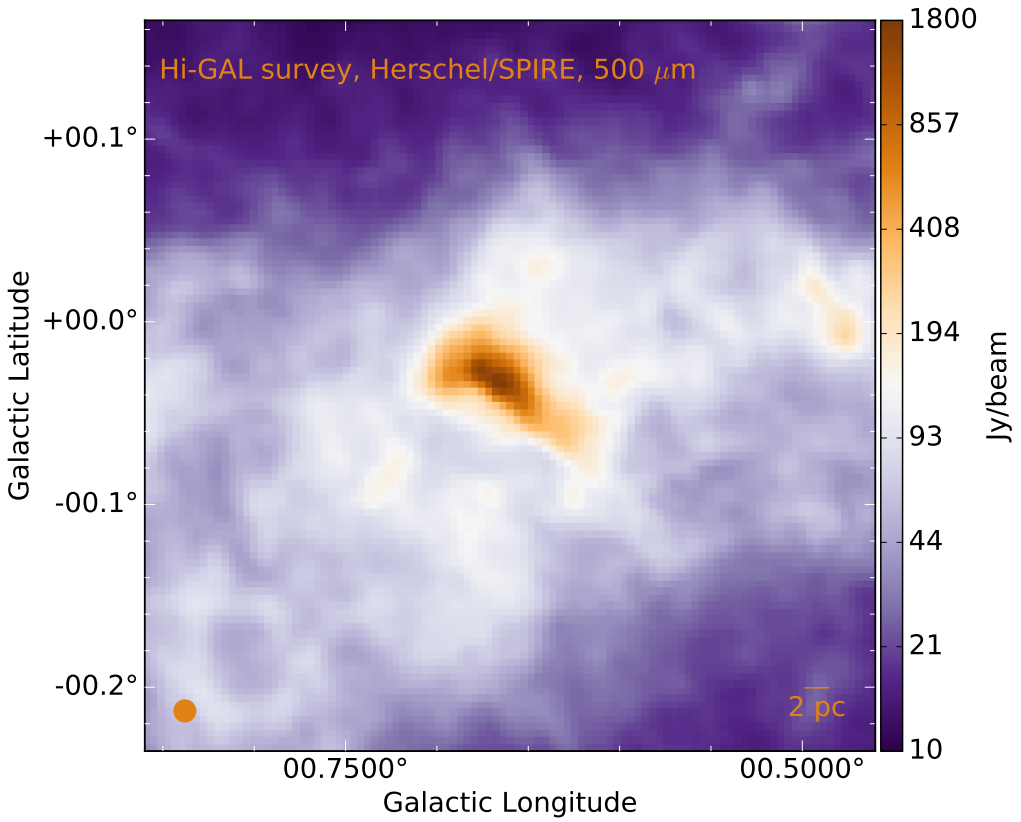
Hi-GAL survey, Herschel/SPIRE, 500 μm
+00.1°
+00.0°
-00.1°
-00.2°
Galactic Latitude
00.7500°
00.5000°
Galactic Longitude
2 pc
1800
857
408
194
93
44
21
10
Jy/beam

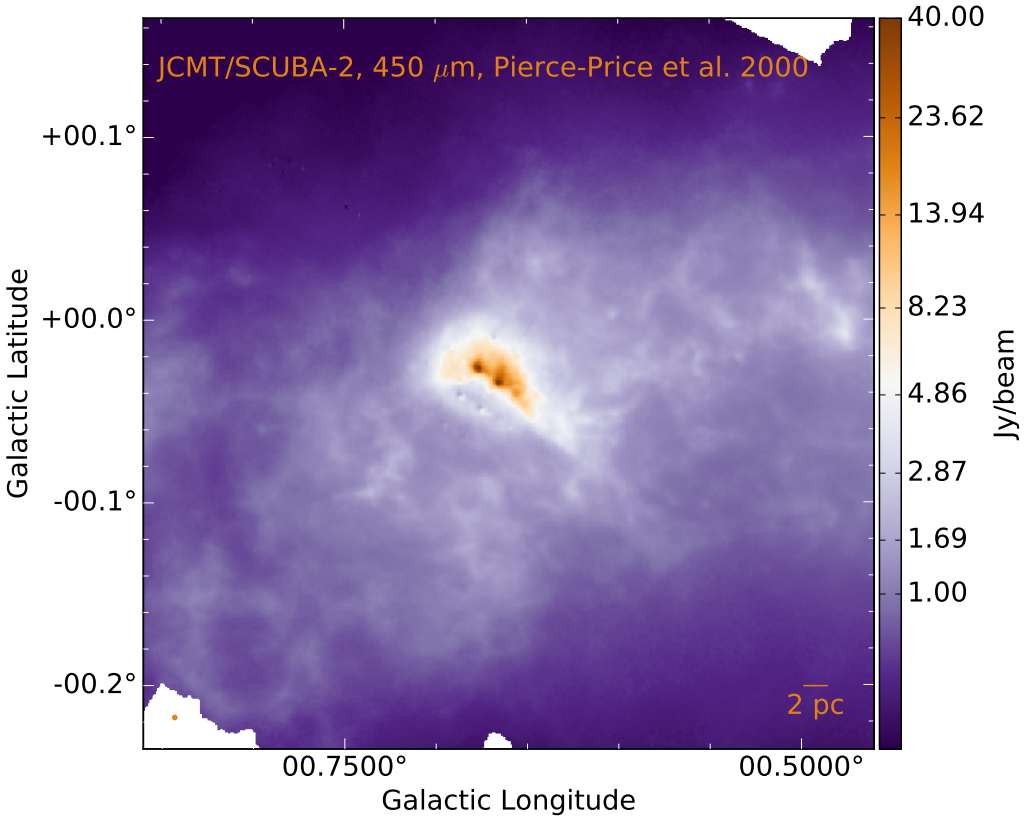
JCMT/SCUBA-2, 450 μm, Pierce-Price et al. 2000
+00.1°
+00.0°
-00.1°
-00.2°
Galactic Latitude
00.7500°
00.5000°
Galactic Longitude
2 pc
40.00
23.62
13.94
8.23
4.86
2.87
1.69
1.00
Jy/beam

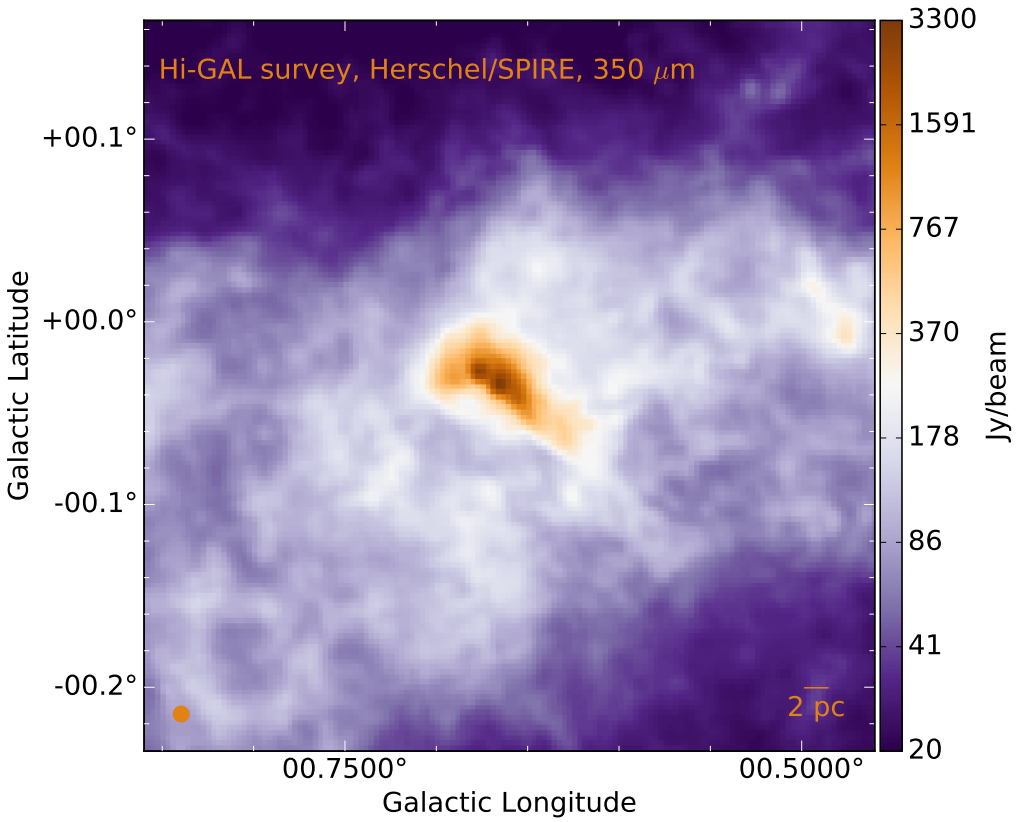
Hi-GAL survey, Herschel/SPIRE, 350 μm
+00.1°
+00.0°
-00.1°
-00.2°
Galactic Latitude
2 pc
00.7500°
00.5000°
Galactic Longitude
3300
1591
767
370
178
86
41
20
Jy/beam

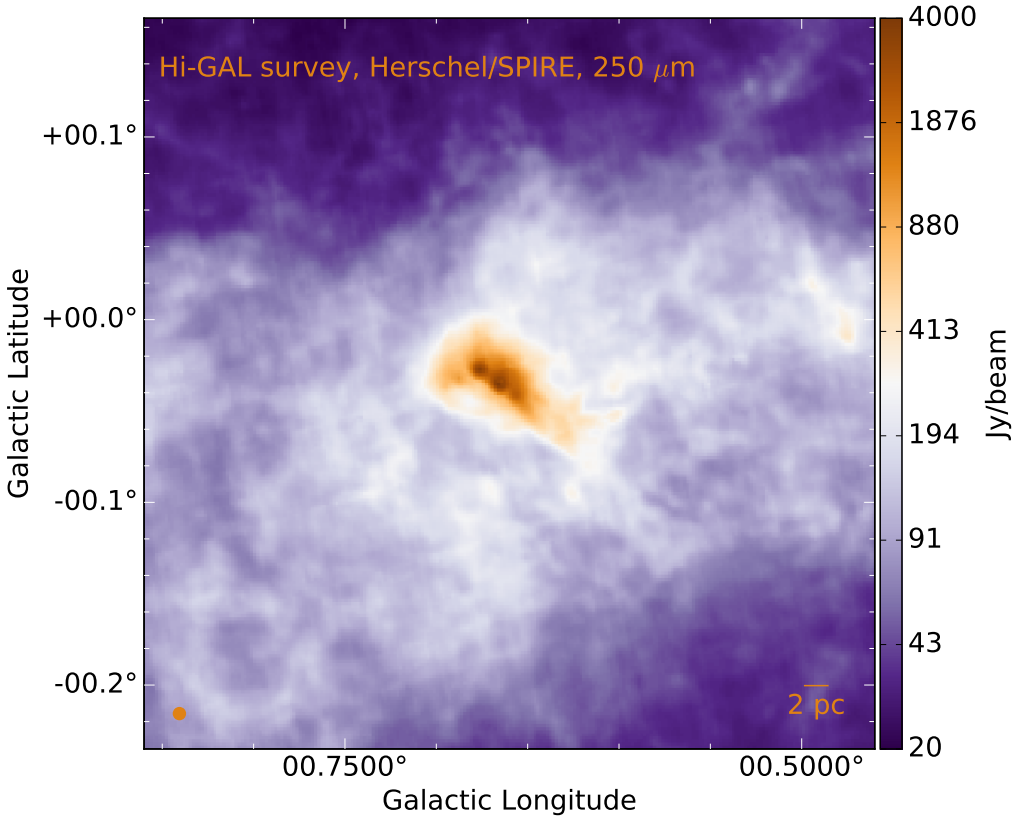
Hi-GAL survey, Herschel/SPIRE, 250 μm
+00.1°
+00.0°
-00.1°
-00.2°
Galactic Latitude
2 pc
00.7500°
00.5000°
Galactic Longitude
4000
1876
880
413
194
91
43
20
Jy/beam

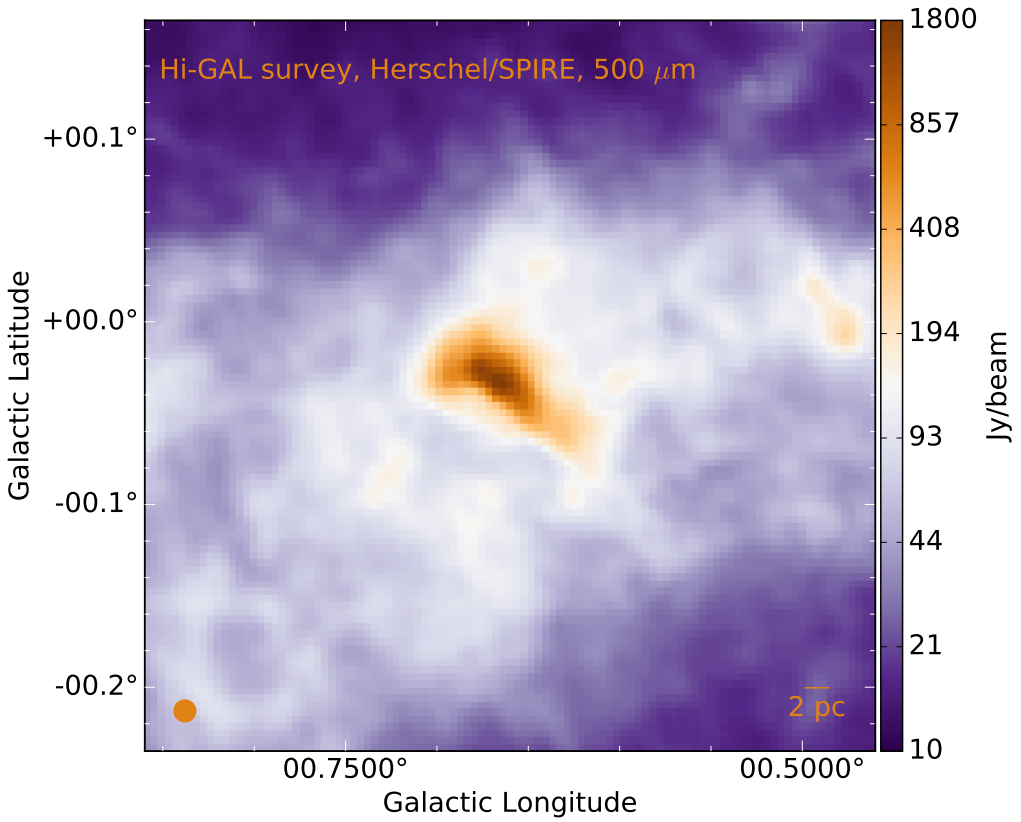
Hi-GAL survey, Herschel/SPIRE, 500 μm
+00.1°
+00.0°
-00.1°
-00.2°
Galactic Latitude
00.7500°
00.5000°
Galactic Longitude
2 pc
1800
857
408
194
93
44
21
10
Jy/beam

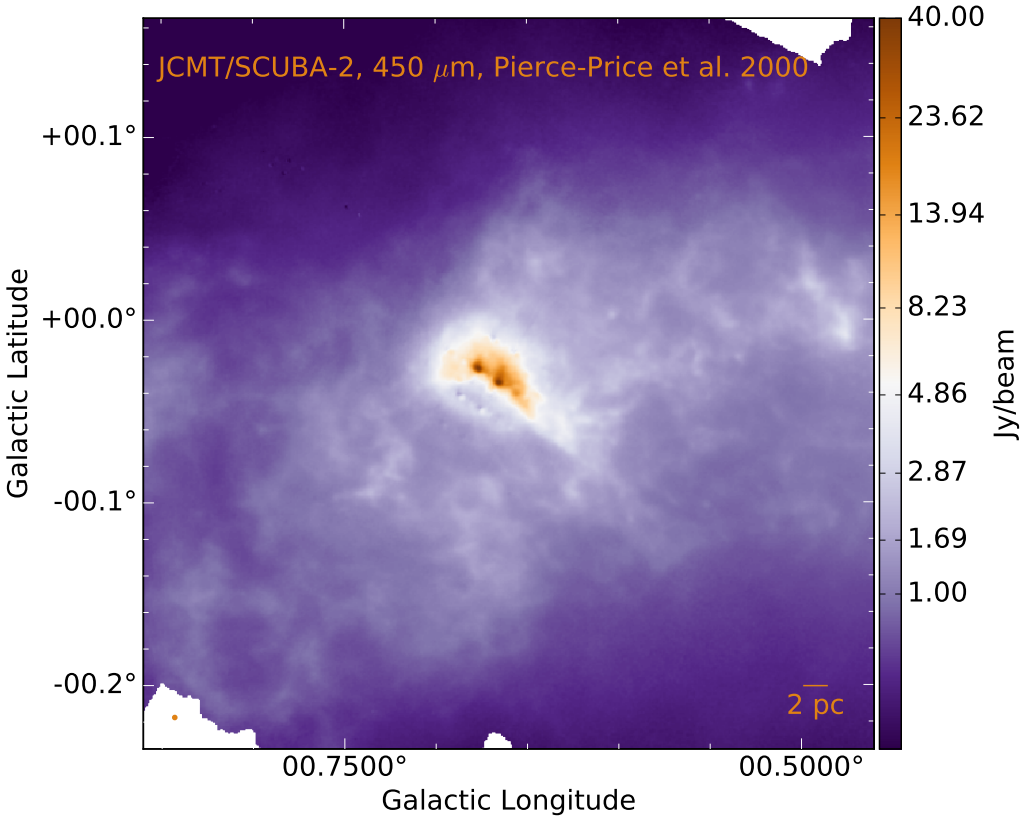
JCMT/SCUBA-2, 450 μm, Pierce-Price et al. 2000
+00.1°
+00.0°
-00.1°
-00.2°
Galactic Latitude
00.7500°
00.5000°
Galactic Longitude
2 pc
40.00
23.62
13.94
8.23
4.86
2.87
1.69
1.00
Jy/beam

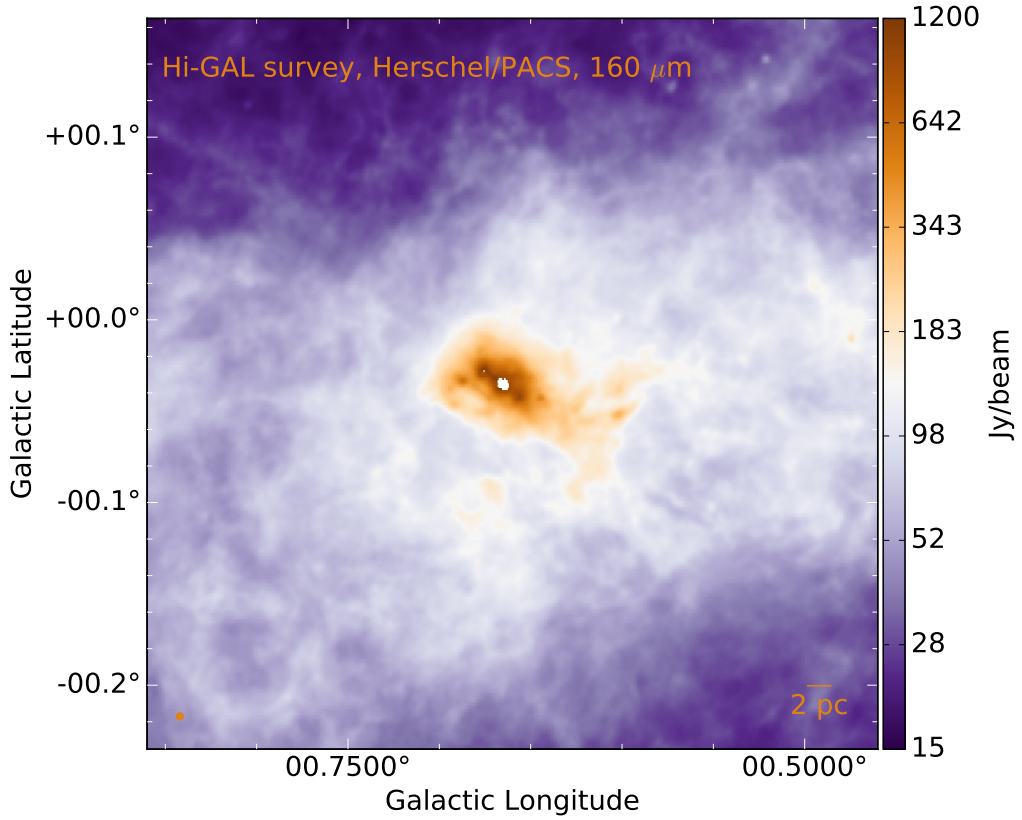
Hi-GAL survey, Herschel/PACS, 160 μm
+00.1°
+00.0°
-00.1°
-00.2°
Galactic Latitude
00.7500°
00.5000°
Galactic Longitude
2 pc
1200
642
343
183
98
52
28
15
Jy/beam

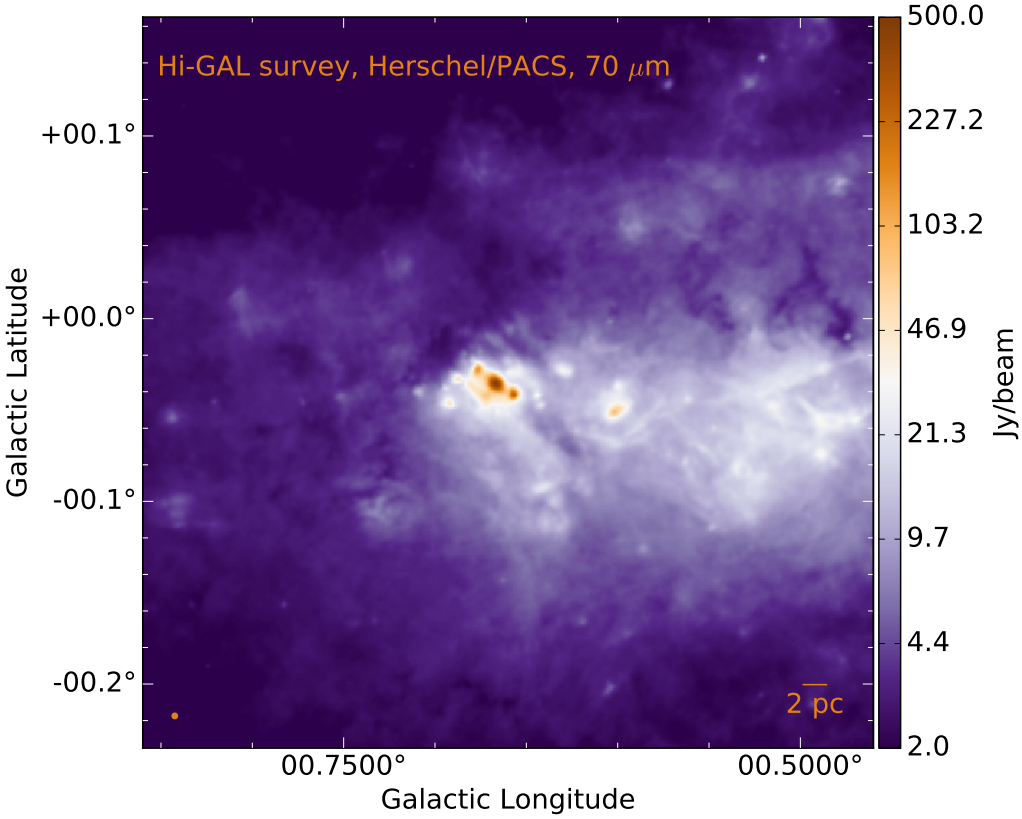
Hi-GAL survey, Herschel/PACS, 70 μm
+00.1°
+00.0°
-00.1°
-00.2°
Galactic Latitude
00.7500°
00.5000°
Galactic Longitude
2 pc
500.0
227.2
103.2
46.9
21.3
9.7
4.4
2.0
Jy/beam

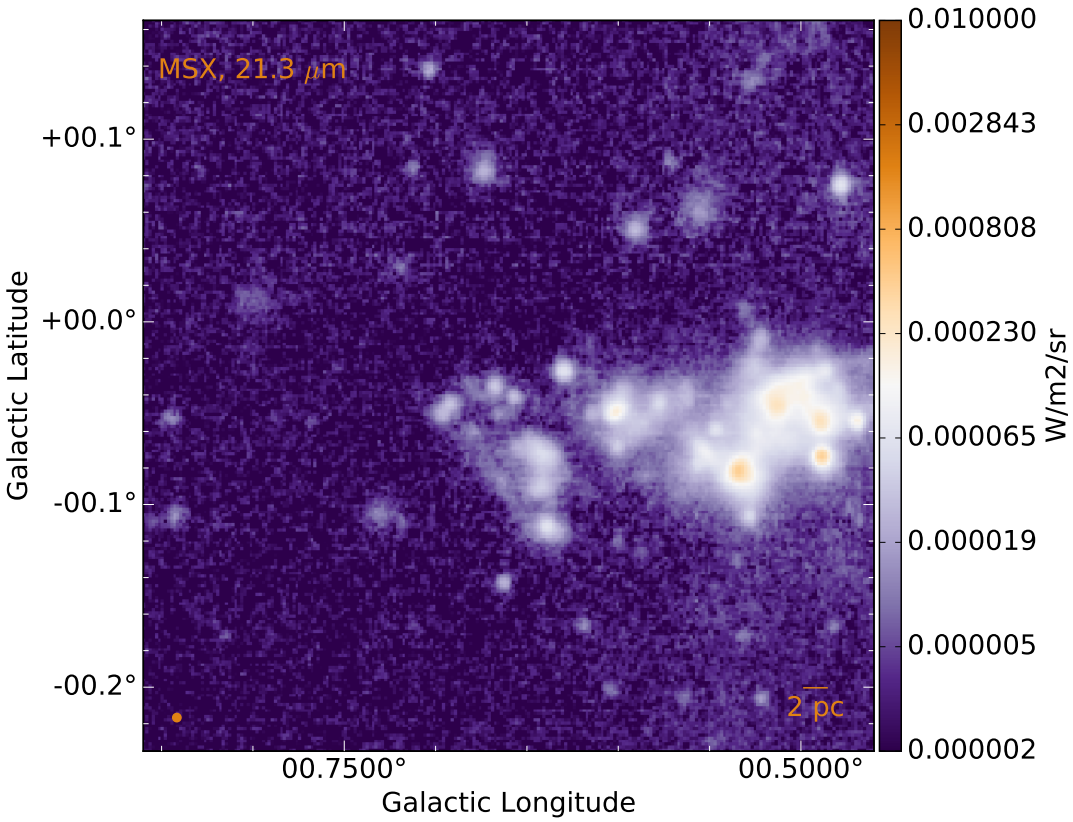
MSX, 21.3 μm
+00.1°
+00.0°
-00.1°
-00.2°
Galactic Latitude
2 pc
00.7500°
00.5000°
Galactic Longitude
0.010000
0.002843
0.000808
0.000230
0.000065
0.000019
0.000005
0.000002
W/m2/sr

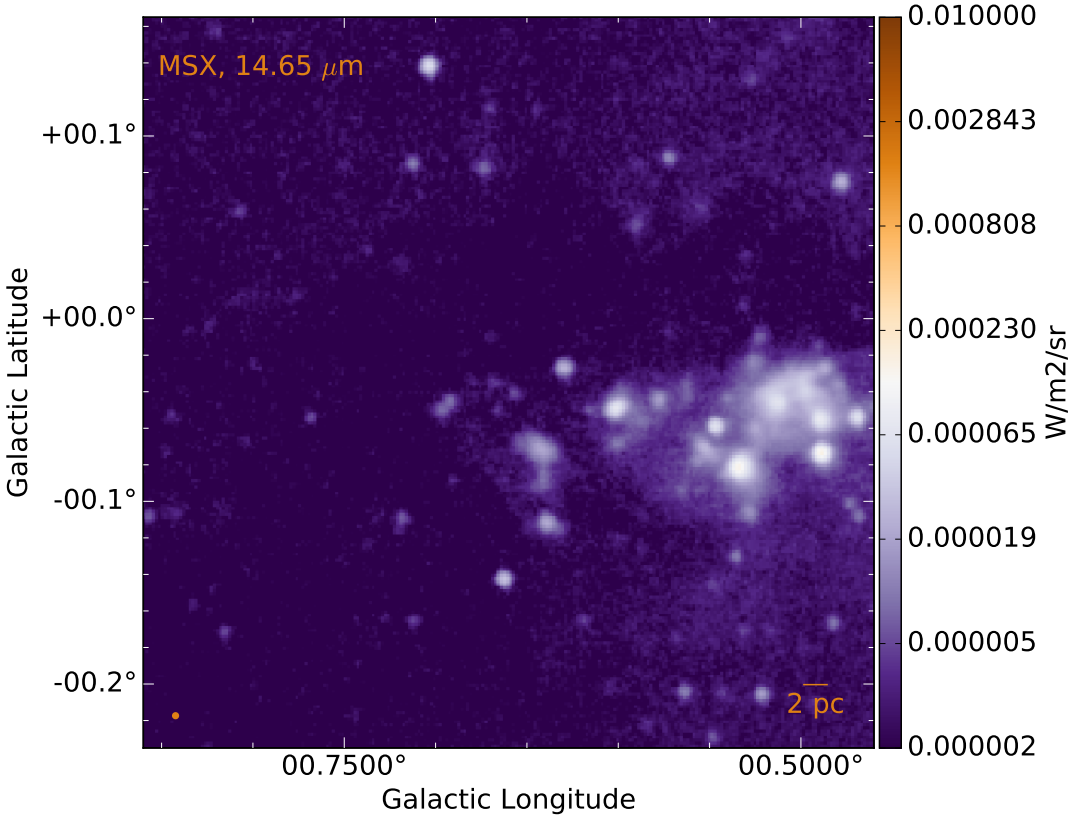
MSX, 14.65 μm
+00.1°
+00.0°
-00.1°
-00.2°
Galactic Latitude
2 pc
00.7500°
00.5000°
Galactic Longitude
0.010000
0.002843
0.000808
0.000230
0.000065
0.000019
0.000005
0.000002
W/m2/sr

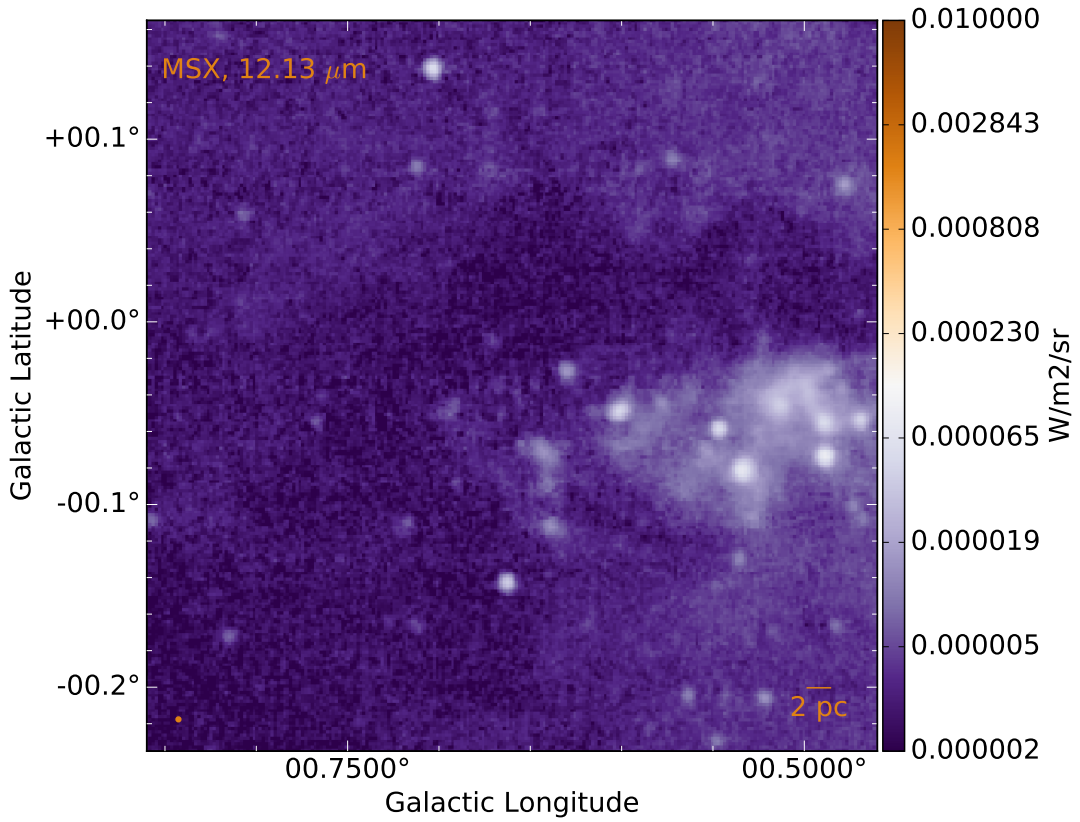
MSX, 12.13 μm
+00.1°
+00.0°
-00.1°
-00.2°
Galactic Latitude
2 pc
00.7500°
00.5000°
Galactic Longitude
0.010000
0.002843
0.000808
0.000230
0.000065
0.000019
0.000005
0.000002
W/m2/sr

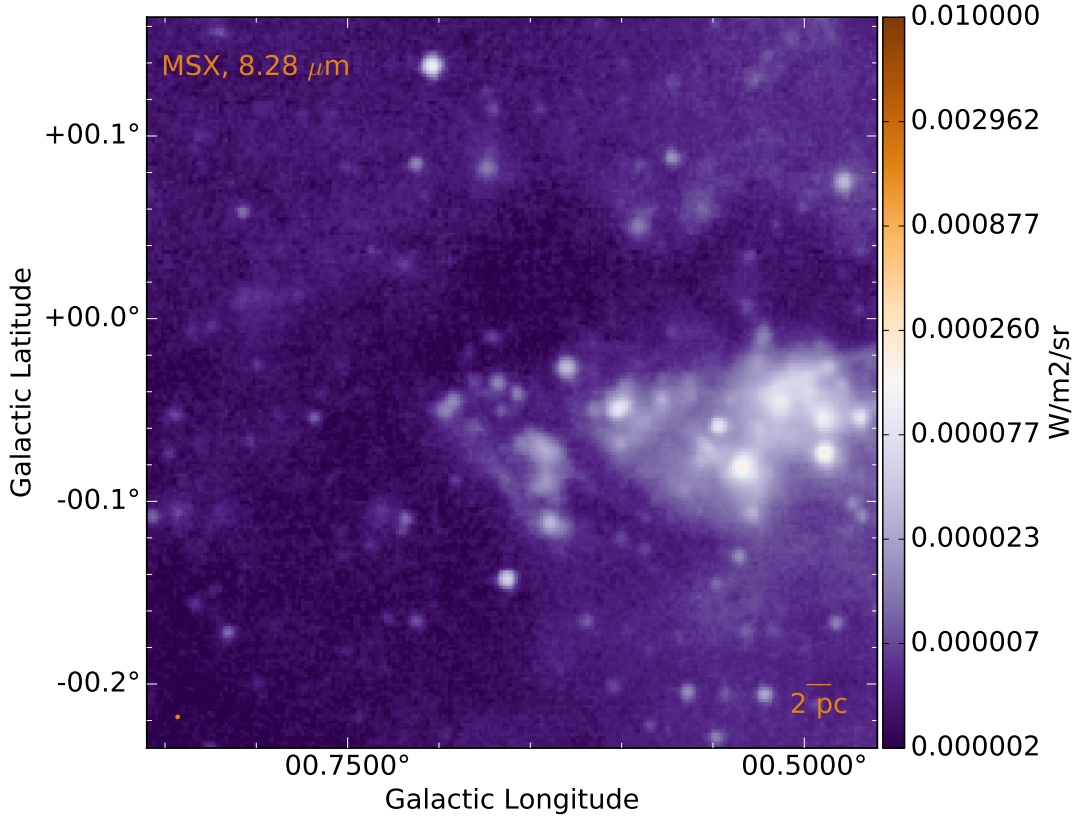
MSX, 8.28 μm
+00.1°
+00.0°
-00.1°
-00.2°
Galactic Latitude
2 pc
00.7500°
00.5000°
Galactic Longitude
0.010000
0.002962
0.000877
0.000260
0.000077
0.000023
0.000007
0.000002
W/m2/sr

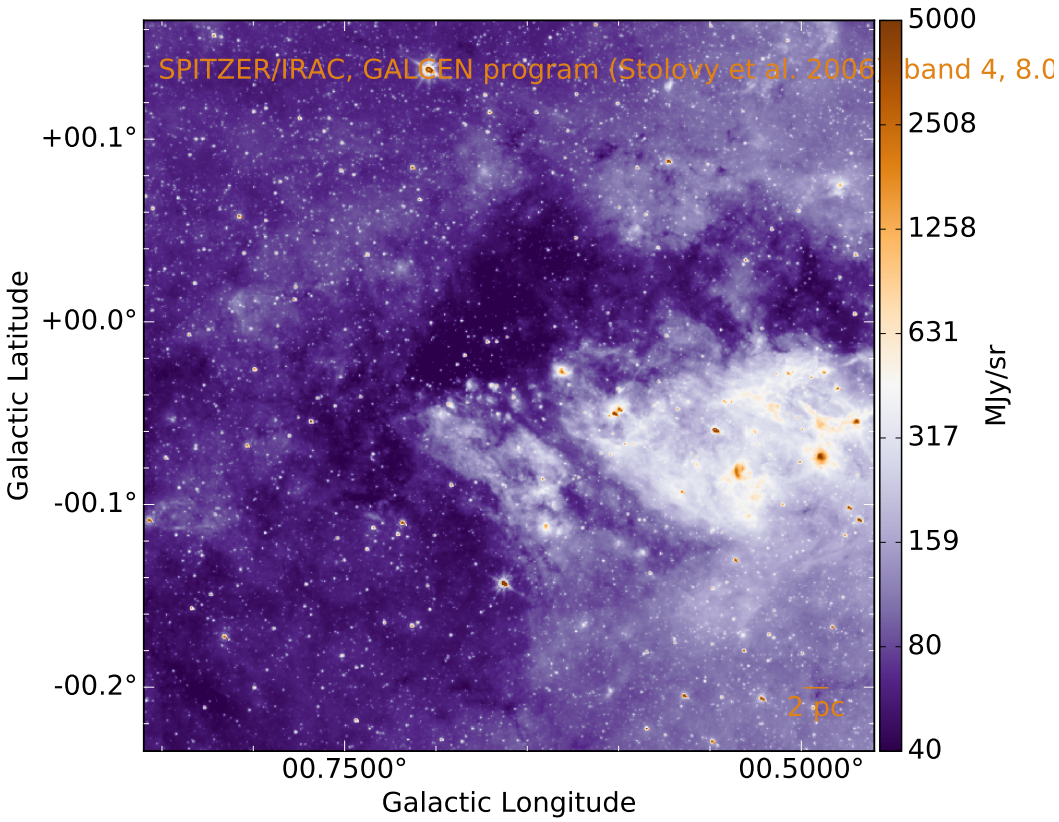
SPITZER/IRAC, GALCEN program (Stolovy et al. 2006
band 4, 8.0
5000
2508
1258
631
317
159
80
40
MJy/sr
+00.1°
+00.0°
-00.1°
-00.2°
Galactic Latitude
00.7500°
00.5000°
Galactic Longitude
2 pc

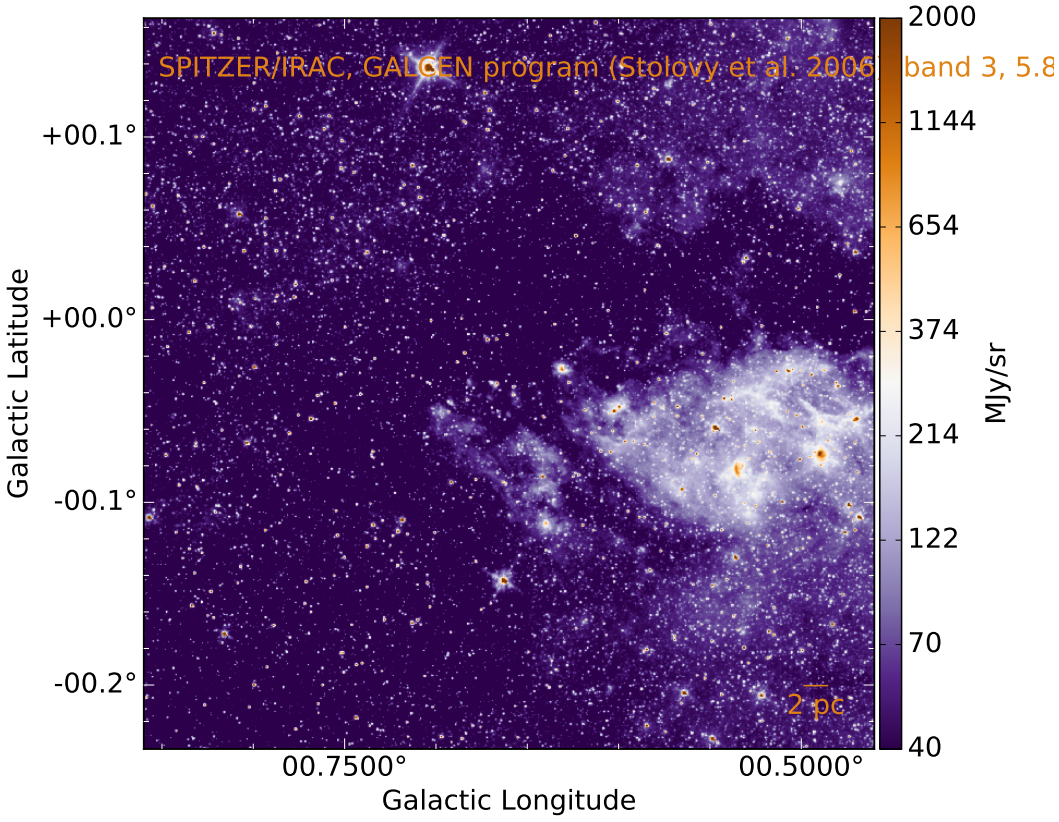
SPITZER/IRAC, GALCEN program (Stolovy et al. 2006
band 3, 5.8
2000
1144
654
374
214
122
70
40
MJy/sr
+00.1°
+00.0°
-00.1°
-00.2°
Galactic Latitude
00.7500°
00.5000°
Galactic Longitude
2 pc

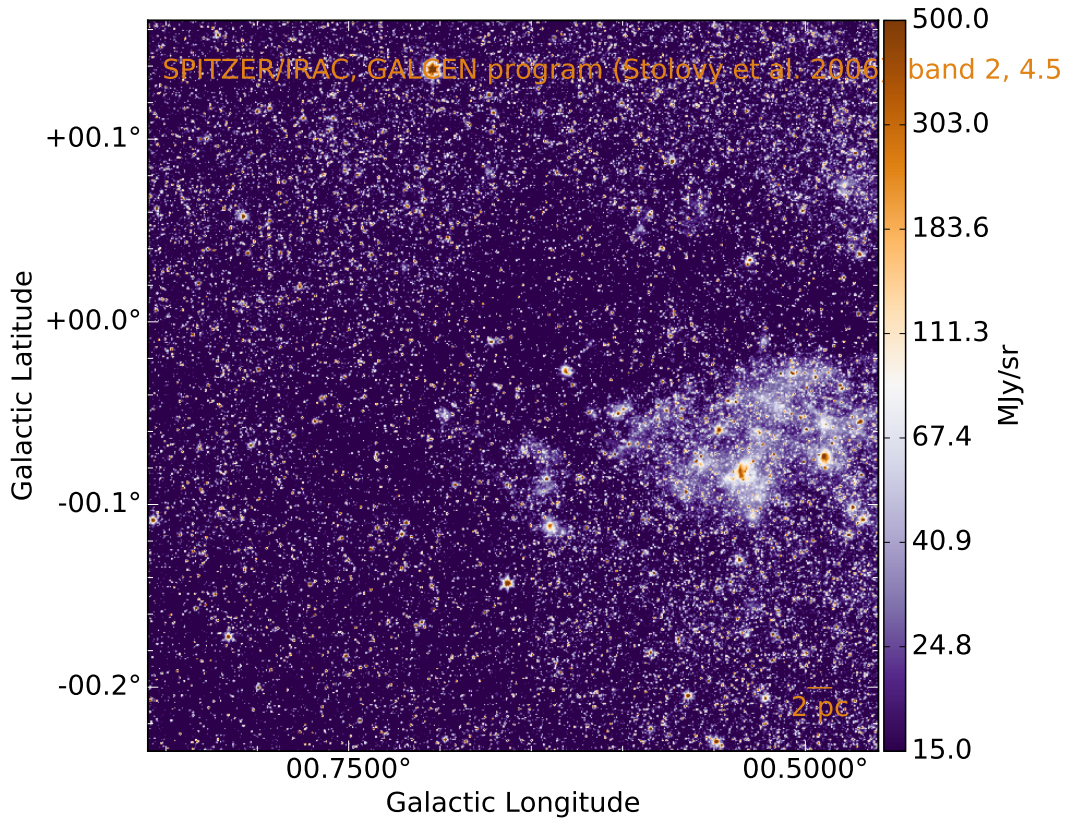
SPITZER/IRAC, GALCEN program (Stolovy et al. 2006)
band 2, 4.5
500.0
303.0
183.6
111.3
67.4
40.9
24.8
15.0
MJy/sr
+00.1°
+00.0°
-00.1°
-00.2°
Galactic Latitude
2 pc
00.7500°
00.5000°
Galactic Longitude

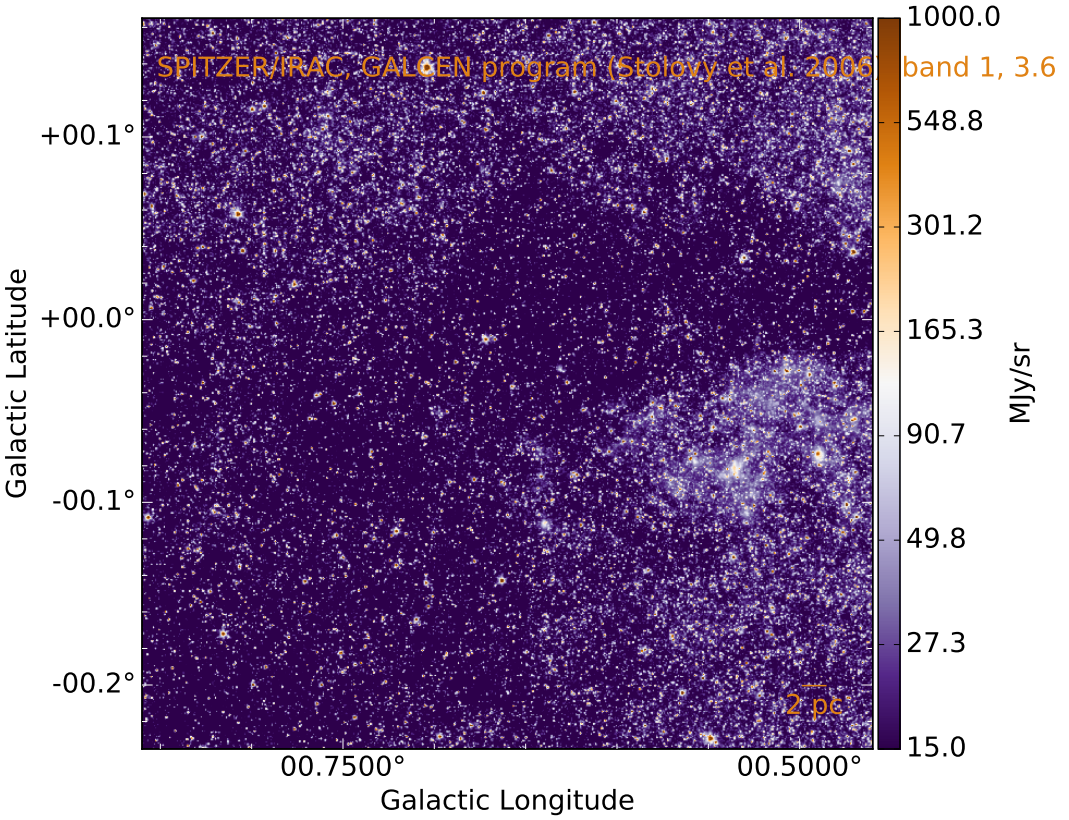
SPITZER/IRAC, GALCEN program (Stolovy et al. 2006)
band 1, 3.6
1000.0
548.8
301.2
165.3
90.7
49.8
27.3
15.0
MJy/sr
+00.1°
+00.0°
-00.1°
-00.2°
Galactic Latitude
2 pc
00.7500°
00.5000°
Galactic Longitude

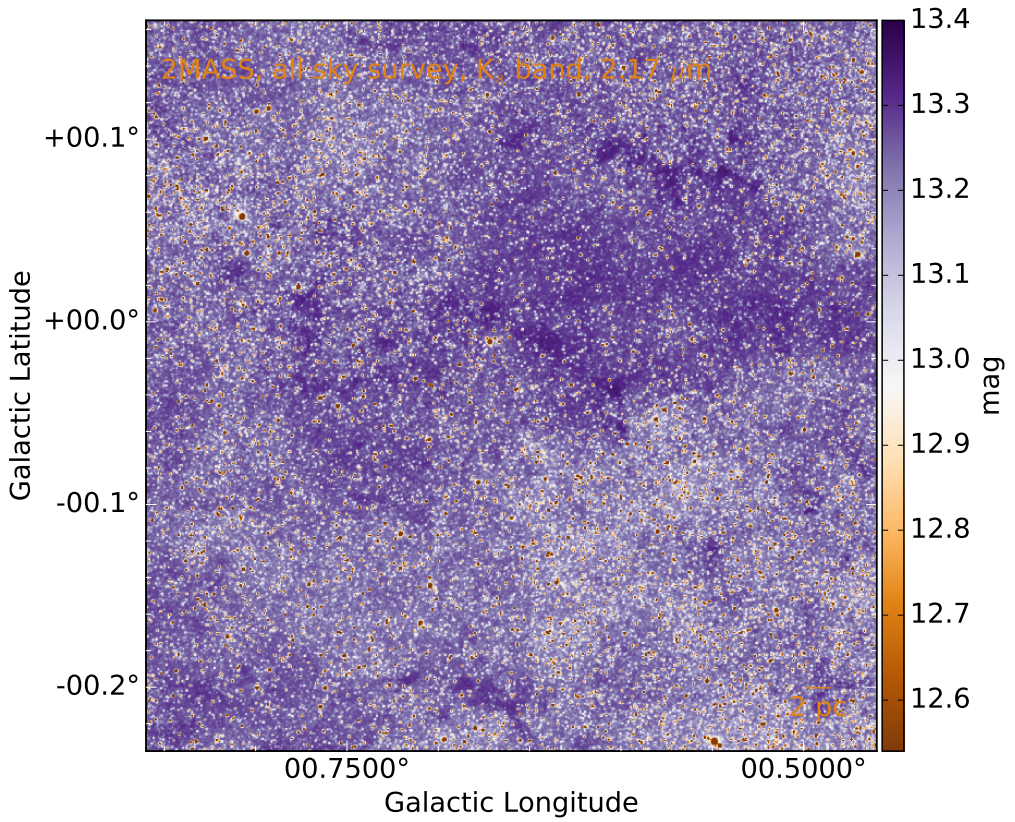
2MASS, all-sky survey, K_s band, 2.17 μm
+00.1°
+00.0°
-00.1°
-00.2°
Galactic Latitude
00.7500°
00.5000°
Galactic Longitude
2 pc
13.4
13.3
13.2
13.1
13.0
12.9
12.8
12.7
12.6
mag

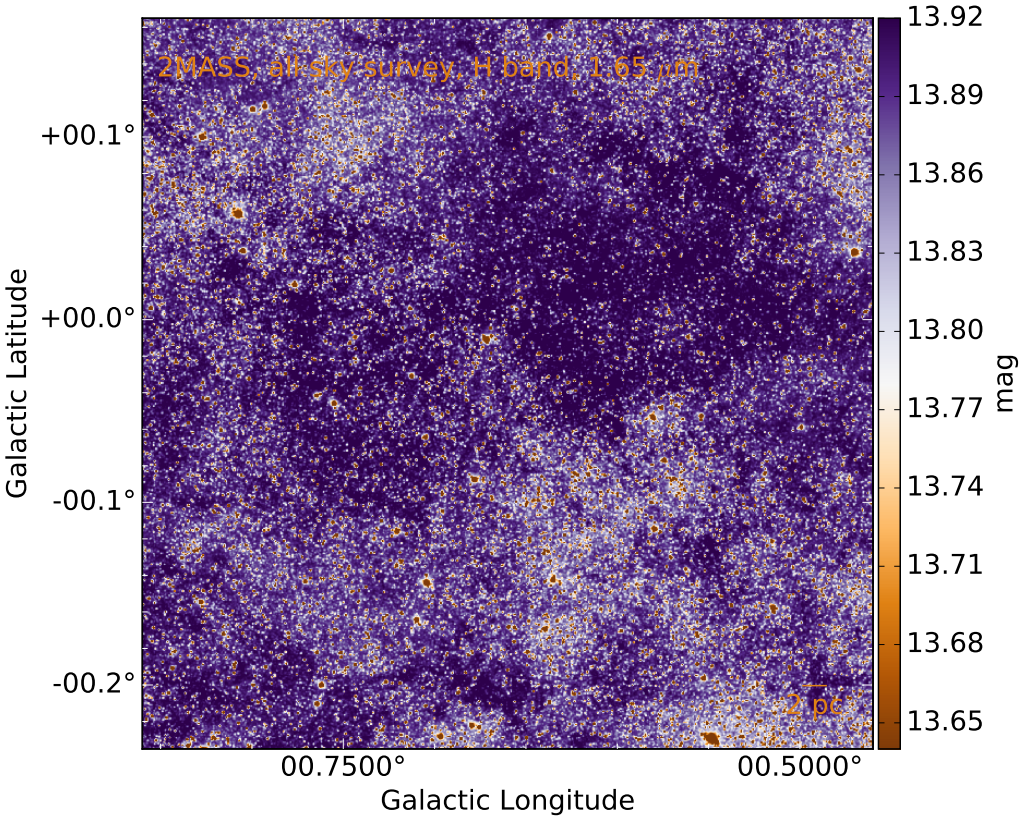
2MASS, all-sky survey, H band, 1.65 μm
+00.1°
+00.0°
-00.1°
-00.2°
Galactic Latitude
00.7500°
00.5000°
Galactic Longitude
2 pc
13.92
13.89
13.86
13.83
13.80
13.77
13.74
13.71
13.68
13.65
mag

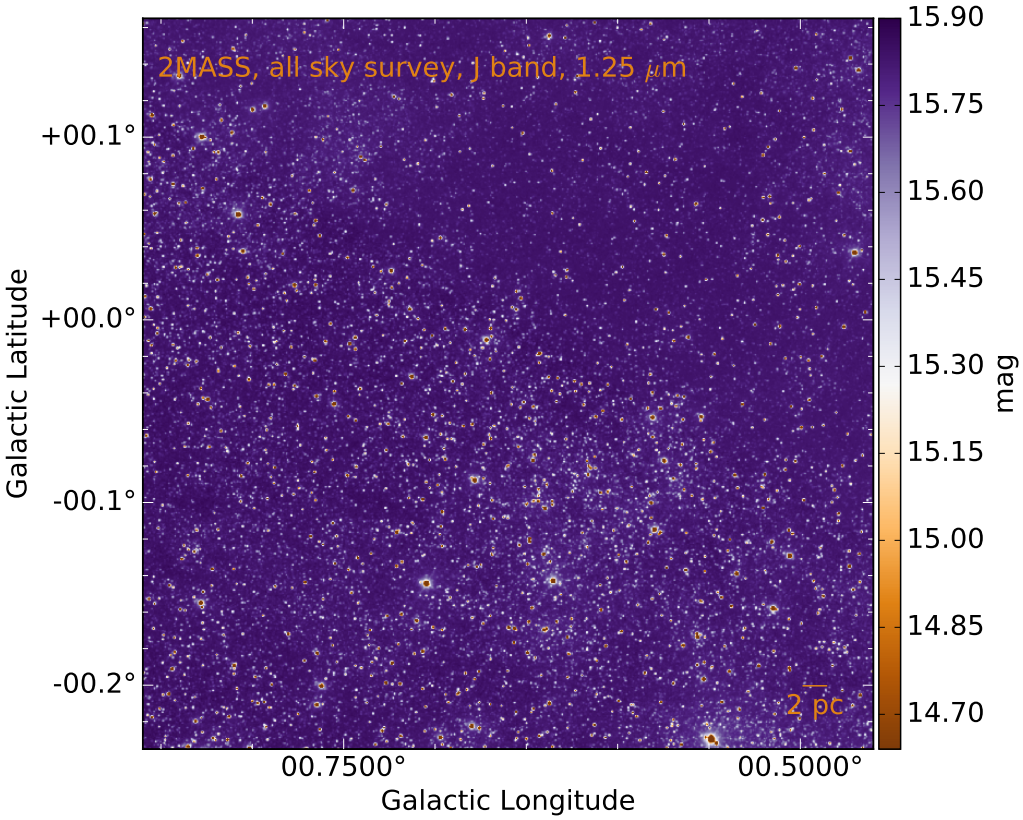
2MASS, all sky survey, J band, 1.25 μm
+00.1°
+00.0°
-00.1°
-00.2°
Galactic Latitude
00.7500°
00.5000°
Galactic Longitude
2 pc
15.90
15.75
15.60
15.45
15.30
15.15
15.00
14.85
14.70
mag

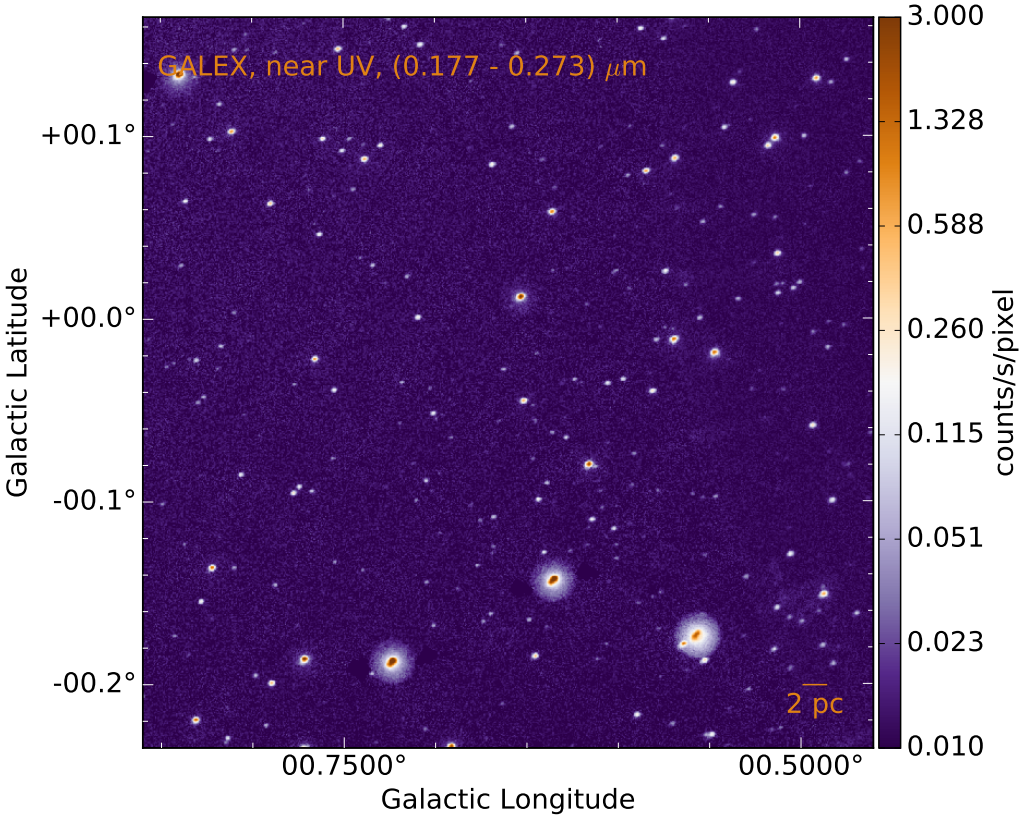
GALEX, near UV, (0.177 - 0.273) μm
+00.1°
+00.0°
-00.1°
-00.2°
Galactic Latitude
00.7500°
00.5000°
Galactic Longitude
2 pc
3.000
1.328
0.588
0.260
0.115
0.051
0.023
0.010
counts/s/pixel

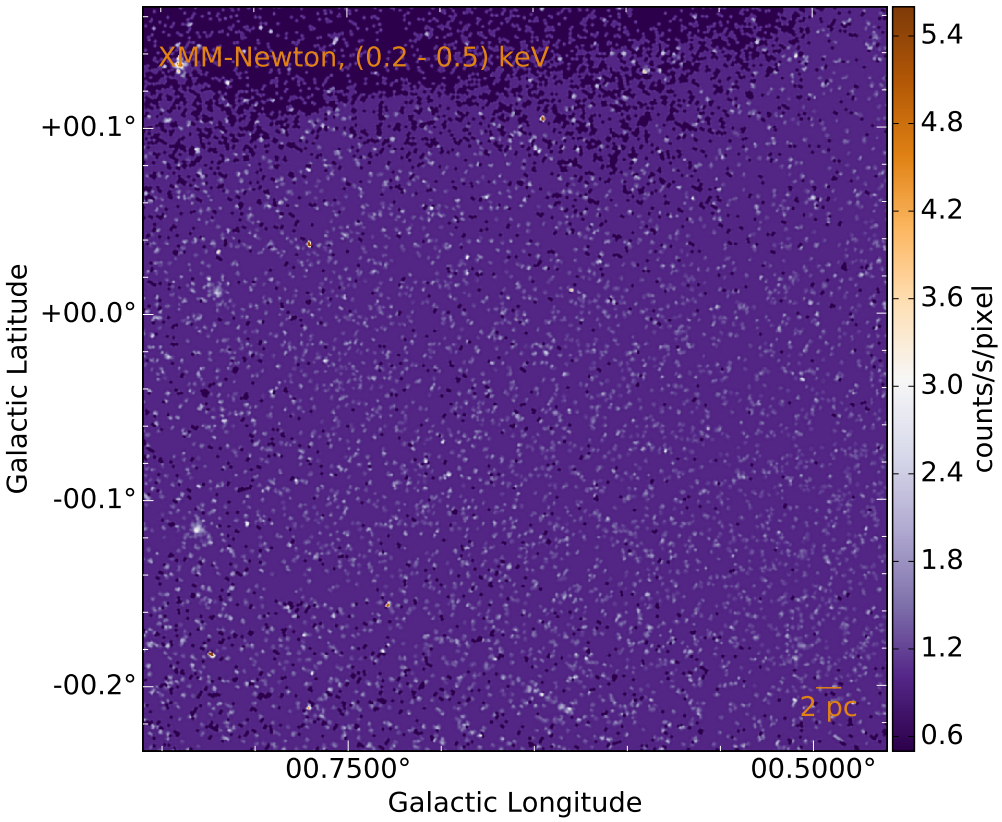
XMM-Newton, (0.2 - 0.5) keV
+00.1°
+00.0°
-00.1°
-00.2°
Galactic Latitude
00.7500°
00.5000°
Galactic Longitude
2 pc
5.4
4.8
4.2
3.6
3.0
2.4
1.8
1.2
0.6
counts/s/pixel

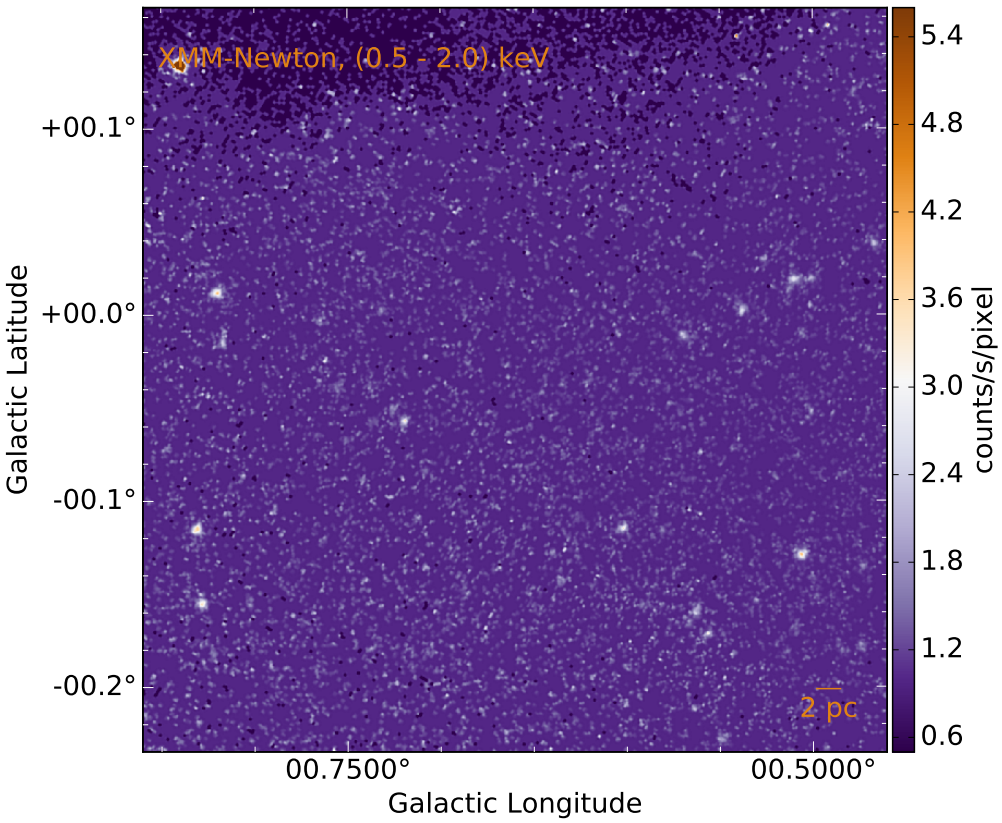
XMM-Newton, (0.5 - 2.0) keV
+00.1°
+00.0°
-00.1°
-00.2°
Galactic Latitude
00.7500°
00.5000°
Galactic Longitude
2 pc
5.4
4.8
4.2
3.6
3.0
2.4
1.8
1.2
0.6
counts/s/pixel

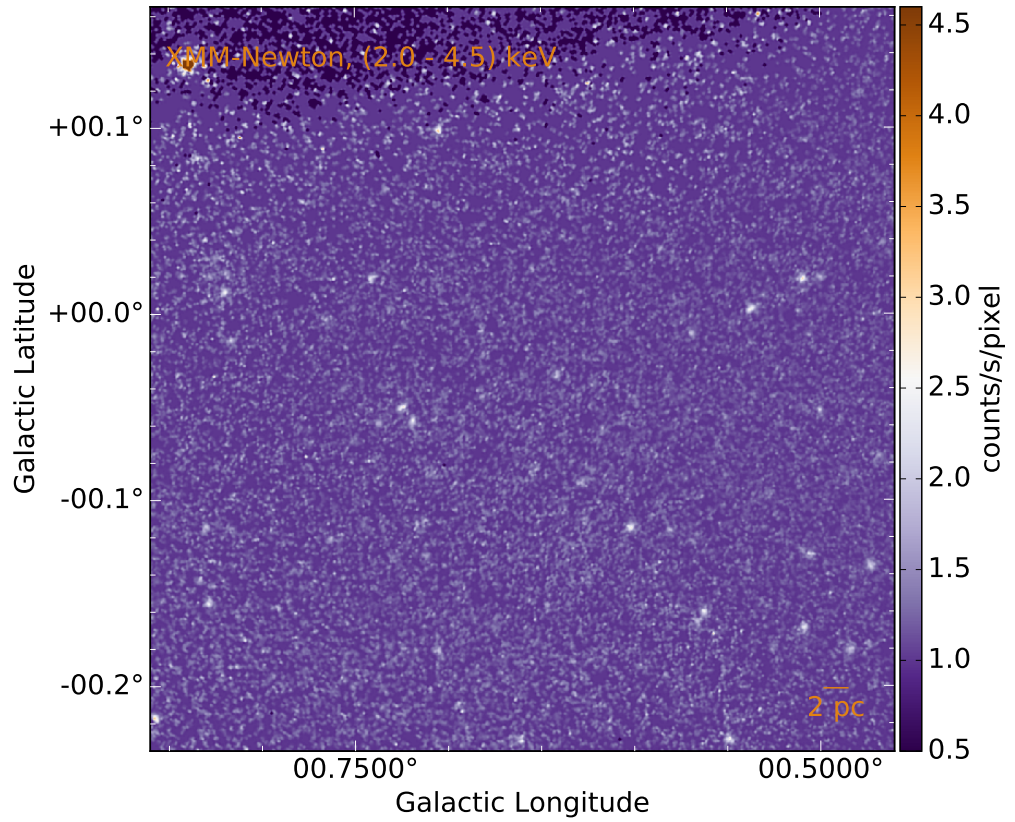
XMM-Newton, (2.0 - 4.5) keV
+00.1°
+00.0°
-00.1°
-00.2°
Galactic Latitude
00.7500°
00.5000°
Galactic Longitude
2 pc
4.5
4.0
3.5
3.0
2.5
2.0
1.5
1.0
0.5
counts/s/pixel

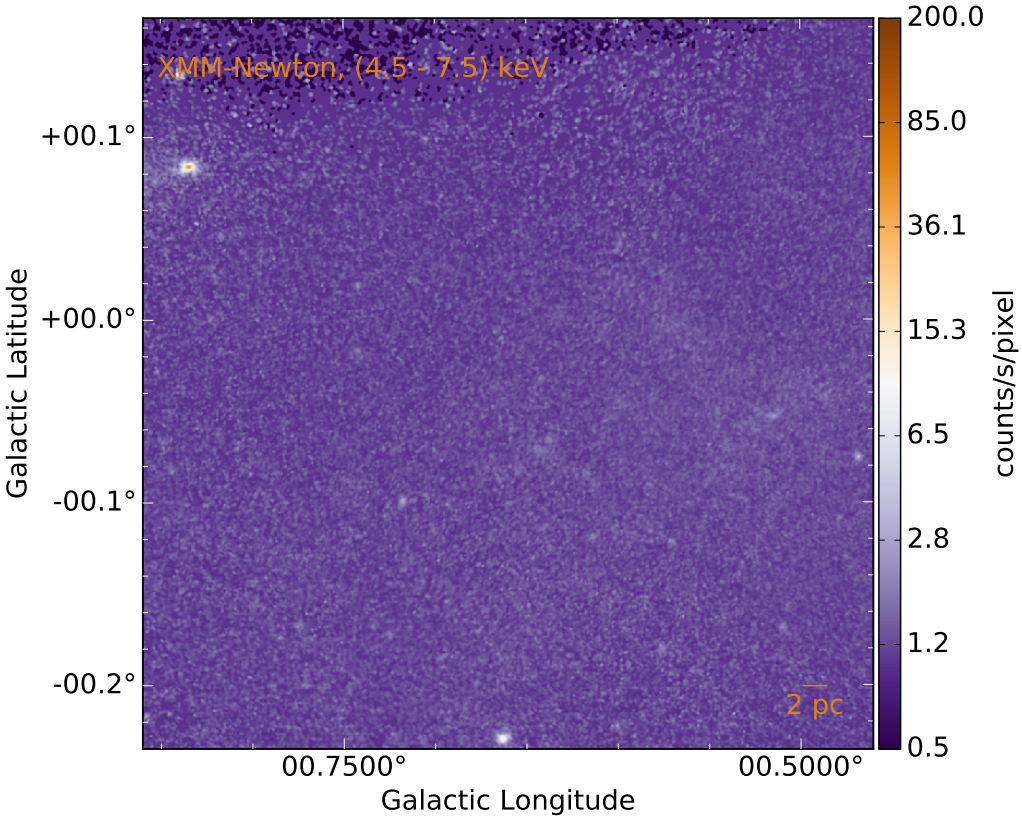
XMM-Newton, (4.5 - 7.5) keV
+00.1°
+00.0°
-00.1°
-00.2°
Galactic Latitude
00.7500°
00.5000°
Galactic Longitude
2 pc
200.0
85.0
36.1
15.3
6.5
2.8
1.2
0.5
counts/s/pixel

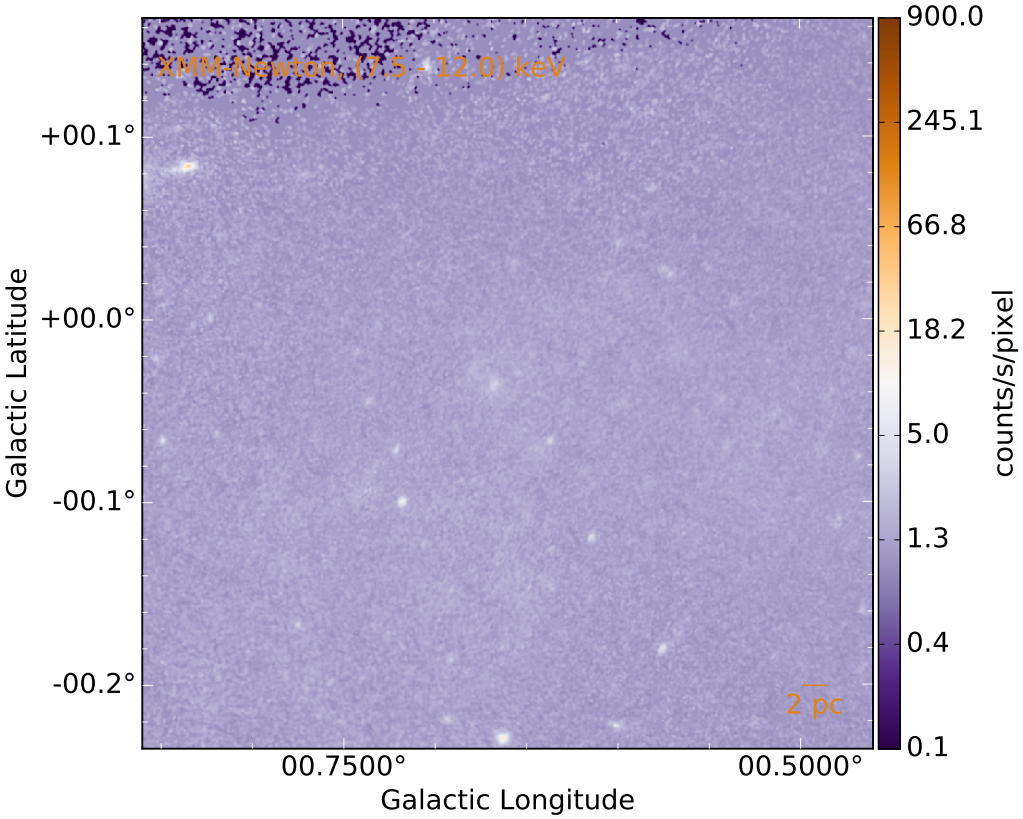
XMM-Newton, (7.5 - 12.0) keV
+00.1°
+00.0°
-00.1°
-00.2°
Galactic Latitude
00.7500°
00.5000°
Galactic Longitude
2 pc
900.0
245.1
66.8
18.2
5.0
1.3
0.4
0.1
counts/s/pixel

Table C.1: Known HII regions in the Sgr B2 region.[a]

ID [1]	Model [2]	RA [3] [h:m:s, J2000]	DEC [4] [d:m:s, J2000]	dz [5] [10^5 au]	r_{obs} [6] [10^3 au]	n_e [7] [10^4 cm^{-3}]	ZAMS [8] type	EM [9] [10^7 pc cm^{-6}]	$\log(\dot{N}_i)$ [10] [s^{-1}]
A1	ABCD	17:47:19.432	-28:23:01.23	0.0	19.400	0.912	O6	2.30	48.86
A2	ABCD	17:47:19.562	-28:22:55.82	0.0	7.910	1.440	O8.5	2.40	48.09
B	ABCD	17:47:19.903	-28:23:02.78	0.0	5.230	4.060	O7.5	12.00	48.44
B1	ABCD	17:47:19.990	-28:23:02.65	0.0	1.370	3.820	B0	2.90	46.65
B9.89	ABCD	17:47:19.695	-28:23:05.78	0.0	2.000	3.410	B0	3.40	47.04
B9.96	ABCD	17:47:19.772	-28:23:10.05	0.0	2.000	3.170	B0	2.90	46.98
B9.99	ABCD	17:47:19.798	-28:23:06.77	0.0	3.510	2.750	O9.5	3.80	47.59
B10.06	ABCD	17:47:19.864	-28:23:01.28	0.0	1.890	4.120	B0	4.60	47.13
B10.10	ABCD	17:47:19.904	-28:23:02.00	0.0	1.440	4.640	B0	4.50	46.88
C	ABCD	17:47:20.001	-28:23:18.19	0.0	6.040	2.020	O9	3.60	48.03
D	ABCD	17:47:20.049	-28:23:12.74	0.0	4.390	3.110	O9	6.10	47.99
E	ABCD	17:47:20.067	-28:23:08.52	0.0	7.800	2.300	O7.5	6.00	48.47
F1a[b]	ABCD	17:47:20.122	-28:23:03.54	0.0	0.731	66.400	O7.5	480.00	48.35
F1b[b]	ABCD	17:47:20.123	-28:23:03.76	0.0	0.315	182.000	O7.5	2000.00	48.45
F1c[b]	ABCD	17:47:20.129	-28:23:03.85	0.0	0.655	83.200	O7	760.00	48.55
F1d[b]	ABCD	17:47:20.134	-28:23:04.20	0.0	0.238	224.000	O7.5	2800.00	48.51
F1e[b]	ABCD	17:47:20.137	-28:23:03.98	0.0	0.731	54.400	O8.5	310.00	48.14
F1f[b]	ABCD	17:47:20.153	-28:23:03.84	0.0	0.901	83.200	O7	760.00	48.55
F1g[b]	ABCD	17:47:20.171	-28:23:03.85	0.0	0.459	177.000	O8	1700.00	48.30
F2a[b]	ABCD	17:47:20.167	-28:23:03.45	0.0	0.323	91.800	O9.5	460.00	47.73
F2b[b]	ABCD	17:47:20.174	-28:23:03.56	0.0	0.417	76.500	O9.5	350.00	47.70
F2c[b]	ABCD	17:47:20.181	-28:23:03.47	0.0	0.502	81.300	O9.5	400.00	47.75

Table C.1: (continued) Known HII regions in Sgr B2.

ID [1]	Model [2]	RA [3] [h:m:s, J2000]	DEC [4] [d:m:s, J2000]	dz [5] [10^5 au]	r_{obs} [6] [10^3 au]	n_e [7] [10^4 cm^{-3}]	ZAMS [8] type	EM [9] [10^7 pc cm^{-6}]	$\log(\dot{N}_i)$ [10] [s^{-1}]
F2d[b]	ABCD	17:47:20.182	-28:23:03.60	0.0	0.493	54.900	O9.5	250.00	47.82
F3a[b]	ABCD	17:47:20.164	-28:23:04.85	0.0	0.621	48.100	O9.5	190.00	47.70
F3b[b]	ABCD	17:47:20.167	-28:23:04.74	0.0	0.264	95.900	O9.5	500.00	47.77
F3c[b]	ABCD	17:47:20.169	-28:23:04.37	0.0	0.306	150.000	O8	1300.00	48.22
F3d[b]	ABCD	17:47:20.189	-28:23:04.58	0.0	2.540	38.500	O5.5	490.00	49.31
F3e[b]	ABCD	17:47:20.223	-28:23:04.64	0.0	0.323	51.600	B0	120.00	47.02
F4a[b]	ABCD	17:47:20.202	-28:23:03.95	0.0	0.187	414.000	O9	3700.00	47.85
F4b[b]	ABCD	17:47:20.226	-28:23:04.23	0.0	0.621	108.000	O8	890.00	48.31
F4c[b]	ABCD	17:47:20.231	-28:23:04.07	0.0	0.723	48.900	O8.5	260.00	48.09
F4d[b]	ABCD	17:47:20.218	-28:23:04.09	0.0	0.655	48.800	O9.5	180.00	47.62
F10.37[b]	ABCD	17:47:20.191	-28:23:05.76	0.0	0.689	62.300	O9.5	240.00	47.58
F10.39[b]	ABCD	17:47:20.206	-28:23:06.45	0.0	0.408	34.400	B0	70.00	46.98
G[b]	ABCD	17:47:20.297	-28:23:02.88	0.0	1.330	35.100	O7	250.00	48.62
F10.27[b]	ABCD	17:47:20.075	-28:23:05.22	0.0	1.760	4.310	B0	4.70	47.08
F10.30[b]	ABCD	17:47:20.107	-28:23:03.02	0.0	0.867	4.810	B0	2.90	46.25
F10.303[b]	ABCD	17:47:20.108	-28:23:03.57	0.0	2.180	9.090	O9	26.00	48.01
F10.318[b]	ABCD	17:47:20.124	-28:23:02.27	0.0	4.120	2.380	O9.5	3.40	47.67
F10.32[b]	ABCD	17:47:20.131	-28:23:00.13	0.0	1.910	3.700	B0	3.80	47.05
F10.33[b]	ABCD	17:47:20.136	-28:23:05.97	0.0	1.530	4.240	B0	4.00	46.88
F10.35[b]	ABCD	17:47:20.152	-28:23:06.60	0.0	1.450	4.070	B0	3.50	46.77
F10.44[b]	ABCD	17:47:20.245	-28:23:06.22	0.0	2.620	2.760	B0	2.90	47.21
G10.44	ABCD	17:47:20.242	-28:23:03.23	0.0	1.370	4.920	B0	4.80	46.87
G10.47	ABCD	17:47:20.270	-28:23:02.25	0.0	1.910	3.670	B0	3.70	47.05

Table C.1: (continued) Known HII regions in Sgr B2.

ID [1]	Model [2]	RA [3] [h:m:s, J2000]	DEC [4] [d:m:s, J2000]	dz [5] [10^5 au]	r_{obs} [6] [10^3 au]	n_e [7] [10^4 cm^{-3}]	ZAMS [8] type	EM [9] [10^7 pc cm^{-6}]	$\log(\dot{N}_i)$ [10] [s^{-1}]
H	ABCD	17:47:20.426	-28:23:44.62	0.0	9.260	2.700	O6	9.80	48.84
I	ABCD	17:47:20.507	-28:23:05.95	0.0	22.000	1.630	O5	8.40	49.52
I10.49	ABCD	17:47:20.304	-28:23:04.45	0.0	2.000	3.440	B0	3.40	47.05
I10.52	ABCD	17:47:20.325	-28:23:08.01	0.0	1.980	4.530	B0	5.90	47.28
J	ABCD	17:47:20.570	-28:22:56.04	0.0	25.500	0.608	O6	1.40	48.86
K1[b]	A	17:47:19.802	-28:22:20.71	0.0	5.340	5.250	O6.5	21.00	48.70
	BCD			-7.0					
K2[b]	A	17:47:19.874	-28:22:18.37	0.0	2.400	12.700	O7.5	56.00	48.42
	BCD			-7.0					
K3[b]	A	17:47:19.897	-28:22:17.07	0.0	3.200	7.610	O7.5	27.00	48.35
	BCD			-7.0					
K4	A	17:47:19.993	-28:22:04.58	0.0	6.280	3.750	O7	13.00	48.62
	BCD			-7.0					
K5	A	17:47:20.266	-28:22:14.67	0.0	34.000	0.819	O5	33.00	49.49
	BCD			-7.0					
K6	A	17:47:20.568	-28:22:08.82	0.0	49.900	0.532	O5	20.00	49.62
	BCD			-7.0					
L	ABCD	17:47:22.661	-28:21:55.77	0.0	17.300	1.420	O5.5	5.10	49.09
L13.30	ABCD	17:47:23.079	-28:21:55.16	0.0	5.680	1.450	O9.5	1.70	47.66
O	ABCD	17:47:22.901	-28:22:49.07	0.0	7.800	0.698	O9.5	0.55	47.44
P	ABCD	17:47:23.621	-28:23:36.02	0.0	7.800	0.777	O9.5	0.68	47.53
Q	ABCD	17:47:24.875	-28:21:44.93	0.0	7.800	0.895	O9.5	0.90	47.65
R	ABCD	17:47:26.464	-28:22:05.11	0.0	28.500	0.535	O6	1.20	48.89

Table C.1: (continued) Known HII regions in Sgr B2.

ID [1]	Model [2]	RA [3] [h:m:s, J2000]	DEC [4] [d:m:s, J2000]	dz [5] [10^5 au]	r_{obs} [6] [10^3 au]	n_e [7] [10^4 cm^{-3}]	ZAMS [8] type	EM [9] [10^7 pc cm^{-6}]	$\log(\dot{N}_i)$ [10] [s^{-1}]
T	ABCD	17:47:27.256	-28:20:58.75	0.0	35.100	0.138	O9	0.10	47.99
U	ABCD	17:47:12.093	-28:22:33.86	0.0	27.300	0.364	O7.5	0.52	48.50
V	ABCD	17:47:13.224	-28:23:47.77	0.0	54.600	0.233	O6	0.43	49.02
W	ABCD	17:47:16.717	-28:23:29.52	0.0	19.500	0.238	O9.5	0.16	47.69
X	ABCD	17:47:17.363	-28:22:03.74	0.0	3.120	2.220	B0	2.20	47.25
X8.33	ABCD	17:47:18.113	-28:22:06.82	0.0	1.900	5.320	B0	7.80	47.36
Y	ABCD	17:47:18.657	-28:22:54.51	0.0	5.630	1.480	O9.5	1.80	47.67
Z	ABCD	17:47:18.689	-28:22:44.78	0.0	19.000	0.607	O7.5	1.00	48.47
Z10.24	ABCD	17:47:20.038	-28:22:41.18	0.0	1.680	6.140	B0	9.20	47.33
AA	ABCD	17:47:19.388	-28:22:18.33	0.0	11.700	1.070	O8	1.90	48.33
BB	ABCD	17:47:22.348	-28:22:17.41	0.0	33.100	0.218	O8	0.24	48.31

Notes:

[a] All values listed in this table are the values used in the different models assuming HII regions are spherical symmetric regions of fully ionized gas with no dust and a single ionizing source.

[b] These regions are optically thick. Their electron density has been increased manually.

[1] ID is the identifier used in the model. We use the same identifiers as (Mehringer et al. 1993; Gaume et al. 1995; De Pree et al. 1998).

[2] Model refers to one of the four model described in this paper.

[3] RA is the right ascension of the HII region given in units of hours:minutes:seconds in the equatorial coordinate system.

[4] DEC is the declination of the HII region given in units of degrees:arcminutes:arcseconds in the equatorial coordinate system.

[5] dz is the displacement along the line of sight with respect to the model center. The z-axis is oriented such that it points towards the observer.

[6] r_{obs} is the observed radius of the HII region.

[7] n_e is the number electron density.

[8] ZAMS refers to the zero age main sequence star embedded in the HII region.

[9] EM is the emission measure.

[10] $\log(\dot{N}_i)$ is the logarithm of the number of Lyman continuum photons.

Table C.2: Small scale structure. Dust density cores in Sgr B2.

ID [1]	Model [2]	RA [3] [h:m:s, J2000]	DEC [4] [d:m:s, J2000]	dz [5] [10^5 au]	r_0 [6] [10^3 au]	n_c [7] [10^7 H_2 cm^{-3}]	η [8]	star [9]
M-SMA-1a	ABCD	17:47:20.197	-28:23:04.36	1.0	3.0	20	5.0	B0
M-SMA-1b	ABCD	17:47:20.170	-28:23:04.60	1.0	3.1	35	5.0	B0.5
M-SMA-1c	ABCD	17:47:20.158	-28:23:05.08	1.0	3.6	10	5.0	B0.5
M-SMA-1d	ABCD	17:47:20.148	-28:23:05.48	1.0	3.6	20	5.0	B0.5
M-SMA-2a	ABCD	17:47:20.152	-28:23:04.18	0.0	3.2	19	5.0	B0.5
M-SMA-2b	ABCD	17:47:20.124	-28:23:04.45	0.0	3.3	14	5.0	B0.5
M-SMA-3	ABCD	17:47:20.100	-28:23:04.04	0.0	2.8	14	5.0	B0.5
M-SMA-4	ABCD	17:47:20.152	-28:23:03.30	0.0	3.4	7	5.0	none
M-SMA-5	ABCD	17:47:20.212	-28:23:04.90	0.0	3.2	7	5.0	B0.5
M-SMA-6	ABCD	17:47:20.175	-28:23:06.08	0.0	3.0	35	5.0	none
M-SMA-7	ABCD	17:47:20.118	-28:23:06.35	0.0	2.9	30	5.0	B0.5
M-SMA-8	ABCD	17:47:20.215	-28:23:06.43	0.0	3.6	4	5.0	none
M-SMA-9	ABCD	17:47:20.250	-28:23:07.10	0.0	2.8	9	5.0	B0.5
M-SMA-10	ABCD	17:47:20.005	-28:23:05.79	0.0	3.3	15	5.0	none
M-SMA-11	ABCD	17:47:20.108	-28:23:03.10	1.0	3.2	20	5.0	B0.5
M-SMA-12	ABCD	17:47:20.136	-28:23:02.24	1.0	3.8	50	5.0	B0
N-SMA-1a	A	17:47:19.912	-28:22:18.25	-5.0	9.0	45	5.0	none
	BCD			-6.95	9.0	45	5.0	none
N-SMA-1b	A	17:47:19.900	-28:22:19.51	-2.0	4.0	75	5.0	none
	BCD			-6.98	4.0	75	5.0	none
N-SMA-2a	A	17:47:19.944	-28:22:13.64	-3.0	6.9	10	5.0	B0.5
	BCD			-6.97	6.9	10	5.0	B0.5

Table C.2: (continued) Small scale structure. Dust density cores in Sgr B2.

ID [1]	Model [2]	RA [3] [h:m:s, J2000]	DEC [4] [d:m:s, J2000]	dz [5] [10^3 au]	r_0 [6] [10^3 au]	n_c [7] [10^7 H_2 cm^{-3}]	η [8]	star [9]
N-SMA-2b	A	17:47:19.880	-28:22:13.80	-30	6.8	10	5.0	B0.5
	BCD			-6.97	6.8	10	5.0	B0.5

Notes:

[1] ID is the identifier used in the model. These identifiers are identical to the ones introduced by Qin et al. 2011. Note: Some of these objects identified by Qin et al. 2011 show an elongated intensity structure. We recover these objects with a superposition of several spherical symmetric clumps. We distinguish these components by adding additional lowercase letters to the identifier introduced by Qin et al. 2011.

[2] Model refers to one of the four model described in this paper.

[3] RA is the right ascension of the density component given in units of hours:minutes:seconds in the equatorial coordinate system.

[4] DEC is the declination of the density component given in units of degrees:arcminutes:arcseconds in the equatorial coordinate system

[5] dz is the displacement along the line of sight with respect to the model center. The z-axis is oriented such that it points towards the observer.

[6] r_0 is the turnover radius defining the component, as described in Eq. 3.2.

[7] n_c is the central density.

[8] η is the exponent of the dust density profile.

[9] This column indicates whether an additional heating source had to be included inside the dust component. If this is the case, the spectral type of the star is given.

Table C.3: Large-scale structure. Dust density envelopes in Sgr B2.

ID [1]	Model [2]	RA [3] [h:m:s, J2000]	DEC [4] [d:m:s, J2000]	dz [5] [10^5 au]	$r_{0,x}$ [6] [10^3 au]	$r_{0,y}$ [6] [10^3 au]	$r_{0,z}$ [6] [10^3 au]	n_0 [7] [10^4 H_2 cm^{-3}]	η [8]	star [9]
NE	ABCD	17:47:22.361	-28:21:31.94	0.0	200	200	200	9.8	2.2	B0
N1	A	17:47:19.912	-28:22:18.25	0.0	40	40	40	200	2.5	none
	B			-7.0	40	40	40	400	2.5	none
	C			-7.0	40	40	40	400	2.5	none
	D			-7.0	40	40	55	300	2.5	none
N2	A	17:47:16.000	-28:21:48.00	0.0	30	30	30	60	1.8	none
	B			-7.0	30	30	30	100	1.8	none
	C			-7.0	30	30	45	90	1.8	none
	D			-7.0	30	30	30	90	1.8	none
M1	AB	17:47:20.056	-28:23:06.46	0.0	30	30	30	200	2.5	none
	C			0.0	60	60	140	30	2.5	none
	D			0.0	60	60	80	70	2.5	none
M2	AB	17:47:17.800	-28:23:00.00	0.0	20	20	20	200	1.8	none
	C			0.0	40	40	80	100	1.8	none
	D			0.0	40	40	50	100	1.8	none
S1	ABCD	17:47:20.465	-28:23:45.25	0.0	30	30	30	90	2.4	B0
S2	ABCD	17:47:19.509	-28:23:52.45	0.0	20	20	20	40	1.8	none
Se	ABCD	17:47:21.525	-28:24:20.58	0.0	50	50	50	50	2.3	none
deepS	ABCD	17:47:20.632	-28:25:30.87	0.0	220	220	220	12	2.2	none

Table C.3: (continued) Large-scale structure. Dust density envelopes in Sgr B2.

Notes:

[1] ID is the identifier used in the model. These identifiers follow the historic naming scheme explained in Sect. 2.3.

[2] Model refers to one of the four model described in this paper.

[3] RA is the right ascension of the density component given in units of hours:minutes:seconds in the equatorial coordinate system.

[4] DEC is the declination of the density component given in units of degrees:arcminutes:arcseconds in the equatorial coordinate system

[5] dz is the displacement along the line of sight with respect to the model center. The z-axis is oriented such that it points towards the observer.

[6] r_x, r_y, r_z are the core turnover radii in each principal direction, as described in Eq. (3.2).

[7] n_c is the central density.

[8] η is the exponent of the dust density profile.

[9] This column indicates whether an additional heating source had to be included inside the dust component. If this is the case, the spectral type of the star is given.

Here I present a re-print of the Sgr B2 continuum paper, published in Astronomy & Astrophysics (Schmiedeke et al. 2016). The data employed in this study were calibrated and provided by my co-authors: C.Comito (HIFI data), T.Csengeri (Atlasgal map), S. Molinari (Hi-GAL maps), S.-L. Qin (SMA maps), and Rainer Rolffs (VLA maps).

For consistent post-processing I re-did the imaging of the interferometric SMA and VLA data. The modeling toolkit PANDORA was designed and written by myself (see Chapter 3), based on some initial work by R. Rolffs. The continuum modeling was exclusively performed by myself. The stellar evolutionary tracks were provided by S. Molinari and plot by myself. The SED using a the modified blackbody approach was setup and performed by myself. The derivation of the parameters of HII regions was done by myself and gained from useful discussions with Á. Sánchez-Monge.

Discussions with my collaborators and helpful comments from the referee.

Astronomy & Astrophysics manuscript no. sgrb2_continuum
February 5, 2016

The physical and chemical structure of Sagittarius B2

I. Three-dimensional thermal dust and free-free continuum modeling on 100 au to 45 pc scales

A. Schmiedeke[1], P. Schilke[1], Th. Möller[1], Á. Sánchez-Monge[1], E. Bergin[2], C. Comito[1], T. Csengeri[3], D.C. Lis[4,5], S. Molinari[6], S.-L. Qin[1,7], and R. Rolffs[1]

[1] I. Physikalisches Institut, Universität zu Köln, Zülpicher Straße 77, D-50937 Köln, Germany
email: schmiedeke@ph1.uni-koeln.de
[2] Department of Astronomy, The University of Michigan, 500 Church Street, Ann Arbor, MI 48109-1042, USA
[3] Max-Planck-Institut für Radioastronomie, Auf dem Hügel 69, D-53121, Bonn, Germany
[4] LERMA, Observatoire de Paris, PSL Research University, CNRS, Sorbonne Universités, UPMC Univ. Paris 06, F-75014, Paris, France
[5] California Institute of Technology, Pasadena, CA 91125, USA
[6] INAF - Istituto di Astrofisica e Planetologia Spaziali, via Fosso del Cavaliere 100, I-00133, Roma, Italy
[7] Department of Astronomy, Yunnan University, and Key Laboratory of Astroparticle Physics of Yunnan Province, Kunming, 650091, China

Received ; Accepted

ABSTRACT

Context. We model the dust and free-free continuum emission in the high-mass star-forming region Sagittarius B2.
Aims. We want to reconstruct the three-dimensional density and dust temperature distribution, as a crucial input to follow-up studies of the gas velocity field and molecular abundances.
Methods. We employ the three-dimensional radiative transfer program RADMC-3D to calculate the dust temperature self-consistently, provided a given initial density distribution. This density distribution of the entire cloud complex is then recursively reconstructed based on available continuum maps, including both single-dish and high-resolution interferometric maps covering a wide frequency range (ν = 40 GHz - 4 THz). The model covers spatial scales from 45 pc down to 100 au, i.e. a spatial dynamic range of 10^5.
Results. We find that the density distribution of Sagittarius B2 can be reasonably well fitted by applying a superposition of spherical cores with Plummer-like density profiles. In order to reproduce the spectral energy distribution, we position Sgr B2(N) along the line of sight behind the plane containing Sgr B2(M). We find that the entire cloud complex comprises a total gas mass of 8.0×10^6 $M_\odot$ within a diameter of 45 pc. This corresponds to an averaged gas density of 170 $M_\odot pc^{-3}$. We estimate stellar masses of 2400 $M_\odot$ and 20700 $M_\odot$ and luminosities of 1.8×10^6 $L_\odot$ and 1.2×10^7 $L_\odot$ for Sgr B2(N) and Sgr B2(M), respectively. We report H_2 column densities of 2.9×10^{24} cm^{-2} for Sgr B2(N) and 2.5×10^{24} cm^{-2} for Sgr B2(M) in a 40″ beam. For Sgr B2(S), we derive a stellar mass of 1100 $M_\odot$, a luminosity of 6.6×10^5 $L_\odot$ and a H_2 column density of 2.2×10^{24} cm^{-2} in a 40″ beam. We calculate a star formation efficiency of 5 % for Sgr B2(N) and 50 % for Sgr B2(M). This indicates that most of the gas content in Sgr B2(M) has already been converted to stars or dispersed.

Key words. radiative transfer – radio continuum: general – stars: formation – stars: massive – ISM: clouds – ISM:individual objects: Sgr B2

1. Introduction

Apart from in-situ measurements in the Solar System, all information gained in astrophysics is deduced from the analysis and interpretation of radiation received with ground or space-based telescopes. Gas and dust, in between the source and the telescope, influences the radiation. So analyzing the radiation received from an astrophysical object not only provides information about the source, but also about the medium in between the object and the observer. Radiative transfer is thus one of the most fundamental phenomena in astrophysics.

As summarized by Steinacker et al. (2013), three-dimensional dust radiative transfer calculations are essential to make progress in many fields of astronomy. Dust grains modify the radiation field in many objects such as protoplanetary disks, evolved stars, reflection nebulae, supernova remnants, molecular clouds, the interstellar medium, galaxies, galactic nuclei, and the high-redshift universe.

In this paper, we focus on the modeling of the dust and free-free continuum emission of the high-mass star forming molecular cloud Sagittarius B2 (hereafter Sgr B2) by applying detailed three-dimensional radiative transfer modelling.

Sgr B2 is one of the most massive molecular clouds in the Galaxy. It is located at a distance of 8.34±0.16 kpc (Reid et al. 2014)[1] and has a projected distance of 107 pc (or 43.4′) from Sgr A*, the compact radio source associated with the supermassive black hole located at the Galactic Center. Hüttemeister et al. (1993) distinguish three different parts in Sgr B2: (i) a low den-

[1] In this paper, we assume a distance to Sgr B2 of 8.5 kpc.

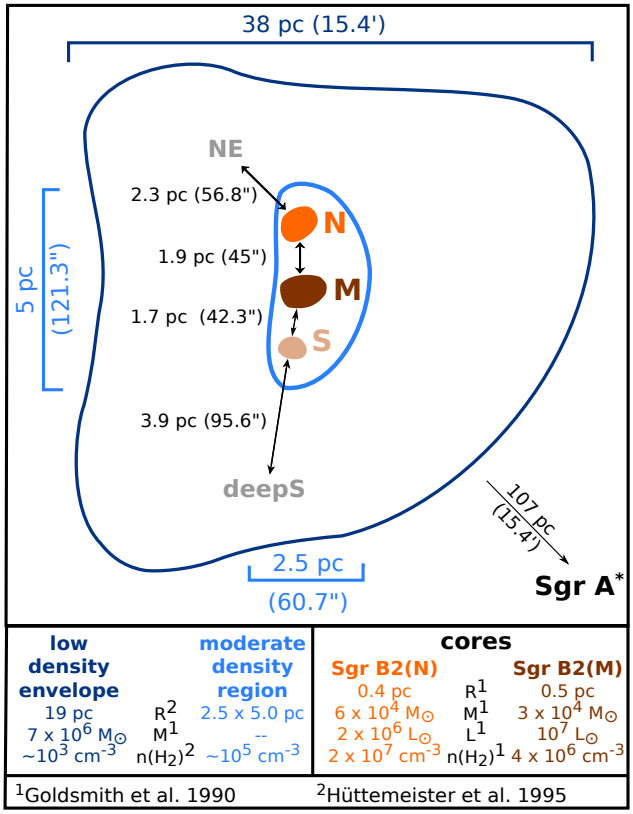

Fig. 1: Sketch of the Sgr B2 region, adapted from Hüttemeister et al. (1995).

sity envelope, (ii) a moderate density region extended around (iii) local hotspots, which are the most compact, densest molecular regions (see Fig. 1). The envelope measures 38 pc (or 15.4′) in diameter (Scoville et al. 1975, corrected for distance) and has a gas mass of 7×10^6 $M_\odot$ (Goldsmith et al. 1990). The average H_2 density $n(H_2) \sim 10^3$ cm^{-3}, and H_2 column density $N(H_2) \sim 10^{23}$ cm^{-2}, are relatively low compared to the central part of the region. The moderate density region extends over 2.5 pc × 5.0 pc around the local hotspots. Its density and H_2 column density are higher, $n(H_2) \sim 10^5$ cm^{-3} and $N(H_2) \sim 10^{24}$ cm^{-2}. Embedded in this intermediate region are the local hotspots. At least three of them are sites of active star formation (Gordon et al. 1993). These three sources are historically named according to their relative location in an equatorial coordinate system: Sgr B2(N)(orth), Sgr B2(M)(ain), and Sgr B2(S)(outh). They are positioned along a north-south line. In projection, Sgr B2(M) is located 1.9 pc (or 45″) south of Sgr B2(N) and Sgr B2(S) is located 1.7 pc (or 42.3″) south of Sgr B2(M), see Fig. 1. These cores have sizes of ∼ 0.5 pc, H_2 densities of $\sim 10^7$ cm^{-3}, and column densities of 10^{25} cm^{-2} (Hüttemeister et al. 1995). Different works, e.g. Goldsmith et al. (1990); Etxaluze et al. (2013), have derived the gas mass of the two cores Sgr B2(N) and SgrB2 (M) in the ranges of 6 – 25 × 10^4 $M_\odot$ and 3 – 23 × 10^4 $M_\odot$, respectively. However, they used different radii (0.4 – 1.6 pc), which makes a comparison of the results impossible.

Sgr B2(N) and Sgr B2(M) are sites of active massive star formation and comprise a plethora of (ultra-compact) HII regions, X-ray sources associated with HII regions, X-ray sources with no radio or IR counterparts (Takagi, Murakami & Koyama 2002), dense cores, embedded protostars, and molecular masers (Goicoechea et al. 2004). More than 70 HII regions have been detected in the whole Sgr B2 cloud complex (see Fig. A.1 ; Mehringer et al. 1993; Gaume et al. 1995; De Pree et al. 1998).

In the observed dust continuum maps, we see an extension of the cloud complex to the north-east. Following the historical naming scheme, we name this region Sgr B2(NE) throughout this paper. This component is located in projection 2.3 pc (or 56.8″) north-east of Sgr B2(N). Another extension is visible towards the south of the cloud. We will name this extension Sgr B2(deepS)outh throughout this paper. This component is located in projection 3.9 pc (or 95.6″) south of Sgr B2(S), see Fig. 1 .

The modeling of the continuum emission of the Sgr B2 complex presented here provides us with the three-dimensional model of the structure (density distribution) of this region. For this multiwavelength, multiscale data is crucial to properly constrain the structure. In the next step this will enable us to model the line shapes (kinematics) and thus constrain molecular gas properties such as the gas velocity field, molecular abundances, etc.

The paper is organized as follows: In Sect. 2 we introduce the observational dataset used throughout the paper. The modeling approach is presented in detail in Sect. 3 . This is followed by the application of the modeling approach to Sgr B2 and the discussion of the results in Sect. 4 . Finally the paper is concluded in Sect. 5. In Sect. A, we present additional figures and in Sect. B we tabulate the setup parameters of all models. In Sect. C we derive physical properties of HII regions.

2. Observations and data reduction

Multiwavelength, multiscale data is crucial to properly constrain the structure of Sgr B2. Towards the hot cores Sgr B2(N) and Sgr B2(M), the Herschel/HIFI spectral surveys provide the continuum information from the sub-mm up to the far-infrared regime. High-resolution interferometric maps towards both hot cores obtained with the Submillimeter Array (SMA) and the Very Large Array (VLA) provide the necessary spatial resolution on small scales. To cover the large-scale structure, we use dust continuum maps obtained within the surveys ATLASGAL and HiGAL, described in detail below. A summary of the data is presented in Table 1. Fig. A.6 provides an overview of the employed datasets and the spatial scales they cover.

2.1. Herschel / HIFI

The Herschel / HIFI guaranteed time key project HEXOS (Herschel / HIFI observations of EXtraOrdinary Sources; Bergin et al. 2010) includes full line surveys of Sgr B2(N) towards α_{J2000} = 17^{h}47^{m}19.88^s, δ_{J2000} = −28°22′18.4″ and Sgr B2(M) towards α_{J2000} = 17^{h}47^{m}20.35^s, δ_{J2000} = -28°23′3.0″, covering the frequency ranges of 480 – 1250 GHz and 1410 – 1910 GHz. The corresponding half-power beam widths are 44.9 – 17.2″ and 15.3 – 11.3″, respectively.

The spectral scans have been calibrated with HIPE version 10.0 (Roelfsema et al. 2012). The resulting double-sideband (DSB) spectra were reduced with the GILDAS CLASS[2] package. Basic data reduction steps included removal of spurious features or otherwise unusable parts of the spectra. The continuum emission was subtracted from the DSB scans by mostly zeroth, first- or more rarely second-degree polynomial fitting. The continuum-subtracted DSB data were deconvolved (sideband separation through pure χ^2 minimization; Comito & Schilke

[2] http://www.iram.fr/IRAMFR/GILDAS

Table 1: Summary of observational data.

Telescope	ν [GHz]	λ [μm]	resolution [″]	center coordinates RA, DEC (J2000) [17:47:s, -28:m:s]	map size [″ × ″]	incl. sources
large-scale						
VLA	23.1	13000	0.27×0.23[1]	20.166, 23:04.76	143×143	Sgr B2
APEX[2]	345	870	19.2	19.943, 23:01.62	1100×1100[3]	Sgr B2
Herschel[4]	600	500	42.5	19.639, 22:57.77	1100×1100[3]	Sgr B2
	857	350	30.3	19.791, 22:59.68	1100×1100[3]	Sgr B2
	1200	250	23.4	19.939, 23:01.64	1100×1100[3]	Sgr B2
Herschel[5]	4283	70	10.4	20.046, 23:02.89	1100×1100[3]	Sgr B2
small-scale						
VLA	40.8	7000	0.15×0.10[6]	19.902, 22:17.8	24×24	Sgr B2(N)
			0.15×0.10[6]	20.202, 23:05.3		Sgr B2(M)
	40.8	7000	0.049×0.079[7]	20.115 23:04.0	10×10	Sgr B2(M)
SMA	342	874	0.37×0.22[8]	19.883, 23:18.4	16×16	Sgr B2(N)
			0.37×0.22[8]	20.158, 23:05.0		Sgr B2(M)
single pointing						
Herschel[9]	480 – 1250	625 – 240	44.9 – 17.2	19.88, 22:18.4	—	Sgr B2(N)
				20.35, 23:03.0	—	Sgr B2(M)
	1410 – 1910	213 – 157	15.3 – 11.3	19.88, 22:18.4	—	Sgr B2(N)
				20.35, 23:03.0	—	Sgr B2(M)

Notes. [(1)] The VLA was in the DnCnBnA hybrid array configuration. [(2)] LABOCA instrument. This map has been combined with the Planck map. [(3)] The coverage of these maps is beyond the extent of Sgr B2. We have thus extracted cutouts. [(4)] SPIRE instrument. [(5)] PACS instrument. [(6)] The VLA was in the BnA hybrid array configuration. [(7)] The VLA was in the A array configuration. [(8)] The SMA was in the compact and in the very extended array configuration. Both data sets have been combined. [(9)] HIFI instrument.

2002) to provide an equivalent single-sideband (SSB) spectrum for each HIFI band.

Since a single full HIFI line survey is actually made up of 14 independent line surveys with seven different local oscillators (HIFI LO bands 1a through 7b), inconsistencies in the continuum level between HIFI bands were expected and indeed observed. A linear least squares fit of the subtracted continuum values as a function of local oscillator (LO) frequency provided a reliable — because unaffected by spectral features — parametrization of the continuum variation across each HIFI band, which was then folded back into each continuum-subtracted SSB spectrum.

Finally, the overall continuum was rendered self-consistent in two steps: the first adjustment consisted of an additive factor for each band, to achieve a zero-continuum level for the observed saturated absorption features. This is based on the absorption of molecules with a high dipole moment. These molecules are located in foreground, i.e. low density, clouds along the line-of-sight towards Sgr B2. Thus they will have a very low excitation temperature. The second adjustment required a multiplicative factor, in order for the continuum values in overlap regions between bands to be consistent with each other.

For Sgr B2(N), the additive factors range between -1.08 and 0.48 K, with a median of 0.05 K; the multiplicative factors range between 0.82 and 1.42, with a median of 1.00. For Sgr B2(M), the additive factors range between -0.87 and +0.34 K, with a median of 0.28 K; the multiplicative factors range between 0.86 and 1.42, with a median of 1.03.

2.2. Submillimeter Array (SMA)

Sgr B2 has been observed with the SMA in the compact and very extended configurations. The observations were carried out on June 11, 2010 using seven antennas and on July 11, 2010 using eight antennas. The phase tracking centers were $\alpha_{J2000} = 17^h47^m19.883^s$, $\delta_{J2000} = -28°22'18.4''$ for Sgr B2(N) and $\alpha_{J2000} = 17^h47^m20.158^s$, $\delta_{J2000} = -28°23'5.0''$ for Sgr B2(M). The data reduction and results are described in detail in Qin et al. (2011). The absolute flux scale is estimated to be accurate to within 20%. Both sources were observed in double-sideband mode, and covered rest frequencies from 342.2 to 346.2 GHz and from 354.2 to 358.2 GHz. The line-free channels have been used to reconstruct the continuum image. We have re-imaged the continuum maps with almost uniform weighting, resulting in a beam of $0.37'' \times 0.22''$, position angle (hereafter: PA) = 17.8 ° with a rms of ∼ 26 mJy/beam.

2.3. Very Large Array (VLA)

To constrain the location and physical parameters of the HII regions in Sgr B2, we used several different data sets obtained with the VLA.

2.3.1. Gaume et al. (1995) map at 1.3 cm covering Sgr B2

Gaume et al. (1995) observed Sgr B2 with the VLA in three configurations, BnA, CnB, and DnC, between February 1989 and October 1989. The central pointing position is $\alpha_{J2000} = 17^h47^m20.166^s$, $\delta_{J2000} = -28°23'4.76''$. The data set and its calibration is described in detail in Gaume et al. (1995). We

used an image of the combined DnCnBnA data, resulting in a beam of $0.27'' \times 0.23''$ (HPBW), PA = 70 °, with an rms of ∼ 0.38 mJy/beam.

2.3.2. Rolffs et al. (2011a) maps at 7 mm covering Sgr B2(N) and Sgr B2(M)

Sgr B2 has been observed with the VLA in the BnA hybrid configuration at 40.7669 GHz, corresponding to 7.5 mm (project AR687). The phase tracking centers were $\alpha_{J2000} = 17^h47^m19.902^s$, $\delta_{J2000} = -28°22'17.8''$ for Sgr B2(N) and $\alpha_{J2000} = 17^h47^m20.202^s$, $\delta_{J2000} = -28°23'5.3''$ for Sgr B2(M). Sgr B2(M) was observed on 2009 January 31, and Sgr B2(N) on February 1. The data set and its calibration is described in detail in Rolffs et al. (2011a). The continuum was fitted using line-free channels. We have re-imaged the continuum map with almost uniform weighting, resulting in a beam of $0.15'' \times 0.10''$ (HPBW), PA = 52.8 °, with a rms of ∼ 0.9 mJy/beam.

2.3.3. De Pree et al. (1998) map at 7 mm covering Sgr B2(M)

De Pree et al. (1998) observed Sgr B2(M) with the VLA using the A configuration on 1996 December 12, and 1997 January 17. The central pointing position is $\alpha_{J2000} = 17^h47^m20.115^s$, $\delta_{J2000} = -28°23'4.02''$. The data set and its calibration is described in detail in De Pree et al. (1998). The image we used has a spatial resolution of $0.049'' \times 0.079''$ (HPBW), PA = 11 °, with an rms of ∼ 0.5 mJy/beam.

2.4. APEX / ATLASGAL project

Carried out using the Large APEX BOlometer CAmera (LABOCA; Siringo et al. 2009), the APEX Telescope Large Area Survey of the Galaxy (ATLASGAL; Schuller et al. 2009) covers the full inner Galactic Plane at 870 µm with a resolution of 19.2″ and an rms below 70 mJy/beam. Each position of the inner Galatic plane has been mapped twice with different scanning directions to avoid striping, using the on-the-fly mapping technique. The pointing accuracy is of the order of 4″ and the flux calibration uncertainty is lower than 15 %. A detailed description of the data reduction is given in Csengeri et al. (2014). This map was recently cross-calibrated using the data of the Planck mission and the large-scale structure that is filtered out during the processing of the LABOCA data has been added back into the map (Csengeri et al. 2015, submitted). We use this improved map in our study.

2.5. Herschel / HiGAL project

The Herschel Hi-GAL survey (Molinari et al. 2010) provides photometric mid-IR observations at 70 µm and 160 µm using PACS (Poglitsch et al. 2010), and sub-milimeter observations at 250 µm, 350 µm, and 500 µm using SPIRE (Griffin et al. 2010). Sgr B2 was observed as part of the Field 0 observations covering the Galactic Center (OD 481; obsids 1342204102, 1342204103). The observations were carried out in PACS/SPIRE parallel mode with a fast scanning speed of $60''s^{-1}$. The data reduction is described in detail in Traficante et al. (2011). This dataset was cross-calibrated using the data of the Planck mission on the long-wavelength side and the data from the IRAS mission on the short wavelength side. The angular resolutions at the five wavelengths, listed by increasing wavelength, are 10.4″, 13.6″, 23.4″, 30.3″, and 42.5″ (Traficante et al. 2011). We note that the 160 µm PACS map is saturated towards Sgr B2(M) and N and is thus not used in our study.

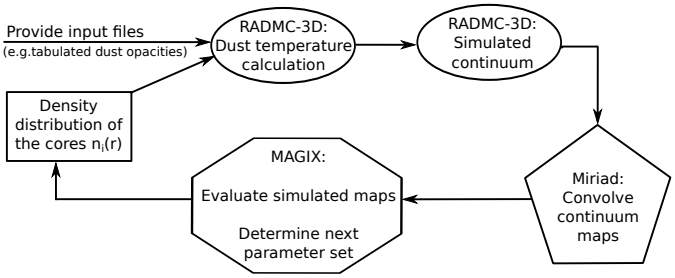

Fig. 2: Flowchart of the modeling framework pandora.

3. Modeling Procedure

We have implemented a framework called *pandora* that follows the flowchart shown in Fig. 2 for the continuum modeling. As part of this framework, we employ the three-dimensional, publicly available radiative transfer program RADMC-3D (Dullemond 2012, version 0.39), Miriad for the post-processing, and MAGIX (Möller et al. 2013) for the optimization of the model input parameters. We describe the model setup and physical parameters in the following subsections. RADMC-3D is written in Fortran90 and allows the user to setup their models in a non-invasive way, i.e. via a separate subroutine. In the following subsections we describe different parts of the setup of our model.

3.1. Coordinate system

We use a positively right-handed cartesian coordinate system. This means that the x-axis points west on the sky, the y-axis points to the north and the z-axis points towards the observer. The origin of this system is located at the center of the model, which is chosen to be Sgr B2(M), i.e. $\alpha_{J2000} = 17^h47^m20.172^s$, $\delta_{J2000} = -28°23'4.58''$.

3.2. Grid refinement

We want to recover the large dynamic range in spatial resolution from 38 pc, i.e. the diameter of the envelope (Scoville et al. 1975, corrected for distance) down to 100 au (small scale structure around the hot cores and HII regions). If we would attempt this with a cartesian grid, i.e. a grid where the elements are unit cubes, this would require 800 billion cells. This is not only computationally unfeasible but also unneccessary when e.g. the density distribution is flat.

We use the adaptive mesh refinement technique (originally presented by Berger & Oliger 1984; Berger & Colella 1989) to locally increase the spatial resolution of our numerical radiative transfer simulation. The initial grid consists of 11^3 cells. We employ the RADMC option to include a tree-based AMR method (Khokhlov 1998, and references therein). This means that, on a cell-by-cell basis, parent cells are refined into children cells resulting in a recursive tree structure. The resulting grid provides high resolution where needed based on the refinement criteria.

In our approach, two criteria are used to check if a cell needs to be refined: (i) the presence of a dust core center within the cell and (ii) the dust density distribution within the cell. Since we cover a large dynamical range, it is crucial to make sure that small clumps are recognized by the refinement routine. Thus as

long as the cell size is larger than twice the radius of a dust core, this cell is refined if the core center is located within the cell. A cell is also refined into eight sub-cells when

$$\frac{|n_{\rm center} - n_i|}{n_{\rm center}} > \epsilon, \tag{1}$$

where $n_{\rm center}$ is the density at the cell center and n_i is the density at the center of the faces or the corners of the cell and ϵ is the allowed maximum density difference, which is set to 10 %.

The grid is refined to level 13, i.e. at least one initial cell has been refined 13 times. This results in a minimum cell size of 100 au and in total ~68 million final cells.

3.3. Heating sources

RADMC-3D provides several methods to include luminous sources. We choose the option to manually specify the individual luminous sources and assume that all stars are point sources, i.e. their radius is not taken into account. We use a two-step approach. In the first step we account for observed early-type high-mass stars by including the known HII regions (Mehringer et al. 1993; Gaume et al. 1995; De Pree et al. 1998, see Table B.1 for a complete list of all parameters). Due to a revised distance of the Galactic Center we estimated the corresponding parameters, see Sect. 3.5. We specify their position and calculate the luminosity and temperature from the Zero-Age-Main-Sequence (hereafter: ZAMS) type using Table 5 from Vacca et al. (1996). Here we assume that each HII region is ionized by a single star. We use the RADMC-3D option to assume simple blackbody spectra for each star, by specifying their blackbody temperature. This accounts for stars down to the B0 spectral type.

In the second step we take later spectral types, i.e. stars which cannot produce HII regions detectable with current observations, with stellar masses between 0.01 $M_\odot$ and ~19.0 $M_\odot$, into account. We do this as follows: Based on the gravitational potential, our algorithm randomly determines positions for the new stars. For this, we follow the procedure explained in the appendix of Aarseth et al. (1974). A luminosity, which is randomly drawn from the initial mass function (IMF) of Kroupa (2001), is assigned to each star.

We do this as follows: Assuming a spherical symmetric star cluster, we specify the radius of this cluster. This radius is determined using a radial histogram of the distributed HII regions (see Fig. A.3). From Kroupa's IMF we then calculate the fraction $f_{\rm HM}$ of the stars in the high mass regime (i.e. between M_1 and M_2; $M_1 < M_2$) to the mass of all stars (i.e. between M_0 and M_2; $M_0 < M_1 < M_2$). The lowest mass boundary M_0 is provided, the mass boundaries M_1 and M_2 are set by the high-mass stars that were distributed within the cluster in the first step described above. The total stellar mass of the cluster $M_{\rm cluster}$ is then calculated from the ratio of the sum of the stellar mass of all high-mass stars distributed between M_1 and M_2 to the ratio $f_{\rm HM}$. We then randomly draw stars between M_0 and M_1 from the IMF until the total stellar mass of the cluster, $M_{\rm cluster}$, is reached.

The model can contain several of these star clusters. After the stars are sprinkled separately within each of these clusters, the entire envelope is treated as a cluster itself and the procedure is repeated once more, i.e. necessary stars are sprinkled everywhere except in the previously mentioned star clusters until the calculated total stellar mass of the computational domain is reached.

We then convert the stellar mass M to luminosity L using the parameterized mass-luminosity relation from Griffiths et al. (1988):

$$\log_{10}\left(\frac{L}{L_\odot}\right) = \begin{cases} 0.006 + 4.16\log_{10}\left(\frac{M}{M_\odot}\right), \\ \qquad\qquad 0.682 < \log_{10}\left(\frac{M}{M_\odot}\right) < 0.461 \\ 0.370 + 3.51\log_{10}\left(\frac{M}{M_\odot}\right), \\ \qquad\qquad \log_{10}\left(\frac{M}{M_\odot}\right) > 0.461 \end{cases} \tag{2}$$

Griffiths et al. (1988) provide two sets of boundaries. One is non-continuous but has a better χ^2 value whereas the other set, which we choose to use, provides a continuous behaviour of the mass-to-luminosity relation while having a slightly worse χ^2 value.

We only include luminosity in terms of ZAMS luminosity. The total luminosity determined in the literature, however, includes contributions from accretion luminosity, as well as from high-mass stars without an HII region (Hosokawa & Omukai 2009). We thus note that the luminosity calculated with our approach is a lower limit. We determine the corresponding effective temperatures of the stars using the fundamental stellar parameters (spectral type, luminosity, effective temperature) compiled by Straizys & Kuriliene (1981). Since we need to provide an effective temperature for each star, the limitation of the tabulated data sets the lower mass limits of the star clusters to 0.2 $M_\odot$.

3.4. Dust density distribution

The overall density structure is obtained by the superposition of the density profiles of all dust cores, i.e. in overlap regions, the density simply adds up. In each cell j, the density is determined as

$$n_j = \sum_{i=1}^{N} n_{i,j}(\boldsymbol{r}) \tag{3}$$

where i is the index of the dust cores and N is the number of cores. Following Qin et al. (2011), we use a modified Plummer-like profile to model the SMA dust density cores as well as the large-scale envelopes. For a subset of our models, we find it useful to introduce elongated density structures (see Sect. 4). We define them as follows:

$$n_i(\boldsymbol{r}) = \frac{n_c}{(1 + |\boldsymbol{r}|^2)^{\eta/2}} \tag{4}$$

where n_c is the central density given in H_2 cm^{-3} and $\boldsymbol{r}$ is given by the Euclidean norm, including scaling factors

$$|\boldsymbol{r}| = \sqrt{\left(\frac{r_x}{r_{0,x}}\right)^2 + \left(\frac{r_y}{r_{0,y}}\right)^2 + \left(\frac{r_z}{r_{0,z}}\right)^2} \tag{5}$$

where $r_{x,y,z}$ are the components of r and $r_{0,x}$, $r_{0,y}$, and $r_{0,z}$ set the size of the cluster core in each of the three principal axes. A spherical symmetric distribution is obtained by setting $r_0 = r_{0,x} = r_{0,y} = r_{0,z}$. The density distribution is flat inside the radius r_0 and approaches a power-law with an exponent η at $r \gg r_0$.

3.5. HII regions

In our model, we consider HII regions as Strömgren spheres, i.e. as a fully ionized, spherical regions of uniform electron density with no dust. There are more than 70 HII regions known in Sgr B2 (Mehringer et al. 1993; Gaume et al. 1995; De Pree et al. 1998).

We obtained the high-resolution interferometric maps presented in Gaume et al. (1995) and De Pree et al. (1998) and performed the following analysis steps. HII regions come in many different shapes, which makes them hard to fit with Gaussians. So in order to match them as best as possible with spheres, we masked everything below three times the rms in the continuum maps and by eye inspection adjusted circles to enclose the observed HII regions. We then integrated the enclosed flux and assuming optical thin emission and a homogeneous, non-expanding HII region, we calculated the number electron density n_e, the emission measure EM, and the number of ionizing photons $\dot{N}_i$ using the following formulas.

$$\left(\frac{\mathrm{EM}}{\mathrm{pc\ cm^{-6}}}\right) = 3.217\times10^{7}\left(\frac{F_\nu}{\mathrm{Jy}}\right)\left(\frac{T_e}{\mathrm{K}}\right)^{0.35}\left(\frac{\nu}{\mathrm{GHz}}\right)^{0.1}\left(\frac{\theta_{\mathrm{source}}}{\mathrm{arcsec}}\right)^{-2} \quad (6)$$

$$\left(\frac{n_e}{\mathrm{cm^{-3}}}\right) = 2.576\times10^{6}\left(\frac{F_\nu}{\mathrm{Jy}}\right)^{0.5}\left(\frac{T_e}{\mathrm{K}}\right)^{0.175}\left(\frac{\nu}{\mathrm{GHz}}\right)^{0.05}\left(\frac{\theta_{\mathrm{source}}}{\mathrm{arcsec}}\right)^{-1.5}\left(\frac{D}{\mathrm{pc}}\right)^{-0.5} \quad (7)$$

$$\left(\frac{\dot{N}_i}{\mathrm{s^{-1}}}\right) = 4.771\times10^{42}\times\left(\frac{F_\nu}{\mathrm{Jy}}\right)\left(\frac{T_e}{\mathrm{K}}\right)^{-0.45}\left(\frac{\nu}{\mathrm{GHz}}\right)^{0.1}\left(\frac{D}{\mathrm{pc}}\right)^{2} \quad (8)$$

Here F_ν is the flux density of the HII region, T_e is the electron temperature, ν is the frequency, D is the distance to the source, and θ_{source} is the angular diameter of the HII region. A derivation of these formulas can be found in the appendix C.

Deriving the number electron density at a certain frequency from the observed flux density assuming optical thin emission will underestimate the number electron density if the HII region is actually optically thick. This underestimate will then lead to the intensity of the (optically thick) HII region being underpredicted by the simulation compared to the observed data at this frequency. To account for this discrepancy, we compare the synthetic intensities obtained from our model setup (see Sect. 3.7) with the observed intensities. From the deviation of the intensity levels, we identify the HII regions which must be optically thick. We then iteratively adjust the flux density values and recalculate the number electron density n_e, the emission measure EM, and the number of ionizing photons $\dot{N}_i$ until we obtain a resonably good match between the observed and synthetic intensities. As our main goal is to model the dust emission here we need to derive the free-free contribution from the HII regions. Hence we did not aim at a very sophisticated model of the HII regions, which would have to include a different geometry and a density structure.

The HII regions detected by Mehringer et al. (1993) were included according to the parameters stated therein. However, Mehringer et al. (1993) assumed a source distance of 7.5 kpc. We have thus re-calculated the radii and the parameters stated above for a distance of 8.5 kpc. But we have not corrected the values to account for the optical depth effects. Thus we note that these values are a lower limit. All parameters, including the radii and the precessed coordinates, are listed in Table B.1.

3.6. Dust temperature calculation

The dust temperature is calculated self-consistently by RADMC-3D using the Monte Carlo method of Bjorkman & Wood (2001), with various improvements, such as the continuous absorption method of Lucy (1999). Initially, all cells have a dust temperature equal to zero. To determine the dust temperature, RADMC-3D first identifies all sources of luminosity, i.e. the total amount of energy available. This amount is divided into photon packages, which are separately emitted by the individual stars one after another. As the photon packages move through the grid, they interact with the dust present (scattering, absorption) causing them to change their direction or wavelength. In the case of absorption, the photon package is immediately re-emitted in a different direction with another wavelength according to Bjorkman & Wood (2001). However, the luminosity fraction each photon package represents remains the same. Whenever a photon package enters a cell, it increases the energy of that cell and thus also increases the temperature of the dust. Photon packages never get lost, they can only escape the model through the outer edge of the grid. After the last photon package has escaped the grid, the dust temperature is obtained. In summary the dust temperature of each cell is basically the sum of the energy fractions of each photon package passing through the cell. In total we use 10 million photon packages.

The calculated temperature is an equilibrium dust temperature, since it is assumed that the amount of energy each dust grain acquires and re-radiates stays the same. For most cases, this is presumably a very good approximation, because the heating and cooling timescales for dust grains are typically very short, compared to any time-dependent dynamics of the system (Choudhury et al. 2015). Thus transiently heated small grains are not important within the wavelength range considered here.

Note, we only consider stars as heating sources (see Sect. 3.3). The calculated dust temperature in the outer parts of the envelope is on average 12 − 15 K. Modified blackbody fitting of SCUBA data (Pierce-Price et al. 2000) and Herschel data Etxaluze et al. (2013) yields average dust temperature values for Sgr B2 (along the line-of-sight) of ∼ 20 K. Apart from line-of-sight effects in the modified blackbody fitting, which do not influence the modeling, part of this discrepancy is most likely due to heating by sources not considered here, e.g. cosmic rays or coupling with the turbulently heated gas.

We furthermore make use of the Modified Random Walk (MRW) method that is implemented in RADMC-3D in the simplified form described in Robitaille (2010). This method prevents a photon package from getting trapped in high-density regions by predicting where the photon will go next. This allows RADMC-3D to make one single large step of the photon package, saving the computation time for the otherwise necessary hundreds or thousands of absorption or scattering events.

3.7. Images and post-processing

We use one dust species throughout the model and do not include scattering events. We use the tabulated dust opacity from Ossenkopf & Henning (1994) for dust without grain mantles and no coagulation, as found to best fit the Sagittarius B2 region by Rolffs et al. (2011b). Including the free-free emission we cover the frequency range from 40 GHz up to 4 THz. Continuum maps at various wavelengths of interest are produced with RADMC-3D.

In order to compare the synthetic maps with real obervations, telescope-dependent post-processing is necessary. For this pur-

pose we employ the data reduction package Miriad (Sault et al. 1995). In case of interferometric observations, we fold the simulated maps with the uv-coverage. The imaging is then performed for both maps (synthetic and observed) with the same imaging parameters. In case of single dish observations, the synthetic maps are convolved with the beam of the telescope at that frequency, which we assumed to be Gaussian. Final maps are then produced for the respective telescopes at various wavelengths in intensity units (Jy/beam).

3.8. Fitting procedure

Three-dimensional modelling intrinsically has many free parameters. For this initial study, we have focused on deriving the density field for a fixed dust setup and, apart from by-hand adjustments to account for optical depths effects, fixed HII regions. Still, the amount of free parameters is large. We have 20 dust core components and 9 components for the large-scale envelope. For each component we modified, in order of increasing importance, the density exponent, a stellar heating source and accordingly a stellar cluster, the position along the line of sight, the displacement in right ascension and declination, the radius and the central density. In total this amounts to approximately 140 free parameters, many of them degenerated.

Concerning the position along the line-of-sight we unfortunately only have limited constraints available for certain sources to fix the three-dimensional structure on all scales. For optically thin radiation, there is no information on the line-of-sight structure. Optically thick radiation comes from a photospheric surface where the opacity exceeds unity. Thus, maps from different wavelengths, with different opacities tracing different radii, can give some constraints on the relative positions of sources along the line-of-sight, but in general it is not possible to fix the absolute positions along the line-of-sight. The more observational data is available the better the full three-dimensional structure could be deduced. We have thus only varied the line-of-sight position in a very limited way. More will be possible when fitting individual molecular lines, because multiple lines from many isotopologues of the same species provide many more surfaces with the opacity exceeding unity, allowing a tomography of the source.

Exploring the complete parameter space of all remaining free parameters is prohibitive in terms of computing time. Thus, we used a hybrid approach to constrain the other parameters mentioned. First, we derive a good guess by varying parameters by hand, and judging the quality visually (χ^2-by-eye). This enabled us to fix the exponent, the presence of stellar heating source/star clusters and the displacement in right ascension and declination. We then employed the model optimizer MAGIX (Möller et al. 2013) to iteratively search for the best solution, i.e. the parameter set with the lowest reduced χ^2 value. For this run, we use the Genetic Algorithm, leaving the central densities and the radii as free parameters. The contribution from the HII regions (e.g. number electron density) was kept fixed during the entire fitting procedure.

We fit the 874 GHz SMA maps, 480 – 1280 and 1440 – 1900 GHz HIFI spectral scans as well as the large scale maps from ATLASGAL at 850 μm, HiGAL SPIRE at 500, 350 and 250 μm and HiGAL PACS at 70 μm.

In total, we have run approximately 2×10^4 different models (multi-core). The runtime for a single run varies between 0.5 and 6.0 hours, depending on the density structure, which, e.g. affects the number of final cells in the grid.

4. Analysis and Discussion

Within the scope of this paper, we will focus the analysis on the regions for which a wealth of data is available, namely Sgr B2(N), Sgr B2(M), and partly Sgr B2(S). We included Sgr B2(NE) and Sgr B2(deepS) in the model. However, we did not attempt to fit these components, since the available dataset is scarce.

4.1. Large scale dust continuum

To recover the large scale structure of the envelope, as visible in the ATLASGAL and Hi-GAL intensity maps, we superimpose many density components having profiles with varying exponents (see Sect. 3.4). While fitting the large-scale dust continuum maps, we noted the following problem. For a model where the density profile for each component is spherically symmetric and all components are located in the z=0 plane (Model A), the 70 μm intensity was always overestimated and the 870 μm intensity was underestimated, especially for the two cores Sgr B2(N) and Sgr B2(M).

By moving Sgr B2(N) along the line of sight behind the plane containing Sgr B2(M) as suggested by e.g. Goldsmith et al. (1990) (Model B), the emission from Sgr B2(N) gets attenuated by the envelope of Sgr B2(M) and an improved fit is possible. However, the general trend of the overestimation of the intensity at 70 μm and underestimation of the intensity at 870 μm remains, especially for Sgr B2(M). This is a sign of the dust column density being underestimated and the luminosity being overestimated.

In a first approach, we have reduced this effect by assuming that the envelopes of both, Sgr B2(N) and Sgr B2(M) are elongated along the line-of-sight, i.e. they basically look like a cigar (Model C). We achieved an improved fit by increasing the radii along the line-of-sight by factors of 1.4 and 2.3 for Sgr B2(N) and Sgr B2(M), respectively. At 70 μm the dust becomes optically thick. So by increasing the dust column density along the line-of-sight, we are able to hide the contribution from the stars. On the other hand, this approach increases the intensity at 870 μm, because it increases the total dust column density, which is proportional to the intensity of the optically thin 870 μm emission.

Another solution would be to decrease the luminosity. The luminosity was calculated assuming a single ionized star in each HII region. However, besides the Lyman continuum emission from the early-type star, additional UV photons could be emitted from accretion shocks in the stellar neighborhood (Cesaroni et al. 2016, submitted) which would lead to assigning an earlier spectral type and thus overestimating the total luminosity. To test this possibility, we have multiplied the luminosity by an arbitrary factor of 0.5 (Model D). While doing so, we of course needed to increase the density to preserve the 870 μm fluxes. In this approach, there was no need for the elongated envelope, except for Sgr B2(M), where the envelope is still slightly elongated. However, the observational and theoretical evidence of this Lyman continuum overluminosity seems to be mainly given for B-type stars (Sánchez-Monge et al. 2013; Smith 2014). Thus it is unclear if O-type stars exhibit the same behavior. Furthermore, the effect of dust inside the HII regions has not been assessed. This will be part of future work, see Sect. 6.

We have kept the number of components in all these models fixed. All parameters of each component are listed in Table B.3. To facilitate the comparison of these different models, we have produced cuts of the intensity along the reversed right as-

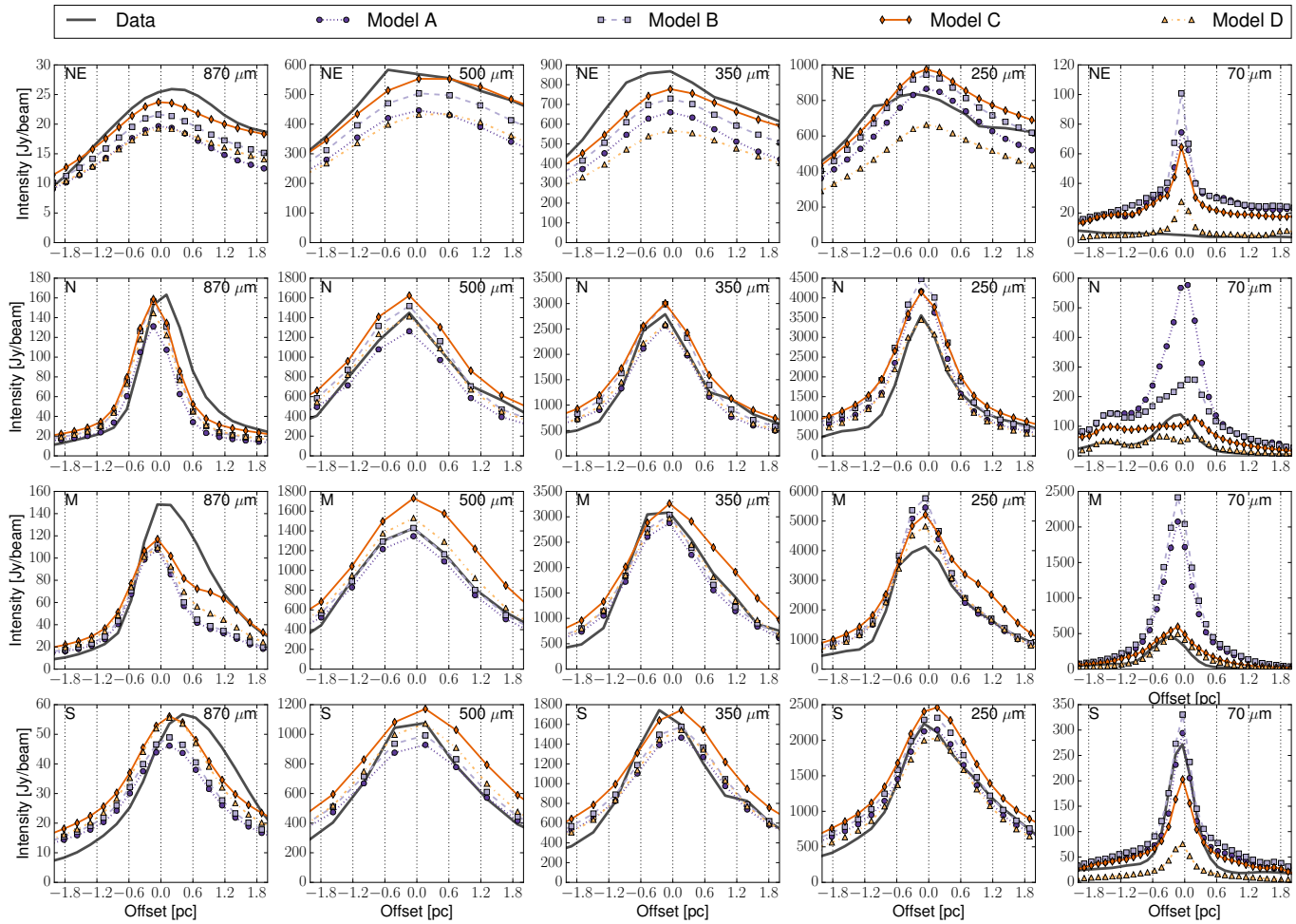

Fig. 3: Intensity cuts along the reversed right-ascension axis at the constant declination of the envelope components of Sgr B2(NE), Sgr B2(N), Sgr B2(M), and Sgr B2(S) from top row to bottom row. The data is plotted in solid black. The wavelength decreases from left to right: 870 μm, 500 μm, 350 μm, 250 μm, and 70 μm. Model A is denoted by the circular markers, Model B by the squared markers, Model C by the diamonds shaped markers and model D by the triangular markers.

cension axis at the constant declination of the components Sgr B2(NE), Sgr B2(N), Sgr B2(M) and Sgr B2(S). These cuts are shown in Fig. 3. For comparison, we also show the observed and synthetic azimuthally averaged radial profile for all four models of the same components in Fig. A.4. We present the ATLASGAL 870 μm, HiGAL-SPIRE 500, 350 and 250 μm, and the HiGAL-PACS 70 μm from left to right, i.e. the wavelength decreases from left to right. These different models show that there is a degeneracy between the dust density, luminosity and the relative location of the different dust density centers and star clusters along the line of sight. So in summary Model A overestimates the 70 μm intensity for both, Sgr B2(N) and Sgr B2(M) while underestimating the intensity for both regions at 870 μm. Model B only improves the discrepancy for Sgr B2(N), but still gives a bad fit for Sgr B2(M). These two models are thus clearly unfavorable to proceed the analysis with them. Model D provides an improved fit, however it remains unclear to which degree the luminosity could be adjusted. We thus choose to use Model C for the following analysis, since it provides a reasonably good fit for Sgr B2(N) and Sgr B2(M) without assuming any modification of the luminosity.

The resulting large-scale single-dish maps of Model C are shown in Fig. 4 . The first row shows the observed maps, the second row the synthetic maps and the third row is a simple difference map between the observed data and synthetics maps. From left to right we have again the same wavelengths as in Fig. 3: ATLASGAL 870μm, SPIRE 500 μm, SPIRE 350 μm, SPIRE 250 μm, and PACS 70 μm. In the observed maps, the two hot cores Sgr B2(N) and Sgr B2(M) are clearly visible. The extension to the north-east, i.e. Sgr B2(NE), and the one to the south, i.e. Sgr B2(S), are also distinguishable.

In both the observed and the synthetic maps, the intensity of Sgr B2(M) is stronger than Sgr B2(N) except for 870 μm where the opposite is the case. So the model reproduces the general behaviour, but is currently incapable to reproduce the absolute intensities. Especially in Sgr B2(M), the model underestimates the flux at 870 μm and slightly overestimates the flux at 70 μm. The observed maps and the intensity cuts (see Figs. 3 and 4) furthermore show a clear asymmetry, i.e. the profile of the continuum emission has at all wavelengths a slope that is steeper on the east side of the peak than on the west side. To quantify the difference of these slopes, we have fitted the intensity profiles, $I \propto r^{-p}$, of Sgr B2(N), Sgr B2(M) and Sgr B2(S) for the wavelengths 870, 500, 350, and 250 μm. For the east side of the peak, we obtain an averaged p of 1.0 and for the west side of the peak we obtain an averaged p of 0.4. Looking at the slopes for the individual sources, we furthermore find that the steepness of the west side of the peak remains unchanged with declination,

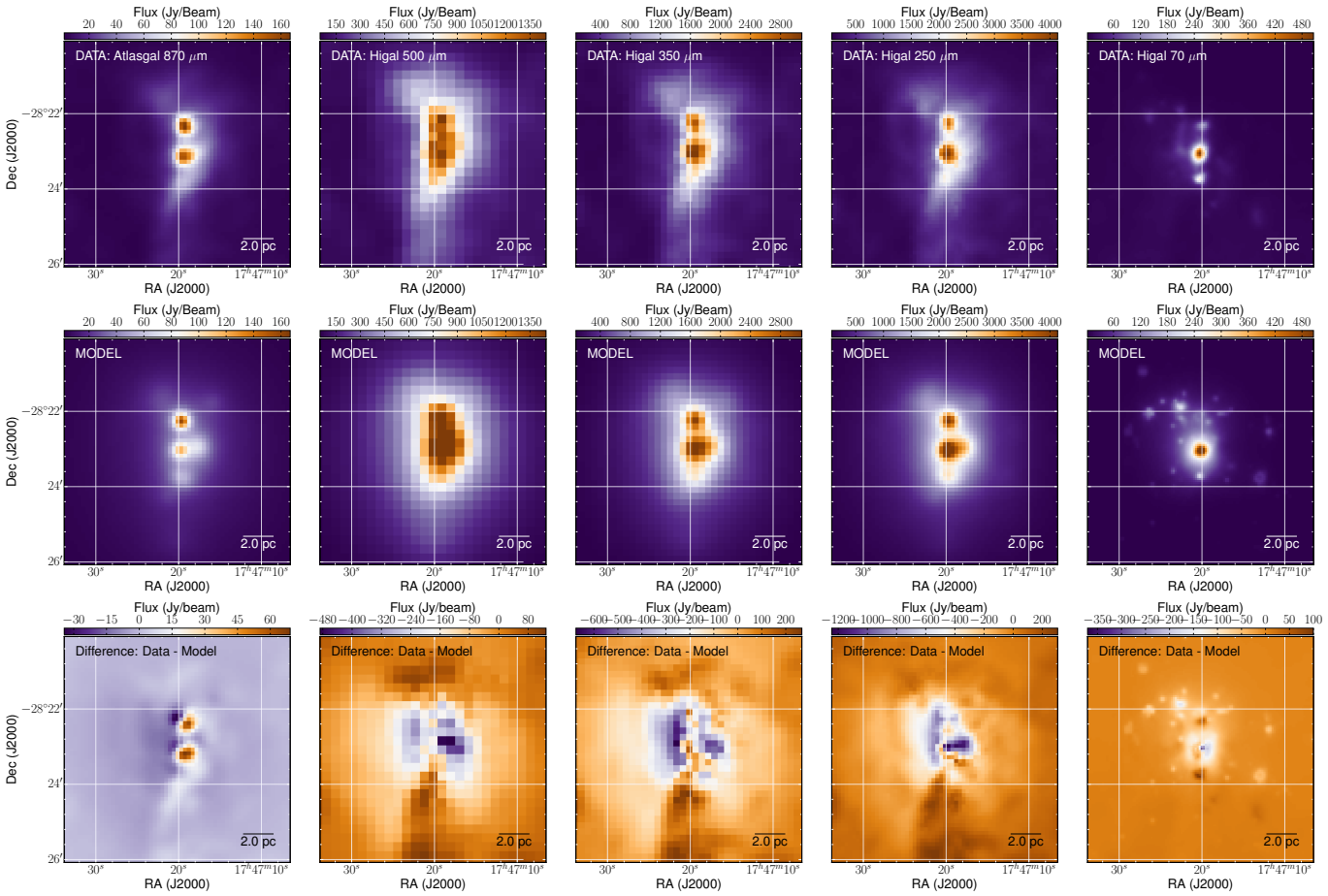

Fig. 4: Sgr B2, large scale continuum maps (Model C). From left to right: ATLASGAL 870 µm, Hi-GAL 500 µm, 350 µm, 250 , and 70 µm. First row: Data. Second row: Simulation. Third row: Difference between data and simulation.

whereas the steepness of the east side of the peak changes significantly with declination. For Sgr B2(N) and Sgr B2(M), p is on average 1.2, whereas it is 0.7 for Sgr B2(S). This asymmetry is impossible to account for using a single spherically symmetric component. If the slope of the intensity profile, i.e. the column density distribution, is p, then the slope of the density profile should be $p + 1(= \eta)$. So based on the fitting of the intensity profile, the east wing should have a density exponent of $\eta = 2.0$ and the west wing should have a density exponent of $\eta = 1.4$.

In the model, we are able to approximate the asymmetry by using a superposition of two components with different exponents for each clump. The east wing is fitted with a density profile having an exponent of $\eta = 2.5$, whereas the west wing is fitted with a density profile having a lower exponent of $\eta = 1.8$. These exponents are in good agreement with the ones derived from the intensity profile fitting mentioned above. This clearly shows that our assumption of spherically symmetric clumps as basis limits the modeling effort.

In addition, it is noticeable that the peak of the intensity profiles is shifted to the west in the 870 µm ATLASGAL maps compared to all Hi-GAL maps by ≈ 0.2 pc, corresponding to $\approx 5''$. This is well within the relative pointing error of the ATLASGAL map (pointing accuracy $\sim 4''$) and the Hi-GAL maps (pointing accuracy $\sim 1''$). Thus we do not attempt to reproduce this shifting ot the peak with our model.

4.2. Small scale dust and free-free continuum

The interferometric maps covering spatial scales up to ~ 0.25 pc are shown for Sgr B2(M) in Fig. 5 and for Sgr B2(N) in Fig. 6. We refer to these spatial scales as the small-scale structure. In addition to the intensity maps at different wavelengths, we also show the physical setup of Sgr B2(M) in Fig. 7. We plot three density isocontours colored using the dust temperature. To allow a view inside the model, we cut it open along the (x, y, 0)-plane. The bubbles visible there are the HII regions that contain no dust. Their dust surface however gets heated by the UV radiation field from the embedded young stellar object. Dust temperatures as high as 600 K are reached.

For the dust cores we find, similar to Qin et al. (2011, for Sgr B2(N)) and Rolffs et al. (2011c, for the hot molecular core G10.47+0.03), a Plummer exponent of $\eta = 5.0$ reproducing the small-scale density structure well. For a comparison, we plot the observed and synthetic azimuthally averaged radial profile of each component in Fig. A.5. The parameters of all dust cores are listed in Table B.2. Note that for some of the dust cores, we had to include an internal heating source by placing B-type stars at the center of the core. These could be e.g. stars that do (not yet) show signs of an HII region. This is also documented in the above mentioned Table B.2. We also had to shift a few of the many HII regions in Sgr B2(M) behind the dust components to produce a good fit. Please note that at frequencies higher than 100 GHz only one high resolution dataset is available in this modeling procedure. Thus our resulting density distribution is

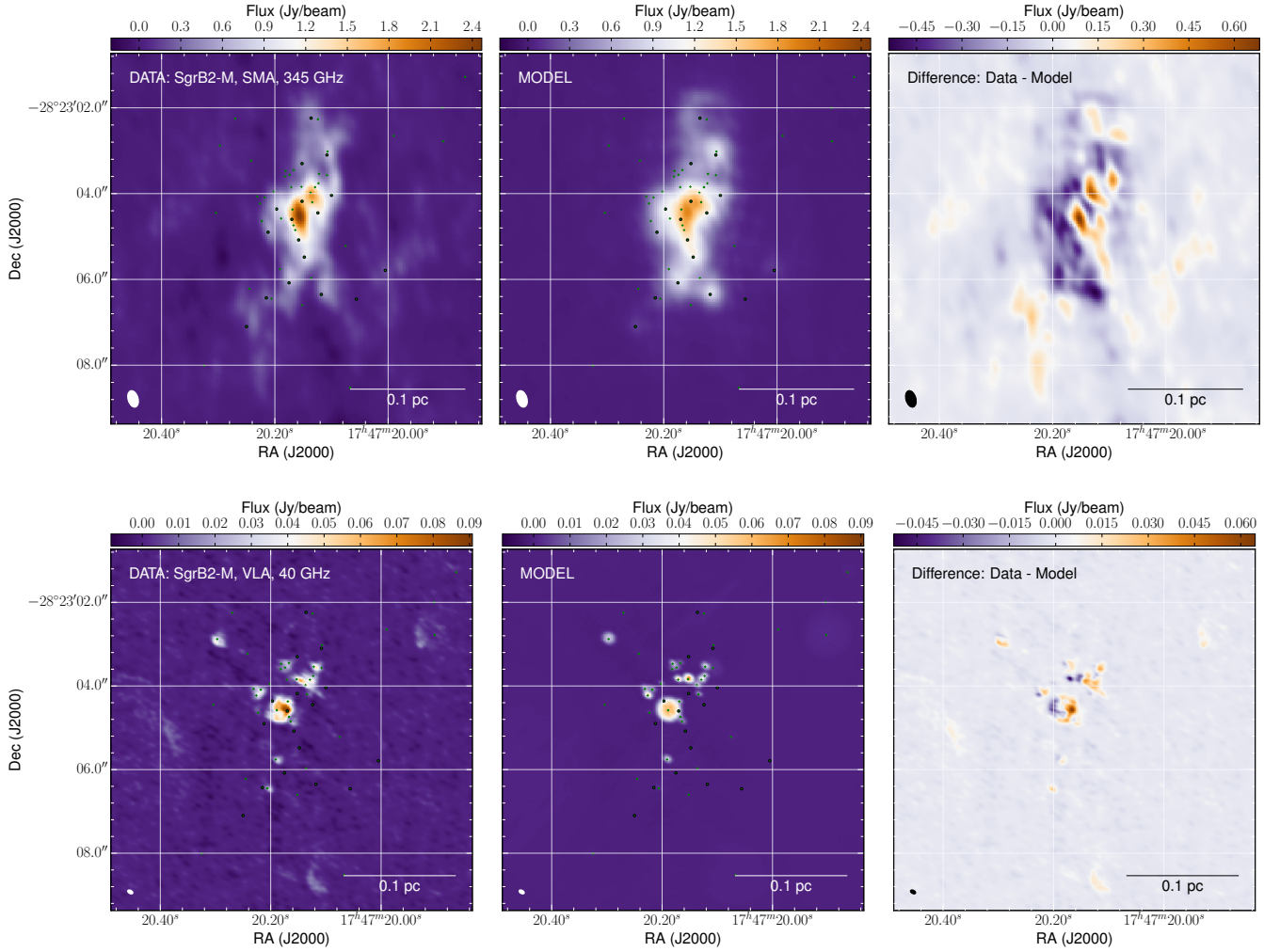

Fig. 5: Interferometric maps of Sgr B2(M). Top row: SMA dust continuum map at 870 µm (i.e. 345 GHz). Bottom row: VLA free-free continuum map at 7 mm (i.e. 40 GHz). Left column: Observations. Middle column: Synthetic maps. Right column: Difference plot. The field of view is the same for both rows. The green pluses denote the center of the HII regions and the black circles denote the center of the density cores.

only one possible solution. Other density distributions, e.g. dust cores with a lower exponent and a smaller radius, might yield similar good fits.

However, when comparing Sgr B2(M) and Sgr B2(N) a clear difference is noticeable. Sgr B2(M) appears to be more fragmented compared to Sgr B2(N), which appears rather monolithic. This has already been noticed by Qin et al. (2011). The model presented here allows us, however, to quantify this difference further. We will do this especially in subsection 4.4. But first we have a look at the stellar population.

4.3. Heating sources

For all four models, we used the same stellar distribution. We account in total for four stellar clusters: Sgr B2(NE), Sgr B2(N), Sgr B2(M), and Sgr B2(S). In Fig. A.3, we plot for each of these clusters a radial distribution histogram of all high-mass stars placed in the model based on observed HII regions (see Sect. 3.5). We use these histograms to determine by-eye the star cluster radii of 0.8, 0.4, 0.5, and 0.35 pc for Sgr B2(NE), Sgr B2(N), Sgr B2(M), and Sgr B2(S), respectively. Within these radii we sprinkle stars separately for each cluster (see Sect. 3.3). We then treat Sgr B2 as a cluster itself and continue to sprinkle stars everywhere, except in the previously mentioned star clusters, until the calculated total stellar mass of Sgr B2 is reached. We call this part the envelope of Sgr B2. The stellar density distribution is plotted in Fig. 8 and the mass distribution of the stellar mass produced with this approach (including the high-mass stars placed by hand) is shown in Fig. 9. Instead of plotting a histogram, we use a kernel density estimate. A histogram has several disadvantages. It is unsmooth and it depends on the end points as well as on the widths of the bins. By using a smooth kernel we obtain a smooth distribution that is independent of the choice of the end points of the bins and only depends on the chosen bandwidth. For our kernel density estimate a bandwidth of 0.217 $M_\odot$ has been calculated in linear space.

The results of applying this star sprinkling algorithm are listed in Table 2. For each cluster we list the radius, the number of initial stars, the total number of stars, the enclosed stellar mass, and the luminosity from the initial and all stars, respectively. Where available, we also list luminosities from Lis & Goldsmith (1990) as a reference. Additionally, this table lists the enclosed gas mass for each of the clusters. It is calculated from

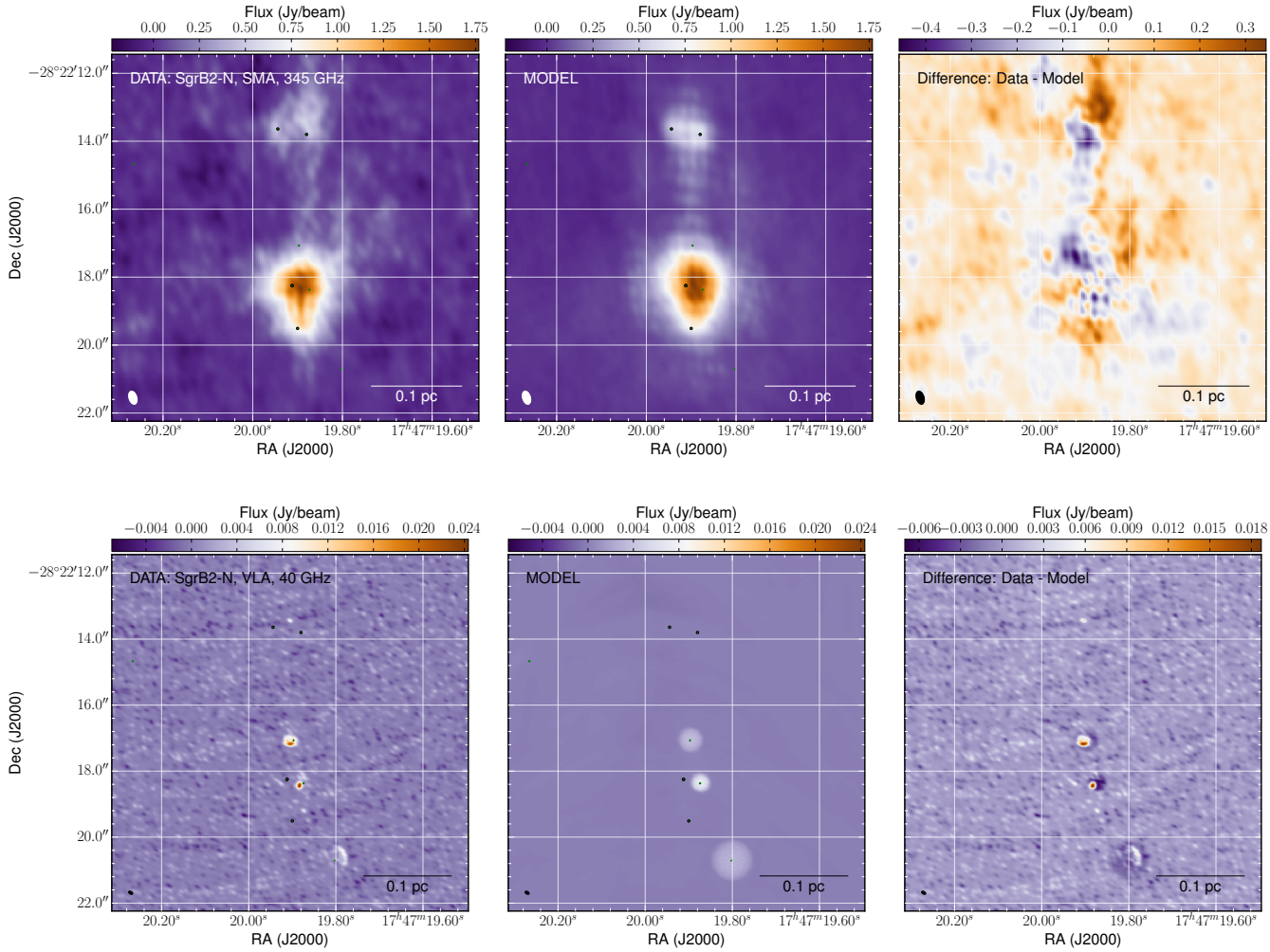

Fig. 6: Same as Fig. 5 for Sgr B2(N).

Table 2: Summary of the star clusters.

	radius [pc]	no. stars (initial)	no. stars (all)	M_* [$M_\odot$] (initial)	M_* [10^3 $M_\odot$] (all)	M_{gas} [$M_\odot$]	L [10^6 $L_\odot$] (initial)	L [10^6 $L_\odot$] (all)	L^a [10^6 $L_\odot$]
Sgr B2(NE)	0.8	2	1282	52	1.2	7777	0.54	0.80	—
Sgr B2(N)	0.4	6	2642	150	2.4	27897	1.38	1.80	1.7
Sgr B2(M)	0.5	60	22705	1295	20.7	9572	7.78	12.10	13.0
Sgr B2(S)	0.35	2	1204	50	1.1	4472	0.45	0.66	—
Envelope	–	19	8929	446	8.0	—	3.32	4.70	—
Sgr B2	22.5	89	36762	1993	33.4	8.0×10^6	13.47	20.06	—

Notes. [(a)] Lis & Goldsmith (1990, their models C)

the dust density distribution assuming a gas-to-dust ratio of 100 (Hildebrand 1983). We calculate the stellar luminosity to mass ratio as 90 $L_\odot M_\odot^{-1}$, 71 $L_\odot M_\odot^{-1}$, 1176 $L_\odot M_\odot^{-1}$, and 120 $L_\odot M_\odot^{-1}$ for Sgr B2(NE). Sgr B2(N), Sgr B2(M), and Sgr B2(S), respectively.

In their appendix, Belloche et al. (2013) also estimate the stellar mass of the entire Sgr B2 region by extrapolating the already distributed stellar mass of all stars embedded in observed ultra-compact HII regions using different IMFs. We apply the same method. However, our total stellar mass is an order of magnitude higher than their result. This difference is explained by the different initial parameters applied and different conversion tables for spectral type to stellar luminosity used. Belloche et al. (2013) calculate a total stellar mass of 675 $M_\odot$ for the 41 ultra-compact HII regions they account for. Their lowest mass star has a mass of 11 $M_\odot$ using the conversion table from Panagia (1973). Using Kroupa's IMF, they extrapolate a total stellar mass of $\sim$ 3900 $M_\odot$ for the mass range of 0.01 – 120 $M_\odot$. In our study, we

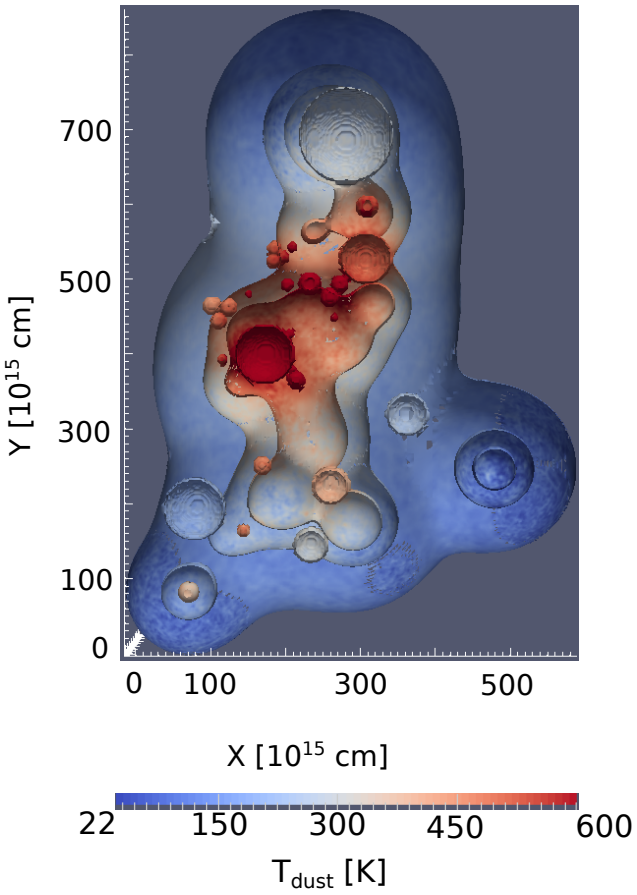

Fig. 7: Impression of the 3d view of the dust density distribution in Sgr B2(M). Three density isocontours are presented, i.e. at densities of $10^{-17.5}$, 10^{-18}, and 10^{-19} g cm^{-3}. They are colored using the dust temperature. The model is cut open at the model center to allow a view inside. The bubbles are the empty half-shells of the distributed HII regions, which are free of dust. The dust on the surface of these HII regions is heated by the UV radiation field from the young stellar object embedded in the HII region. This dust is thus very hot, exceeding dust temperatures of 600 K (dark red spots). Visible here are mainly the HII regions detected by (De Pree et al. 1998, F1a – F4d).

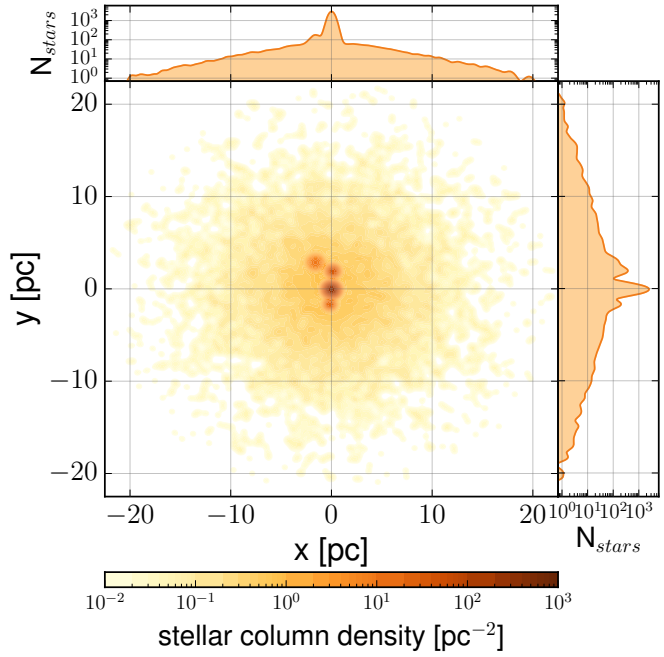

Fig. 8: Center map: Stellar column density map of Sgr B2. The projected distribution of the stars along the x- and y-axis are shown in the right and top panel, respectively.

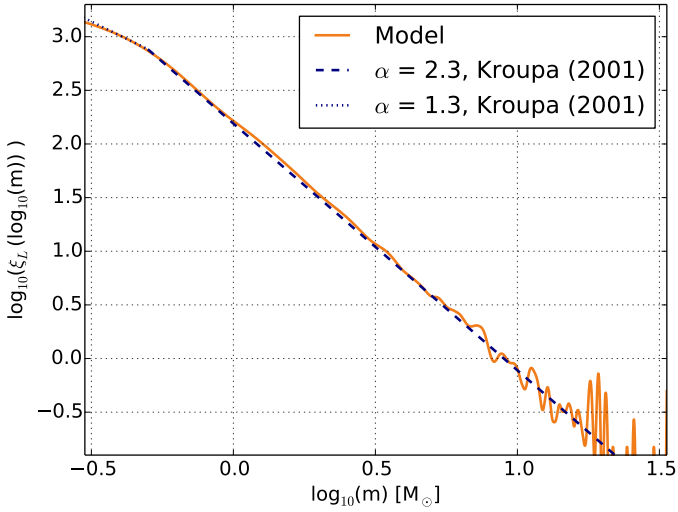

Fig. 9: Mass distribution of the stellar population contained in the Sgr B2 complex, indicated by the orange line. The dotted and dashed blue lines indicate the corresponding segmented IMF from Kroupa (2001).

account for more than twice the number of HII regions, of which the embedded lowest mass star has a mass of 18 $M_\odot$ using the conversion table from Vacca et al. (1996).

We infer a large population of low- and intermediate mass stars. These low- and intermediate mass stars contain the major fraction of the stellar mass, but the high-mass stars contribute the major fraction of the luminosity. To evaluate the influence of the additional low- and intermediate mass stars, we have performed a simulation excluding these stellar populations. The intensity levels in the large-scale maps are unaffected. We then investigated the dust temperature profiles. Figure 10 shows the density and dust temperature profile along the line-of-sight towards the two hot cores. These line-of-sight profiles are obtained within a 0.5 arcsec beam. Differences in dust temperature on the order of 5-40 K (<10%) are only visible on very small scales towards the cores. The envelope temperature is only affected marginally.

4.4. Mass distribution and star formation efficiency

From the model we obtain the three-dimensional distribution of the stellar and gas mass. We can thus investigate the star formation efficiency (hereafter SFE), i.e. the fraction of gas that has been processed into stars. We calculate the SFE using the standard definition (e.g. Myers et al. 1986; Federrath & Klessen 2013):

$$\mathrm{SFE} = \frac{M_*}{M_* + M_{\mathrm{gas}}} \tag{9}$$

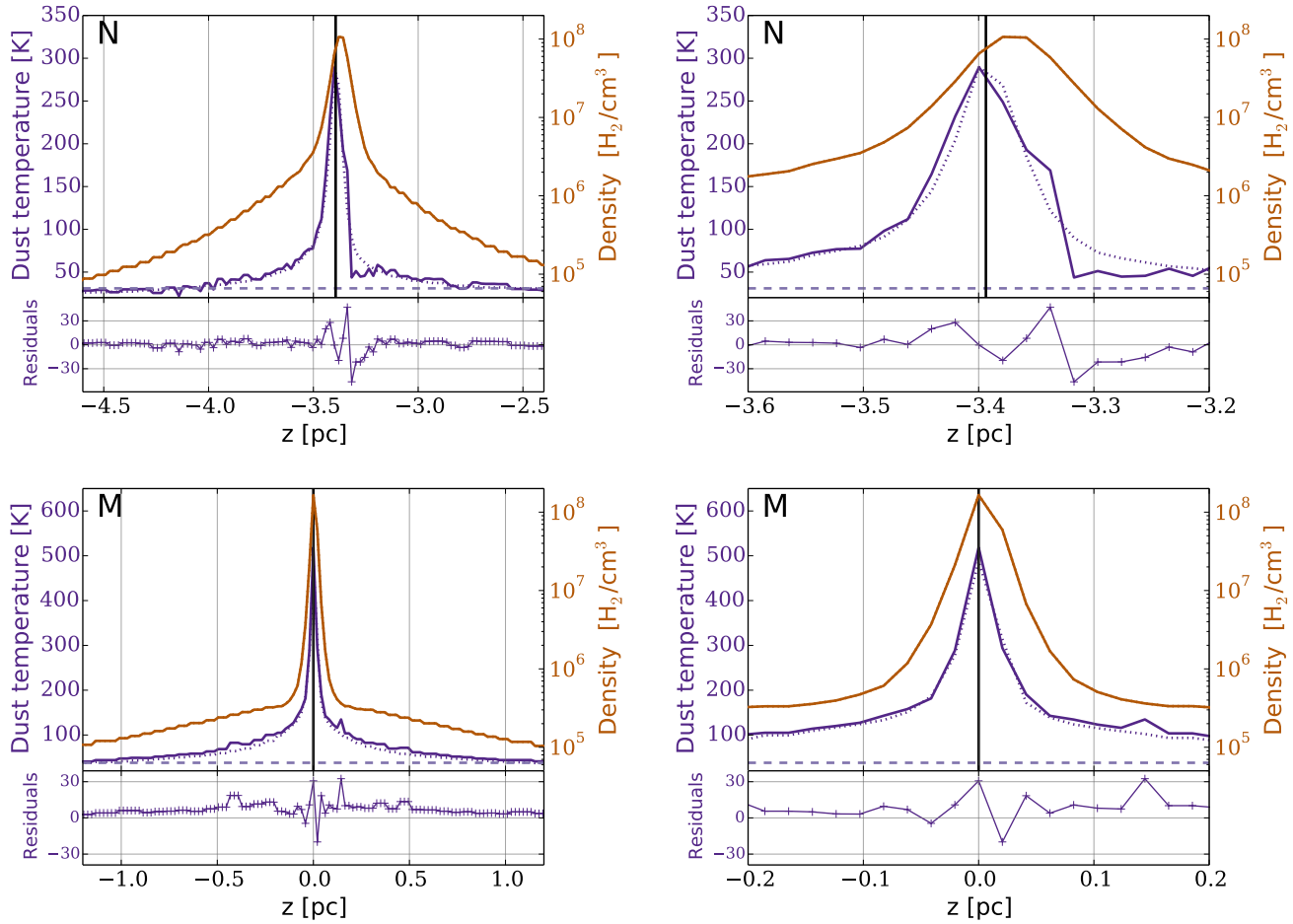

Fig. 10: Density and dust temperature profile along the line-of-sight towards the two hot cores Sgr B2(N) (top) and Sgr B2(M) (bottom). This is obtained with a pixel resolution of 0.5″. The left panels show the profile along 2 pc around the hot cores, whereas the panels on the right show a zoom-in view of the inner 0.4 pc. The solid lines show the resulting distributions when including the star clusters. In addition, we show the temperature profile for the same model but without the extrapolated population of low- and intermediate-mass stars (dotted line). The bottom panel of each plot shows the residuals.

where M_* is the stellar mass and $M_{\rm gas}$ is the gas mass. In Fig. 11 we show the radial distribution of the stellar and gas mass around all four star clusters: Sgr B2(NE), Sgr B2(N), Sgr B2(M), and Sgr B2(S) as well as the derived radially resolved star formation efficiency. For Sgr B2(M) we derive star formation efficiencies of on average 50 %, for Sgr B2(N) the derived value is 5 % and thus significantly lower. Lada & Lada (2003) suggest that the SFE of a cluster increases with time and can reach a maximum value of typically 30 % by the time the cluster emerges from its parental cloud core. This indicates, that Sgr B2(M) has already lost a significant portion of its gas mass through conversion into stars and dispersion. This stellar cluster is emerging from the parental cloud, whereas Sgr B2(N) is still forming stars. This agrees well with the findings by Vogel et al. (1987). For Sgr B2(NE) as well as Sgr B2(S), we calculate rather high average star formation efficiencies of ~ 30 %.

These results have to be taken with caution. The SFE depends on the distributed gas and stellar mass. From the cross cuts in Fig. 3, we think the derived gas masses on large scales are reasonable for all clusters. But while our star sprinkling algorithm will always distribute the same amount of stars if the number of initial stars and their mass is unchanged, the volume within which these stars are placed is set by the star cluster radius. A larger cluster radius effectively decreases the stellar mass density thus causing a lower SFE.

However, to interpret these results, we analyse the relationship between the gas mass of the clusters and their total luminosity. This allows us to study the evolution of the young stellar objects during the phase when they are still embedded in their parental cloud. We follow the same steps outlined in Molinari et al. (2008) and use their evolutionary tracks. In these evolutionary models, the fast accretion phase is stopped when the tracks approach the line where HII regions are found (at a few thousands solar masses). To match the order of magnitude provided by the massive clusters studied here, we had to arbitrarily extend this line. Please note that these evolutionary models assume that a single massive star is forming, which is clearly not the case for at least Sgr B2(N) and Sgr B2(M). We present all tracks in Fig. 12. The five least massive tracks are the ones presented in Molinari et al. (2008). To obtain the two most massive ones, we had to stop the accretion when the central star reaches 80 and 220 $M_\odot$, respectively. Based on the instantaneous accretion rates along the tracks, we estimate that in reality the forming star reaches the ZAMS earlier than reaching the HII line. In particular around 50 $M_\odot$ for the first track and 75 $M_\odot$ for the second. The track luminosity where this occurs is around 4.8 $\times 10^5$ $L_\odot$ for the

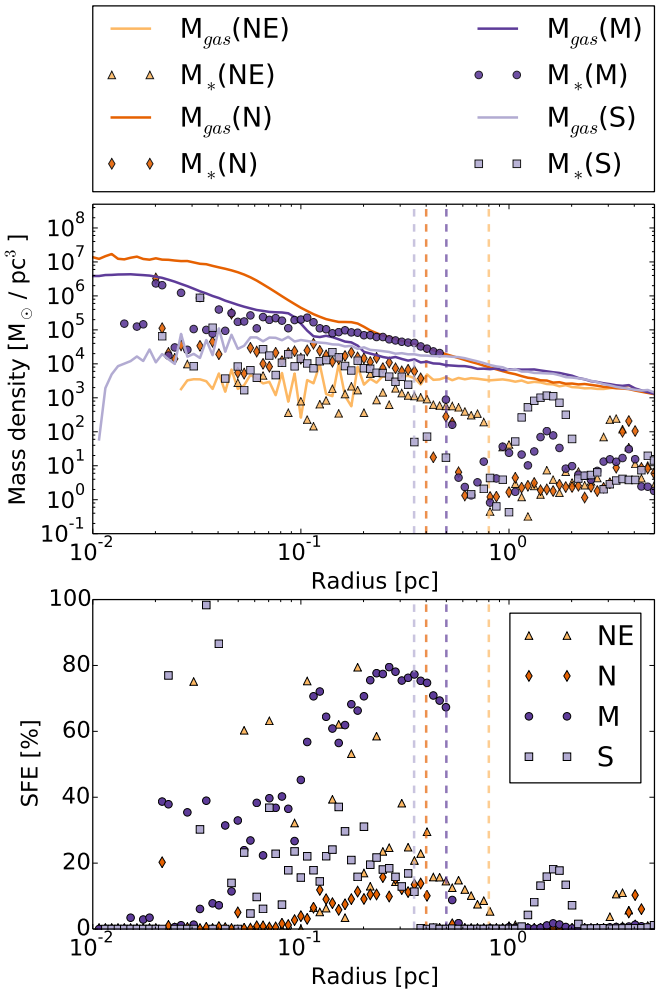

Fig. 11: Top:Radial distribution of the gas and stellar mass density around Sgr B2(NE), Sgr B2(N), Sgr B2(M) and Sgr B2(S). Bottom: Calculated star formation efficiency for Sgr B2(NE), Sgr B2(N), Sgr B2(M), and Sgr B2(S). The vertical dashed lines mark the extent of each star cluster. The same colors belong to the same clusters.

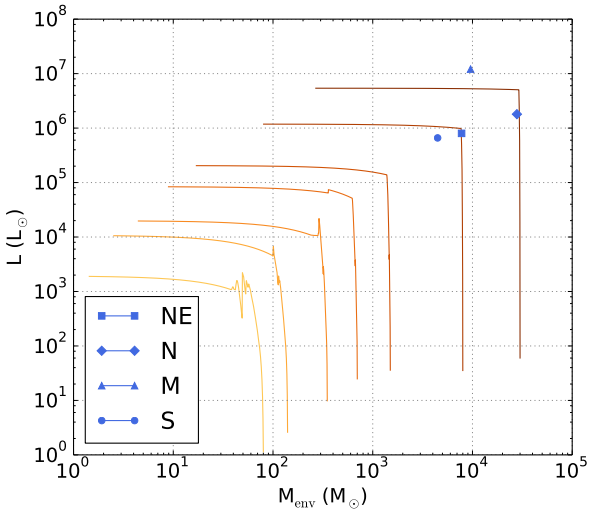

Fig. 12: Luminosity-Mass diagram for the four clusters presented here. The five evolutionary tracks with the lowest initial envelope mass are taken from Molinari et al. (2008). The two highest mass tracks are obtained by extending the evolutionary model from Molinari et al. (2008).

first track and around 10^6 L$_\odot$ for the second track. If we assume a single massive star is forming, then these tracks suggest that Sgr B2(S) should be compatible with HII regions (at least one HII region is observed towards Sgr B2(S)), and Sgr B2(NE) as well as Sgr B2(N) are reaching the ZAMS now. For Sgr B2(M) we do not obtain any useful interpretation. Apart from the fact that a realistic calculation would use a stellar cluster rather than a single star, to reach this relation between gas mass and luminosity in full accretion would require producing a star of a very large mass; or else a star with much larger initial clump mass which would reach the location of M during the ZAMS evolution.

Kruijssen et al. (2015) presented an orbital structure of the Central Molecular Zone (CMZ), i.e. the central few 100 pc of the Milky Way and derived an evolutionary timeline. According to their model, the orbital time between G0.253 (the Brick) and Sgr B2 is $\Delta t = 0.43$ Myr. Given the uncertainties in the ages and the age difference, we can only say that the approximate age is compatible with star formation beginning when Sgr B2 was at the position where G0.253 is now. However, the scenario is not able to shed light on the different development stages of the various sources in the region, because on the scales considered by the gaseous streams model all Sgr B2 sources are cospatial.

4.5. Column density map and probability density function

We convert the dust density to gas density by assuming a gas-to-dust ratio of 100 (Hildebrand 1983), and that 73 % of the gas is in H_2 (Cox 2000). An H_2 column density map of the whole cloud complex is then obtained by simply summing up the H_2 density distribution along the line-of-sight. The map of the full model with a resolution of 0.1″ and zoom-ins to Sgr B2(N) and Sgr B2(M) are shown in Fig. A.2. The HII regions are clearly visible in the zoom-in maps due to their lack of dust.

The propability density function (hereafter: PDF) of the H_2 column density within molecular clouds is commonly used as a tool to investigate the influence of various competing star formation processes within them (see e.g. Kainulainen et al. 2009; Schneider et al. 2013; Federrath & Klessen 2013).

Unfortunately observational data covering the intermediate scales of Sgr B2 (see Fig. A.6) are lacking. This affects the scales from $\sim 10 - 20$″, corresponding to $\sim 0.4 - 0.8$ pc. So while the total flux on these scales is recovered in the Hi-GAL and ATLASGAL maps, its exact distribution is uncertain. We thus refrain from showing the PDF obtained from the H_2 column density map of the model. More observational data is needed.

4.6. Fitting the spectral energy distribution (SED) towards N and M

The fit of the spectral energy distribution towards Sgr B2(N) and Sgr B2(M) obtained with HIFI is shown in Fig. 13. The fluxes from the simulated maps are convolved to the frequency-dependent beam of the 3.5 m Herschel telescope. This kind of fitting thus does not suffer from the necessary convolution to the worst spatial resolution required for modified blackbody fitting. For comparison with previous studies towards Sgr B2(M) and Sgr B2(N) (e.g. Goldsmith et al. 1992; Etxaluze et al. 2013), we

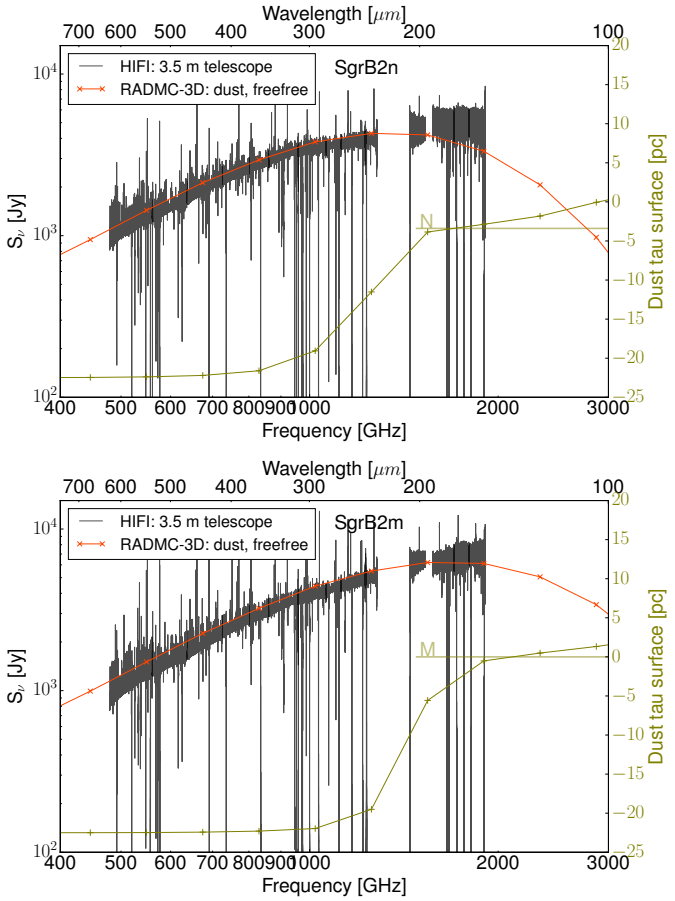

Fig. 13: Spectral energy distribution of the HIFI data (in grey). The data is unsmoothed, what looks like noise are actually individual spectral lines. The best fit towards Sgr B2(M) and N are represented by the solid orange line. The synthetic intensity maps have been convolved to the frequency dependent beam of the 3.5 m Herschel telescope. The fit includes dust and free-free emission. The surface, where the dust optical depth equals one is plotted in olive, the corresponding axis is shown on the right. The z-axis points towards the observer, Sgr B2(M) is located at z = 0 and Sgr B2(N) is located at z = 7×10^5 au. A tau surface datapoint at -22.5 pc indicates that the dust is optically thin at the corresponding frequency.

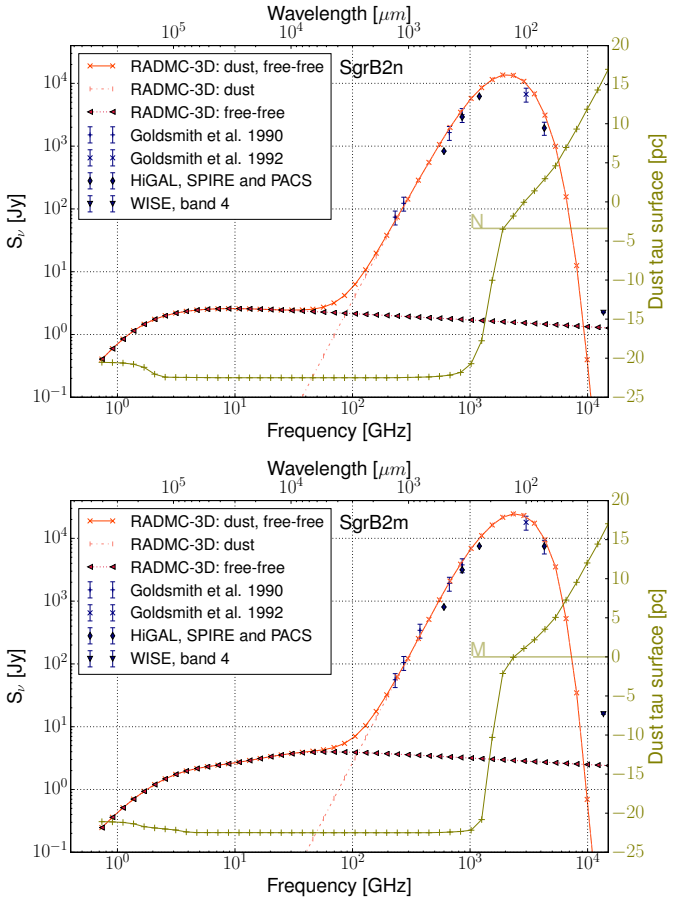

Fig. 14: Spectral energy distribution plots using a fixed beam-size of 30″. The orange solid line is the RADMC-3D dust and free-free best fit, the orange dotted line represents the free-free contribution, the dashed-dotted line represents the contribution from dust emission. The different dark blue markers represent the observational results from Goldsmith et al. (1990, 1992), as well as from Hi-GAL and WISE maps. The surface, where the dust optical depth equals one is plotted in olive, the corresponding axis is shown on the right. The z-axis points towards the observer, Sgr B2(M) is located at z = 0 and Sgr B2(N) is located at z = 7×10^5 au. A tau surface datapoint at -22.5 pc indicates that the dust is optically thin at the corresponding frequency.

have convolved our continuum maps with a beam of 30″ and extracted the flux towards both sources (see Fig. 14). The agreement between observations and simulation in the ranges, where observational data is available is very good. We note however that the model is not able to reproduce fluxes at wavelengths shorter than 70 µm.

Full three-dimensional continuum radiative transfer modeling has so far been performed for disks, and ρ Oph D (Steinacker et al. 2005). However, this has to our best knowledge not been attempted for Sgr B2, which limits our possibilities of comparison. So in order to compare our results to the work from other authors working on Sgr B2 (e.g. Lis & Goldsmith 1989; Goldsmith et al. 1990; Etxaluze et al. 2013), we have applied the modified black body fitting technique to our synthetic maps.

The intensity I of a blackbody at frequency ν is given by the Planck function

$$I_\nu = \frac{2\,h\,\nu^3}{c^2}\left(e^{\frac{h\nu}{kT}} - 1\right)^{-1}, \tag{10}$$

where h is the Planck constant, k is the Boltzmann constant, c is the speed of light in vacuum and T is the temperature of the blackbody.

This equation is multiplied by the factor $1 - e^{-\tau}$, where the optical depth τ is given by

$$\tau = \mu_{H_2}\, m_H\, \kappa_\nu\, N(H_2), \tag{11}$$

μ_{H_2} is the mean molecular weight of hydrogen, m_H is the mass of hydrogen, $N(H_2)$ is the hydrogen column density. The dust opacity κ_ν is determined as a continuous function of frequency ν, by fitting a power-law to the dust opacities given by Ossenkopf & Henning (1994):

$$\kappa_\nu = \frac{\kappa_0}{\chi_d}\left(\frac{\nu}{\nu_0}\right)^\beta, \tag{12}$$

where κ_0 is the reference dust opacity and χ_d is the gas-to-dust mass ratio.

Table 3: Results from modified blackbody fitting of Sgr B2(N) in the upper part and Sgr B2(M) in the bottom part. For each core, we list results from three different approaches.

Sgr B2(N)	T_d [K]	$N(H_2)$ [10^{24} cm^{-2}]	β
3d model[a]	—	2.6	—
blackbody fitting[b]	31	2.9	1.8
Etxaluze et al. (2013)[c]	30	7.0	2.2

Sgr B2(M)	T_d [K]	$N(H_2)$ [10^{24} cm^{-2}]	β
3d model[a]	—	2.3	—
blackbody fitting[b]	36	2.5	1.9
Etxaluze et al. (2013)[c]	37	5.0	2.3

Notes.
[(a)] Hydrogen column density in a 40″ beam directly taken from the model. This serves as the reference value.
[(b)] Result from the modified black body fitting performed in the course of this paper.
[(c)] Results obtained by Etxaluze et al. (2013).

For this, we have extracted the flux within a beam of 40″ towards the SPIRE FTS pointing positions, given in Etxaluze et al. (2013), namely $\alpha_{J2000} = 17^h47^m20.00^s$, $\delta_{J2000} = -28°22'17.44''$ (Sgr B2(N)) and $\alpha_{J2000} = 17^h47^m20.30^s$, $\delta_{J2000} = -28°23'4.1''$ (Sgr B2(M)).

We apply MAGIX (Möller et al. 2013) using first the Genetic Algorithm to find the global best solution, followed by a Levenberg-Marquardt fit to obtain the local best fits for both cores, Sgr B2(M) and Sgr B2(N). The dust temperature T_d, the dust spectral index β and the hydrogen column density $N(H_2)$ where left as free parameters. The mean molecular weight μ_{H_2} is assumed to be 2.8 (Kauffmann et al. 2008), the gas-to-dust mass ratio χ_d is assumed to be 100 (Hildebrand 1983), the reference dust opacity $\kappa_{500\mu m}$ is 1.773 cm^{2}g^{-1} assuming no grain mantles and no coagulation (Ossenkopf & Henning 1994).

We perform a fit covering the frequency range from 450 GHz to 2.87 THz, i.e. excluding the optically thick regime. The resulting SEDs are shown in Fig. 15. Our results are summarized in Table 3. For Sgr B2(N), we obtain a dust temperature T_d of ∼ 31 K, a dust spectral index β of 1.8 and a column density $N(H_2)$ of 2.9×10^{24} cm^{-2}. For Sgr B2(M) we obtain a dust temperature T_d of ∼ 36 K, a dust spectral index β of 1.9 and a column density $N(H_2)$ of 2.5×10^{24} cm^{-2}.

These values are the averaged values in a 40″ beam and are thus the results for the envelopes of Sgr B2(N) and Sgr B2(M). The fitted dust temperature values correspond to radii of 2.0 and 1.3 pc for Sgr B2(N) and Sgr B2(M), respectively (see Fig. 10).

Recently Etxaluze et al. (2013) convolved the Herschel/SPIRE FTS spectral scan maps covering the wavelength range from 194 µm to 671 µm to 40″ and performed modified black body fits towards Sgr B2(N) and Sgr B2(M). They find spectral indices β of 2.2 and 2.3, dust temperatures T_d of 30 K and 37 K, and column densities $N(H_2)$ of 7×10^{24} cm^{-2} and 5×10^{24} cm^{-2} for Sgr B2(N) and Sgr B2(M), respectively. Assuming a distance of 8.5 kpc, a mean molecular weight μ_{H_2} of 2.3, and a dust opacity of $\kappa_{250\mu m}$ of 5.17 cm^2 g^{-1} (Li & Draine 2001), they then estimate dust masses of 2500 $M_\odot$ and 2300 $M_\odot$ and luminosities of 1.1×10^6 $L_\odot$ and 5×10^6 $L_\odot$ for Sgr B2(N) and Sgr B2(M), respectively.

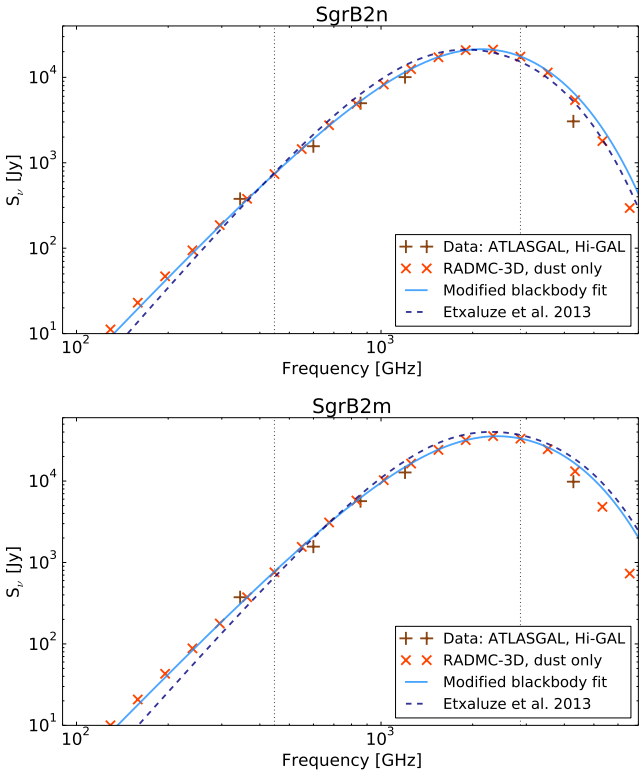

Fig. 15: Spectral energy distribution from the modified blackbody fitting for a beamsize of 40″. The brown pluses represent the observed flux densities obtained from the ATLASGAL and Hi-GAL maps. The orange markers are the flux densities obtained with RADMC-3D including only dust. The solid blue line is the fitted SED and the dotted blue line is the SED from Etxaluze et al. (2013). Top: Sgr B2(N), bottom: Sgr B2(M).

The derived dust temperatures from our study and the ones from Etxaluze et al. (2013) agree very well. But we obtain lower dust spectral indices for which we see two reasons. On the one hand our modeling setup is limited such that only a single dust species is considered. On the other hand different datasets are considered in both studies. We include the ATLASGAL 870 µm map, as well as the Hi-GAL 500, 350, 250, and 70 µm maps, all cross-calibrated with Planck data and in the case of the Hi-GAL map also cross-calibrated with IRAS data, whereas Etxaluze et al. (2013) only considered Hi-GAL data. This could introduce differences in the fluxes which may result in different dust spectral indices as well as different column densities. So this might also explain why we derive a factor of two difference in the dust column densities.

An important point is the resolution of the observation. We have calculated high resolution (i.e. the pixel size equals 0.1″) synthetic intensity maps covering the same frequency range as the SED plotted in Fig. 13 and Fig. 14. We have then convolved these images with decreasing beamsizes from 30″ down to 0.5″. We extract the SEDs towards the Herschel/HIFI positions of Sgr B2(N) and Sgr B2(M) as specified above for each beamsize and also extract the respective τ = 1 surface at each wavelength. This is shown in Fig. 16. From these two SEDs, we can clearly see, that towards the position of Sgr B2(N) the free-free emission becomes optically thicker for smaller beamsizes. This indicates that an HII region is located along the line-of-sight. Furthermore the dust also becomes optically thick towards Sgr B2(N) with

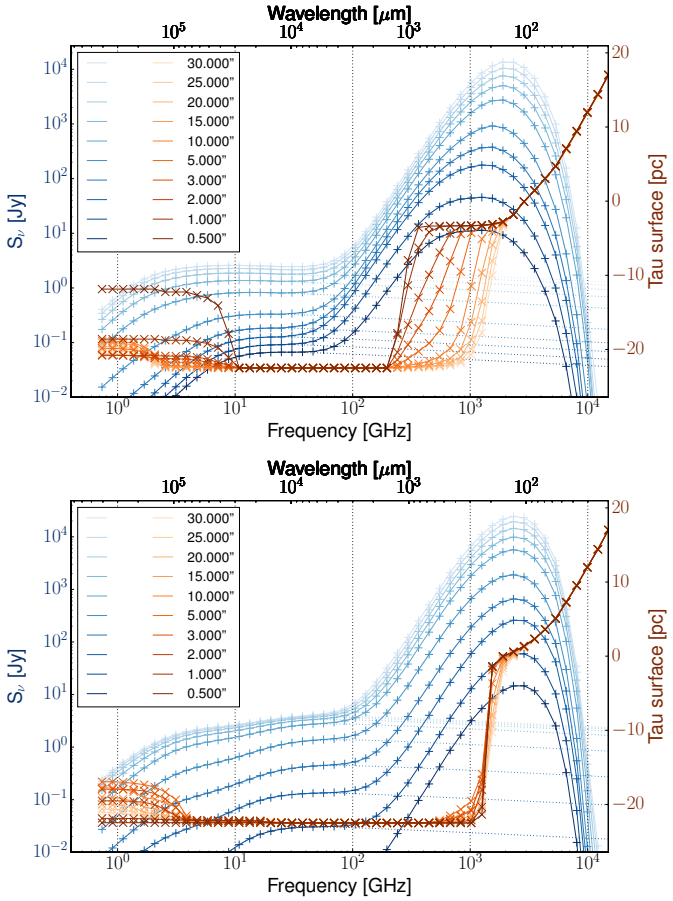

Fig. 16: Top: Sgr B2(N), bottom: Sgr B2(M). The SED convolved with different beam sizes is plotted in blue. For each beam, the combined dust and free-free emission is indicated with the solid blue line, and the contributions from the free-free emission is indicated with the dotted blue line. The $\tau = 1$ surface, i.e. the place along the line-of-sight where the optical depth τ equals one is plotted in orange. Darker colors indicate a smaller beam size.

decreasing beamsize, leaving a very narrow frequency range of 100-200 GHz, where the dust is optically thin while still dominating over the free-free emission. The contribution of free-free emission at 100 GHz is in the order of 30 %, which is still a significant fraction of the overall emission at this frequency. For Sgr B2(M) the dust remains optically thin for this specific position up to 600 GHz. However, at 100 GHz, the fraction of free-free emission is in the order of 70 % for Sgr B2(M), indicating that the free-free emission still dominates at this frequency. Looking at the short-frequency range it is interesting to note that the free-free is partly optically thick for intermediate beamsizes, but turns optically thin for small beamsizes. This shows that there is no HII region located along the line-of-sight towards the position of the Herschel/HIFI beam on small scales. Given that there are a lot of HII regions located along the line-of-sight towards Sgr B2(M) this shows that the pointing choice might be crucial for high-resolution observations. It furthermore shows that if instead of a smooth dust density distribution we would assume a clumpy distribution, this clumping would change the photon penetration depth at certain sightlines.

5. Conclusions

We successfully reconstruct a possible three dimensional density distribution of Sgr B2, recovering the continuum structures covering a wide frequency range (ν = 40 GHz – 4 THz) on scales from 100 au to 45 pc. We employ the publicly available three-dimensional radiative transfer program RADMC-3D and calculate the dust temperature self-consistently.

- We find that the density field of Sgr B2 can be reasonably well fitted by a superposition of spherical symmetric density cores with Plummer-like profiles.
- To reproduce the spectral energy distribution, we locate Sgr B2(N) along the line of sight behind the plane containing Sgr B2(M).
- Sgr B2 comprises a total gas mass of 8.0×10^6 $M_\odot$ within a diameter of 45 pc. This corresponds to an average gas density of 170 $M_\odot pc^{-3}$. For Sgr B2(N) we find a stellar mass of 2400 $M_\odot$, a luminosity of 1.8×10^6 $L_\odot$, a H_2 column density of $2.9.7 \times 10^{24}$ cm^{-2} in a 40″ beam. For Sgr B2(M) we derive a stellar mass of 20700 $M_\odot$, a luminosity of 1.2×10^7 $L_\odot$, a H_2 column density of 2.5×10^{24} cm^{-2} in a 40″ beam. For Sgr B2(S) we find a stellar mass of 1100 $M_\odot$, a luminosity of 6.6×10^5 $L_\odot$, a H_2 column density of 2.2×10^{24} cm^{-2} in a 40″ beam.
- The calculated star formation efficiency is very low for Sgr B2(N), ~5 %, and much higher for Sgr B2(M), ~50 %. This indicates that most of the gas in Sgr B2(M) has already been converted to stars or dispersed.

6. Outlook

The setup of the density structure and temperature field presented here opens the stage of a plethora of different applications and improvements. We list some of them

- **High resolution, envelope covering maps** With the current state of telescopes, it is now possible to efficiently map larger portions of the sky at high resolution. As indicated in Fig. A.6, maps with high angular resolution of Sgr B2 are missing. However they are necessary to improve the setup of the envelope. Currently there is for example only one map available, that resolves dust structures down to ~ 0.01 pc towards Sgr B2(N) and Sgr B2(M). To constrain the dust properties properly, at least another map covering similar scales at a different wavelength is needed. Studying spatial variations of the dust properties on scales smaller than 10″ in the entire envelope is impossible with the data sets currently available. However, this could be partly achieved by using the Atacama Compact Array (ACA).
- **Physical setup:** The physical setup of the model presented here sets the stage for future improvements. By including the possibility to spatially vary the composition of dust, the influence of different compositions can be tested. The treatment of the HII regions can be improved, eventually leading the way to also model radio recombination lines and thus getting access to the ionized gas content. Furthermore the effect of a clumpy density structure can be tested as well as the influence of dusty HII regions.
- **Molecular line studies:** Ultimately, one wants to model molecular lines. The setup of the density and temperature structure presented here builds the foundation for such follow-up studies. By keeping the density structure fixed,

the remaining main free parameters are the molecular abundance and the velocity field. By modeling a variety of different species, including their isotopologues, different surfaces where the opacity exceeds unity can be sampled, allowing a tomography of the source. Having one model for the whole region, also requires to find a solution of the velocity field that fits the plethora of available molecular line data.

- **(M)HD simulations:** While the work presented here focuses only on the modeling of a specific source - Sgr B2 - it builds a bridge between theoretical work, e.g. from (M)HD simulations, and observational work.
- **Chemical models:** Combining the radiative transfer modeling efforts with sophisticated chemical modeling, would allow to fix the molecular abundances.
- **Planning observations:** The model enables us to examine the full parameter space, finding combinations of e.g. transitions, molecules, wavelengths that would allow to constrain a degenerate parameter observationally. Thus it is a useful tool to plan new observations. In Fig. 17 for example we show a prediction of high-resolution continuum maps at different wavelengths. They could be observed e.g. with ALMA. These maps indicate that in order to search for fragmentation and determine its level, it is necessary to obtain multi-wavelength observations as there is no single wavelength unaffected by optical thickness effects or free-free continuum contribution.

Acknowledgements. We thank the anonymous referee for insightful comments that greatly improved this paper. We furthermore thank C. de Pree for providing the VLA continuum maps presented in Gaume et al. (1995); De Pree et al. (1998). This research is carried out within the Collaborative Research Centre 956, sub-project A6, funded by the Deutsche Forschungsgemeinschaft (DFG). DCL acknowledges support for this work provided by NASA through an award issued by JPL/Caltech. SLQ is partly supported by the NSFC under grant Nos. 11373026, 11433004, by the Top Talents Program of Yunnan Province. This research has made use of NASA's Astrophysics Data System, Astropy, a community-developed core Python package for Astronomy (Astropy Collaboration et al. 2013), APLpy, an open-source plotting package for Python hosted at http://aplpy.github.com, and the SIMBAD database, operated at CDS, Strasbourg, France. Herschel is an ESA space observatory with science instruments provided by European-led Principal Investigator consortia and with important participation from NASA. HIFI has been designed and built by a consortium of institutes and university departments from across Europe, Canada and the United States under the leadership of SRON Netherlands Institute for Space Research, Groningen, The Netherlands and with major contributions from Germany, France and the US. Consortium members are: Canada: CSA, U.Waterloo; France: CESR, LAB, LERMA, IRAM; Germany: KOSMA, MPIfR, MPS; Ireland, NUI Maynooth; Italy: ASI, IFSI-INAF, Osservatorio Astrofisico di Arcetri-INAF; Netherlands: SRON, TUD; Poland: CAMK, CBK; Spain: Observatorio Astronómico Nacional (IGN), Centro de Astrobiología (CSIC-INTA). Sweden: Chalmers University of Technology - MC2, RSS & GARD; Onsala Space Observatory; Swedish National Space Board, Stockholm University - Stockholm Observatory; Switzerland: ETH Zurich, FHNW; USA: Caltech, JPL, NHSC. The ATLASGAL project is a collaboration between the Max-Planck-Gesellschaft, the European Southern Observatory (ESO) and the Universidad de Chile. It includes projects E-181.C-0885, E-078.F-9040(A), M-079.C-9501(A), M-081.C-9501(A) plus Chilean data. The National Radio Astronomy Observatory is a facility of the National Science Foundation operated under cooperative agreement by Associated Universities, Inc. The Submillimeter Array is a joint project between the Smithsonian Astrophysical Observatory and the Academia Sinica Institute of Astronomy and Astrophysics and is funded by the Smithsonian Institution and the Academia Sinica.

References

Aarseth, S. J., Henon, M., & Wielen, R. 1974, A&A, 37, 183
Altenhoff, W., Mezger, P. G., Wendker, H., & Westerhout, G. 1960, Ver"offentlichungen der Universitätssternwarte Bonn, 59, 48
Astropy Collaboration, Robitaille, T. P., Tollerud, E. J., et al. 2013, A&A, 558, A33
Belloche, A., Müller, H. S. P., Menten, K. M., Schilke, P., & Comito, C. 2013, A&A, 559, A47
Berger, M. J. & Colella, P. 1989, Journal of Computational Physics, 82, 64
Berger, M. J. & Oliger, J. 1984, Journal of Computational Physics, 53, 484
Bergin, E. A., Phillips, T. G., Comito, C., et al. 2010, A&A, 521, L20
Bjorkman, J. E. & Wood, K. 2001, ApJ, 554, 615
Choudhury, R., Schilke, P., Stéphan, G., et al. 2015, ArXiv e-prints
Comito, C. & Schilke, P. 2002, A&A, 395, 357
Cox, A. N. 2000, Allen's astrophysical quantities
Csengeri, T., Urquhart, J. S., Schuller, F., et al. 2014, A&A, 565, A75
De Pree, C. G., Goss, W. M., & Gaume, R. A. 1998, ApJ, 500, 847
Dullemond, C. P. 2012, RADMC-3D, ASCL
Etxaluze, M., Goicoechea, J. R., Cernicharo, J., et al. 2013, A&A, 556, A137
Federrath, C. & Klessen, R. S. 2013, ApJ, 763, 51
Gaume, R. A., Claussen, M. J., de Pree, C. G., Goss, W. M., & Mehringer, D. M. 1995, ApJ, 449, 663
Goicoechea, J. R., Rodríguez-Fernández, N. J., & Cernicharo, J. 2004, ApJ, 600, 214
Goldsmith, P. F., Lis, D. C., Hills, R., & Lasenby, J. 1990, ApJ, 350, 186
Goldsmith, P. F., Lis, D. C., Lester, D. F., & Harvey, P. M. 1992, ApJ, 389, 338
Gordon, M. A., Berkermann, U., Mezger, P. G., et al. 1993, A&A, 280, 208
Griffin, M. J., Abergel, A., Abreu, A., et al. 2010, A&A, 518, L3
Griffiths, S. C., Hicks, R. B., & Milone, E. F. 1988, JRASC, 82, 1
Hildebrand, R. H. 1983, QJRAS, 24, 267
Hosokawa, T. & Omukai, K. 2009, ApJ, 691, 823
Hüttemeister, S., Wilson, T. L., Henkel, C., & Mauersberger, R. 1993, A&A, 276, 445
Hüttemeister, S., Wilson, T. L., Mauersberger, R., et al. 1995, A&A, 294, 667
Kainulainen, J., Beuther, H., Henning, T., & Plume, R. 2009, A&A, 508, L35
Kauffmann, J., Bertoldi, F., Bourke, T. L., Evans, II, N. J., & Lee, C. W. 2008, A&A, 487, 993
Khokhlov, A. 1998, Journal of Computational Physics, 143, 519
Kroupa, P. 2001, MNRAS, 322, 231
Kruijssen, J. M. D., Dale, J. E., & Longmore, S. N. 2015, MNRAS, 447, 1059
Lada, C. J. & Lada, E. A. 2003, ARA&A, 41, 57
Li, A. & Draine, B. T. 2001, ApJ, 554, 778
Lis, D. C. & Goldsmith, P. F. 1989, ApJ, 337, 704
Lis, D. C. & Goldsmith, P. F. 1990, ApJ, 356, 195
Lucy, L. B. 1999, A&A, 344, 282
Mehringer, D. M., Palmer, P., Goss, W. M., & Yusef-Zadeh, F. 1993, ApJ, 412, 684
Mezger, P. G. & Henderson, A. P. 1967, ApJ, 147, 471
Molinari, S., Pezzuto, S., Cesaroni, R., et al. 2008, A&A, 481, 345
Molinari, S., Swinyard, B., Bally, J., et al. 2010, A&A, 518, L100
Möller, T., Bernst, I., Panoglou, D., et al. 2013, A&A, 549, A21
Myers, P. C., Dame, T. M., Thaddeus, P., et al. 1986, ApJ, 301, 398
Ossenkopf, V. & Henning, T. 1994, A&A, 291, 943
Oster, L. 1961, Reviews of Modern Physics, 33, 525
Panagia, N. 1973, AJ, 78, 929
Pierce-Price, D., Richer, J. S., Greaves, J. S., et al. 2000, ApJ, 545, L121
Poglitsch, A., Waelkens, C., Geis, N., et al. 2010, A&A, 518, L2
Qin, S.-L., Schilke, P., Rolffs, R., et al. 2011, A&A, 530, L9
Reid, M. J., Menten, K. M., Brunthaler, A., et al. 2014, ApJ, 783, 130
Robitaille, T. P. 2010, A&A, 520, A70
Roelfsema, P. R., Helmich, F. P., Teyssier, D., et al. 2012, A&A, 537, A17
Rolffs, R., Schilke, P., Wyrowski, F., et al. 2011a, A&A, 529, A76
Rolffs, R., Schilke, P., Wyrowski, F., et al. 2011b, A&A, 527, A68
Rolffs, R., Schilke, P., Zhang, Q., & Zapata, L. 2011c, A&A, 536, A33
Rubin, R. H. 1968, ApJ, 154, 391
Rybicki, G. B. & Lightman, A. P. 1986, Radiative Processes in Astrophysics, 400
Sánchez-Monge, Á., Beltrán, M. T., Cesaroni, R., et al. 2013, A&A, 550, A21
Sault, R. J., Teuben, P. J., & Wright, M. C. H. 1995, in Astronomical Society of the Pacific Conference Series, Vol. 77, Astronomical Data Analysis Software and Systems IV, ed. R. A. Shaw, H. E. Payne, & J. J. E. Hayes, 433
Schneider, N., André, P., Könyves, V., et al. 2013, ApJ, 766, L17
Schuller, F., Menten, K. M., Contreras, Y., et al. 2009, A&A, 504, 415
Scoville, N. Z., Solomon, P. M., & Penzias, A. A. 1975, ApJ, 201, 352
Seaton, M. J. 1959, MNRAS, 119, 81
Siringo, G., Kreysa, E., Kovács, A., et al. 2009, A&A, 497, 945
Smith, M. D. 2014, MNRAS, 438, 1051
Steinacker, J., Bacmann, A., Henning, T., Klessen, R., & Stickel, M. 2005, A&A, 434, 167
Steinacker, J., Baes, M., & Gordon, K. 2013, ArXiv e-prints
Straizys, V. & Kuriliene, G. 1981, Ap&SS, 80, 353
Traficante, A., Calzoletti, L., Veneziani, M., et al. 2011, MNRAS, 416, 2932
Vacca, W. D., Garmany, C. D., & Shull, J. M. 1996, ApJ, 460, 914
Vogel, S. N., Genzel, R., & Palmer, P. 1987, ApJ, 316, 243

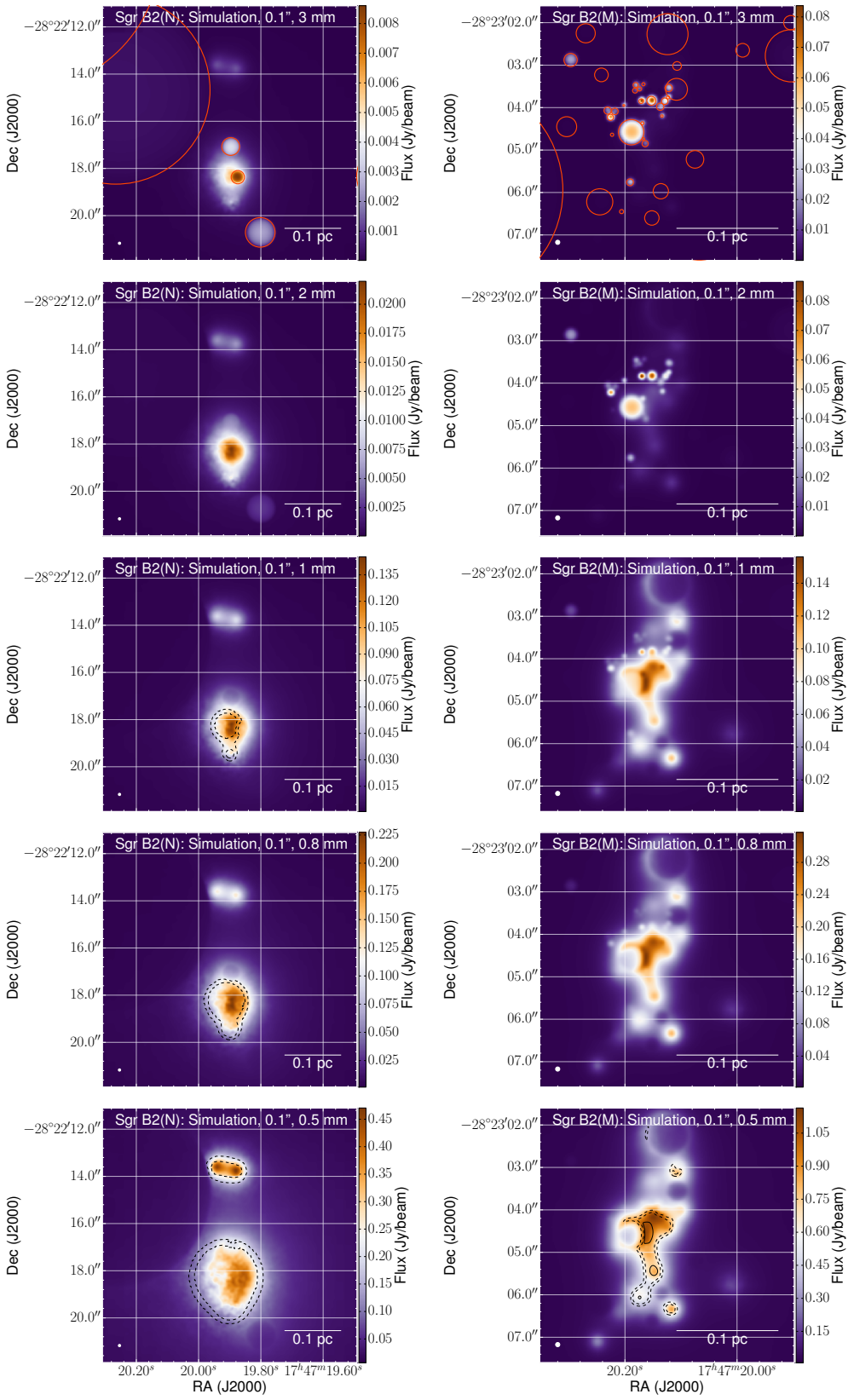

Fig. 17: Simulation of high-resolution continuum maps towards Sgr B2(N), left, and Sgr B2(M), right with a resolution of 0.1″ at decreasing wavelengths from top to bottom. Observations like this are possible with ALMA. The red circles in the maps in the top row indicate the location and extent of the HII regions. Maps having black dashed (and solid) contours are affected by optical thickness. The black dashed contours in maps of Sgr B2(N) indicate where the $\tau = 1$ surface equals -3.50, and -3.39 pc, respectively. The black (dashed and solid) contours in maps of Sgr B2(M) show where the $\tau = 1$ surface equals -1.0, -0.05, and 0.0 pc, respectively. These maps indicate that, especially for Sgr B2(M), the free-free emission contributes significantly at 3 and 2 mm. On the other hand, the dust becomes optically thick at ∼0.5 mm for Sgr B2(M), and already at ∼1 mm for Sgr B2(N).

Appendix A: Figures

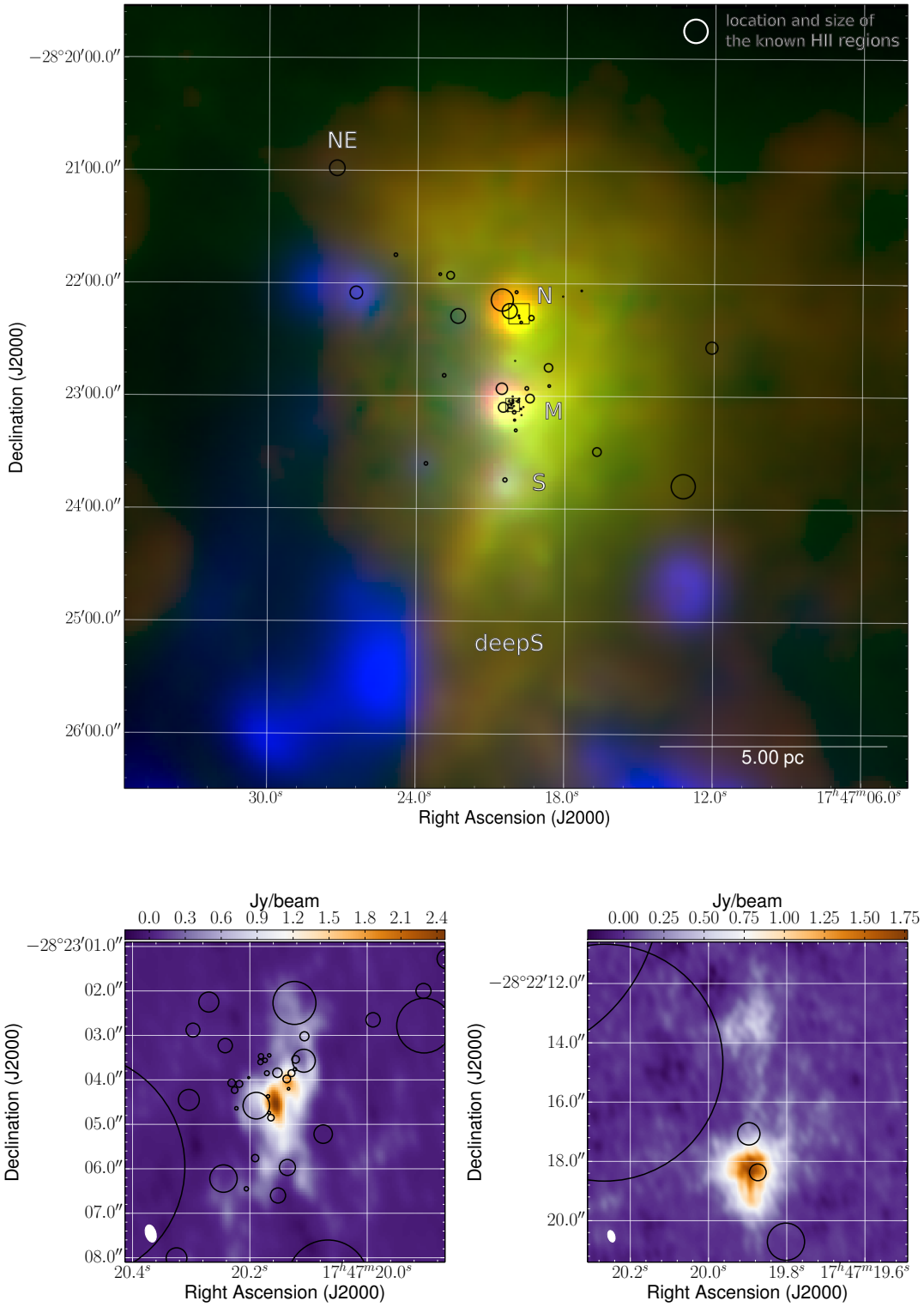

Fig. A.1: Top: Three color composite map of the large-scale structure of Sgr B2. Blue: JCMT - SCUBA 850 µm, green: CSO – Sharc II 350 µm, red: Herschel – PACS 70 µm. Bottom left: Zoom-in to Sgr B2(M), SMA data. Bottom right: Zoom-in to Sgr B2(N), SMA data. The black circles mark the extent of the HII regions. The rectangles in the upper map indicate the zoom-in region of the bottom maps.

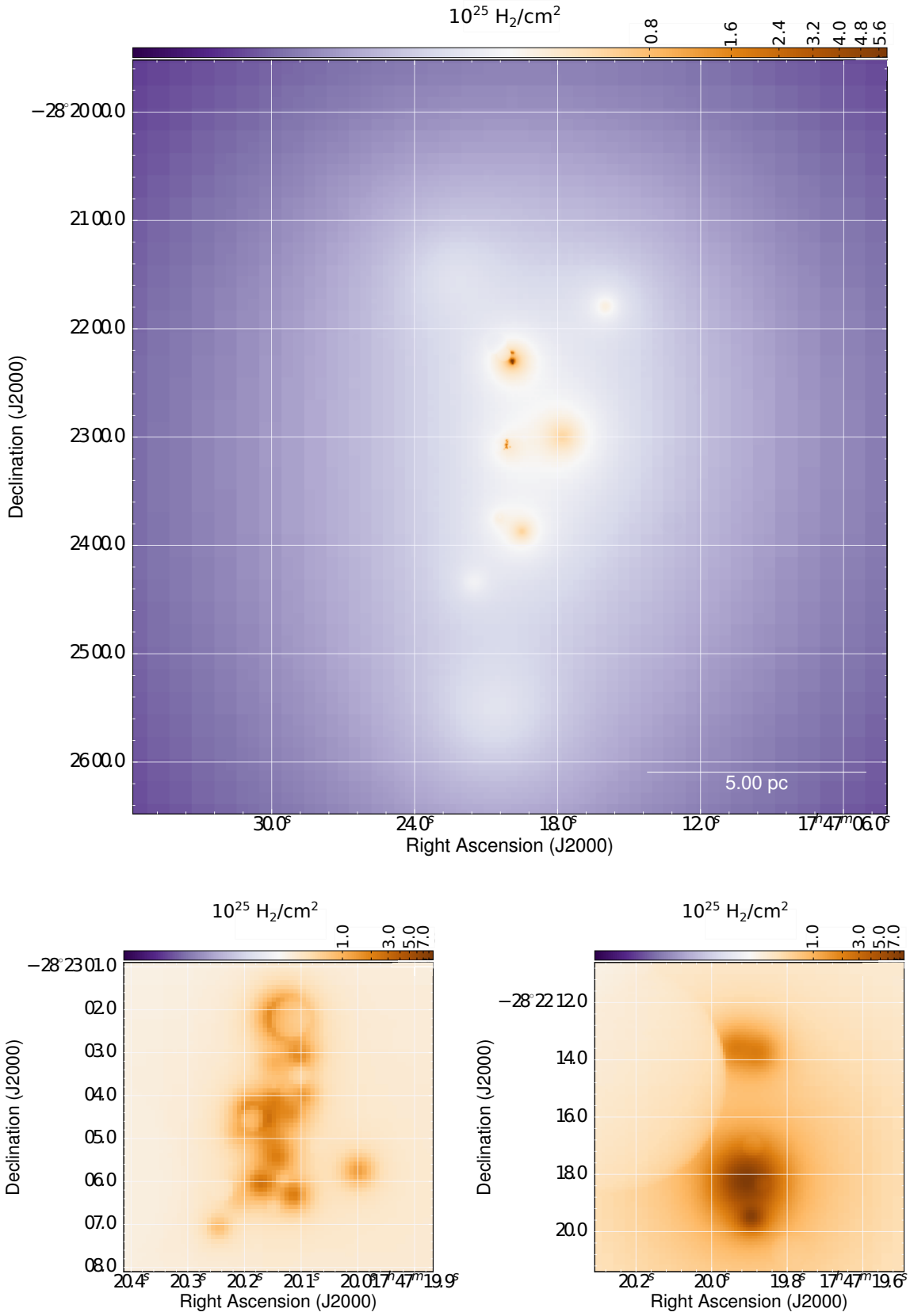

Fig. A.2: Top: Hydrogen column density map of the whole cloud complex. The pixel resolution is 0.5 arcsec. Bottom left: Zoom-in to Sgr B2(M). Bottom right: Zoom-in to Sgr B2(N). The HII regions are visible due to their lack of dust.

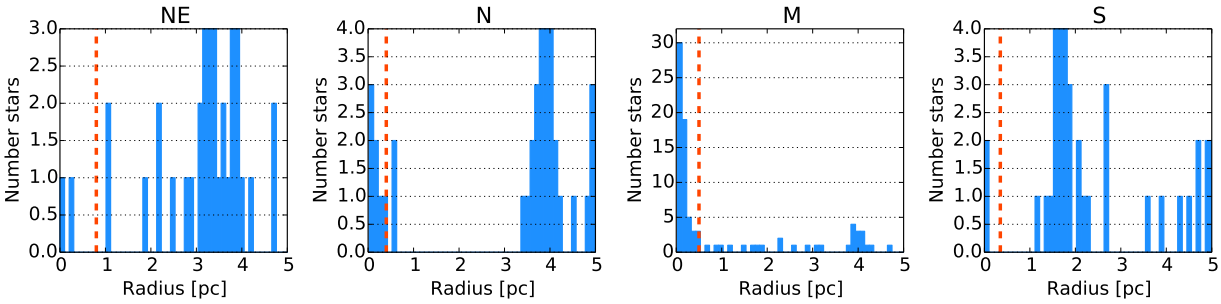

Fig. A.3: Histogram of the known high-mass stars around the star clusters to determine the star cluster radius. The dashed line indicates the star cluster radius determined based on a by-eye inspection of these histograms.

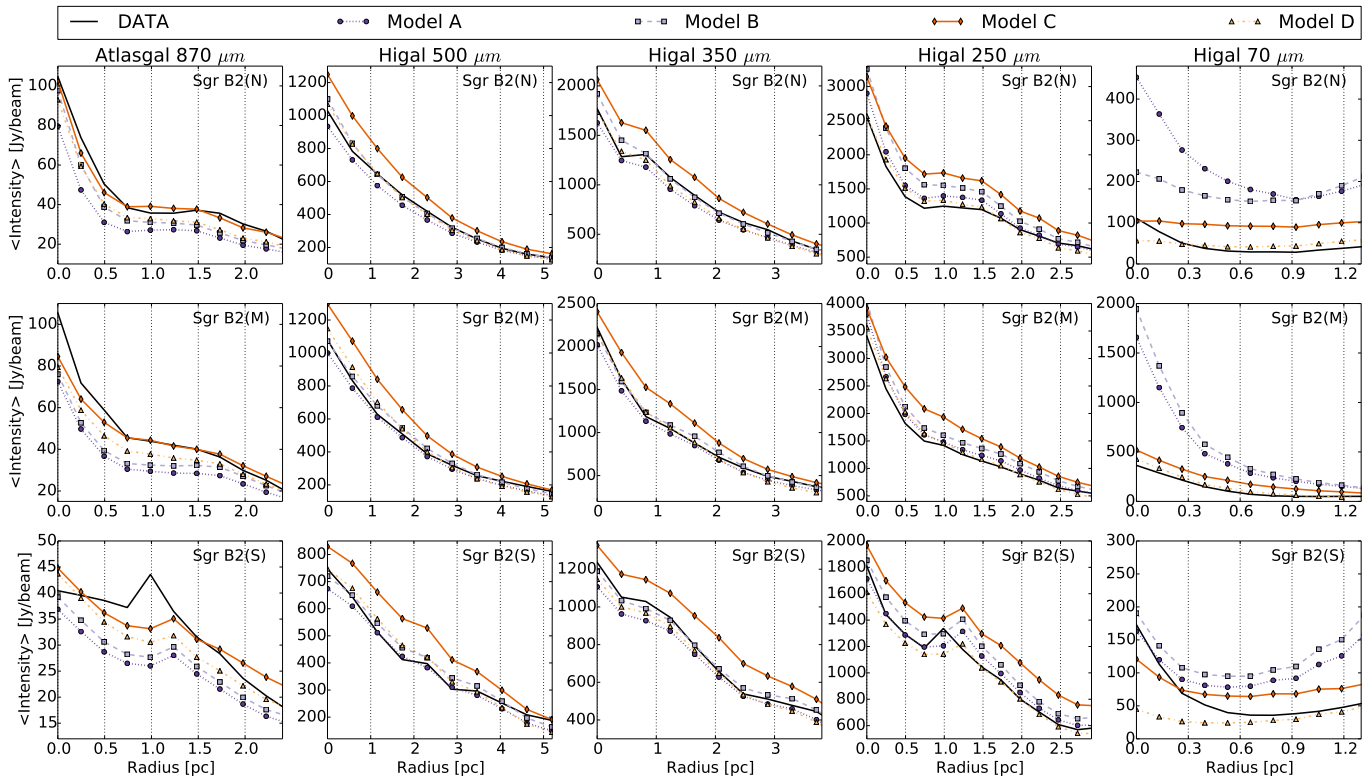

Fig. A.4: Azimuthally averaged radial profiles of the large-scale structure around the position of the envelope components of Sgr B2(N) (top row), Sgr B2(M), (middle row) and Sgr B2(S) (bottom row). The data is plotted in solid black. The wavelengths decreases from left to right: 870 μm, 500 μm, 350 μm, 250 μm, and 70 μm.

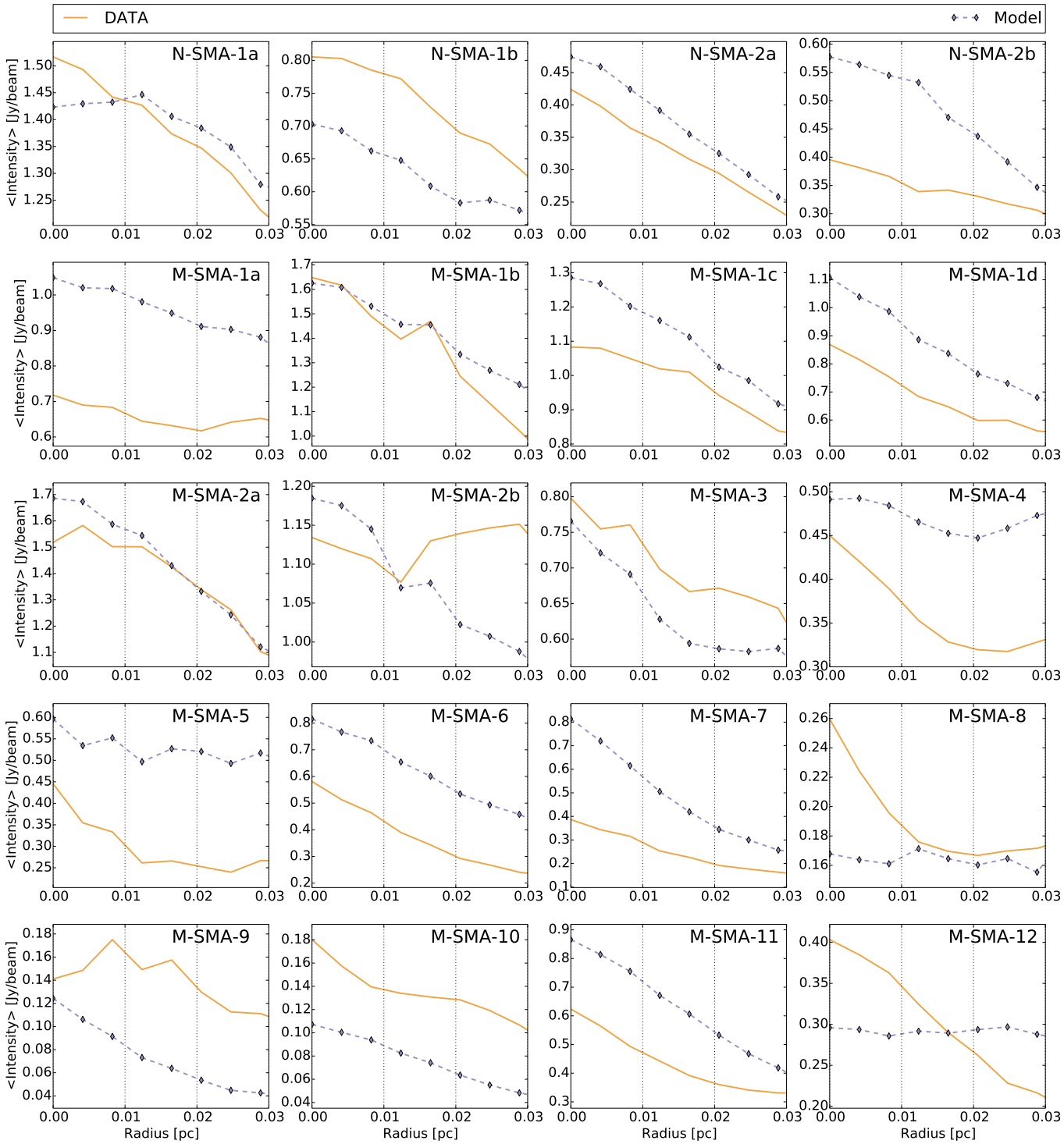

Fig. A.5: Radial profiles of the averaged intensity of the small-scale SMA structure around the position of the small-scale density components listed in Tab. B.2. For each of the four different models (A – D) described in this paper, the setup of the small-scale structure was fixed. The data is plotted in solid Orange, the model is shown in dashed blue. The identifier of the components are written in the upper right corner of each subplot.

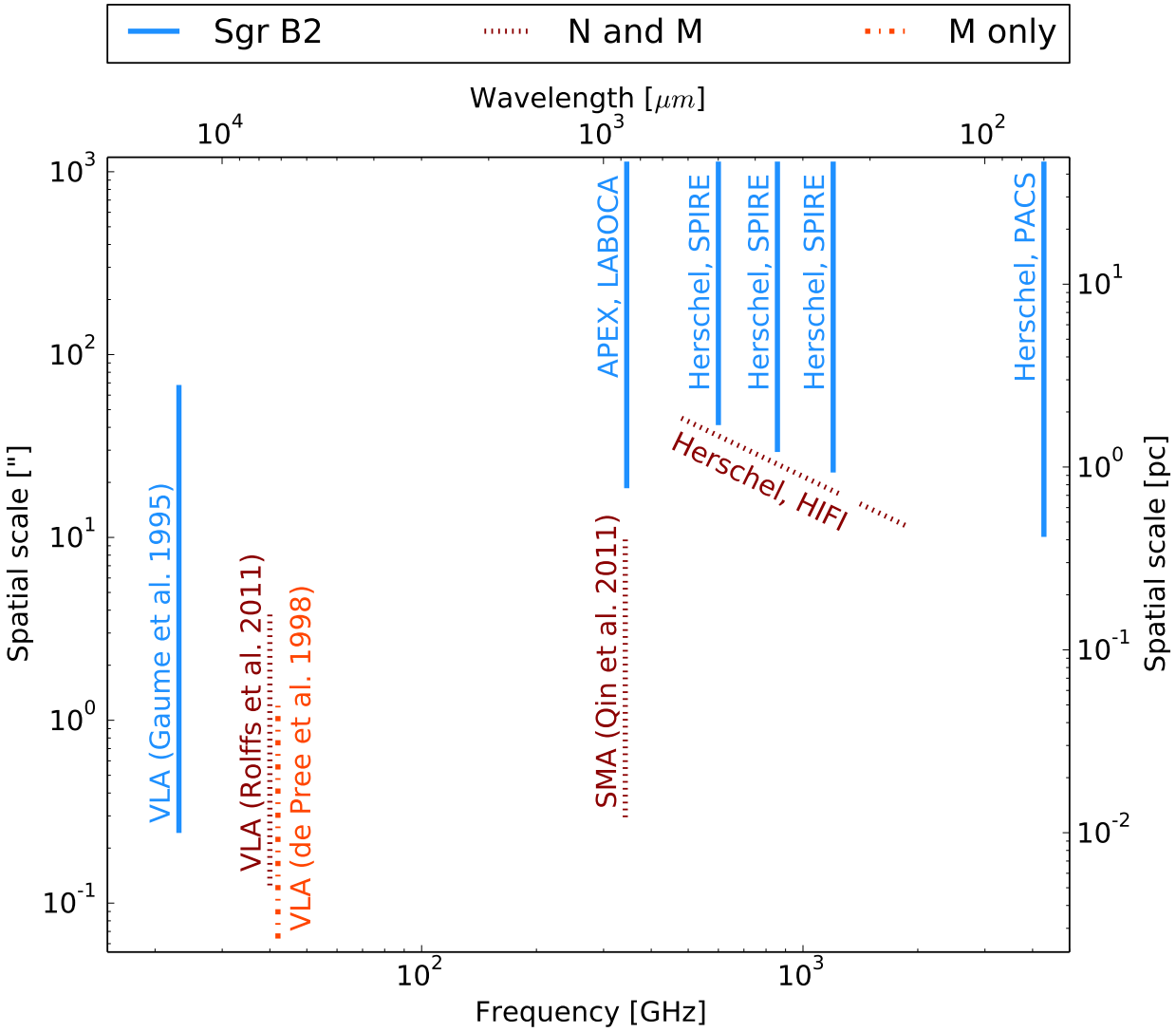

Fig. A.6: Covered spatial scales versus frequency of the different data employed in this study.

Appendix B: Tables

Table B.1: Known HII regions in the Sgr B2 region.[a]

ID[1]	Model[2]	RA[3] [h:m:s, J2000]	DEC[4] [d:m:s, J2000]	dz[5] [10^5 au]	r_{obs}[6] [10^3 au]	n_e[7] [10^4 cm^{-3}]	ZAMS[8] type	EM[9] [10^7 pc cm^{-6}]	$\log(\dot{N}_i)$[10] [s^{-1}]
A1	ABCD	17:47:19.432	-28:23:01.23	0.0	19.400	0.912	O6	2.30	48.86
A2	ABCD	17:47:19.562	-28:22:55.82	0.0	7.910	1.440	O8.5	2.40	48.09
B	ABCD	17:47:19.903	-28:23:02.78	0.0	5.230	4.060	O7.5	12.00	48.44
B1	ABCD	17:47:19.990	-28:23:02.65	0.0	1.370	3.820	B0	2.90	46.65
B9.89	ABCD	17:47:19.695	-28:23:05.78	0.0	2.000	3.410	B0	3.40	47.04
B9.96	ABCD	17:47:19.772	-28:23:10.05	0.0	2.000	3.170	B0	2.90	46.98
B9.99	ABCD	17:47:19.798	-28:23:06.77	0.0	3.510	2.750	O9.5	3.80	47.59
B10.06	ABCD	17:47:19.864	-28:23:01.28	0.0	1.890	4.120	B0	4.60	47.13
B10.10	ABCD	17:47:19.904	-28:23:02.00	0.0	1.440	4.640	B0	4.50	46.88
C	ABCD	17:47:20.001	-28:23:18.19	0.0	6.040	2.020	O9	3.60	48.03
D	ABCD	17:47:20.049	-28:23:12.74	0.0	4.390	3.110	O9	6.10	47.99
E	ABCD	17:47:20.067	-28:23:08.52	0.0	7.800	2.300	O7.5	6.00	48.47
F1a[b]	ABCD	17:47:20.122	-28:23:03.54	0.0	0.731	66.400	O7.5	480.00	48.35
F1b[b]	ABCD	17:47:20.123	-28:23:03.76	0.0	0.315	182.000	O7.5	2000.00	48.45
F1c[b]	ABCD	17:47:20.129	-28:23:03.85	0.0	0.655	83.200	O7	760.00	48.55
F1d[b]	ABCD	17:47:20.134	-28:23:04.20	0.0	0.238	224.000	O7.5	2800.00	48.51
F1e[b]	ABCD	17:47:20.137	-28:23:03.98	0.0	0.731	54.400	O8.5	310.00	48.14
F1f[b]	ABCD	17:47:20.153	-28:23:03.84	0.0	0.901	83.200	O7	760.00	48.55
F1g[b]	ABCD	17:47:20.171	-28:23:03.85	0.0	0.459	177.000	O8	1700.00	48.30
F2a[b]	ABCD	17:47:20.167	-28:23:03.45	0.0	0.323	91.800	O9.5	460.00	47.73
F2b[b]	ABCD	17:47:20.174	-28:23:03.56	0.0	0.417	76.500	O9.5	350.00	47.70
F2c[b]	ABCD	17:47:20.181	-28:23:03.47	0.0	0.502	81.300	O9.5	400.00	47.75
F2d[b]	ABCD	17:47:20.182	-28:23:03.60	0.0	0.493	54.900	O9.5	250.00	47.82
F3a[b]	ABCD	17:47:20.164	-28:23:04.85	0.0	0.621	48.100	O9.5	190.00	47.70
F3b[b]	ABCD	17:47:20.167	-28:23:04.74	0.0	0.264	95.900	O9.5	500.00	47.77
F3c[b]	ABCD	17:47:20.169	-28:23:04.37	0.0	0.306	150.000	O8	1300.00	48.22
F3d[b]	ABCD	17:47:20.189	-28:23:04.58	0.0	2.540	38.500	O5.5	490.00	49.31
F3e[b]	ABCD	17:47:20.223	-28:23:04.64	0.0	0.323	51.600	B0	120.00	47.02
F4a[b]	ABCD	17:47:20.202	-28:23:03.95	0.0	0.187	414.000	O9	3700.00	47.85
F4b[b]	ABCD	17:47:20.226	-28:23:04.23	0.0	0.621	108.000	O8	890.00	48.31
F4c[b]	ABCD	17:47:20.231	-28:23:04.07	0.0	0.723	48.900	O8.5	260.00	48.09
F4d[b]	ABCD	17:47:20.218	-28:23:04.09	0.0	0.655	48.800	O9.5	180.00	47.62
F10.37[b]	ABCD	17:47:20.191	-28:23:05.76	0.0	0.689	62.300	O9.5	240.00	47.58
F10.39[b]	ABCD	17:47:20.206	-28:23:06.45	0.0	0.408	34.400	B0	70.00	46.98
G[b]	ABCD	17:47:20.297	-28:23:02.88	0.0	1.330	35.100	O7	250.00	48.62
F10.27[b]	ABCD	17:47:20.075	-28:23:05.22	0.0	1.760	4.310	B0	4.70	47.08
F10.30[b]	ABCD	17:47:20.107	-28:23:03.02	0.0	0.867	4.810	B0	2.90	46.25
F10.303[b]	ABCD	17:47:20.108	-28:23:03.57	0.0	2.180	9.090	O9	26.00	48.01
F10.318[b]	ABCD	17:47:20.124	-28:23:02.27	0.0	4.120	2.380	O9.5	3.40	47.67
F10.32[b]	ABCD	17:47:20.131	-28:23:00.13	0.0	1.910	3.700	B0	3.80	47.05
F10.33[b]	ABCD	17:47:20.136	-28:23:05.97	0.0	1.530	4.240	B0	4.00	46.88
F10.35[b]	ABCD	17:47:20.152	-28:23:06.60	0.0	1.450	4.070	B0	3.50	46.77
F10.44[b]	ABCD	17:47:20.245	-28:23:06.22	0.0	2.620	2.760	B0	2.90	47.21
G10.44	ABCD	17:47:20.242	-28:23:03.23	0.0	1.370	4.920	B0	4.80	46.87
G10.47	ABCD	17:47:20.270	-28:23:02.25	0.0	1.910	3.670	B0	3.70	47.05
H	ABCD	17:47:20.426	-28:23:44.62	0.0	9.260	2.700	O6	9.80	48.84
I	ABCD	17:47:20.507	-28:23:05.95	0.0	22.000	1.630	O5	8.40	49.52
I10.49	ABCD	17:47:20.304	-28:23:04.45	0.0	2.000	3.440	B0	3.40	47.05
I10.52	ABCD	17:47:20.325	-28:23:08.01	0.0	1.980	4.530	B0	5.90	47.28
J	ABCD	17:47:20.570	-28:22:56.04	0.0	25.500	0.608	O6	1.40	48.86
K1[b]	A	17:47:19.802	-28:22:20.71	0.0	5.340	5.250	O6.5	21.00	48.70
	BCD			-7.0					
K2[b]	A	17:47:19.874	-28:22:18.37	0.0	2.400	12.700	O7.5	56.00	48.42
	BCD			-7.0					

Table B.1: (continued) Known HII regions in Sgr B2.

ID[1]	Model[2]	RA[3] [h:m:s, J2000]	DEC[4] [d:m:s, J2000]	dz[5] [10^5 au]	r_{obs}[6] [10^3 au]	n_e[7] [10^4 cm^{-3}]	ZAMS[8] type	EM[9] [10^7 pc cm^{-6}]	$\log(\dot{N}_i)$[10] [s^{-1}]
K3[b]	A	17:47:19.897	-28:22:17.07	0.0	3.200	7.610	O7.5	27.00	48.35
	BCD			-7.0					
K4	A	17:47:19.993	-28:22:04.58	0.0	6.280	3.750	O7	13.00	48.62
	BCD			-7.0					
K5	A	17:47:20.266	-28:22:14.67	0.0	34.000	0.819	O5	33.00	49.49
	BCD			-7.0					
K6	A	17:47:20.568	-28:22:08.82	0.0	49.900	0.532	O5	20.00	49.62
	BCD			-7.0					
L	ABCD	17:47:22.661	-28:21:55.77	0.0	17.300	1.420	O5.5	5.10	49.09
L13.30	ABCD	17:47:23.079	-28:21:55.16	0.0	5.680	1.450	O9.5	1.70	47.66
O	ABCD	17:47:22.901	-28:22:49.07	0.0	7.800	0.698	O9.5	0.55	47.44
P	ABCD	17:47:23.621	-28:23:36.02	0.0	7.800	0.777	O9.5	0.68	47.53
Q	ABCD	17:47:24.875	-28:21:44.93	0.0	7.800	0.895	O9.5	0.90	47.65
R	ABCD	17:47:26.464	-28:22:05.11	0.0	28.500	0.535	O6	1.20	48.89
T	ABCD	17:47:27.256	-28:20:58.75	0.0	35.100	0.138	O9	0.10	47.99
U	ABCD	17:47:12.093	-28:22:33.86	0.0	27.300	0.364	O7.5	0.52	48.50
V	ABCD	17:47:13.224	-28:23:47.77	0.0	54.600	0.233	O6	0.43	49.02
W	ABCD	17:47:16.717	-28:23:29.52	0.0	19.500	0.238	O9.5	0.16	47.69
X	ABCD	17:47:17.363	-28:22:03.74	0.0	3.120	2.220	B0	2.20	47.25
X8.33	ABCD	17:47:18.113	-28:22:06.82	0.0	1.900	5.320	B0	7.80	47.36
Y	ABCD	17:47:18.657	-28:22:54.51	0.0	5.630	1.480	O9.5	1.80	47.67
Z	ABCD	17:47:18.689	-28:22:44.78	0.0	19.000	0.607	O7.5	1.00	48.47
Z10.24	ABCD	17:47:20.038	-28:22:41.18	0.0	1.680	6.140	B0	9.20	47.33
AA	ABCD	17:47:19.388	-28:22:18.33	0.0	11.700	1.070	O8	1.90	48.33
BB	ABCD	17:47:22.348	-28:22:17.41	0.0	33.100	0.218	O8	0.24	48.31

Notes. [a] All values listed in this table are the values used in the different models assuming HII regions are spherical symmetric regions of fully ionized gas with no dust and a single ionizing source.
[b] These regions are optically thick. Their electron density has been increased manually.
[1] ID is the identifier used in the model. We use the same identifiers as Mehringer et al. (1993); Gaume et al. (1995); De Pree et al. (1998).
[2] Model refers to one of the four model described in this paper.
[3] RA is the right ascension of the HII region given in units of hours:minutes:seconds in the equatorial coordinate system.
[4] DEC is the declination of the HII region given in units of degrees:arcminutes:arcseconds in the equatorial coordinate system.
[5] dz is the displacement along the line of sight with respect to the model center. The z-axis is oriented such that it points towards the observer.
[6] r_{obs} is the observed radius of the HII region.
[7] n_e is the number electron density.
[8] ZAMS refers to the zero age main sequence star embedded in the HII region.
[9] EM is the emission measure.
[10] $\log(\dot{N}_i)$ is the logarithm of the number of Lyman continuum photons.

Table B.2: Small scale structure: Dust density components in Sgr B2.

ID[1]	Model[2]	RA[3] [h:m:s, J2000]	DEC[4] [d:m:s, J2000]	dz[5] [10^5 au]	r_0[6] [10^3 au]	n_c[7] [10^7 H_2 cm^{-3}]	η[8]	star[9]
M-SMA-1a	ABCD	17:47:20.197	-28:23:04.36	1.0	3.0	20	5.0	B0
M-SMA-1b	ABCD	17:47:20.170	-28:23:04.60	1.0	3.1	35	5.0	B0.5
M-SMA-1c	ABCD	17:47:20.158	-28:23:05.08	1.0	3.6	10	5.0	B0.5
M-SMA-1d	ABCD	17:47:20.148	-28:23:05.48	1.0	3.6	20	5.0	B0.5
M-SMA-2a	ABCD	17:47:20.152	-28:23:04.18	0.0	3.2	19	5.0	B0.5
M-SMA-2b	ABCD	17:47:20.124	-28:23:04.45	0.0	3.3	14	5.0	B0.5
M-SMA-3	ABCD	17:47:20.100	-28:23:04.04	0.0	2.8	14	5.0	B0.5
M-SMA-4	ABCD	17:47:20.152	-28:23:03.30	0.0	3.4	7	5.0	none
M-SMA-5	ABCD	17:47:20.212	-28:23:04.90	0.0	3.2	7	5.0	B0.5
M-SMA-6	ABCD	17:47:20.175	-28:23:06.08	0.0	3.0	35	5.0	none
M-SMA-7	ABCD	17:47:20.118	-28:23:06.35	0.0	2.9	30	5.0	B0.5
M-SMA-8	ABCD	17:47:20.215	-28:23:06.43	0.0	3.6	4	5.0	none
M-SMA-9	ABCD	17:47:20.250	-28:23:07.10	0.0	2.8	9	5.0	B0.5
M-SMA-10	ABCD	17:47:20.005	-28:23:05.79	0.0	3.3	15	5.0	none
M-SMA-11	ABCD	17:47:20.108	-28:23:03.10	1.0	3.2	20	5.0	B0.5
M-SMA-12	ABCD	17:47:20.136	-28:23:02.24	1.0	3.8	50	5.0	B0
N-SMA-1a	A	17:47:19.912	-28:22:18.25	-5.0	9.0	45	5.0	none
	BCD			-6.95	9.0	45	5.0	none
N-SMA-1b	A	17:47:19.900	-28:22:19.51	-2.0	4.0	75	5.0	none
	BCD			-6.98	4.0	75	5.0	none
N-SMA-2a	A	17:47:19.944	-28:22:13.64	-3.0	6.9	10	5.0	B0.5
	BCD			-6.97	6.9	10	5.0	B0.5
N-SMA-2b	A	17:47:19.880	-28:22:13.80	-30	6.8	10	5.0	B0.5
	BCD			-6.97	6.8	10	5.0	B0.5

Notes.
[1] ID is the identifier used in the model. These identifiers are identical to the ones introduced by Qin et al. (2011). Note: Some of these objects identified by Qin et al. (2011) show an elongated intensity structure. We recover these objects with a superposition of several spherical symmetric clumps. We distinguish these components by adding additional lowercase letters to the identifier introduced by Qin et al. (2011).
[2] Model refers to one of the four model described in this paper.
[3] RA is the right ascension of the density component given in units of hours:minutes:seconds in the equatorial coordinate system.
[4] DEC is the declination of the density component given in units of degrees:arcminutes:arcseconds in the equatorial coordinate system.
[5] dz is the displacement along the line of sight with respect to the model center. The z-axis is oriented such that it points towards the observer.
[6] r_0 is the radius defining the component, as described in Eq. 4.
[7] n_c is the central density.
[8] η is the exponent of the dust density profile.
[9] This column indicates whether an additional heating source had to be included inside the dust component. If this is the case, the spectral type of the star is given.

Table B.3: Large-scale structure: Dust density envelopes in Sgr B2.

ID[1]	Model[2]	RA[3] [h:m:s, J2000]	DEC[4] [d:m:s, J2000]	dz[5] [10^5 au]	$r_{0,x}$[6] [10^3 au]	$r_{0,y}$[6] [10^3 au]	$r_{0,z}$[6] [10^3 au]	n_0[7] [10^4 H_2 cm^{-3}]	η[8]	star[9]
NE	ABCD	17:47:22.361	-28:21:31.94	0.0	200	200	200	9.8	2.2	B0
N1	A	17:47:19.912	-28:22:18.25	0.0	40	40	40	200	2.5	none
	B			-7.0	40	40	40	400	2.5	none
	C			-7.0	40	40	40	400	2.5	none
	D			-7.0	40	40	55	300	2.5	none
N2	A	17:47:16.000	-28:21:48.00	0.0	30	30	30	60	1.8	none
	B			-7.0	30	30	30	100	1.8	none
	C			-7.0	30	30	45	90	1.8	none
	D			-7.0	30	30	30	90	1.8	none
M1	AB	17:47:20.056	-28:23:06.46	0.0	30	30	30	200	2.5	none
	C			0.0	60	60	140	30	2.5	none
	D			0.0	60	60	80	70	2.5	none
M2	AB	17:47:17.800	-28:23:00.00	0.0	20	20	20	200	1.8	none
	C			0.0	40	40	80	100	1.8	none
	D			0.0	40	40	50	100	1.8	none
S1	ABCD	17:47:20.465	-28:23:45.25	0.0	30	30	30	90	2.4	B0
S2	ABCD	17:47:19.509	-28:23:52.45	0.0	20	20	20	40	1.8	none
Se	ABCD	17:47:21.525	-28:24:20.58	0.0	50	50	50	50	2.3	none
deepS	ABCD	17:47:20.632	-28:25:30.87	0.0	220	220	220	12	2.2	none

Notes.
[1] ID is the identifier used in the model. These identifiers follow the historic naming scheme explained in Sect. 1.
[2] Model refers to one of the four model described in this paper.
[3] RA is the right ascension of the density component given in in units of hours:minutes:seconds in the equatorial system.
[4] DEC is the declination. Both coordinates are given in units of degrees:arcminutes:arcseconds in the equatorial system.
[5] dz is the displacement along the line of sight with respect to the model center. The z-axis is oriented such that it points towards the observer.
[6] r_x, r_y, r_z are the core radii in each principal direction, as described in Eq. 4.
[7] n_e is the central density.
[8] η is the exponent of the dust density profile.
[9] This column indicates whether an additional heating source had to be included inside the dust component. If this is the case, the spectral type of the star is given.

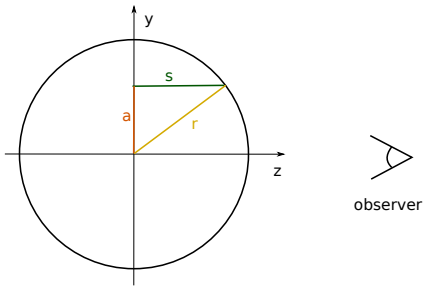

Fig. C.1: Sketch of the HII region. Cut along the line of sight. The integration path along-the line of sight for the calculation of the emission measure is marked.

Appendix C: Derivation of the physical parameters of HII regions

We consider HII regions as Strömgren spheres. They are fully ionized and contain no dust. Here we derive the emission measure, the electron density, and the total flux of ionizing photons for such a region. We assume an electron density distribution that equals n_e within the radius r_0 of the HII region and is zero elsewhere. We can then calculate the emission measure EM by integrating the number of electrons and number of ions along the line-of-sight. The factor accounts for both sides of the sphere.

$$EM = 2 \int_0^{z'} n_e n_i dz \tag{C.1}$$

If we assume that the HII regions only contain hydrogen, it follows that the electron density n_e equals the ion density n_i. Since the electron density n_e is uniform within the HII region, we can rewrite Eq. C.1 taking the geometry given in Fig. C.1 into account.

$$EM = 2\, n_e^2 \sqrt{r_0^2 - a^2} \tag{C.2}$$

$$= 2\, n_e^2\, D\, \theta_0 \sqrt{1 - \left(\frac{\theta_a}{\theta_0}\right)^2} \tag{C.3}$$

$$= 2\, n_e^2\, D\, \theta_0\, \psi(\theta_a) \tag{C.4}$$

where D is the distance to the source, $\theta_0 = r_0/D$ is the radius of the HII region in angular units, and $\theta_a = \sqrt{x^2 + y^2}/D$ is the angular position in the x-y plane ($z = 0$). If we want to calculate the maximum emission measure, we set $a = 0$ and the term $\sqrt{1 - \left(\frac{\theta_a}{\theta_0}\right)^2}$ vanishes. Introducing the angular source diameter $\theta_{\rm source} = 2\theta_0$, we obtain

$$EM = n_e^2\, D\, \theta_{\rm source} \tag{C.5}$$

However, neither the emission measure nor the electron density are known. So we need another equation to solve Eq. C.5. Integrating the specific intensity I_ν over the angular size of the source $\Omega_{\rm source}$ yields the flux density F_ν

$$F_\nu = \int_{\Omega_{\rm source}} I_\nu d\Omega \tag{C.6}$$

The general solution of the radiative transfer equation for the specific continuum intensity is e.g. given by Rybicki & Lightman (1986) as

$$I_\nu = I_0\, e^{-\tau_\nu} + \int_0^{\tau_\nu} S_\nu\, e^{-(\tau_\nu - \tau'_\nu)} d\tau'$$
$$= I_0\, e^{-\tau_\nu} + S_\nu (1 - e^{-\tau_\nu}) \tag{C.7}$$

where S_ν is the source function of the HII region and I_0 is the background intensity. We assume an HII region with uniform temperature and negligible background temperature, i.e. $I_\nu(0) \ll S_\nu$. The intensity I_ν is then given by

$$I_\nu = S_\nu (1 - e^{-\tau_\nu}) \tag{C.8}$$

We have to distinguish two cases for the optical depth τ_ν:

$$I_\nu = \begin{cases} S_\nu \tau_\nu & \text{if } \tau_\nu \ll 1 \quad \text{(optical thin)} \\ S_\nu & \text{if } \tau_\nu \gg 1 \quad \text{(optical thick)} \end{cases} \tag{C.9}$$

The source function S_ν for the free-free radiation can be defined using the Planck function B_ν at an electron temperature T_e

$$S_\nu = B_\nu(T_e)$$
$$\approx \frac{2kT_e\nu^2}{c^2} \tag{C.10}$$

where k is the Boltzman constant, c is the speed of light in vacuum and h is the Planck constant. The second step holds if $h\nu \ll kT$ (Rayleigh-Jeans approximation). The optical path length for free-free emission was derived by Oster (1961), an approximation is given by Altenhoff et al. (1960).

$$\tau_{\rm Altenhoff} = 8.235 \times 10^{-2} \left(\frac{T_e}{\rm K}\right)^{-1.35} \left(\frac{\nu}{\rm GHz}\right)^{-2.1} \left(\frac{\rm EM}{\rm pc\ cm^{-6}}\right) \tag{C.11}$$

This approximation deviates in the region of interest, i.e. $5 \times 10^3 \leq T_e \leq 1.2 \times 10^4$ K and 100MHz $\leq \nu \leq$ 35 GHz, less than 10% (Mezger & Henderson 1967).

Putting everything together, and assuming optical thin emission, we obtain

$$\left(\frac{F_\nu}{Jy}\right) = 2.525 \times 10^3 \left(\frac{T_e}{\rm K}\right)^{-0.35} \left(\frac{\nu}{\rm GHz}\right)^{-0.1} \left(\frac{\rm EM}{\rm pc\ cm^{-6}}\right) \Omega_{\rm source} \tag{C.12}$$

Usually one fits a Gaussian to the data and extracts the flux density and the full width at half maximum from this fit. However, we determine the total flux in a given circular aperture. We thus calculate the solid angle for the given density distribution as follows.

$$\Omega_{\rm source} = 2\pi \int_0^{\theta_0} \theta_a \psi(\theta_a)\, d\theta_a$$
$$= \frac{\pi}{6} \theta^2_{\rm source}$$
$$= 1.231 \times 10^{-11} \left(\frac{\theta_{\rm source}}{\rm arcsec}\right)^2 \tag{C.13}$$

Now we obtain the following expression for the emission measure for a circular aperture

$$\left(\frac{\rm EM}{\rm pc\ cm^{-6}}\right) = 3.217 \times 10^7 \left(\frac{F_\nu}{\rm Jy}\right) \left(\frac{T_e}{\rm K}\right)^{0.35} \left(\frac{\nu}{\rm GHz}\right)^{0.1} \left(\frac{\theta_{\rm source}}{\rm arcsec}\right)^{-2} \tag{C.14}$$

From that we can derive an expression to calculate the electron density

$$\left(\frac{n_e}{\rm cm^{-3}}\right) = 2.576 \times 10^6 \left(\frac{F_\nu}{\rm Jy}\right)^{0.5} \left(\frac{T_e}{\rm K}\right)^{0.175} \left(\frac{\nu}{\rm GHz}\right)^{0.05}$$
$$\times \left(\frac{\theta_{\rm source}}{\rm arcsec}\right)^{-1.5} \left(\frac{D}{\rm pc}\right)^{-0.5} \tag{C.15}$$

To derive the flux of ionizing photons, $\dot{N}_{\rm i}$, we balance the number of recombinations and photoionizations within the HII region. In a Strömgren sphere, this yields

$$\dot{N}_{\rm i} = \int n_e^2(\beta - \beta_1) dV \tag{C.16}$$

where β and β_1 are the rate coefficients for recombinations to all levels and to the ground state, respectively. Thus $(\beta - \beta_1)$ provides the recombination coefficient to level 2 or higher. Rubin (1968) approximate the recombination coefficient given by Seaton (1959) for electron temperatures T_e generally found in HII regions as

$$\left(\frac{\beta - \beta_1}{\rm cm^3\ s^{-1}}\right) = 4.1 \times 10^{-10} \left(\frac{T_e}{\rm K}\right)^{-0.8} \tag{C.17}$$

Including Eq. C.17 in Eq. C.16 and solving the integral for a spherical symmetric clump yields:

$$\left(\frac{\dot{N}_{\rm i}}{\rm s^{-1}}\right) = \frac{4}{3}\pi \left(\frac{r_0}{\rm cm}\right)^3 \left(\frac{n_e}{\rm cm^{-3}}\right)^2 \times 4.1 \times 10^{-10} \left(\frac{T_e}{\rm K}\right)^{-0.8} \tag{C.18}$$

Converting the radius r_0 to the angular diameter $\theta_{\rm source}$ of the HII region and using Eq. 7 yields an expression for the total flux of ionizing photons, given in practical units as

$$\left(\frac{\dot{N}_{\rm i}}{\rm s^{-1}}\right) = 4.771 \times 10^{42} \times \left(\frac{F_\nu}{\rm Jy}\right) \left(\frac{T_e}{\rm K}\right)^{-0.45} \left(\frac{\nu}{\rm GHz}\right)^{0.1} \left(\frac{D}{\rm pc}\right)^2 \tag{C.19}$$

This research is carried out within the Collaborative Research Centre (CRC) 956, sub-project A6, funded by the Deutsche Forschungsgesellschaft (DFG).

Technical

My work made extensive use of python packages: Astropy, a community-developed core Python package for Astronomy (Astropy Collaboration et al. 2013), Aplpy, an open source plotting package for Python[1], Kapteyn, matplotlib, pandas, scipy, numpy, pp, to just name a few of the ones used on a regular basis. My work furthermore made use of many software packages, either related to astronomy or to the more general tasks of data visualization and image processing: kvis, ds9, Gildas, Montage, HIPE, inkscape, gimp, paraview. Montage is funded by the National Science Foundation under Grant Number ACI-1440620, and was previously funded by the National Aeronautics and Space Administration's Earth Science Technology Office, Computation Technologies Project, under Cooperative Agreement Number NCC5-626 between NASA and the California Institute of Technology.

Without profiling codes and debuggers, an immeasurable amount of time would have been wasted on randomly searching for bottlenecks of my codes or finding bugs. So thanks to valgrind, gdb etc for the constant support.

Furthermore, this work would have taken much longer without the many contributors to *stackoverflow*[2]. Without their crowd-knowledge, some bugs would have taken much longer to find and eliminate. Similarly,

[1] Aplpy is hosted at http://aplpy.github.com
[2] http://www.stackoverflow.com

whenever there was a LaTeX related problem that I could not figure out myself the crowd-knowledge stored in tex.stackexchange[3] usually quickly helped me.

Observational

This research has made extensive use of NASA's Astrophysics Data System (ADS), SIMBAD database, operated at CDS, Strasbourg, France, and the NASA/ IPAC Infrared Science Archive, which is operated by the Jet Propulsion Laboratory, California Institute of Technology, under contract with the National Aeronautics and Space Administration.

The ATLASGAL project is a collaboration between the Max-Planck-Gesellschaft, the European Southern Observatory (ESO) and the Universidad de Chile. It includes projects E-181.C-0885, E-078.F-9040(A), M-079.C-9501(A), M-081.C-9501(A) plus Chilean data.

Herschel is an ESA space observatory with science instruments provided by European-led Principal Investigator consortia and with important participation from NASA. HIFI has been designed and built by a consortium of institutes and university departments from across Europe, Canada and the United States under the leadership of SRON Netherlands Institute for Space Research, Groningen, The Netherlands and with major contributions from Germany, France and the US. Consortium members are: Canada: CSA, U.Waterloo; France: CESR, LAB, LERMA, IRAM; Germany: KOSMA, MPIfR, MPS; Ireland, NUI Maynooth; Italy: ASI, IFSI-INAF, Osservatorio Astrofisico di Arcetri-INAF; Netherlands: SRON, TUD; Poland: CAMK, CBK; Spain: Observatorio Astronómico Nacional (IGN), Centro de Astrobiología (CSIC-INTA). Sweden: Chalmers University of Technology - MC2, RSS & GARD; Onsala Space Observatory; Swedish National Space Board, Stockholm University - Stockholm Observatory; Switzerland: ETH Zurich, FHNW; USA: Caltech, JPL, NHSC.

The National Radio Astronomy Observatory is a facility of the National Science Foundation operated under cooperative agreement by Associated Universities, Inc.

The Submillimeter Array is a joint project between the Smithsonian Astrophysical Observatory and the Academia Sinica Institute of Astronomy and Astrophysics and is funded by the Smithsonian Institution and the Academia Sinica.

Atlas Images were obtained as part of the Two Micron All Sky Survey (2MASS), which is a joint project of the University of Massachusetts and the Infrared Processing and Analysis Center/California Institute of Technology, funded by the National Aeronautics and Space Administration and the National Science Foundation.

[3] http://tex.stackexchange.com/

Personal

Finally, let's get personal. While all of this is my own work, it would not have been possible without the help, guidance, friendship and support from and by many people.

First and foremost, I wish to express my sincerest gratitude to my mentor and advisor, Prof. Dr. Peter Schilke. I am most thankful for the independence you allowed me in all aspects of my research. While you were always ready to support me with suggestions and challenges, you did not dictate the course of my research (and by extension my thesis). I also wish to thank my thesis committee, namely Prof. Dr. Stefanie Walch-Gassner, Prof. Dr. Susanne Crewell, and Dr. Álvaro Sánchez-Monge.

I was very lucky to have the CRC 956 support my work with a thesis advisory committee. I would like to thank my members of this committee for taking the time off their busy schedules to support me with very helpful discussions and plenty of useful suggestions, namely Prof. Dr. Peter Schilke, Prof. Dr. Jürgen Stutzki, and Dr. Friedrich Wyrowski. I would also like to thank Dr. Susanne Herbst, the coordinator of the CRC for her support to schedule the thesis advisory committee meetings.

The CRC also supported my three month research visit at Caltech, Pasadena to work with Dr. Darek Lis on the extension of the three-dimensional model of Sgr B2 to the large scales. I would like to thank Dr. Darek Lis for providing me the opportunity to spent three month in California, as well as the support and advise he provided during my stay at Caltech. I furthermore would like to thank John Carpenter for giving me the opportunity to observe with Combined Array for Research in Millimeter-wave Astronomy (CARMA) for the last time before is was closed only 1.5 years later. May you rest in peace CARMA. The staff and my fellow observers during that week at CARMA, which taught me a lot about interferometric observations, mainly Dr. Nikolaus Volgenau and Dr. Luca Ricci.

The (longer-term) members of my working group (in alphabetical order): Marzieh Arzhini, Irina Bernst, Denis Büchel, Dr. Philipp Carlhoff, Dr. Rumpa

Choudhury, Dr. Claudia Comito, Ümit Kavak, Fanyi Meng, Dr. Thomas Möller, Dr. Despina Panoglou, Stefan Pols, Dr. Sheng-Li Qin, Dr. Rainer Rolffs, Mahya Sadaghiani, Dr. Álvaro Sánchez-Monge, Gwendoline Stéphan, Sümeyye Suri, and Dr. Alexander Zernickel. You all, made my daily working life certainly more interesting, and I enjoyed the lunch-break discussions.

Mein Langzeit-Bürokollege, sowohl im Hauptgebäude als auch im Exil, Thomas: Vielen lieben Dank für unzählige Diskussionen über Pandora, numerische Simulationen, Optimierung, Python, Programmierung im Allgemeinen, astronomischen Methoden und vieles, vieles, was ich gerade vergesse. Álvaro, mi español es malísimo, so I will not try to put this into Spanish: Thank you very much for your constant support, for always lending me an ear and helping me in straighting out aspects of Pandora, Sagittarius B2, HII regions, interferometry, post-processing, not to forget unit conversions!

I am very grateful for the support I received from members of the spectroscopy group. Besonderer Dank geht an Dr. Monika Körber, Dr. Lars Kluge und Dr. Sven Thorwirth, die geduldig meine diversen Fragen zur Molekülphysik beantwortet haben. Many thanks also to Dr. Oskar Asvany, Dr. Pavol Jusko, Dr. Monika Körber, Dr. Lars Kluge, Dr. Sabrina Gärtner and Alexander Stoffels for showing me their laboratories, explaining me their experiments and letting me actually use a screwdriver now and then. This was a very nice change to otherwise daily routines (i.e. bug hunting). And no, I did not screw up any of their experiments.

Dr. Frank Schlöder und Dr. Thomas Möller sei für ihre unermüdliche Betreuung unserer Server gedankt. Ohne die tatkräftige Unterstützung unserer Verwaltung hätten viele administrative Aufgaben deutlich mehr Zeit gekostet. Vielen Dank dafür an Tanja Bodendorf, Stefanie Krämer, Bettina Krause, Maxi Limbach, Anke Pyschny, Mariia Soloviova. Auch wenn ich kein BCGS Student war und sie somit offiziell nicht für mich zuständig war, Dr. Petra Neugebauer-Guenther hatte immer ein offenes Ohr für mich. Vielen Dank dafür.

My fellow students (yeah, and post-Docs), you made this time an experience I will not forget. Thank you for tea breaks, coffee breaks, movie and board game evenings, science and non-science discussions: Alexander, Álvaro, Angela, Anna, Annika, Baschtl, Christian, Cristian, Daniel, Denis, Gerold, Gwendonline, Lars, Marcus, Martin, Marzieh, Monika, Moritz, Nastaran, Norma, Oliver, Pablo, Pavol, Paul, Pia, Philipp, Prabesh, Sabrina, Silke, Sina, Sümeyye, and Timo. Im pretty sure, Ive messed this list up and unintentionally forgot someone. If so, I owe you at least a coffee (or tea or beer...).

Ein grosses Dankeschön geht auch an meine Freunde einfach weil es sie gibt und sie immer für mich da sind!

Meinem grossen Bruder ist ein ebenso grosser Dank geschuldet. Ohne dich hätte ich als Kind Computer wahrscheinlich nur aus der Ferne betrachtet und auch meine Liebe zur Naturwissenschaft nicht oder nur wesentlich später entdeckt. Ich danke meinen Eltern! Ihr habe mich unermüdlich in jedem Schritt dieser Berg- und Talfahrt, genannt Doktorarbeit, unterstützt.

Vielen Dank!
Many thanks!
¡Muchas gracias!
Merci beaucoup!
Teşekkür ederim!
Grazie mille!

Aarseth, S. J., M. Henon & R. Wielen (1974). “A comparison of numerical methods for the study of star cluster dynamics”. In: 0.24 A&A 37, 183 (cit. on p. 40).

ALMA Partnership, C. L. Brogan, L. M. Pérez, T. R. Hunter, W. R. F. Dent, A. S. Hales, R. E. Hills, S. Corder, E. B. Fomalont, C. Vlahakis, Y. Asaki, D. Barkats, A. Hirota, J. A. Hodge, C. M. V. Impellizzeri, R. Kneissl, E. Liuzzo, R. Lucas, N. Marcelino, S. Matsushita, K. Nakanishi, N. Phillips, A. M. S. Richards, I. Toledo, R. Aladro, D. Broguiere, J. R. Cortes, P. C. Cortes, D. Espada, F. Galarza, D. Garcia-Appadoo, L. Guzman-Ramirez, E. M. Humphreys, T. Jung, S. Kameno, R. A. Laing, S. Leon, G. Marconi, A. Mignano, B. Nikolic, L.-A. Nyman, M. Radiszcz, A. Remijan, J. A. Rodón, T. Sawada, S. Takahashi, R. P. J. Tilanus, B. Vila Vilaro, L. C. Watson, T. Wiklind, E. Akiyama, E. Chapillon, I. de Gregorio-Monsalvo, J. Di Francesco, F. Gueth, A. Kawamura, C.-F. Lee, Q. Nguyen Luong, J. Mangum, V. Pietu, P. Sanhueza, K. Saigo, S. Takakuwa, C. Ubach, T. van Kempen, A. Wootten, A. Castro-Carrizo, H. Francke, J. Gallardo, J. Garcia, S. Gonzalez, T. Hill, T. Kaminski, Y. Kurono, H.-Y. Liu, C. Lopez, F. Morales, K. Plarre, G. Schieven, L. Testi, L. Videla, E. Villard, P. Andreani, J. E. Hibbard & K. Tatematsu (2015). “The 2014 ALMA Long Baseline Campaign: First Results from High Angular Resolution Observations toward the HL Tau Region”. In: 0.24 ApJ 808, L3, L3 (cit. on p. 18).

Altenhoff, W., P. G. Mezger, H. Wendker & G. Westerhout (1960). “Veröffentlichungen der Universitätssternwarte Bonn”. In: 0.24 Ver"offentlichungen der Universitätssternwarte Bonn 59, 48 (cit. on p. 130).

André, P., J. Di Francesco, D. Ward-Thompson, S.-I. Inutsuka, R. E. Pudritz & J. E. Pineda (2014). "From Filamentary Networks to Dense Cores in Molecular Clouds: Toward a New Paradigm for Star Formation". In: 0.24 Protostars and Planets VI, 27–51 (cit. on pp. 8, 11).

Astropy Collaboration, T. P. Robitaille, E. J. Tollerud, P. Greenfield, M. Droettboom, E. Bray, T. Aldcroft, M. Davis, A. Ginsburg, A. M. Price-Whelan, W. E. Kerzendorf, A. Conley, N. Crighton, K. Barbary, D. Muna, H. Ferguson, F. Grollier, M. M. Parikh, P. H. Nair, H. M. Unther, C. Deil, J. Woillez, S. Conseil, R. Kramer, J. E. H. Turner, L. Singer, R. Fox, B. A. Weaver, V. Zabalza, Z. I. Edwards, K. Azalee Bostroem, D. J. Burke, A. R. Casey, S. M. Crawford, N. Dencheva, J. Ely, T. Jenness, K. Labrie, P. L. Lim, F. Pierfederici, A. Pontzen, A. Ptak, B. Refsdal, M. Servillat & O. Streicher (2013). "Astropy: A community Python package for astronomy". In: 0.24 A&A 558, A33, A33 (cit. on p. I).

Bacmann, A., P. André & D. Ward-Thompson (2001). "The Structure of Prestellar Cores as Derived from ISO Observations". In: 0.24 From Darkness to Light: Origin and Evolution of Young Stellar Clusters. Ed. by T. Montmerle & P. André. Vol. 243. Astronomical Society of the Pacific Conference Series, 113 (cit. on p. 12).

Belloche, A., H. S. P. Müller, K. M. Menten, P. Schilke & C. Comito (2013). "Complex organic molecules in the interstellar medium: IRAM 30 m line survey of Sagittarius B2(N) and (M)". In: 0.24 A&A 559, A47, A47 (cit. on p. 87).

Berger, M. J. & P. Colella (1989). "Local adaptive mesh refinement for shock hydrodynamics". In: 0.24 Journal of Computational Physics 82, 64–84 (cit. on p. 46).

Berger, M. J. & J. Oliger (1984). "Adaptive Mesh Refinement for Hyperbolic Partial Differential Equations". In: 0.24 Journal of Computational Physics 53, 484–512 (cit. on p. 46).

Bergin, E. A., T. G. Phillips, C. Comito, N. R. Crockett, D. C. Lis, P. Schilke, S. Wang, T. A. Bell, G. A. Blake, B. Bumble, E. Caux, S. Cabrit, C. Ceccarelli, J. Cernicharo, F. Daniel, T. de Graauw, M.-L. Dubernet, M. Emprechtinger, P. Encrenaz, E. Falgarone, M. Gerin, T. F. Giesen, J. R. Goicoechea, P. F. Goldsmith, H. Gupta, P. Hartogh, F. P. Helmich, E. Herbst, C. Joblin, D. Johnstone, J. H. Kawamura, W. D. Langer, W. B. Latter, S. D. Lord, S. Maret, P. G. Martin, G. J. Melnick, K. M. Menten, P. Morris, H. S. P. Müller, J. A. Murphy, D. A. Neufeld, V. Ossenkopf, L. Pagani, J. C. Pearson, M. Pérault, R. Plume, P. Roelfsema, S.-L. Qin, M. Salez, S. Schlemmer, J. Stutzki, A. G. G. M. Tielens, N. Trappe, F. F. S. van der Tak, C. Vastel, H. W. Yorke, S. Yu & J. Zmuidzinas (2010). "Herschel observations of EXtra-Ordinary Sources (HEXOS): The present and future of spectral surveys with Herschel/HIFI". In: 0.24 A&A 521, L20, L20 (cit. on p. 65).

Bergin, E. A. & M. Tafalla (2007). "Cold Dark Clouds: The Initial Conditions for Star Formation". In: 0.24 ARA&A 45, 339–396 (cit. on pp. 9, 12, 13).

Beuther, H., E. B. Churchwell, C. F. McKee & J. C. Tan (2007). “The Formation of Massive Stars”. In: 0.24 Protostars and Planets V, 165–180 (cit. on p. 8).

Bjorkman, J. E. & K. Wood (2001). “Radiative Equilibrium and Temperature Correction in Monte Carlo Radiation Transfer”. In: 0.24 ApJ 554, 615–623 (cit. on p. 42).

Black, J. H. & E. F. van Dishoeck (1987). “Fluorescent excitation of interstellar H2”. In: 0.24 ApJ 322, 412–449 (cit. on p. 11).

Bonnor, W. B. (1956). “Boyle’s Law and gravitational instability”. In: 0.24 MNRAS 116, 351 (cit. on p. 12).

Brinch, C. & M. R. Hogerheijde (2010). “LIME - a flexible, non-LTE line excitation and radiation transfer method for millimeter and far-infrared wavelengths”. In: 0.24 A&A 523, A25, A25 (cit. on pp. 36, 47).

Caselli, P., C. M. Walmsley, M. Tafalla, L. Dore & P. C. Myers (1999). “CO Depletion in the Starless Cloud Core L1544”. In: 0.24 ApJ 523, L165–L169 (cit. on p. 13).

Casuso, E. & J. E. Beckman (2010). “Explaining the Galactic Interstellar Dust Grain Size Distribution Function”. In: 0.24 AJ 139, 1406–1412 (cit. on p. 9).

Ceccarelli, C. (2004). “The Hot Corinos of Solar Type Protostars”. In: 0.24 Star Formation in the Interstellar Medium: In Honor of David Hollenbach. Ed. by D. Johnstone, F. C. Adams, D. N. C. Lin, D. A. Neufeeld & E. C. Ostriker. Vol. 323. Astronomical Society of the Pacific Conference Series, 195 (cit. on p. 15).

Cernicharo, J. (1991). “The Physical Conditions of Low Mass Star Forming Regions”. In: 0.24 NATO Advanced Science Institutes (ASI) Series C. Ed. by C. J. Lada & N. D. Kylafis. Vol. 342. NATO Advanced Science Institutes (ASI) Series C, 287 (cit. on p. 9).

Chabrier, G. (2003). “Galactic Stellar and Substellar Initial Mass Function”. In: 0.24 PASP 115, 763–795 (cit. on p. 14).

Chira, R.-A., R. J. Smith, R. S. Klessen, A. M. Stutz & R. Shetty (2014). “Line profiles of cores within clusters - III. What is the most reliable tracer of core collapse in dense clusters?” In: 0.24 MNRAS 444, 874–886 (cit. on p. 19).

Choudhury, R., P. Schilke, G. Stéphan, E. Bergin, T. Möller, A. Schmiedeke & A. Zernickel (2015). “Evolution of complex organic molecules in hot molecular cores. Synthetic spectra at (sub-)mm wavebands”. In: 0.24 A&A 575, A68, A68 (cit. on pp. 38, 43).

Comito, C. & P. Schilke (2002). “Reconstructing reality: Strategies for sideband deconvolution”. In: 0.24 A&A 395, 357 (cit. on p. 67).

Cox, A. N. (2000). 0.24 Allen’s astrophysical quantities (cit. on p. 90).

Crutcher, R., C. Heiles & T. Troland (2003). “Observations of Interstellar Magnetic Fields”. In: 0.24 Turbulence and Magnetic Fields in Astrophysics. Ed. by E. Falgarone & T. Passot. Vol. 614. Lecture Notes in Physics, Berlin Springer Verlag, 155–181 (cit. on p. 13).

Csengeri, T., J. S. Urquhart, F. Schuller, F. Motte, S. Bontemps, F. Wyrowski, K. M. Menten, L. Bronfman, H. Beuther, T. Henning, L. Testi, A. Zavagno & M. Walmsley (2014). “The ATLASGAL survey: a catalog of dust condensations in the Galactic plane”. In: 0.24 A&A 565, A75, A75 (cit. on p. 69).

Csengeri, T., A. Weiss, F. Wyrowski, K. M. Menten, J. S. Urquhart, S. Leurini, F. Schuller, H. Beuther, S. Bontemps, L. Bronfman, T. Henning & N. Schneider (2016). “The ATLASGAL survey: distribution of cold dust in the Galactic plane. Combination with Planck data”. In: 0.24 A&A 585, A104, A104 (cit. on pp. 69, 139).

Dale, J. E., B. Ercolano & I. A. Bonnell (2012). “Ionizing feedback from massive stars in massive clusters - II. Disruption of bound clusters by photoionization”. In: 0.24 MNRAS 424, 377–392 (cit. on p. 18).

De Pree, C. G., W. M. Goss & R. A. Gaume (1998). “Ionized Gas in Sagittarius B2 Main on Scales of 0.065 Arcsecond (600 AU)”. In: 0.24 ApJ 500, 847 (cit. on pp. 24, 69, 72, 73, 83, 175).

De Vicente, P., J. Martin-Pintado & T. L. Wilson (1997). “A hot ring in the Sagittarius B2 molecular cloud.” In: 0.24 A&A 320, 957 (cit. on pp. 44, 104).

Dobbs, C. L., M. R. Krumholz, J. Ballesteros-Paredes, A. D. Bolatto, Y. Fukui, M. Heyer, M.-M. M. Low, E. C. Ostriker & E. Vázquez-Semadeni (2014). “Formation of Molecular Clouds and Global Conditions for Star Formation”. In: 0.24 Protostars and Planets VI, 3–26 (cit. on pp. 8, 11).

Draine, B. T. (2011). 0.24 Physics of the Interstellar and Intergalactic Medium (cit. on pp. 10, 25).

Dullemond, C. P. (2012). 0.24 RADMC-3D. ASCL (cit. on pp. 36, 47).

Ebert, R. (1955). “Über die Verdichtung von H I-Gebieten. Mit 5 Textabbildungen”. In: 0.24 ZAp 37, 217 (cit. on p. 12).

Elmegreen, B. G. & J. Scalo (2004). “Interstellar Turbulence I: Observations and Processes”. In: 0.24 ARA&A 42, 211–273 (cit. on p. 11).

Espinoza, P., F. J. Selman & J. Melnick (2009). “The massive star initial mass function of the Arches cluster”. In: 0.24 A&A 501, 563 (cit. on p. 3).

Etxaluze, M., J. R. Goicoechea, J. Cernicharo, E. T. Polehampton, A. Noriega-Crespo, S. Molinari, B. M. Swinyard, R. Wu & J. Bally (2013). “Herschel observations of the Sagittarius B2 cores: Hydrides, warm CO, and cold dust”. In: 0.24 A&A 556, A137, A137 (cit. on pp. 24, 85, 92, 94, 95).

Evans, N. (2003). “Studying Infall”. In: 0.24 SFChem 2002: Chemistry as a Diagnostic of Star Formation. Ed. by C. L. Curry & M. Fich, 157 (cit. on pp. 13, 32).

Evans II, N. J. (1999). “Physical Conditions in Regions of Star Formation”. In: 0.24 ARA&A 37, 311–362 (cit. on p. 13).

Federrath, C. & R. S. Klessen (2013). “On the Star Formation Efficiency of Turbulent Magnetized Clouds”. In: 0.24 ApJ 763, 51, 51 (cit. on pp. 88, 90).

Ferrière, K. M. (2001). “The interstellar environment of our galaxy”. In: 0.24 Reviews of Modern Physics 73, 1031–1066 (cit. on pp. 9, 19).

Field, G. B. (1975). “The composition of interstellar dust”. In: 0.24 The Dusty Universe. Ed. by G. B. Field & A. G. W. Cameron, 89–112 (cit. on p. 9).

Field, G. B., D. W. Goldsmith & H. J. Habing (1969). “Cosmic-Ray Heating of the Interstellar Gas”. In: 0.24 ApJ 155, L149 (cit. on p. 10).

Figer, D. F., I. S. McLean & M. Morris (1999). “Massive Stars in the Quintuplet Cluster”. In: 0.24 ApJ 514, 202 (cit. on p. 3).

Gaume, R. A., M. J. Claussen, C. G. de Pree, W. M. Goss & D. M. Mehringer (1995). “The Sagittarius B2 Star-forming Region. I. Sensitive 1.3 Centimeter Continuum Observations”. In: 0.24 ApJ 449, 663 (cit. on pp. 24, 68, 72, 73, 175).

Ginsburg, A., J. Glenn, E. Rosolowsky, T. P. Ellsworth-Bowers, C. Battersby, M. Dunham, M. Merello, Y. Shirley, J. Bally, N. J. Evans II, G. Stringfellow & J. Aguirre (2013). “The Bolocam Galactic Plane Survey. IX. Data Release 2 and Outer Galaxy Extension”. In: 0.24 ApJS 208, 14, 14 (cit. on pp. 136, 139).

Ginsburg, A., C. Henkel, Y. Ao, D. Riquelme, J. Kauffmann, T. Pillai, E. A. C. Mills, M. A. Requena-Torres, K. Immer, L. Testi, J. Ott, J. Bally, C. Battersby, J. Darling, S. Aalto, T. Stanke, S. Kendrew, J. M. D. Kruijssen, S. Longmore, J. Dale, R. Guesten & K. M. Menten (2016). “Dense gas in the Galactic central molecular zone is warm and heated by turbulence”. In: 0.24 A&A 586, A50, A50 (cit. on p. 20).

Goicoechea, J. R., N. J. Rodrıguez-Fernández & J. Cernicharo (2004). “The Far-Infrared Spectrum of the Sagittarius B2 Region: Extended Molecular Absorption, Photodissociation, and Photoionization”. In: 0.24 ApJ 600, 214 (cit. on p. 24).

Goldsmith, P. F. (2001). “Molecular Depletion and Thermal Balance in Dark Cloud Cores”. In: 0.24 ApJ 557, 736–746 (cit. on p. 13).

Goldsmith, P. F. & W. D. Langer (1978). “Molecular cooling and thermal balance of dense interstellar clouds”. In: 0.24 ApJ 222, 881–895 (cit. on p. 13).

Goldsmith, P. F., D. C. Lis, R. Hills & J. Lasenby (1990). “High angular resolution submillimeter observations of Sagittarius B2”. In: 0.24 ApJ 350, 186 (cit. on pp. 23, 24, 73, 92, 93).

Goldsmith, P. F., D. C. Lis, D. F. Lester & P. M. Harvey (1992). “High angular resolution far-infrared observations of Sagittarius B2”. In: 0.24 ApJ 389, 338 (cit. on pp. 92, 93).

Gordon, M. A., U. Berkermann, P. G. Mezger, R. Zylka, C. G. T. Haslam, E. Kreysa, A. Sievers & R. Lemke (1993). “Anatomy of the Sagittarius complex. 3: Morphology and characteristics of the SGR B2 giant molecular giant molecular cloud”. In: 0.24 A&A 280, 208 (cit. on p. 24).

Griffin, M. J. et al. (2010). “The Herschel-SPIRE instrument and its in-flight performance”. In: 0.24 A&A 518, L3, L3 (cit. on p. 69).

Griffiths, S. C., R. B. Hicks & E. F. Milone (1988). “A re-examination of mass-luminosity relations from binary-star data”. In: 0.24 JRASC 82, 1–12 (cit. on p. 42).

Heitsch, F., A. Burkert, L. W. Hartmann, A. D. Slyz & J. E. G. Devriendt (2005). “Formation of Structure in Molecular Clouds: A Case Study”. In: 0.24 ApJ 633, L113–L116 (cit. on p. 10).

Heitsch, F., M.-M. Mac Low & R. S. Klessen (2001). “Gravitational Collapse in Turbulent Molecular Clouds. II. Magnetohydrodynamical Turbulence”. In: 0.24 ApJ 547, 280–291 (cit. on p. 14).

Henshaw, J. D., S. N. Longmore, J. M. D. Kruijssen, B. Davies, J. Bally, A. Barnes, C. Battersby, M. Burton, M. R. Cunningham, J. E. Dale, A. Ginsburg, K. Immer, P. A. Jones, S. Kendrew, E. A. C. Mills, S. Molinari, T. J. T. Moore, J. Ott, T. Pillai, J. Rathborne, P. Schilke, A. Schmiedeke, L. Testi, D. Walker, A. Walsh & Q. Zhang (2016). “Molecular gas kinematics within the central 250 pc of the Milky Way”. In: 0.24 MNRAS 457, 2675–2702 (cit. on p. 22).

Herbst, E., Q. Chang & H. M. Cuppen (2005). “Chemistry on interstellar grains”. In: 0.24 Journal of Physics Conference Series 6, 18–35 (cit. on p. 9).

Hildebrand, R. H. (1983). “The Determination of Cloud Masses and Dust Characteristics from Submillimetre Thermal Emission”. In: 0.24 QJRAS 24, 267 (cit. on pp. 9, 85, 90, 92).

Hosokawa, T. & K. Omukai (2009). “Evolution of Massive Protostars with High Accretion Rates”. In: 0.24 ApJ 691, 823–846 (cit. on p. 42).

Hüttemeister, S., T. L. Wilson, C. Henkel & R. Mauersberger (1993). “A Multilevel Study of Ammonia in Star Forming Regions - Part Five - the SAGITTARIUS-B2 Region”. In: 0.24 A&A 276, 445 (cit. on p. 23).

Hüttemeister, S., T. L. Wilson, R. Mauersberger, C. Lemme, G. Dahmen & C. Henkel (1995). “A multilevel study of ammonia in star-forming regions. 6: The envelope of Sagittarius B2”. In: 0.24 A&A 294, 667 (cit. on p. 24).

Ibáñez-Mejıa, J. C., M.-M. Mac Low, R. S. Klessen & C. Baczynski (2016). “Gravitational contraction versus Supernova driving and the origin of the velocity dispersion-size relation in molecular clouds”. In: 0.24 ApJ (cit. on p. 11).

Johnstone, D., C. D. Wilson, G. Moriarty-Schieven, G. Joncas, G. Smith, E. Gregersen & M. Fich (2000). "Large-Area Mapping at 850 Microns. II. Analysis of the Clump Distribution in the ρ Ophiuchi Molecular Cloud". In: 0.24 ApJ 545, 327–339 (cit. on p. 11).

Kainulainen, J., H. Beuther, T. Henning & R. Plume (2009). "Probing the evolution of molecular cloud structure. From quiescence to birth". In: 0.24 A&A 508, L35–L38 (cit. on p. 90).

Kauffmann, J., F. Bertoldi, T. L. Bourke, N. J. Evans II & C. W. Lee (2008). "MAMBO mapping of Spitzer c2d small clouds and cores". In: 0.24 A&A 487, 993–1017 (cit. on p. 92).

Khokhlov, A. (1998). "Fully Threaded Tree Algorithms for Adaptive Refinement Fluid Dynamics Simulations". In: 0.24 Journal of Computational Physics 143, 519–543 (cit. on p. 46).

Klessen, R. S. (2011). "Star Formation in Molecular Clouds". In: 0.24 EAS Publications Series. Ed. by C. Charbonnel & T. Montmerle. Vol. 51. EAS Publications Series, 133–167 (cit. on pp. 8, 9, 11–13).

Klessen, R. S. & P. Hennebelle (2010). "Accretion-driven turbulence as universal process: galaxies, molecular clouds, and protostellar disks". In: 0.24 A&A 520, A17, A17 (cit. on p. 11).

Könyves, V., P. André, A. Men'shchikov, N. Schneider, D. Arzoumanian, S. Bontemps, M. Attard, F. Motte, P. Didelon, A. Maury, A. Abergel, B. Ali, J.-P. Baluteau, J.-P. Bernard, L. Cambrésy, P. Cox, J. di Francesco, A. M. di Giorgio, M. J. Griffin, P. Hargrave, M. Huang, J. Kirk, J. Z. Li, P. Martin, V. Minier, S. Molinari, G. Olofsson, S. Pezzuto, D. Russeil, H. Roussel, P. Saraceno, M. Sauvage, B. Sibthorpe, L. Spinoglio, L. Testi, D. Ward-Thompson, G. White, C. D. Wilson, A. Woodcraft & A. Zavagno (2010). "The Aquila prestellar core population revealed by Herschel". In: 0.24 A&A 518, L106, L106 (cit. on pp. 11, 12).

Koyama, H. & S.-i. Inutsuka (2002). "An Origin of Supersonic Motions in Interstellar Clouds". In: 0.24 ApJ 564, L97–L100 (cit. on p. 10).

Kroupa, P. (2001). "On the variation of the initial mass function". In: 0.24 MNRAS 322, 231–246 (cit. on pp. 14, 40, 86).

Kruijssen, J. M. D., J. E. Dale & S. N. Longmore (2015). "The dynamical evolution of molecular clouds near the Galactic Centre - I. Orbital structure and evolutionary timeline". In: 0.24 MNRAS 447, 1059–1079 (cit. on pp. 20, 89).

Kurtz, S. (2005). "Hypercompact HII regions". In: 0.24 Massive Star Birth: A Crossroads of Astrophysics. Ed. by R. Cesaroni, M. Felli, E. Churchwell & M. Walmsley. Vol. 227. IAU Symposium, 111–119 (cit. on p. 17).

Lada, C. J. & E. A. Lada (2003). "Embedded Clusters in Molecular Clouds". In: 0.24 ARA&A 41, 57 (cit. on pp. 4, 19, 88).

Lada, C. J. & B. A. Wilking (1984). “The nature of the embedded population in the Rho Ophiuchi dark cloud - Mid-infrared observations”. In: 0.24 ApJ 287, 610–621 (cit. on p. 16).

Langer, W. D., T. Velusamy, D. Li & P. F. Goldsmith (2005). “Star Forming Conditions of Quiescent Pre-Stellar Cores in Orion”. In: 0.24 Protostars and Planets V Posters. Vol. 1286, 8179 (cit. on p. 13).

Larson, R. B. (1994). “The Evolution of Molecular Clouds”. In: 0.24 The Structure and Content of Molecular Clouds. Ed. by T. L. Wilson & K. J. Johnston. Vol. 439. Lecture Notes in Physics, Berlin Springer Verlag, 13 (cit. on p. 11).

Lebouteiller, V., J. Bernard-Salas, D. G. Whelan, B. Brandl, F. Galliano, V. Charmandaris, S. Madden & D. Kunth (2011). “Influence of the Environment on Polycyclic Aromatic Hydrocarbon Emission in Star-forming Regions”. In: 0.24 ApJ 728, 45, 45 (cit. on p. 9).

Leger, A. & J. L. Puget (1984). “Identification of the ’unidentified’ IR emission features of interstellar dust?” In: 0.24 A&A 137, L5–L8 (cit. on p. 9).

Li, A. & B. T. Draine (2001). “Infrared Emission from Interstellar Dust. II. The Diffuse Interstellar Medium”. In: 0.24 ApJ 554, 778–802 (cit. on p. 94).

Lis, D. C. & P. F. Goldsmith (1989). “CO isotope studies and mass of the Sagittarius B2 molecular cloud”. In: 0.24 ApJ 337, 704 (cit. on pp. vii, ix, 92).

— (1990). “Modeling of the continuum and molecular line emission from the Sagittarius B2 molecular cloud”. In: 0.24 ApJ 356, 195 (cit. on pp. 85, 86).

Mathis, J. S., W. Rumpl & K. H. Nordsieck (1977). “The size distribution of interstellar grains”. In: 0.24 ApJ 217, 425–433 (cit. on p. 9).

Matzner, C. D. (2002). “On the Role of Massive Stars in the Support and Destruction of Giant Molecular Clouds”. In: 0.24 ApJ 566, 302–314 (cit. on p. 18).

McKee, C. F. & E. C. Ostriker (2007). “Theory of Star Formation”. In: 0.24 ARA&A 45, 565–687 (cit. on p. 8).

Mehringer, D. M., P. Palmer, W. M. Goss & F. Yusef-Zadeh (1993). “Radio continuum and radio recombination line observations of Sagittarius B2”. In: 0.24 ApJ 412, 684 (cit. on pp. 24, 72, 73, 175).

Mezger, P. G. & A. P. Henderson (1967). “Galactic H II Regions. I. Observations of Their Continuum Radiation at the Frequency 5 GHz”. In: 0.24 ApJ 147, 471 (cit. on p. 130).

Molinari, S., J. Bally, S. Glover, T. Moore, A. Noreiga-Crespo, R. Plume, L. Testi, E. Vázquez-Semadeni, A. Zavagno, J.-P. Bernard & P. Martin (2014). “The Milky Way as a Star Formation Engine”. In: 0.24 Protostars and Planets VI, 125–148 (cit. on p. 8).

Molinari, S., S. Pezzuto, R. Cesaroni, J. Brand, F. Faustini & L. Testi (2008). “The evolution of the spectral energy distribution in massive young stellar objects”. In: 0.24 A&A 481, 345–365 (cit. on pp. 88–90).

Molinari, S., E. Schisano, F. Faustini, M. Pestalozzi, A. M. di Giorgio & S. Liu (2011). “Source extraction and photometry for the far-infrared and sub-millimeter continuum in the presence of complex backgrounds”. In: 0.24 A&A 530, A133, A133 (cit. on p. 20).

Molinari, S. et al. (2010a). “Clouds, filaments, and protostars: The Herschel Hi-GAL Milky Way”. In: 0.24 A&A 518, L100, L100 (cit. on p. 11).

Molinari, S. et al. (2010b). “Hi-GAL: The Herschel Infrared Galactic Plane Survey”. In: 0.24 PASP 122, 314–325 (cit. on pp. 69, 139).

Möller, T., I. Bernst, D. Panoglou, D. Muders, V. Ossenkopf, M. Röllig & P. Schilke (2013). “Modeling and Analysis Generic Interface for eXternal numerical codes (MAGIX)”. In: 0.24 A&A 549, A21, A21 (cit. on pp. 38, 48, 49, 92).

Morgan, J. W. & E. Anders (1980). “Chemical Composition of Earth, Venus, and Mercury”. In: 0.24 Proceedings of the National Academy of Science 77, 6973–6977 (cit. on p. 7).

Morris, M. & E. Serabyn (1996). “The Galactic Center Environment”. In: 0.24 ARA&A 34, 645 (cit. on p. 20).

Motte, F., P. Andre & R. Neri (1998). “The initial conditions of star formation in the rho Ophiuchi main cloud: wide-field millimeter continuum mapping”. In: 0.24 A&A 336, 150–172 (cit. on p. 11).

Myers, P. C., T. M. Dame, P. Thaddeus, R. S. Cohen, R. F. Silverberg, E. Dwek & M. G. Hauser (1986). “Molecular clouds and star formation in the inner galaxy - A comparison of CO, H II, and far-infrared surveys”. In: 0.24 ApJ 301, 398–422 (cit. on p. 88).

Nakamura, F. & Z.-Y. Li (2007). “Protostellar Turbulence Driven by Collimated Outflows”. In: 0.24 ApJ 662, 395–412 (cit. on p. 14).

Offner, S. S. R., P. C. Clark, P. Hennebelle, N. Bastian, M. R. Bate, P. F. Hopkins, E. Moraux & A. P. Whitworth (2014). “The Origin and Universality of the Stellar Initial Mass Function”. In: 0.24 Protostars and Planets VI, 53–75 (cit. on p. 12).

Ossenkopf, V. & T. Henning (1994). “Dust opacities for protostellar cores”. In: 0.24 A&A 291, 943 (cit. on p. 92).

Oster, L. (1961). “Emission, Absorption, and Conductivity of a Fully Ionized Gas at Radio Frequencies”. In: 0.24 Reviews of Modern Physics 33, 525–543 (cit. on pp. 129, 130).

Panagia, N. (1973). “Some Physical parameters of early-type stars”. In: 0.24 AJ 78, 929 (cit. on p. 87).

Parkin, T. J., C. D. Wilson, K. Foyle, M. Baes, G. J. Bendo, A. Boselli, M. Boquien, A. Cooray, D. Cormier, J. I. Davies, S. A. Eales, M. Galametz, H. L. Gomez, V. Lebouteiller, S. Madden, E. Mentuch, M. J. Page, M. Pohlen, A. Remy, H. Roussel, M. Sauvage, M. W. L. Smith & L. Spinoglio (2012). "The gas-to-dust mass ratio of Centaurus A as seen by Herschel". In: 0.24 MNRAS 422, 2291–2301 (cit. on p. 9).

Peters, T., R. Banerjee & R. S. Klessen (2008). "Ionization front-driven turbulence in the clumpy interstellar medium". In: 0.24 Physica Scripta Volume T 132.1, 014026, 014026 (cit. on p. 11).

Peters, T., R. Banerjee, R. S. Klessen & M.-M. Mac Low (2011). "The Interplay of Magnetic Fields, Fragmentation, and Ionization Feedback in High-mass Star Formation". In: 0.24 ApJ 729, 72, 72 (cit. on p. 14).

Pierce-Price, D., J. S. Richer, J. S. Greaves, W. S. Holland, T. Jenness, A. N. Lasenby, G. J. White, H. E. Matthews, D. Ward-Thompson, W. R. F. Dent, R. Zylka, P. Mezger, T. Hasegawa, T. Oka, A. Omont & G. Gilmore (2000). "A Deep Submillimeter Survey of the Galactic Center". In: 0.24 ApJ 545, L121–L125 (cit. on pp. 85, 139).

Planck Collaboration, A. Abergel, P. A. R. Ade, N. Aghanim, M. I. R. Alves, G. Aniano, C. Armitage-Caplan, M. Arnaud, M. Ashdown, F. Atrio-Barandela & et al. (2014). "Planck 2013 results. XI. All-sky model of thermal dust emission". In: 0.24 A&A 571, A11, A11 (cit. on p. 9).

Plummer, H. C. (1911). "On the problem of distribution in globular star clusters". In: 0.24 MNRAS 71, 460 (cit. on p. 12).

Poglitsch, A., C. Waelkens, N. Geis, H. Feuchtgruber, B. Vandenbussche, L. Rodriguez, O. Krause, E. Renotte, C. van Hoof, P. Saraceno, J. Cepa, F. Kerschbaum, P. Agnèse, B. Ali, B. Altieri, P. Andreani, J.-L. Augueres, Z. Balog, L. Barl, O. H. Bauer, N. Belbachir, M. Benedettini, N. Billot, O. Boulade, H. Bischof, J. Blommaert, E. Callut, C. Cara, R. Cerulli, D. Cesarsky, A. Contursi, Y. Creten, W. De Meester, V. Doublier, E. Doumayrou, L. Duband, K. Exter, R. Genzel, J.-M. Gillis, U. Grözinger, T. Henning, J. Herreros, R. Huygen, M. Inguscio, G. Jakob, C. Jamar, C. Jean, J. de Jong, R. Katterloher, C. Kiss, U. Klaas, D. Lemke, D. Lutz, S. Madden, B. Marquet, J. Martignac, A. Mazy, P. Merken, F. Montfort, L. Morbidelli, T. Müller, M. Nielbock, K. Okumura, R. Orfei, R. Ottensamer, S. Pezzuto, P. Popesso, J. Putzeys, S. Regibo, V. Reveret, P. Royer, M. Sauvage, J. Schreiber, J. Stegmaier, D. Schmitt, J. Schubert, E. Sturm, M. Thiel, G. Tofani, R. Vavrek, M. Wetzstein, E. Wieprecht & E. Wiezorrek (2010). "The Photodetector Array Camera and Spectrometer (PACS) on the Herschel Space Observatory". In: 0.24 A&A 518, L2, L2 (cit. on p. 69).

Ponti, G., M. R. Morris, R. Terrier, F. Haberl, R. Sturm, M. Clavel, S. Soldi, A. Goldwurm, P. Predehl, K. Nandra, G. Bélanger, R. S. Warwick & V. Tatischeff (2015). "The XMM-Newton view of the central degrees of the Milky Way". In: 0.24 MNRAS 453, 172–213 (cit. on p. 139).

Portegies Zwart, S. F., S. L. W. McMillan & M. Gieles (2010). “Young Massive Star Clusters”. In: 0.24 ARA&A 48, 431 (cit. on pp. 3, 17).

Price, S. D., M. P. Egan, S. J. Carey, D. R. Mizuno & T. A. Kuchar (2001). “Midcourse Space Experiment Survey of the Galactic Plane”. In: 0.24 AJ 121, 2819–2842 (cit. on p. 139).

Qin, S.-L., P. Schilke, R. Rolffs, C. Comito, D. C. Lis & Q. Zhang (2011). “Submillimeter continuum observations of Sagittarius B2 at subarcsecond spatial resolution”. In: 0.24 A&A 530, L9, L9 (cit. on pp. 12, 38, 68, 82, 83, 177).

Reid, M. J., K. M. Menten, A. Brunthaler, X. W. Zheng, T. M. Dame, Y. Xu, Y. Wu, B. Zhang, A. Sanna, M. Sato, K. Hachisuka, Y. K. Choi, K. Immer, L. Moscadelli, K. L. J. Rygl & A. Bartkiewicz (2014). “Trigonometric Parallaxes of High Mass Star Forming Regions: The Structure and Kinematics of the Milky Way”. In: 0.24 ApJ 783, 130, 130 (cit. on pp. vii, ix, 3, 23).

Robitaille, T. P. (2010). “On the modified random walk algorithm for Monte-Carlo radiation transfer”. In: 0.24 A&A 520, A70, A70 (cit. on p. 43).

Roelfsema, P. R., F. P. Helmich, D. Teyssier, V. Ossenkopf, P. Morris, M. Olberg, R. Shipman, C. Risacher, M. Akyilmaz, R. Assendorp, I. M. Avruch, D. Beintema, N. Biver, A. Boogert, C. Borys, J. Braine, M. Caris, E. Caux, J. Cernicharo, O. Coeur-Joly, C. Comito, G. de Lange, B. Delforge, P. Dieleman, L. Dubbeldam, T. de Graauw, K. Edwards, M. Fich, F. Flederus, C. Gal, A. di Giorgio, F. Herpin, D. R. Higgins, A. Hoac, R. Huisman, C. Jarchow, W. Jellema, A. de Jonge, D. Kester, T. Klein, J. Kooi, C. Kramer, W. Laauwen, B. Larsson, C. Leinz, S. Lord, A. Lorenzani, W. Luinge, A. Marston, J. Martın-Pintado, C. McCoey, M. Melchior, M. Michalska, R. Moreno, H. Müller, W. Nowosielski, Y. Okada, P. Orleański, T. G. Phillips, J. Pearson, D. Rabois, L. Ravera, J. Rector, M. Rengel, H. Sagawa, W. Salomons, E. Sánchez-Suárez, R. Schieder, F. Schlöder, F. Schmülling, M. Soldati, J. Stutzki, B. Thomas, A. G. G. M. Tielens, C. Vastel, K. Wildeman, Q. Xie, M. Xilouris, C. Wafelbakker, N. Whyborn, P. Zaal, T. Bell, P. Bjerkeli, E. De Beck, T. Cavalié, N. R. Crockett, P. Hily-Blant, M. Kama, T. Kaminski, B. Leflóch, R. Lombaert, M. de Luca, Z. Makai, M. Marseille, Z. Nagy, S. Pacheco, M. H. D. van der Wiel, S. Wang & U. Yıldız (2012). “In-orbit performance of Herschel-HIFI”. In: 0.24 A&A 537, A17, A17 (cit. on p. 65).

Rolffs, R. (2011). “Structure of Hot Molecular Cores”. PhD thesis. University of Cologne, Germany (cit. on p. 36).

Rolffs, R., P. Schilke, C. Comito, E. A. Bergin, F. F. S. van der Tak, D. C. Lis, S.-L. Qin, K. M. Menten, R. Güsten, T. A. Bell, G. A. Blake, E. Caux, C. Ceccarelli, J. Cernicharo, N. R. Crockett, F. Daniel, M.-L. Dubernet, M. Emprechtinger, P. Encrenaz, M. Gerin, T. F. Giesen, J. R. Goicoechea, P. F. Goldsmith, H. Gupta, E. Herbst, C. Joblin, D. Johnstone, W. D. Langer, W. D. Latter, S. D. Lord, S. Maret, P. G. Martin, G. J. Melnick, P. Morris, H. S. P. Müller, J. A. Murphy, V. Ossenkopf, J. C. Pearson, M. Pérault, T. G. Phillips, R. Plume, S. Schlemmer, J. Stutzki, N. Trappe, C. Vastel, S. Wang, H. W. Yorke, S. Yu, J. Zmuidzinas, M. C. Diez-Gonzalez, R. Bachiller, J. Martin-Pintado, W. Baechtold,

M. Olberg, L. H. Nordh, J. J. Gill & G. Chattopadhyay (2010). “Reversal of infall in SgrB2(M) revealed by Herschel/HIFI observations of HCN lines at THz frequencies”. In: 0.24 A&A 521, L46, L46 (cit. on pp. 45, 106).

Rolffs, R., P. Schilke, F. Wyrowski, C. Dullemond, K. M. Menten, S. Thorwirth & A. Belloche (2011a). “Hot HCN around young massive stars at 0.1” resolution”. In: 0.24 A&A 529, A76, A76 (cit. on p. 68).

Rolffs, R., P. Schilke, Q. Zhang & L. Zapata (2011b). “Structure of the hot molecular core G10.47+0.03”. In: 0.24 A&A 536, A33, A33 (cit. on p. 82).

Rubin, R. H. (1968). “A Discussion of the Sizes and Excitation of H II Regions”. In: 0.24 ApJ 154, 391 (cit. on p. 132).

Rybicki, G. B. & A. P. Lightman (1986). 0.24 Radiative Processes in Astrophysics, 400 (cit. on p. 25).

Salpeter, E. E. (1955). “The Luminosity Function and Stellar Evolution.” In: 0.24 ApJ 121, 161 (cit. on p. 14).

Sánchez-Monge, Á. (2011). “Massive Star Formation: ionized and molecular gas emission in the first evolutionary stages”. PhD thesis. Universitat de Barcelona (cit. on p. 133).

Sánchez-Monge, Á., M. T. Beltrán, R. Cesaroni, F. Fontani, J. Brand, S. Molinari, L. Testi & M. Burton (2013). “Different evolutionary stages in massive star formation. Centimeter continuum and H_2O maser emission with ATCA”. In: 0.24 A&A 550, A21, A21 (cit. on p. 74).

Sault, R. J., P. J. Teuben & M. C. H. Wright (1995). “A Retrospective View of MIRIAD”. In: 0.24 Astronomical Data Analysis Software and Systems IV. Ed. by R. A. Shaw, H. E. Payne & J. J. E. Hayes. Vol. 77. Astronomical Society of the Pacific Conference Series, 433 (cit. on pp. 36, 48).

Sawada, T., T. Hasegawa, T. Handa & R. J. Cohen (2004). “A molecular face-on view of the Galactic Centre region”. In: 0.24 MNRAS 349, 1167–1178 (cit. on p. 20).

Scalo, J. & B. G. Elmegreen (2004). “Interstellar Turbulence II: Implications and Effects”. In: 0.24 ARA&A 42, 275–316 (cit. on p. 11).

Schmiedeke, A., P. Schilke, T. Möller, Á. Sánchez-Monge, E. Bergin, C. Comito, T. Csengeri, D. C. Lis, S. Molinari, S.-L. Qin & R. Rolffs (2016). “The physical and chemical structure of Sagittarius B2. I. Three-dimensional thermal dust and free-free continuum modeling on 100 au to 45 pc scales”. In: 0.24 A&A 588, A143, A143 (cit. on pp. 65, 71, 181).

Schneider, N., P. André, V. Könyves, S. Bontemps, F. Motte, C. Federrath, D. Ward-Thompson, D. Arzoumanian, M. Benedettini, E. Bressert, P. Didelon, J. Di Francesco, M. Griffin, M. Hennemann, T. Hill, P. Palmeirim, S. Pezzuto, N. Peretto, A. Roy, K. L. J. Rygl, L. Spinoglio & G. White

(2013). “What Determines the Density Structure of Molecular Clouds? A Case Study of Orion B with Herschel”. In: 0.24 ApJ 766, L17, L17 (cit. on p. 90).

Schneider, N., T. Csengeri, S. Bontemps, F. Motte, R. Simon, P. Hennebelle, C. Federrath & R. Klessen (2010). “Dynamic star formation in the massive DR21 filament”. In: 0.24 A&A 520, A49, A49 (cit. on p. 11).

Schuller, F., K. M. Menten, Y. Contreras, F. Wyrowski, P. Schilke, L. Bronfman, T. Henning, C. M. Walmsley, H. Beuther, S. Bontemps, R. Cesaroni, L. Deharveng, G. Garay, F. Herpin, B. Lefloch, H. Linz, D. Mardones, V. Minier, S. Molinari, F. Motte, L.-Å. Nyman, V. Reveret, C. Risacher, D. Russeil, N. Schneider, L. Testi, T. Troost, T. Vasyunina, M. Wienen, A. Zavagno, A. Kovacs, E. Kreysa, G. Siringo & A. Weiß (2009). “ATLASGAL - The APEX telescope large area survey of the galaxy at 870 μm”. In: 0.24 A&A 504, 415–427 (cit. on p. 69).

Scoville, N. Z., P. M. Solomon & A. A. Penzias (1975). “The molecular cloud Sagittarius B2”. In: 0.24 ApJ 201, 352 (cit. on pp. 23, 71).

Seab, C. G. (1987). “Grain destruction, formation, and evolution”. In: 0.24 Interstellar Processes. Ed. by D. J. Hollenbach & H. A. Thronson Jr. Vol. 134. Astrophysics and Space Science Library, 491–512 (cit. on p. 9).

Seaton, M. J. (1959). “Radiative recombination of hydrogenic ions”. In: 0.24 MNRAS 119, 81 (cit. on p. 132).

Seifried, D., Á. Sánchez-Monge, S. Walch & R. Banerjee (2016). “Revealing the dynamics of Class 0 protostellar discs with ALMA”. In: 0.24 ArXiv e-prints (cit. on p. 19).

Shu, F. H., F. C. Adams & S. Lizano (1987). “Star formation in molecular clouds - Observation and theory”. In: 0.24 ARA&A 25, 23 (cit. on pp. 14, 15).

Skrutskie, M. F., R. M. Cutri, R. Stiening, M. D. Weinberg, S. Schneider, J. M. Carpenter, C. Beichman, R. Capps, T. Chester, J. Elias, J. Huchra, J. Liebert, C. Lonsdale, D. G. Monet, S. Price, P. Seitzer, T. Jarrett, J. D. Kirkpatrick, J. E. Gizis, E. Howard, T. Evans, J. Fowler, L. Fullmer, R. Hurt, R. Light, E. L. Kopan, K. A. Marsh, H. L. McCallon, R. Tam, S. Van Dyk & S. Wheelock (2006). “The Two Micron All Sky Survey (2MASS)”. In: 0.24 AJ 131, 1163–1183 (cit. on p. 139).

Smith, M. D. (2014). “Evolutionary tracks of massive stars during formation”. In: 0.24 MNRAS 438, 1051–1066 (cit. on p. 74).

Smith, R. J., R. Shetty, H. Beuther, R. S. Klessen & I. A. Bonnell (2013). “Line Profiles of Cores within Clusters. II. Signatures of Dynamical Collapse during High-mass Star Formation”. In: 0.24 ApJ 771, 24, 24 (cit. on p. 19).

Steinacker, J., A. Bacmann, T. Henning, R. Klessen & M. Stickel (2005). “3D continuum radiative transfer in complex dust configurations. II. 3D structure of the dense molecular cloud core ρ Oph D”. In: 0.24 A&A 434, 167–180 (cit. on pp. 36, 92).

Steinacker, J., M. Baes & K. D. Gordon (2013). “Three-Dimensional Dust Radiative Transfer*”. In: 0.24 ARA&A 51, 63–104 (cit. on pp. 35, 36).

Sternberg, A. (1988). “The infrared response of molecular hydrogen gas to ultraviolet radiation - A scaling law”. In: 0.24 ApJ 332, 400–409 (cit. on p. 11).

Stolovy, S., S. Ramirez, R. G. Arendt, A. Cotera, F. Yusef-Zadeh, C. Law, D. Gezari, K. Sellgren, J. Karr, H. Moseley & H. A. Smith (2006). “A mid-infrared survey of the inner 2 $\times$ 1.5 degrees of the Galaxy with Spitzer/IRAC”. In: 0.24 Journal of Physics Conference Series 54, 176–182 (cit. on p. 139).

Straizys, V. & G. Kuriliene (1981). “Fundamental stellar parameters derived from the evolutionary tracks”. In: 0.24 Ap&SS 80, 353–368 (cit. on p. 42).

Tafalla, M., P. C. Myers, P. Caselli, C. M. Walmsley & C. Comito (2002). “Systematic Molecular Differentiation in Starless Cores”. In: 0.24 ApJ 569, 815–835 (cit. on p. 13).

Tan, J. C., M. T. Beltrán, P. Caselli, F. Fontani, A. Fuente, M. R. Krumholz, C. F. McKee & A. Stolte (2014). “Massive Star Formation”. In: 0.24 Protostars and Planets VI, 149–172 (cit. on p. 8).

Traficante, A., L. Calzoletti, M. Veneziani, B. Ali, G. de Gasperis, A. M. di Giorgio, F. Faustini, D. Ikhenaode, S. Molinari, P. Natoli, M. Pestalozzi, S. Pezzuto, F. Piacentini, L. Piazzo, G. Polenta & E. Schisano (2011). “Data reduction pipeline for the Hi-GAL survey”. In: 0.24 MNRAS 416, 2932–2943 (cit. on p. 69).

Vacca, W. D., C. D. Garmany & J. M. Shull (1996). “The Lyman-Continuum Fluxes and Stellar Parameters of O and Early B-Type Stars”. In: 0.24 ApJ 460, 914 (cit. on pp. 40, 52, 87).

van Dishoeck, E. F. & J. H. Black (1986). “Comprehensive models of diffuse interstellar clouds - Physical conditions and molecular abundances”. In: 0.24 ApJS 62, 109–145 (cit. on p. 11).

van Dishoeck, E. F. & G. A. Blake (1998). “Chemical Evolution of Star-Forming Regions”. In: 0.24 ARA&A 36, 317 (cit. on pp. 15, 16).

Van Loo, S., M. J. Butler & J. C. Tan (2013). “Kiloparsec-scale Simulations of Star Formation in Disk Galaxies. I. The Unmagnetized and Zero-feedback Limit”. In: 0.24 ApJ 764, 36, 36 (cit. on p. 9).

Vázquez-Semadeni, E., G. C. Gómez, A.-K. Jappsen, J. Ballesteros-Paredes & R. S. Klessen (2009). “High- and Low-Mass Star-Forming Regions from Hierarchical Gravitational Fragmentation. High Local Star Formation Rates with Low Global Efficiencies”. In: 0.24 ApJ 707, 1023–1033 (cit. on p. 11).

Vogel, S. N., R. Genzel & P. Palmer (1987). “The dispersal of dense protostellar material - NH3 hot cores and outflows in Sagittarius B2”. In: 0.24 ApJ 316, 243 (cit. on p. 88).

Walch, S., P. Girichidis, T. Naab, A. Gatto, S. C. O. Glover, R. Wünsch, R. S. Klessen, P. C. Clark, T. Peters, D. Derigs & C. Baczynski (2015). “The SILCC (SImulating the LifeCycle of molecular Clouds) project - I. Chemical evolution of the supernova-driven ISM”. In: 0.24 MNRAS 454, 238–268 (cit. on p. 18).

Ward-Thompson, D., P. André & J. M. Kirk (2002). “The initial conditions of isolated star formation - V. ISOPHOT imaging and the temperature and energy balance of pre-stellar cores”. In: 0.24 MNRAS 329, 257–276 (cit. on p. 13).

Ward-Thompson, D., F. Motte & P. Andre (1999). “The initial conditions of isolated star formation - III. Millimetre continuum mapping of pre-stellar cores”. In: 0.24 MNRAS 305, 143–150 (cit. on p. 12).

Ward-Thompson, D. & A. P. Whitworth (2011). 0.24 An Introduction to Star Formation (cit. on p. 25).

Whitworth, A. (1979). “The erosion and dispersal of massive molecular clouds by young stars”. In: 0.24 MNRAS 186, 59–67 (cit. on p. 18).

Wilson, T. L. & R. Rood (1994). “Abundances in the Interstellar Medium”. In: 0.24 ARA&A 32, 191 (cit. on p. 101).

Wolfire, M. G., D. Hollenbach & C. F. McKee (2010). “The Dark Molecular Gas”. In: 0.24 ApJ 716, 1191–1207 (cit. on p. 11).

Wolfire, M. G., D. Hollenbach, C. F. McKee, A. G. G. M. Tielens & E. L. O. Bakes (1995). “The neutral atomic phases of the interstellar medium”. In: 0.24 ApJ 443, 152–168 (cit. on p. 10).

Wooden, D. H., S. B. Charnley & P. Ehrenfreund (2004). “Composition and evolution of interstellar clouds”. In: 0.24 Comets II. Ed. by M. C. Festou, H. U. Keller & H. A. Weaver, 33–66 (cit. on p. 10).

Yusef-Zadeh, F., J. W. Hewitt & W. Cotton (2004). “A 20 Centimeter Survey of the Galactic Center Region. I. Detection of Numerous Linear Filaments”. In: 0.24 ApJS 155, 421–550 (cit. on pp. 136, 139).

Zernickel, A. (2015). “Submm Observations of Massive Star Formation in the Giant Molecular Cloud NGC 6334 : Gas Kinematics with Radiative Transfer Models”. PhD thesis. I. Physikalisches Institut der Universität zu Köln, Zülpicher Straße 77, 50937, Köln, Germany <EMAIL>zernickel@ph1.uni-koeln.de</EMAIL> (cit. on pp. 43, 123).

Zhang, Q., Y. Wang, T. Pillai & J. Rathborne (2009). “Fragmentation at the Earliest Phase of Massive Star Formation”. In: 0.24 ApJ 696, 268–273 (cit. on p. 8).

Zinnecker, H. & H. W. Yorke (2007). “Toward Understanding Massive Star Formation”. In: 0.24 ARA&A 45, 481–563 (cit. on pp. 8, 15).

2MASS Two Micron All Sky Survey. 136, 137

ALMA Atacama Large Millimeter Array. vii, 3, 18, 35, 38
AMR adaptive mesh refinement. 47, 71
APEX Atacama Pathfinder Experiment. 136, 137
ATLASGAL APEX Telescope Large Area Survey of the Galaxy. 69, 80, 136, 137

BGPS Bolocam Galactic Plane Survey. 136, 137

CARMA Combined Array for Research in Millimeter-wave Astronomy. III
CDMS Cologne Database of Molecular Spectroscopy. 29, 99
CMF core mass function. 12
CMZ Central Molecular Zone. XXIII, XXVII, 7, 9, 20, 22, 89, 123, 135, 137, 152
CNM cold neutral medium. 10
COM complex organic molecule. 15
CRC Collaborative Research Centre. I, III
CSO Caltech Submillimeter Observatory. 136, 137

DFG Deutsche Forschungsgesellschaft. I
DN data number. 135

EPIC European Photon Imaging Cameras. 136, 137

FWHM full-width at half-maximum. 45

GALEX Galaxy Evolution Explorer. 136, 137
GMC giant molecular cloud. 8, 11, 17–19

Hi-GAL Herschel Infrared Galactic Plane Survey. 69, 136, 137
HIM hot ionized medium. 10

IGM intergalactic medium. 9
IMF initial mass function. XXIII, 14, 40–42, 87
IRAC Infrared Array Camera. 135–137
ISM interstellar medium. XXVII, 8–11, 101

JCMT James Clerk Maxwell Telescope. 136, 137

LABOCA Large APEX Bolocam Camera. 136, 137
LSR local standard of rest. 20

MRW Modified Random Walk. 43, 57, 59
MSX Midcourse Space Experiment. 136, 137

PACS Photodetector Array Camera & Spectrometer. 69, 136, 137
PAH polycyclic aromatic hydrocarbon. 9
PDF probability density function. 12

SCUBA-2 Submillimetre Common-User Bolometer Array 2. 136, 137
SED spectral energy distribution. 15, 17, 49, 90
Sgr B2 Sagittarius B2. vii, x, 3–5, 7, 44, 51, 56, 57, 65, 71, 85, 89, 90, 99, 100, 113, 121–123, 135, 137, 152
SMA Submillimeter Array. 36, 48, 65, 68
SPIRE Spectral and Photometric Imaging Receiver. 69, 136, 137

VAMDC Virtual Atomic and Molecular Data Centre. 29
VLA Very Large Array. vii, 18, 35, 65, 137

WIM warm ionized medium. 10
WNM warm neutral medium. 10

XMM-Newton X-ray Multi-Mirror Mission. 136, 137

YMC young massive cluster. 3, 4, 17

ZAMS Zero-Age-Main-Sequence. 39, 40, 42, 52, 89

Erklärung

Ich versichere, dass ich die von mir vorgelegte Dissertation selbständig angefertigt, die benutzten Quellen und Hilfsmittel vollständig angegeben und die Stellen der Arbeit – einschließlich Tabellen, Karten und Abbildungen –, die anderen Werken im Wortlaut oder dem Sinn nach entnommen sind, in jedem Einzelfall als Entlehnung kenntlich gemacht habe; dass diese Dissertation noch keiner anderen Fakultät oder Universität zur Prüfung vorgelegen hat; dass sie – abgesehen von unten angegebenen Teilpublikationen – noch nicht veröffentlich worden ist, sowie, dass ich eine solche Veröffentlichung vor Abschluss des Promotionsverfahrens nicht vornehmen werde.

Die Bestimmungen der Promotionsordnung sind mir bekannt. Die von mir vorgelegte Dissertation ist von Prof. Dr. Peter Schilke betreut worden.

Nachfolgend genannte Teilpublikationen liegen vor:

- **The physical and chemical structure of Sagittarius B2. I. Three-dimensional thermal dust and free-free continuum modeling on 100 au to 45 pc scales** A. Schmiedeke, P. Schilke, Th. Möller, Á. Sánchez-Monge, E. Bergin, C. Comito, T. Csengeri, D. C. Lis, S. Molinari, S.-L. Qin, and R. Rolffs, 2016, A&A, 588, A143

Ich versichere, dass ich alle Angaben wahrheitsgemäß nach bestem Wissen und Gewissen gemacht habe und verpflichte mich, jedmögliche, die obigen Angaben betreffenden Veränderungen, dem Dekanat unverzüglich mitzuteilen.

Köln, 02. Mai 2016

Anika Schmiedeke